PRECIPITATION REACTIONS IN A CR-MN-N AUSTENITIC STEEL WITH NIOBIUM AND VANADIUM ADDITIONS

BY

JANET ANN BASSON

A thesis submitted to the Faculty of Engineering of the University of Cape Town in fulfilment of the requirements for the degree of Doctor of Philosophy.

CENTRE FOR MATERIALS ENGINEERING
DEPARTMENT OF MECHANICAL ENGINEERING
UNIVERSITY OF CAPE TOWN
MARCH 2000

ABSTRACT

PRECIPITATION REACTIONS IN A CR-MN-N STEEL CONTAINING NIOBIUM AND VANADIUM ADDITIONS

By: Janet Ann Basson

The work presented in this thesis is an investigation of the influence of niobium and vanadium on the microstructural evolution of a high nitrogen steel alloy during various ageing treatments. The motivation for the niobium and vanadium additions was to induce precipitate reactions that would result in a homogeneous distribution of particles and consequently improve the hardness of the steel. These steels were intended for applications requiring good wear resistance, thus both materials' hardness and capacity for plastic work should be optimised. It was important therefore to limit the associated loss in the materials' capacity for plastic work that can result from precipitation reactions.

Eight alloy compositions, with different levels of niobium and vanadium, were selected for investigation. Specimens of these alloys were first solution treated at 1300°C and then aged at 1100°C, 1000°C and 800°C for various times. The precipitate evolution during ageing was characterised using light microscopy, and the precipitate composition and crystallography were identified using x-ray mapping and electron diffraction techniques.

Both MX precipitation and M_2X precipitation were observed in the range of alloys investigated, but of particular interest was the formation of M_2X precipitates in a discontinuous cellular manner, which frequently competed with the MX precipitation reaction. The niobium and vanadium balance in the alloys determined the nature of the reaction that occurred at each temperature, which in turn affected the mechanical properties of the steel. M_2X precipitation embrittled the steel, whereas MX precipitation improved the strength, without reducing the materials' ability to plastically deform. Improved wear performance of the high nitrogen steel alloys is strongly dependent on the niobium and vanadium balance in the alloy because of the effect of these additions on precipitation reactions.

ACKNOWLEDGEMENTS

There are many people to thank for their assistance with this thesis and in particular I would like to thank:

Associate Professor R. D. Knutsen and Dr C. I. Lang, my supervisors for the duration of this PhD project, for their endless encouragement and support, many fruitful scientific discussions and for being friends and mentors over the years.

Columbus Joint Venture for their financial assistance and in particular Lucien Matthews and John Tarborton for their advice and technical support.

The National Research Foundation for their financial assistance.

The staff at the electron microscope unit at the University of Cape Town for their help with the electron microscopy techniques used during this project. In particular, Professor B.T. Sewell for his help in organising a transmission electron microscope with convergent beam electron diffraction facilities for my use in the Western Cape. Mr D. Gerneke for his help with the x-ray mapping techniques used in this project. Mr M A Jaffer for his help with the TEM work.

Dr S. Takaihichi and Ms T. Stander from the Department of Virology at the University of Stellenbosch Medical School for their help with the Philips CM 12 transmission electron microscope during the time that I used the instrument.

Professor P. Zilla from the Cape Heart Centre at the University of Cape Town Medical School, for allowing me the use of the Philips 420 transmission electron microscope. I would also like to thanks Ms N Samodien for her assistance with the instrument and development of negatives.

Mr D Johnston from Philips for his assistance with both the Philips CM 12 and the Philips 420 transmission electron microscope and for his patience in answering my many questions.

Glen Newins for his help in rebuilding the vacuum furnace many times during this project, for machining large numbers very hard high nitrogen steel specimens, and for all the laughs and encouragement.

Peter Jacobs for his eager help in the workshop.

Mira Topic for her assistance and encouragement over the years.

Julie Henry for her administrative assistance and friendship.

James Petersen for his patience in printing of the many photographs shown in this project.

Adriaan Loedolff for his assistance in the laboratory.

The students in the department over the years for all the great times and who have all made this time enjoyable and memorable.

My very special friends, Caryn, Liesl, Milly, Nina, Ingrid, Carol, Angela, Steve, Werner, Alastair, Murray, and Jonathan for their understanding and endless support.

My family for their endless support and encouragement and mom for proof reading the thesis.

Finally, my husband Deon, for inspiring me everyday to dream bigger dreams, for believing in me and for his incredible support, patience and encouragement.

Dedicated to Deon

LIST OF ABBREVIATIONS

CBED – Convergent Beam Electron Diffraction

CIIM – Chemically Induced Boundary Migration

DCP – Discontinuous Cellular Precipitation

DIGM – Diffusion Induced Boundary Migration

EBDS – Electron Backscattered Diffraction

FCC – Face Centred Cubic

HCP – Hexagonal Close packed

HNS – High Nitrogen Steel

K-M – Kossel-Möllenstedt

SAD – Selected Area Diffraction

SEM – Scanning Electron Microscope

TEM – Transmission Electron Microscope

V_{in} – Index for the influence of vanadium on precipitate formation in the high nitrogen steel alloys at 1100°C.

XRD – X-Ray Diffraction

Indexing conventions used in this thesis:

Miller Index :(111) = (-111)

TABLE OF CONTENTS

1. INTRODUCTION

High nitrogen steel alloys are used widely today in many engineering applications. The popularity of this engineering material has developed from extensive research conducted on nitrogen alloyed steels over the last ten years. The benefits of nitrogen additions to stainless steels have been known since the 1930s, but complications associated with the manufacture of alloys with appreciable nitrogen additions limited the use of this element. More recently, manufacturing methods have improved and high nitrogen steels, with up to 1 wt% nitrogen additions, are available commercially. The nitrogen is either introduced to the steel by applying a high nitrogen pressure to the melt, or by improving the solubility of the nitrogen in the melt by appropriate alloying. A range of similar alloys, with different nitrogen contents, are currently produced by Columbus Stainless for commercial use and have been allocated the trade name CROMANITE™.

A cast high nitrogen steel alloy, similar to CROMANITE™, but with greater nitrogen levels, was intended for applications requiring good wear resistance, pertinent to the mining industry in South Africa as liners for ore chutes and floor pans of ore carrying trucks. The excellent combination of high strength and good toughness exhibited by these materials makes them suitable candidates for such applications. It was thought that the addition of niobium and vanadium to the steel would induce precipitation reactions, such that a homogeneous distribution of precipitates would form in the austenite and improve the strength of the steel. Similar precipitation reactions occur in high strength low alloy (HSLA) steels as a result of niobium and vanadium additions and these precipitates are partly responsible for the high strength of these materials. Thus the motivation for the addition of niobium and vanadium to the high nitrogen steel alloy was for further improvement of the mechanical performance of the steel, with specific emphasis on the wear resistance of the steel.

In spite of the large amount of research that has been completed in the last ten years on high nitrogen steels, there has been little investigation of the effect of precipitate forming elements such as niobium, vanadium, titanium, zirconium and tungsten on the microstructural evolution in high nitrogen steels. In addition, few results have been reported on the mechanical behaviour of high nitrogen steels containing precipitates other than chromium nitrides. A significant amount of work has been published on the addition of precipitate forming elements such as niobium and vanadium to conventional stainless steels with regard to the improvement of creep resistance. Some comparisons can be made between precipitate evolution in these steels and high nitrogen steels. In addition, the nature of precipitate formation in HSLA steels due to additions such as niobium and vanadium can be used to explain observations in the high nitrogen steel.

The objective of the current study was to determine the optimum niobium and vanadium levels that should be added to the high nitrogen steel base composition so that a distribution of precipitates would form and improve the wear performance of the steel. An initial investigation of precipitate evolution in a range of five alloys, with different niobium and vanadium levels, showed that that these additions result in precipitation reactions that would not otherwise be expected in the steel. Further, these elements also influence the formation of chromium nitrides, a form of precipitation that was expected in the steel. From these initial observations it was decided that three more alloys, with different combinations of niobium and vanadium, were required for a complete characterisation of the influence of niobium and vanadium additions to the high nitrogen steel base alloy.

The objective of this thesis is to characterise the influence of niobium and vanadium additions on the microstructural evolution in high nitrogen steel alloys. Eight different alloys were studied with different levels of niobium and vanadium additions such that the combined effect of the elements on the microstructure could be evaluated as well as the individual influence of each element. Three different ageing temperatures were chosen so that the influence of niobium and vanadium on the precipitation reactions that were expected to occur in the high nitrogen steel alloy could be characterised.

Further, the selection of ageing temperatures allowed an investigation of those precipitation reactions that were a consequence of the niobium and vanadium additions to the high nitrogen steel base composition.

The solidification behaviour of the alloys determined the nature of the microstructure in the solution treated condition, which in turn influenced the behaviour of the steel subsequent to ageing treatments. Evidence of precipitate formation during solidification therefore motivated a study of the influence of niobium and vanadium additions on the solidification behaviour of the high nitrogen steel alloys. The discontinuous cellular precipitation of chromium nitrides commonly observed in high nitrogen steels was given much attention, since niobium and vanadium additions showed a profound influence on this reaction. The formation of fine niobium and vanadium rich nitrides showed the most potential for improved wear properties; thus the influence of ageing time on the growth of these precipitates and consequent influence on mechanical behaviour was also investigated.

The effect of the different forms of precipitation on the tensile properties of the alloys was evaluated. Alloys in which precipitate reactions resulted in a good combination of strength and ductility were selected for abrasive wear tests, to determine whether or not these precipitation reactions did in fact achieve the objective of improving the wear performance of the high nitrogen steel alloys.

2. LITERATURE REVIEW

2.1 HIGH NITROGEN STEELS - BACKGROUND

Austenitic stainless steels account for the largest consumption of stainless steels world wide[1], and are known for their good corrosion resistance and excellent formability[2,3]. The strength of austenitics is inherently low, of the order of 300MPa[2], and owing to their popularity there has been a demand to improve the strength of austenitic stainless steels. Attempts to improve the strength of austenitics, by cold work, substitutional solid solution strengthening and precipitation of intermetallic phases have not been successful in optimising both the strength and toughness of the steel[2-4]. Irvine *et al* investigated the possibilities of improving the strength of austenitics, both by solid solution strengthening and by precipitation hardening[4]. Although solid solution strengthening by substitutional elements makes little contribution to the strength of austenitic stainless steels, the addition of interstitial elements improves the strength considerably, without a notable loss in toughness[4,5,6],[7]. Figure 2.1.1 shows the effect of various alloy elements on the strength of austenitic steels and shows that nitrogen has the most profound effect on improving strength by solid solution strengthening.

The influence of nitrogen additions on austenitic steels has been the subject of research since the 1940s, but mainly as a substitute for nickel additions, and usually added in combination with manganese[8]. Nitrogen stabilises the austenite phase, and prevents the transformation to martensite during rapid cooling and deformation, providing a cheaper alternative to nickel[8,9]. Because of high nickel costs and reduced availability, in the 1950s a nickel free austenitic stainless steel was produced with an alternative composition of 0.5 wt% nitrogen and 15 wt% manganese[8]. Currently, nickel free stainless steels show a cost advantage over the AISI 316 and 304 grades and consequently high nitrogen steels have been more popular[10,11]. Columbus Stainless in South Africa, have manufactured an austenitic nickel free steel, containing nitrogen additions in excess of 0.5 wt% and manganese levels greater than 12 wt% and given the steel the trade name CROMANITE™[12].

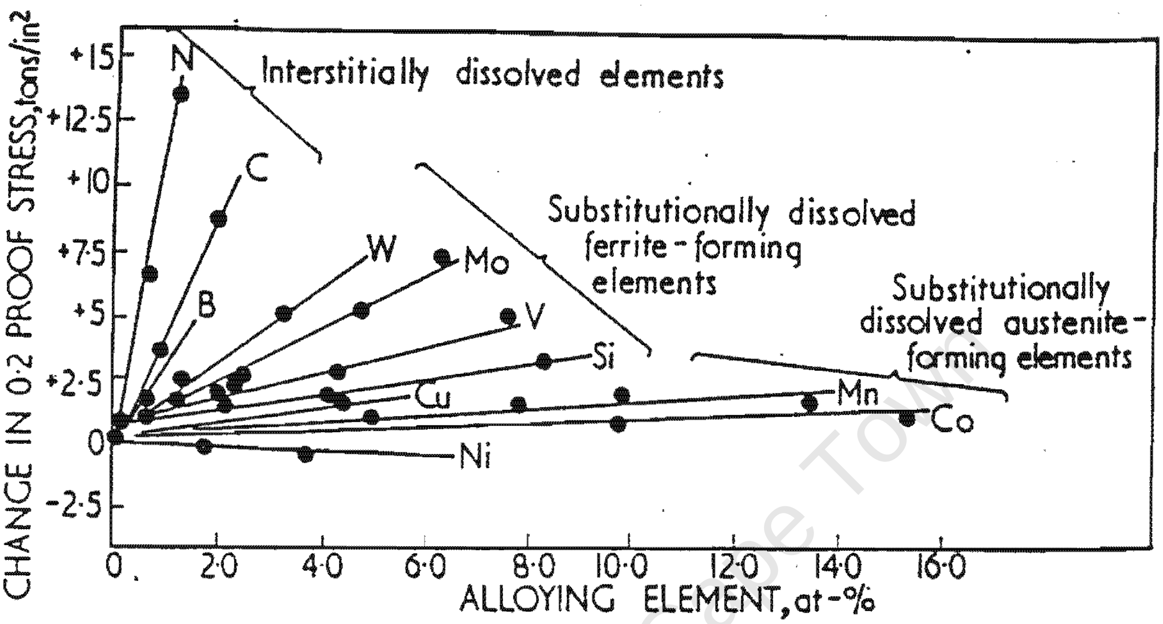

Fig.2.1.1 The effect of alloy elements on the solid solution strengthening of austenitic stainless steels after Irvine et al[4].

A disadvantage of alloying steels with nitrogen is its low solubility in the steel melt and consequent complications during manufacture. The solubility of nitrogen in liquid iron is approximately 0.045 wt% at 1600°C at atmospheric pressure, but can be improved by employing a nitrogen overpressure to the melt and by appropriate alloy additions[13,14,16]. The remarkable effect of nitrogen on the strength of austenitics has motivated for improved manufacturing techniques, which have resulted in nitrogen levels of up to 1 wt%[13]. There are two methods whereby nitrogen can be introduced in the melt, first by nitrogen pick-up via a reaction at the gas-melt interface, and second by the introduction of nitrided materials or nitride compounds in the melt[13]. The most common method used to manufacture commercial high nitrogen steels is pressurised electro-slag remelting (PSER), where the nitrogen is introduced into the melt by addition of nitrided material or by nitride compounds and the nitrogen in the melt is kept stable by a nitrogen pressure above the melt[13,15,16]. To avoid degassing, the melt is often allowed to solidify under nitrogen pressure[15,16]. Nitrogen can also be introduced in the steel by powder metallurgy routes where metal powders are first nitrided, and then compacted by hot isostatic pressing (HIP)[15,16]. Alternatively the metal powders are combined with chromium nitride powder and then HIPed[16]. The benefits of nitrogen on austenitics can also be realised by nitriding finished metal parts, but this strengthening effect is limited to thin sections, or the surfaces of larger sections[13,16].

It is possible, with the correct alloy chemistry, to cast high nitrogen steels at atmospheric pressure[14]. Figure 2.1.2 shows the influence of alloy additions on the activity coefficient (f_N) of nitrogen in the melt, which is used to indicate the degree of solubility of nitrogen in the melt, a low value of f_N meaning a high solubility[14]. Manganese and chromium additions greatly improve the solubility of nitrogen in the melt[14]. Other elements such as niobium, titanium, vanadium and zirconium also improve the nitrogen solubility, but their use is limited to low levels since they have a tendency to form nitrides[10,13,16]. The CROMANITE™ alloy is cast at atmospheric pressure and the nitrogen levels are achieved by correct alloy additions[12].

Manganese has little influence on the strength of austenitic stainless steels but the advantage of alloying with this element is its effect on nitrogen solubility and its ability to stabilise the austenite phase[17,18]. Manganese also increases the work hardening ability of the austenitics and consequently improves the toughness[17,18]. Likewise nitrogen additions also improve the work hardening ability and toughness of the steel[6,7,17,18]. It has been reported that high nitrogen-manganese steels have the best combination of strength and toughness of all materials available today (figure 2.1.3)[7].

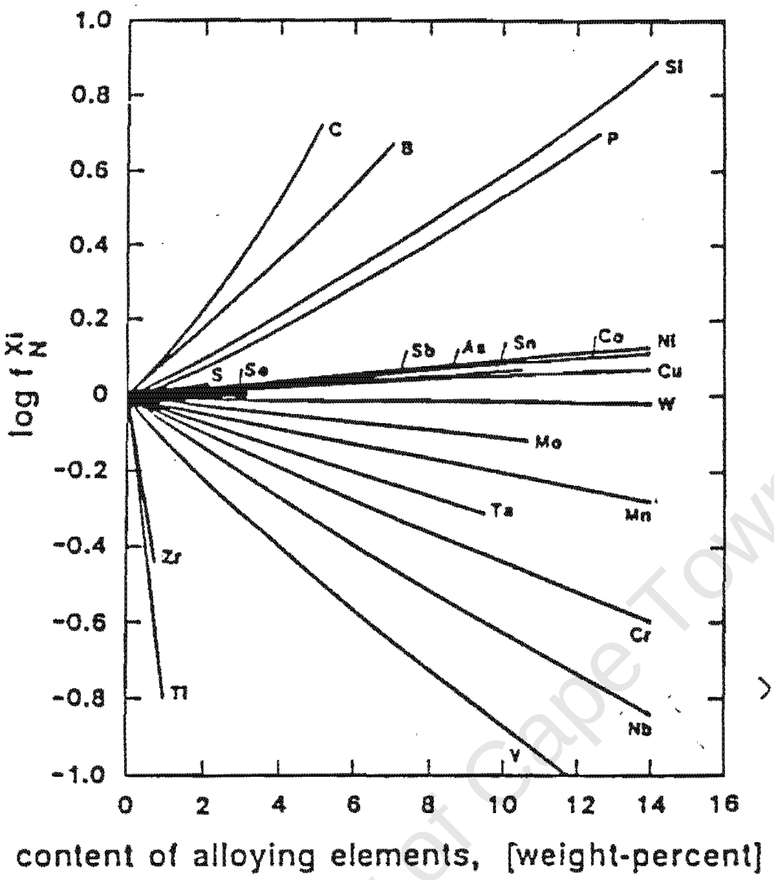

Fig. 2.1.2 The influence of alloy additions on the solubility of nitrogen in the melt represented by the parameter, f_N *after Rechsteiner et al*[14].

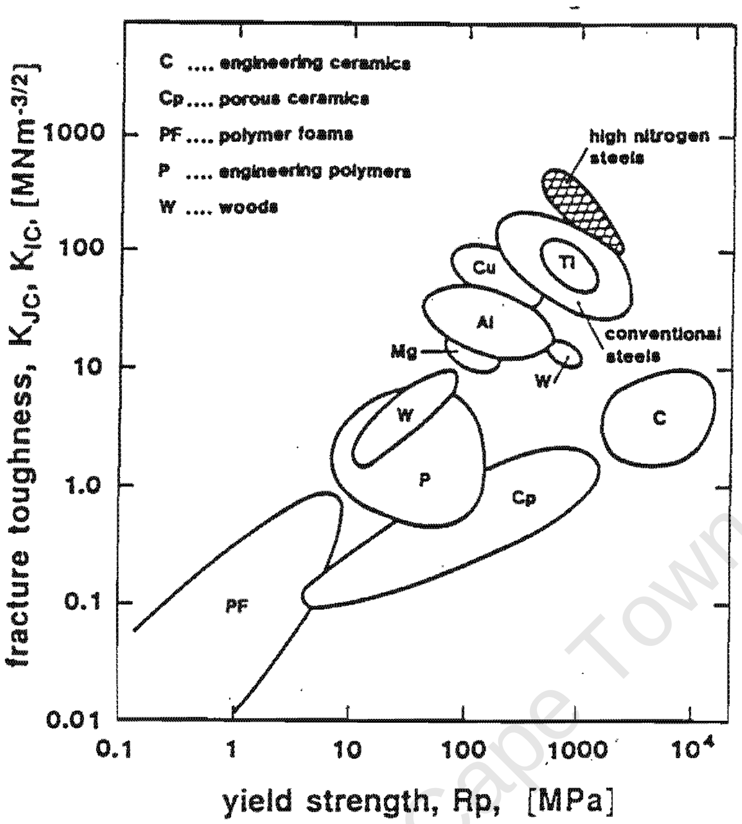

Fig. 2.1.3 The relationship between strength and toughness of materials available today, after Speidel[7].

Nitrogen improves the strength of austenitics via several different strengthening mechanisms. The nitrogen atoms in solution in the austenite cause the face centred cubic (FCC) structure to be distorted, which hinders dislocation motion, thus increasing the yield strength[19,20]. The degree of distortion is often measured in terms of a change in lattice parameter of the austenite, and is used as an indication of the nitrogen concentration on the steel[19]. In addition to this solid solution strengthening effect, nitrogen additions improve the capability of grain boundaries to act as obstacles to dislocation movement, consequently increasing the factor K_y, used in the Hall-Petch relationship (an equation that relates increased yield stress with decreasing grain size)[19,20,21]. Nitrogen additions to austenitics lower the stacking fault energy of the steel considerably[19,22,23]. Reduced stacking fault energy promotes planar arrays of dislocations[24], which enhances the effect of grain boundaries to resist dislocation motion[21]. Nitrogen alloyed steels therefore demonstrate a greater yield strength for a given grain size than steels without nitrogen additions[19-25]. The effect of nitrogen levels on the Hall-Petch factor, K_y at three different temperatures, 20°C, 300°C and 600°C is shown figure 2.1.4[21].

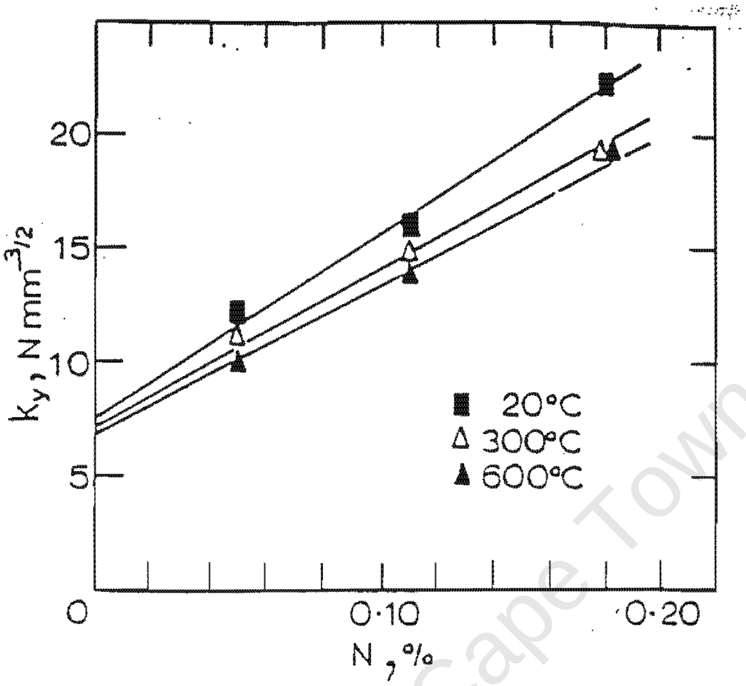

Fig.2.1.4 The effect of nitrogen content on the Hall-Petch factor, K_y for austenitic steels after Norström[21].

A further consequence of reduced stacking fault energy in the steel, is the ability of the material to work harden considerably before failure[24,26,27]. In materials with low SFE, deformation occurs by planar slip, as opposed to cross slip[24] and in high nitrogen steels this effect is illustrated by both planar glide and deformation twinning occurring at lower strains[24,25]. Further, the deformation structure is initially characterised by the intersection of glide planes and later by intersection of twin planes and second order twinning[24,28]. It is these deformation characteristics that account for the enhanced work hardening ability of high nitrogen steels.

High nitrogen steels have been observed to lose their toughness at low temperatures. It has been observed that when HNS fracture at temperatures below 100K, flat facets are observed on the fracture surfaces[29]. Brittle fracture therefore occurred by some sort of cleavage mechanism but since there are no river lines and only straight facets, another mechanism must govern brittle fracture[29]. The reasons that have been given for the flat facets on the fracture surface are linked to the low stacking fault energy of these materials as a result of high nitrogen and manganese contents[29]. Since the stacking fault energy is low, cross slip of dislocations is inhibited and dislocation motion is strongly planar. The planarity of glide results in large amounts of slip on the {111} planes. This can lead to the formation of slip bands, which have been identified as the flat facets on the fracture surface[29]. Muller *et al* gave another explanation for brittle fracture, and said that the intersection of mechanical twins (both first order and second order) results in stress concentration at the point of intersection and finally results in crack initiation and crack propagation along the twin planes[30].

The high strength and good toughness of high nitrogen steels make these materials suitable for a wide range of applications, such as wire ropes, springs and bolt materials[13]. The CROMANITE™ steel, produced in South Africa, was intended for wear applications, specifically in the mining industry and consequently has been used as liners for chutes, lifter bars in ore crushers and liners for lorries that transport ore[12]. It was thought that the addition of precipitate forming elements such as niobium and vanadium might result in increased hardness of the steel, thus making it better suited for wear applications.

2.2 PRECIPITATION REACTIONS IN HIGH NITROGEN STEELS

Different precipitation reactions are favourable in high nitrogen steels: some are a result of the addition of precipitate forming elements and others are a consequence of the high chromium and nitrogen levels in the steel. In the sections that follow, the precipitation reactions that commonly occur in high nitrogen steels are discussed first. These reactions are restricted to different forms of chromium nitride precipitation observed in high nitrogen steels. A discussion of the discontinuous cellular mode of precipitation follows, with particular reference to chromium nitride precipitation in high nitrogen steels. Two possible precipitation reactions are possible in steels as a consequence of niobium and vanadium: those that form during solidification and are often characterised by a eutectic reaction and those that occur during ageing. Both of these types of reactions are discussed with emphasis on the factors that control their evolution, as well as their effect on mechanical properties.

2.2.1 CHROMIUM NITRIDE PRECIPITATION

Chromium nitrides are notorious for their deleterious effect on the corrosion integrity and toughness of austenitic stainless steels therefore much attention has accordingly been given to the formation of these precipitates[2,3]. Chromium nitrides in austenitics have been reported to exist in various different stoichiometric forms, such as $Cr_3(CN)_7$, Cr_2N, $Cr_{23}(CN)_6$ and CrN, depending on the composition of the steel. The Cr_2N, CrN and $Cr_{23}(CN)_6$ have been observed in high nitrogen steels, with Cr_2N being the most common[2,3,31,32]. Cr_2N precipitates have been reported to form both continuously (ie. by nucleation and growth of a precipitate phase at a heterogeneous nucleation site) and also by discontinuous cellular precipitation of Cr_2N lamellae[2,3,31,32]. The discontinuous cellular precipitation reaction is characterised by the formation of alternate lamellae of precipitate and matrix, less saturated with solute, which develop into a cell behind a migrating boundary. Further discussions on the nature of the discontinuous cellular precipitation and its importance to the current work will follow.

2.2.1.1 THERMODYNAMICS OF CHROMIUM NITRIDE PRECIPITATE FORMATION

Chromium nitride precipitates form in austenitic stainless steels during prolonged exposure to temperatures in the range of 500°C to 1000°C; the type of chromium nitride that forms in this temperature range depends on the alloy composition[2,3,29,32,33,34,35]. In steels with similar carbon and nitrogen levels, the $M_{23}(CN)_6$ precipitate has been shown to co-exist with the Cr_2N precipitate when the C/N ratio is greater than 0.15, but at higher nitrogen levels only the Cr_2N precipitate was observed[35]. The activation energy for the formation of Cr_2N in these steels was shown to be less than for the formation of $M_{23}(CN)_6$ precipitates and could be decreased further by increasing the nitrogen content[35]. Thus in steels highly alloyed with nitrogen, the Cr_2N precipitate is expected to form in preference to the $M_{23}CN_6$ precipitate.

In the Fe-Cr-N ternary system, CrN precipitates formed on ageing between 600°C and 1000°C,[36]. These precipitates occurred continuously at short ageing times and then change to a discontinuous form of precipitate after longer ageing times[36,37]. Similar behaviour was observed in AISI 316LN type steels, in which Cr_2N precipitation occurs continuously after long ageing times of 100 hours, but after extended ageing, up to 500 hours, the precipitates formed discontinuously[33]. The discontinuous cellular precipitation of Cr_2N in austenitic stainless steels was favoured by the high supersaturation of nitrogen in the steel, and has been observed at temperatures between 700°C and 1000°C[31].

It has been reported that other phases may form during ageing at 800°C-1000°C in high nitrogen steels[32,38,39]. The addition of molybdenum can result in the formation of Laves phase and sigma phase[39]. Z-phase has also been reported to occur, during ageing treatments at 1000°C, when niobium is added in small amounts to an austenitic stainless steel (Nitronic 50)[38]. Sigma phase was also observed to form in high nitrogen steels on ageing at 800°C and was found at the migration front of a discontinuous cell of Cr_2N precipitation[32]. Sigma phase was identified in high nitrogen steels to have a tetragonal structure with lattice parameters $a=b=0.8800$ nm and $c=0.454430$ nm[32,40].

2.2.1.2 CRYSTALLOGRAPHY OF CHROMIUM NITRIDE PRECIPITATES

Precipitate stoichiometry: Cr_2N

Several different values for the lattice parameter of chromium nitrides have been reported for high nitrogen steels. Values have been given by Goldschmidt for chromium nitrides, based on the Cr-N binary system, of a = 4.759-4.805 Å and c = 4.438–4.479 Å[41]. Vanderschaeve *et al* have quoted values for Cr_2N precipitates in high nitrogen–manganese steels of a = 4.18Å and c = 4.44 Å[32] and Simmons *et al* have given the same values for a 15 wt%Cr – 15 wt%Ni steel[42]. In contrast, Mukherjee *et al* have given values of a = 2.275Å and c = 4.483Å, also for alloys with high manganese levels and low nickel levels; however the nitrogen levels were not as high as in the work by Vanderschaeve[40]. Sundaraman *et al* have shown that it is possible that a Cr_2N precipitate may form, in steels alloyed with nitrogen, with two possible lattice parameter values[43]. Diffraction patterns taken from the precipitates show that a type A nitride can form with a = 2.748Å and c = 4.438Å, and a type B nitride can form with a = 4.76 Å and c = 4.438Å. The difference between the type A and type B nitrides arises from the arrangement of nitrogen atoms in the HCP sublattice of the Cr_2N precipitate. Type B nitrides contain a hexagonal arrangement of chromium atoms with the nitrogen atoms arranged in the octahedral sublattice. The type A nitride contains nitrogen atoms that have a disordered arrangement in the interstitial sites of the HCP lattice of the Cr_2N precipitate[43].

The orientation relationship for HCP crystals in an FCC matrix is such that the close packed planes and directions are parallel[44]:

$$(111)\gamma//(0001)\ Cr_2N\ ;\ [1\text{-}10]\gamma//[1\text{-}210]Cr_2N$$

Presser and Silcock have given a different orientation relationship for Cr_2N in austenite, as follows[45]:

$$(110)\gamma//(0001)Cr_2N\ \&\ \{1\text{-}12]\gamma//[2\text{-}1\text{-}10]Cr_2N$$

The Cr_2N precipitates nucleate as coherent zones that have been shown to be spherical, but grow into plate shaped precipitates because of the high misfit strain energy between the Cr_2N precipitate and the austenite matrix[43]. Sundaraman *et al* have shown that the type A nitride is an early form of the nitride precipitate and that after further ageing it develops into the type B nitride. Sundaraman *et al* have shown that the misfit strain energy between the Cr_2N precipitate and the matrix is taken up elastically in the matrix, which can result in the formation of defects such as dislocations and stacking faults[43]. In high nitrogen–manganese steels, twins have been reported to occur between the precipitate lamellae[29,45].

Furuhara *et al* discussed the growth of a HCP precipitate from the austenite with a plate-like morphology, and postulated that broad faces of the precipitate will possess a semicoherent interface with the austenite while the narrow interfaces will possess an incoherent interface[46]. Owing to growth ledges that would be expected on the semicoherent face of the precipitate, self accommodation of shear strain at the interface is facilitated by the formation of partial dislocations[46,47]. These partials would form on the {111} plane which coincides with the orientation relationship of HCP precipitates with FCC crystals[44,46]. Stacking faults have been observed during the precipitation of cementite from austenite on the broad faces of the plate-like precipitates[48]. These observations were made in high manganese-high carbon steels. It is known that these elements reduce the stacking fault energy of the steel, which would then promote the formation of partial dislocations and stacking faults. A possible explanation for the occurrence of twins might lie in a combination of the low stacking fault energy associated with high nitrogen steels and the formation of partial dislocations within the austenite between precipitate lamellae during precipitate growth.

Precipitate Stoichiometry: $M_{23}(CN)_6$

The crystal structure of the $M_{23}(CN)_6$ precipitate is FCC with a lattice parameter that varies between 10.56Å and 10.70Å, depending on the composition of the steel. The formation of these precipitates is favoured when the steel contains significant levels of carbon[35,39]. The metallic constituent, M contains mostly chromium, but has been reported also to contain elements such as nickel, molybdenum and iron[49]. These precipitates have a cube-cube orientation relationship with the austenite matrix[35,39]. $M_{23}(CN)_6$ precipitates are more detrimental to the corrosion resistance of austenitics since they remove a greater amount of chromium from solid solution than the Cr_2N precipitates.

Precipitate Stoichiometry: CrN

The CrN precipitate has a NaCl FCC crystal structure and has been reported to have a lattice parameter of 4.14 Å[42], similar to the values given by Goldschmidt for the Cr-N binary system[39]. These precipitates were also reported by Simmons *et al,* to occur discontinuously where twinning between the precipitate lamellae was also observed[42]. In addition, when these precipitates occurred continuously, the precipitate/matrix regions were highly deformed, indicating that there is a large amount of misfit strain energy between the precipitate and the matrix[42]. It has also been reported that the CrN-type precipitates in Fe-18 wt%Cr alloys have a distorted NaCl FCC structure, with lattice parameters a = 3.97 Å and c = 4.12 Å[37].

2.2.2 DISCONTINUOUS CELLULAR PRECIPITATION

A Brief Description

Discontinuous cellular precipitation (DCP) is a precipitation reaction that results in the formation of a two-phase lamellar structure behind a moving boundary or reaction front[50,51]. The two-phase structure consists of a precipitate and a less saturated matrix phase, which grows behind a reaction front as it migrates into the solute rich matrix. The discontinuous precipitation reaction has been observed to take three different forms, for which Williams and Butler have given the following descriptions[50]:

Type 1 Reaction:

$$\alpha \quad \rightarrow \quad \alpha' + \beta$$

The type 1 reaction results in the transformation of single phase α, supersaturated with solute, behind a moving boundary into alternate lamellae of β precipitate and less saturated α'. This reaction is typical to high nitrogen steels, which are usually fully austenitic and supersaturated with nitrogen prior to ageing treatments. The austenite decomposes into alternate lamellae of precipitate (either Cr_2N or

$M_{23}C_6$[31,32,34]) and austenite, less saturated with nitrogen and to a lesser degree, less saturated with chromium[29,30,32].

Type 2 Reaction:

$$\alpha + \gamma \rightarrow \alpha' + \gamma'$$

In the case of the type 2 reaction, the microstructure consists of a two-phase structure prior to precipitation: a supersaturated matrix α and a coherent precipitate γ[45,51]. This reaction is characterised by coarsening of the γ precipitate already present in the microstructure, into a lamellar form behind a moving boundary. This type of reaction is often termed discontinuous coarsening, characterised by a decrease in the solute saturation in the matrix to α' and in some cases the coherency of the precipitate γ will decrease and transform to γ'.

Type 3 Reaction:

$$\alpha + \gamma \rightarrow \alpha' + \delta$$

This reaction is similar to type 2 reaction, but instead of the same precipitate simply coarsening, the original precipitate γ, transforms into a new precipitate δ, with a lamellar structure together with a simultaneous decrease in solution saturation in the matrix[50]. As a consequence, alternate lamellae of less saturated matrix α' and the δ precipitate form behind a moving boundary. The γ precipitate is usually a coherent metastable precipitate and transforms to a more thermodynamically stable δ precipitate[50].

It is only the type 1 reaction that is relevant to the current study, therefore further attention will not be given to reaction types 2 and 3 in the present review. Much work has been completed since the 1950s on discontinuous cellular precipitation in an attempt to understand the mechanisms and driving forces which govern this reaction[50]. Most of this work has been completed on binary alloy systems but in some cases the effect of third elements has also been studied. More recently, the discontinuous reaction has been investigated in steels, first in the form of $M_{23}C_6$

precipitation[34] and later, with the development of high nitrogen steels, the precipitation of Cr_2N[31,32]. Cellular precipitation has also been recognised in austenitic steels alloyed with nickel and titanium, where titanium rich precipitates have formed discontinuously[4]. The discontinuous coarsening reaction is also relevant to the current work. This reaction is observed once discontinuous cellular precipitation has occurred extensively in material and results in the formation of new precipitate colonies with a wider interlamellar spacing, than in the old precipitate colonies[52]. The new precipitate colonies nucleate on the precipitate cell boundaries that are already present after the first discontinuous reaction[52]. The second discontinuous reaction, or discontinuous coarsening reaction, proceeds more slowly than the first reaction[52].

Discontinuous cellular precipitation is different to continuous precipitation, which involves the nucleation of a second phase particle on a heterogeneous nucleation site such as a grain boundary or dislocation. Growth of the particle is then facilitated by diffusion of solute to that particle, either by volume diffusion or by boundary diffusion. This type of precipitation reaction is what is normally expected to occur in a supersaturated solid solution and typical examples include the precipitation of $CuAl_2$ in the aluminium–copper binary system. Precipitate evolution in such cases results in the classic formation of GP zones, followed by coherent precipitates and finally incoherent precipitates. Discontinuous cellular precipitation is morphologically similar to eutectoid precipitation reactions, such as the formation of pearlite in the Fe-C system, but the reaction mechanics of DCP are different to eutectoid precipitation. The migration of a reaction front is not required for the pearlitic reaction, in which a co-operation between forward nucleation and edgewise growth of the ferrite and cementite lamellae results in a pearlite colony. A boundary between the austenite and the pearlite is indeed established, as a consequence of the reaction, but this boundary plays no role in the evolution of the pearlite colony. During discontinuous cellular precipitation on the other hand, boundary migration is of fundamental importance.

Many theories have been proposed to explain the occurrence of the discontinuous reaction in different alloy systems. In many instances, discontinuous cellular precipitation is observed under specific conditions of composition and temperature within a particular alloy system and out of this range the same precipitate is observed to form continuously. There are, very simply, three requirements for the discontinuous reaction to occur. Nucleation of the precipitate phase must take place on a grain boundary; boundary diffusion of solute should be permitted; and the boundary on which the precipitates have formed must be mobile. It is the mobility of the boundary that mechanistically separates continuous precipitation from the discontinuous cellular precipitation reaction. The cause of boundary migration, simultaneously with the formation of grain boundary allotriomorphs, must therefore be established in order to explain the mechanism for the reaction in a particular system. Many authors have proposed theories for the origin of boundary migration during discontinuous cellular precipitation, but these theories are often specific to the system that was studied. No unified theory exists therefore to explain the origin of the boundary migration necessary for discontinuous cellular precipitation across the spectrum of alloy systems in which it has been observed.

2.2.2.1 THEORIES PROPOSED FOR NUCLEATION AND GROWTH OF DISCONTINUOUS PRECIPITATION

One of the first theories proposed for the nucleation of discontinuous cellular precipitates was developed from the work of Turnbull and co-authors[53,54,55,56,57]. The work was completed on the lead-tin binary system, in which the precipitate and the matrix possessed a specific orientation relationship, such that the close packed planes were parallel and there was appreciable misfit between the two phases[53,54].

The mechanism that was proposed by Tu and Turnbull is named the 'Pucker mechanism[53,54] since it results in puckering of the grain boundaries on which the precipitate nucleates[53,54]. The 'Pucker mechanism' is dependent on the interfacial energy relationship between the precipitate and the matrix and is best explained with the aid of figure 2.2.1 (a)-(e). A plate-like precipitate nucleates on the grain boundary and possesses a plate-like or disc like morphology (figure2.2.1 (a)). One side of the precipitate has a high interfacial energy with grain 2 in the matrix, while the other side has a low interfacial energy with the matrix in grain 1 in the matrix. The precipitate will grow into the grain with which it has the lowest interfacial energy, (grain 1 in figure 2.2.1 (a)) since this is more energetically favourable, and seek a favourable orientation with the matrix, further reducing the interfacial energy. As the precipitate seeks the favourable orientation for growth, the grain boundary is pulled into the so-called 'puckered' configuration (figure 2.2.1 (b)). The boundary then migrates so that the edge of the precipitate with the greater interfacial energy is exchanged for a lower interfacial energy with the other grain as shown in figure 2.2.1 (c). As the boundary moves along the edge of the precipitate, it is now favourably aligned for the nucleation of a second plate or disc, so that it can grow with the most energetically favourable orientation relationship (figure 2.2.1 (d)). The formation of a second precipitate therefore, is more energetically favourable than the first, since the boundary is aligned such that it does not have to rotate to the preferred orientation. This causes a self-perpetuating process of nucleation and growth of many adjacent plates, which then develop into a colony of lamellae and a discontinuous cell, shown in figure 2.2.1 (e)[53,54].

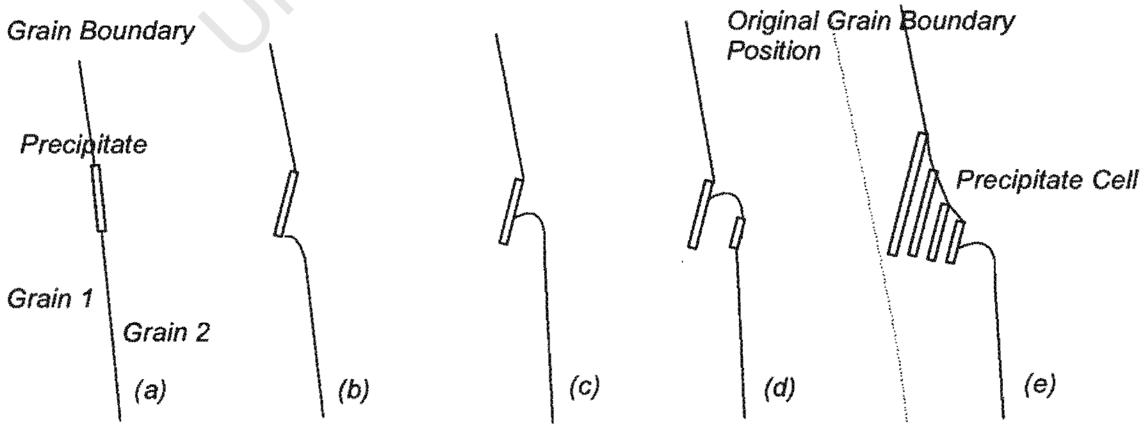

Fig.2.2.1 (a)-(e) Different stages in the 'pucker mechanism' nucleation of a discontinuous precipitate cell after Tu and Turnbull[53,54].

Tu and Turnbull emphasised the role of anisotropic interfacial energies between the precipitate and adjacent grains as the key factor that leads to the puckering of the grain boundary, boundary migration and the formation of a precipitate cell[53,54]. It is the difference in interfacial energies between the precipitates and adjacent grains that would drive the boundary migration necessary for the DCP reaction to occur[53,54]. Aaronson and Aaron argued that this difference in interfacial energy between the precipitate and adjacent grains, would not be sufficient to overcome the energy associated with the extra grain boundary area that develops during both the 'puckering' of the grain boundary and during growth of the cell[58]. The 'puckering' of the grain boundary therefore could not account for the migration necessary for the development of the precipitate cell[58].

Earlier work by Turnbull and co-workers showed that the rate of nucleation of a precipitate cell was proportional to the supersaturation of solute in the matrix. They also observed that there existed a temperature range where discontinuous cellular precipitation is favourable and outside of the temperature range, precipitation did not occur discontinuously[55,56]. This explains the observation that the DCP reaction is frequently observed in a specific temperature range and at a specific alloy composition.

Nes and Billdal[59] showed that the balance of interfacial energies between the matrix, the precipitate and the grain boundary, causes the precipitate to have the smallest possible contact area with the grain boundary. Precipitates with rod or plate-like morphology will orientate themselves such that the long axis of the precipitate is at 90° to the grain boundary with the tip connected to the boundary. Unlike the Tu and Turnbull theory[53,54], they showed that the orientation relationship between precipitate and matrix was of little significance. In the system that they worked on however, the matrix and precipitate possessed a similar lattice parameter and a low energy interface was possible without a particular orientation relationship[59].

Nes and Billdal proposed a different mechanism for the origin of boundary migration and the development of a precipitate cell. Their theory, illustrated in figure 2.2.2 (a)-(c), suggests that boundary diffusion causes the initial growth of the precipitate nucleus in the boundary/precipitate interface and pulls the boundary into a cusp (figure 2.2.2 (a)-(c))[59]. This induces a catalytic effect, which results in nucleation and growth of additional precipitates on either side of the original precipitate, as shown in figure 2.2.2 (b). Growth of these precipitates pulls the grain boundary by a capillary effect and results in a colony of alternate lamellar precipitates and matrix, shown in figure 2.2.2 (c)[59]. The migration of the boundary necessary for the DCP reaction is the result of the capillary effect on the grain boundary. Finally, Nes and Billdal said that boundary diffusion of solute controls the kinetics of the reaction[59].

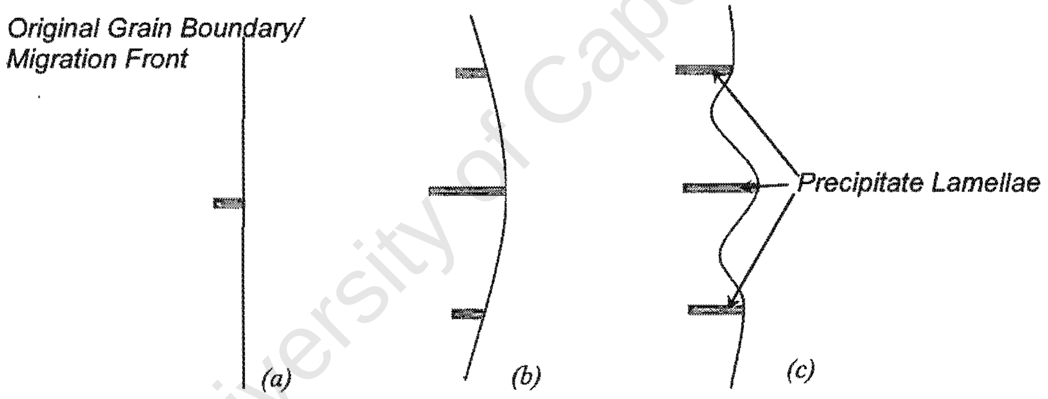

Fig.2.2.2 (a)-(b) Various stages of the nucleation mechanism for discontinuous cellular precipitation after Nes and Billdal[59].

Tu later added to the original work by Tu and Turnbull and also emphasised the role of boundary migration in the development of discontinuous cellular precipitation[57]. Tu reiterated the influence of the 'pucker mechanism' on boundary migration, but said that it might be supplemented by another effect. Tu proposed that although the torque on the boundary, applied by the precipitate, initiates boundary migration, further migration is driven by the search for solute to feed growth of the precipitate, which also emphasises the role of boundary diffusion of solute[57].

Meyrick proposed that in alloys where the solute tends to segregate to the grain boundaries, thereby reducing the grain boundary energy, discontinuous precipitation is favoured[60]. As the solute collects on a grain boundary, in order to decrease the boundary energy, a precipitate forms and consumes the solute at the boundary. A driving force then develops for the boundary to migrate in order to gather new solute and decrease the boundary energy. This accounts for the migration necessary for the development of the DCP reaction[60]. Meyrick said that such grain boundary migration is only energetically favourable if there is a relationship between the composition of the grain boundary and the energy of the boundary[60]. This mechanism also emphasises the role of the boundary diffusion of solute, and contributes to the argument given by Tu[57].

So far the theories that have been reviewed have shown that the boundary migration necessary for discontinuous cellular precipitate reaction is the result of precipitate nucleation on the grain boundaries. In contrast, Fournelle and Clark have proposed that boundary migration occurs independently of precipitate nucleation[61]. Grain boundary migration will occur at all ageing temperatures since any polycrystalline material will seek to decrease the grain boundary area by grain growth which accounts for the initial migration of the grain boundary[61]. Precipitates form on the grain boundary during migration (figure 2.2.3 (a)) in the form of grain boundary allotriomorphs and further migration of the grain boundary causes the boundary to bow between the allotriomorphs, in search of solute (figure 2.2.3 (b), (c))[61]. Thus further migration of the boundary is driven by a compositional gradient across the boundary. The growth of the precipitates is then fed by solute diffusion along the grain boundary as it migrates into the supersaturated matrix[61]. The precipitates therefore act as sinks for the solute and are simultaneously pulled along by the advancing boundary, eventually resulting in a precipitate cell[61].

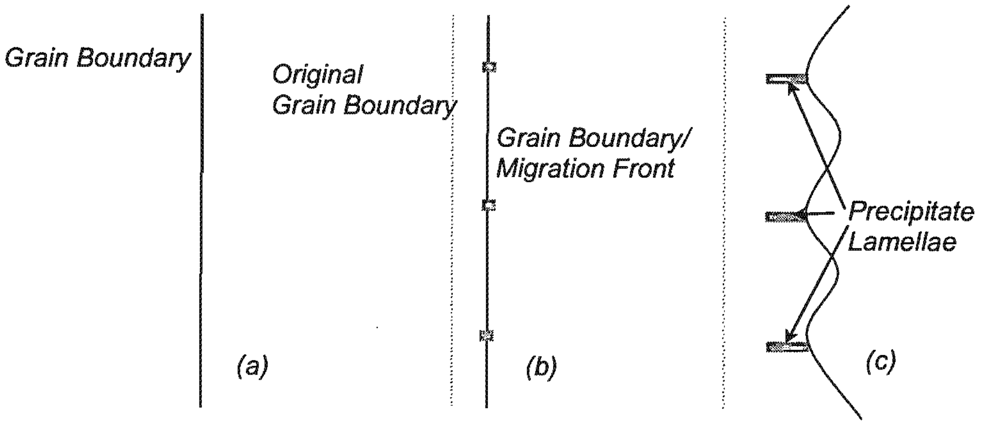

Fig. 2.2.3 (a)-(c) The nucleation mechanism for discontinuous cellular precipitation after Fournelle and Clarke[61].

Hornbogen proposed some conditions that favour the discontinuous cellular reaction: both a large driving force for precipitation and high boundary mobility favour the formation of DCP over continuous precipitation[62]. Additional factors that favour discontinuous precipitation are a high nucleation rate and fast boundary diffusion of solute[62]. Hornbogen showed that the supersaturation of solute in the matrix phase significantly increases the driving force for discontinuous cellular precipitation. Finally, Hornbogen also proposed that the build up of strain energy at the reaction front, as a consequence of solute build up, also contributes to the driving force for the discontinuous cellular reaction[62].

The strain energy at the migration front is a result of either a concentration or depletion of solute atoms at the boundary and results in distortion of the matrix in that region. The build up of strain energy at the boundary has been reported to increase the driving force for discontinuous cellular precipitation and was originally proposed by Sulonen[63]. This effect has been termed 'the coherency strain model' and suggests that rapid boundary diffusion, evident during the discontinuous reaction, together with thermal fluctuations of the boundary, result in a solute enriched or depleted area ahead of the migration front, in the grain consumed by the reaction[63]. The composition of this zone is in equilibrium with the matrix, but because of the solute level, the lattice parameter of that region is different to the rest of the matrix and is also coherent with the matrix. The result is a build up of strain energy in this coherent zone and a driving force then develops for the boundary to migrate in the direction of the unconsumed grain[57]. Sulonen confirmed this theory in later work, by observing the effect of both tensile and compressive stress on the discontinuous reaction[64].

In order for the coherency strain model to operate, boundary diffusion is necessary and should be greater than volume diffusion. When volume diffusion dominates, precipitation should occur continuously, because the driving force for migration is lost. The coherency strain model might therefore explain the narrow temperature range in which the discontinuous cellular precipitation reaction is observed[55-57].

Hillert and Lagneborg also proposed that the coherency strain model could contribute to the driving force for the discontinuous cellular precipitation of $M_{23}C_6$ precipitates in an austenitic stainless steel[34]. They argued however, that chromium does not affect the lattice parameter significantly to create sufficient strain energy in the coherent zone ahead of the boundary. Instead they suggested that once the boundary begins to migrate, a steep concentration gradient is established between the boundary and the retracting grain, which drives further migration[34]. Further, their observations showed that the boundary frequently bulges out ahead of the lamellar precipitates. From this observation they concluded that the effect of interfacial energy between the precipitate and the matrix on boundary migration described by Turnbull and co-workers, could not explain the occurrence of the reaction in this case[34]. Later Hillert showed by calculation that the coherency strain energy in such a diffusion zone, ahead of the migrating front, makes a feasible contribution to the driving force required for the nucleation of the discontinuous precipitate cell. This is valid only if the atoms have a significant effect on the lattice parameter of the matrix[65].

The coherency strain model suggests that there exists a driving force for boundary migration, which is indirectly related to precipitate nucleation and growth and is linked to the diffusion process needed to facilitate precipitate formation. Although the formation of a precipitate is necessary for a diffusion zone to occur, boundary migration has been observed without a precipitate reaction, as a result of a similar driving force, viz., the coherency strain model. This is different from those models that are related to the interfacial energy relationship between the precipitate and the matrix, and the models that suggest that boundary migration results from a type of capillary effect which is a direct result of growth of the precipitates. In terms of the coherency strain model, the origin of boundary migration lies in the boundary diffusion of solute, rather than the growth of the precipitates themselves, however the precipitates act as convenient sinks for the boundary diffusion of solute. Hillert and Lagneborg said the discontinuous cellular reaction is a co-operative process between precipitate growth and boundary migration and both are equally important to the occurrence of the reaction[34].

From the work reviewed here, several conditions can be said to favour the discontinuous reaction. The reaction is frequently observed when the driving force for precipitation is high, often favoured by a high solute supersaturation in the matrix. Further, the reaction is often limited to a specific temperature range and this might relate to the importance of boundary diffusion of solute. When the temperature is high, volume diffusion becomes important and thus might compete with boundary diffusion. On the other hand, when the temperature is low, both volume diffusion and boundary diffusion are frozen out.

Most of the theories for growth of discontinuous cellular precipitation assume that the precipitates grow behind a planar front, with a constant interlamellar spacing[50]. These conditions are only achieved when the reaction is well established and steady state conditions have been achieved. Even in this case there is much experimental evidence to suggest that the growth of the migration front is seldom planar and that the precipitates do not generally have a constant spacing, especially in the case of high nitrogen steels[31]. The factors that control the kinetics of the reaction are the driving force for the reaction and the diffusivity of the solute atoms[50]. A review of the growth theories shows that growth of the discontinuous cell is generally proportional to the diffusion coefficient of the solute, the concentration gradient ahead of the moving front and the interfacial energy between the precipitate and the matrix. The interlamellar spacing between the precipitates is inversely proportional to growth rate of the cell[50].

The driving force for discontinuous cellular growth can be quantified in terms of five factors: the chemical driving force, coherency strain effects, the effect of interfacial energy, the effect of prior matrix deformation and the effect of compositional gradients as a result of rapid boundary migration[50]. Growth of discontinuous cellular precipitation in most alloy systems is affected in some way by each of these contributions to the driving force.

A decrease in the chemical free energy results from the phase change that occurs during discontinuous cellular precipitation[50,65]. Coherency strain energy effects, first proposed by Sulonen[63,64], were acknowledged by Williams and Butler to contribute to the total driving force for the reaction[50]. The effect of interfacial energy is also important and more relevant to type 2 and 3 reactions, where the precipitates already present in the matrix transform to lamellar precipitates with a lower interfacial energy with the matrix[50]. Prior matrix deformation of the material would also enhance the reaction kinetics and thus contribute to the driving force, which was observed by Fournelle and Clarke[61]. Finally, Hillert and Lagneborg discussed the influence of a steep compositional gradient, as a result of rapid boundary migration on the driving force for boundary migration during discontinuous cellular precipitation[34].

2.2.2.2 DIFFUSION INDUCED BOUNDARY MIGRATION

A Brief Description

The discontinuous cellular precipitation reaction requires grain boundary diffusion of solute together with boundary migration. The occurrence of boundary migration as a result of the boundary diffusion of solute has been observed in several alloy systems, without the formation of lamellar precipitates. This phenomenon has been named diffusion induced grain boundary migration, abbreviated DIGM[66]. Recently, DIGM has been generalised to include interfaces other than grain boundaries, and has been termed chemically induced interface migration, abbreviated CIIM[67]; DIGM then represents a special case of CIIM.

Diffusion induced grain boundary migration is described by King as the lateral motion of a boundary together with diffusion of solute along it[66]. The solute atoms do not migrate with the boundary; instead boundary migration leaves the solute behind in an alloyed or dealloyed zone. The source of the solute could be an active atmosphere in which the material is placed, or could result from a coupling of two different materials at elevated temperature[66]. DIGM is initiated by a bulge that expands the grain boundary and eventually 'tears' the boundary loose; once the boundary is migrating, the process is self sustained[68]. For DIGM to occur there must be a source of solute atoms and the boundary diffusion of those solute atoms should be significantly greater than the lattice diffusion, therefore the phenomenon is especially prolific at temperatures where lattice diffusion is frozen out, ie., 0.3-0.5Tm[66]. Similarly to DCP, DIGM has been most widely noted in binary systems, involving substitutional atoms and to a lesser degree in ternary alloys. DIGM has however, recently been observed in the iron-nickel system, which shows that DIGM is relevant to steels[69]. Many parallels can be drawn between DCP and DIGM and as a consequence, the driving forces and mechanism that govern DIGM phenomena have been shown to be relevant to DCP reaction[66,67,70].

2.2.2.3 PARALLELS BETWEEN DIGM AND DCP

The most fundamental similarity between DIGM and DCP is that both require the simultaneous boundary diffusion of solute and mobility of the boundary[50,66]. Both have been observed to result in a region of different composition behind the migration front, which in the case of DIGM will either be an alloyed or dealloyed zone, depending on the flux of atoms in the boundary. In the case of DCP, a two-phase structure forms behind the migration front, consisting of precipitates plus a desaturated matrix. In the case of DIGM, the boundary diffusion of solute originates from some external source, while in DCP the precipitates act as sinks for the boundary diffusion of solute.

The alloyed zone that develops behind the migration front during DIGM has the same orientation as the grain that is expanding, and the migrating boundary maintains its misorientation with the grain that is consumed[66,71]. Similar observations are noted in DCP (figure 2.2.4 (a) and (b)), but the grain that grows is generally the one in which the precipitates have the lowest interfacial energy. In the case of DIGM, the original boundary is frequently identified by an array of dislocations, which originate from the misfit between the alloyed zone and original matrix, which have different compositions and therefore lattice parameters[66].

King affirmed that the discontinuous cellular precipitation reaction is a phenomenon related to DIGM and has further proposed that whatever mechanisms and driving forces apply to the migration of the interface during DIGM can be applied to the discontinuous cellular reaction[66]. The driving forces and mechanisms for DIGM are therefore reviewed with a view to relating these to the discontinuous cellular reaction.

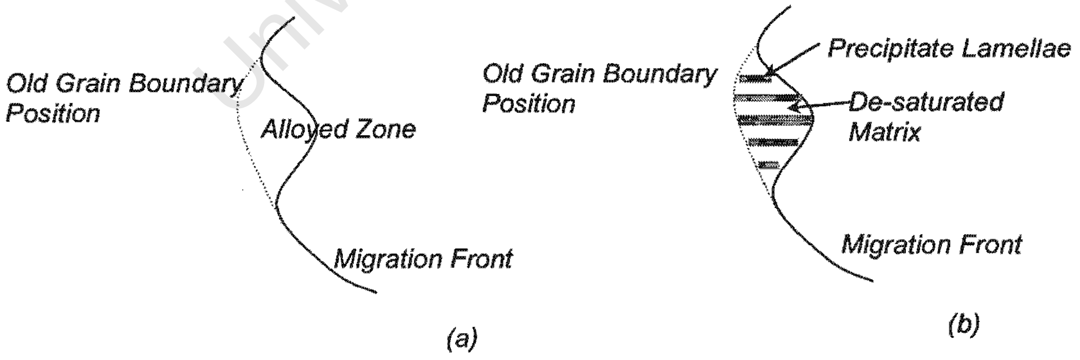

Figure 2.2.4 A schematic representation of (a) DIGM & (b) DCP.

2.2.2.4 *THE DRIVING FORCES FOR DIGM*

In order for DIGM to occur, both a driving force and a mechanism for boundary migration are required[66]. The most obvious contribution to the driving force would be the change in chemical free energy, derived from the free energy of mixing as the boundary migrates and leaves behind a mixture of solute and solvent atoms in the so-called alloyed zone. It has been argued, however, that this is not sufficient to explain the formation of a critical nucleus required to initiate boundary migration and result in the formation of an alloyed zone[66].

The second driving force that has been proposed for the boundary migration associated with DIGM is the same as that proposed by Sulonen for the discontinuous cellular reaction: the coherency strain model[63,64]. Hillert added to the work by Sulonen, and said that the coherency strain effect would play a role in the driving force for DIGM if the solute atoms have a significant effect on either increasing or decreasing the lattice parameter of the parent phase[70]. Yoon also discussed the coherency strain model with reference to CIIM and said that there is considerable experimental evidence to show that this theory presents a valid driving force for boundary migration[67].

Rabkin also expanded on the coherency strain theory, but said that the concentration gradient of solute ahead of the boundary could also drive migration, instead of the strain energy[71]. This proposal is valid when the solute atoms exert little strain energy on the matrix, in the case where solute and solvent atoms are of similar size. When there is a significant difference in the size of the atoms, the strain energy that is developed makes a greater contribution to the driving force than the concentration gradient[71,72]. This argument agrees with that of Hillert and Lagneborg for DCP in an austenitic stainless steel, as discussed.

An additional driving force DIGM has been proposed on the basis of solute-boundary interaction models[73,74]. Louat, later supported by Kasen, said that there exists some minimum boundary energy value associated with a specific level of solute in the boundary[74]. As solute atoms diffuse out of the boundary into the alloyed zone, a driving force exists for the boundary to acquire fresh solute, in order to maintain an equilibrium composition[73]. This theory can be equally applied to dealloying of the diffusion zone: as atoms are removed from the alloyed zone by boundary diffusion, there is again a driving force for the boundary to migrate in search of solute and the equilibrium composition.

On the basis of the theories reviewed it seems reasonable that none of the driving forces proposed for DIGM can account for the total energy required for the boundary migration and the formation of an alloyed zone. Instead, a co-operation between the different driving forces presented accounts for the process and each becomes important during the different stages of development of the alloyed zone.

2.2.2.6 DISCONTINUOUS CELLULAR PRECIPITATION IN HIGH NITROGEN STEELS

The discontinuous cellular precipitation reaction in high nitrogen steels can be described as follows[31,32]:

$$\gamma \rightarrow \gamma` + Cr_2N$$

where $\gamma`$ is the less saturated austenite and Cr_2N is the precipitate. The precipitate that forms is not always Cr_2N, but could be $M_{23}(CN)_6$ and even CrN, at different temperatures and alloy compositions, as has been discussed[34,42].

Vanderschaeve *et al* suggested that the nucleation of the Cr_2N precipitates in high nitrogen steels shows evidence of the 'pucker mechanism' proposed by Tu and Turnbull[32]. Both Kikuchi *et al*[31] and Vanderschaeve *et al*[32] have discussed the growth features of discontinuous precipitation in high nitrogen steels. These authors found that the growth features of discontinuous precipitate cells in high nitrogen steels are different to those in binary and ternary systems consisting only of substitutional elements.

The discontinuous precipitation reaction in high nitrogen steels is not a steady state reaction, in contrast to reactions in substitutional binary systems. The reaction rate decreases with increasing reaction time (figure 2.2.5) and stops when the nitrogen concentration in the matrix is still high[31,32]. These features are further demonstrated by the increase in interlamellar spacing with growth of the precipitate cell[31,32]. Since the precipitate that forms in high nitrogen steels consists of a substitutional element and interstitial elements, the growth of the precipitates cells is certain to be different to that in binary substitutional systems. Nitrogen diffuses rapidly through the lattice, thus feeding the growth of the precipitates, while chromium diffuses along the boundaries in order to feed precipitate growth. Chromium also diffuses through the lattice but this is more sluggish. The nature of diffusion of both of these elements is at some point responsible for the non steady state growth features of discontinuous cellular precipitation in high nitrogen steels and can explain the differences that are observed[31].

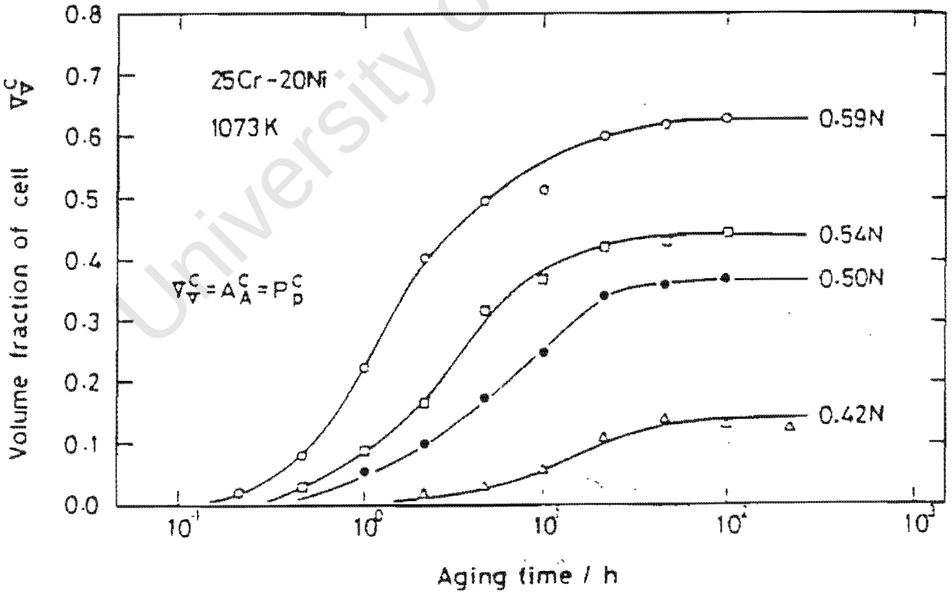

Fig. 2.2.5 The change in volume fraction of precipitate cells with ageing time at 800°C after Kikuchi et al[31].

The decrease in the migration rate results from fast volume diffusion of nitrogen from the supersaturated matrix, to the austenite behind the reaction front, which is less saturated in nitrogen[31]. The driving force for the volume diffusion is the homogenisation of nitrogen of the austenite phase. This has not been observed in alloy systems that do not involve substitutional elements, and is therefore an artefact of the nitrogen content.

Explanations for the stoppage of the cell boundary were given by Kikuchi *et al*[31] and contributions were also made by Vanderschaeve *et al*[32]. The authors proposed that a diffusion zone exists ahead of the migrating boundary, as a result of the volume diffusion of substitutional elements. The width of the diffusion zone is defined as D_b/v and would be constant at a constant migration rate. Since the migration rate of the cell boundary in high nitrogen steels is not constant, but decreases because of the volume diffusion of nitrogen into the cells, the diffusion zone increases, by definition of the equation D_b/v[31,32]. Kikuchi *et al* proposed that this increase in the width of the diffusion zone results in a loss of the chemical driving force for the reaction, which finally results in stoppage of the cell boundary[32].

Kikuchi *et al* showed that the volume fraction of cellular precipitation in alloys with different nitrogen levels, increased with nitrogen content for a constant ageing temperature and ageing time. Figure 2.2.6 plots the migration rate of precipitate cell boundaries as a function of nitrogen content, measured by the change in lattice parameter associated with nitrogen supersaturation. The result shows that as nitrogen levels are increased in austenitic stainless steel alloys, a greater amount of discontinuous precipitation can be expected. In addition, increased nitrogen supersaturation in high nitrogen steels contributes to the driving force for the discontinuous reaction[31].

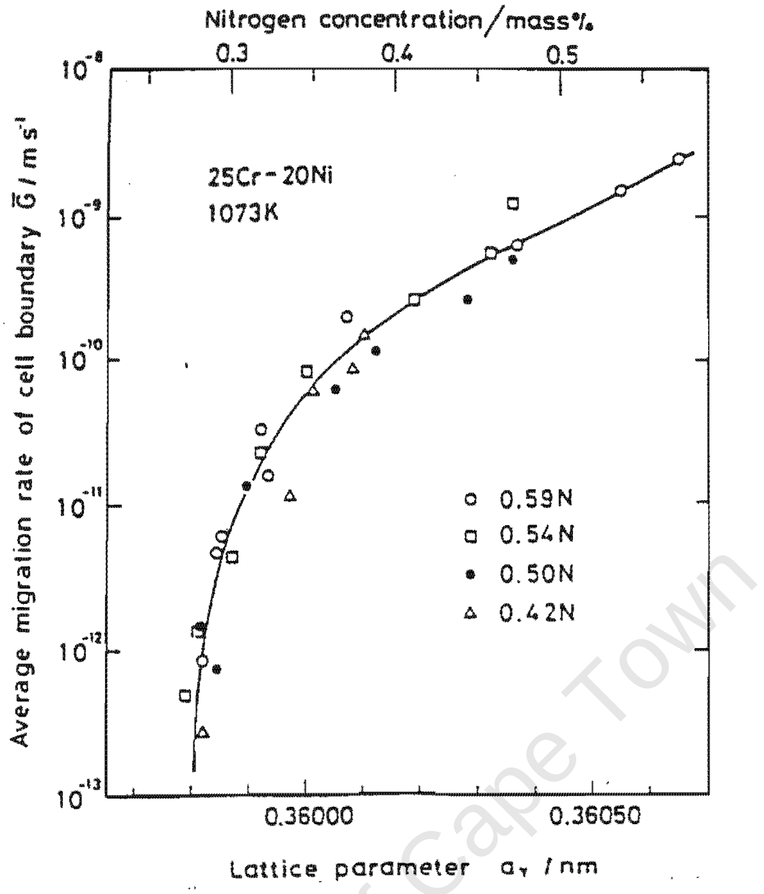

Fig. 2.2.6 The migration rate of the cell boundary vs the nitrogen level in the untransformed matrix, measured by lattice parameter, after Kikuchi et al[31].

Faulkner investigated the discontinuous precipitation of $M_{23}(CN)_6$ in an austenitic steel; which like the precipitation of Cr_2N involves both substitutional and interstitial atoms[75]. Faulkner showed that there is a narrow temperature range in which the reaction will proceed discontinuously, and out of this range it will proceed as a continuous reaction. The author showed that the rapid volume diffusion of carbon, and the slower volume diffusion of chromium control boundary migration during the discontinuous reaction[75]. If the boundary velocity is slowed down to below a minimum value, precipitation will proceed as a continuous reaction[75]. This minimum value corresponds to a concentration gradient of chromium ahead of the migration, while the maximum boundary velocity is characterised by a carbon depleted zone ahead of the boundary[75]. Faulkner has also shown that the discontinuous reaction occurred more prolifically at higher carbon levels[75], which again supports the argument that the supersaturation of solute in the matrix favours the discontinuous reaction. In addition, the individual effect of substitutional and interstitial elements on the discontinuous reaction was highlighted in this work[75].

Ainsely *et al* also showed the importance of solute saturation in the matrix to the driving force for discontinuous cellular precipitation[76,77]. The authors studied the Fe-13Mn-2V-0.8C austenitic steel, in which the precipitation of vanadium carbides with a NaCl FCC crystal structure occurred discontinuously. The authors associated the decreased migration rate with a loss of supersaturation of the solute atoms, vanadium and carbon, as the reaction proceeded. For discontinuous precipitation to occur favourably over continuous precipitation there had to be a high level of both vanadium and carbon in the steel. In alloys with lower levels of both vanadium and carbon, discontinuous cellular precipitation did not occur and precipitates developed continuously instead[77]. Ainsely *et al* also proposed that a decrease in supersaturation could originate from the formation of continuous precipitates, which would also result in slowing of the grain boundary. Further the continuous precipitates might also have pinned the grain boundaries, thus slowing down or even stopping the growth of a precipitate cell[77].

Ainsely *et al* further observed that the characteristics of the precipitates that formed by discontinuous precipitation were dependent on the migration rate of the cell boundary[76]. In the case of a highly mobile grain boundary, lamellae that formed were unfragmented, but when the boundary migration was slower, the precipitates that formed within the cell were particulate in nature[76].

2.2.2.7 THE EFFECT OF ALLOY ADDITIONS ON THE OCCURRENCE OF DISCONTINUOUS CELLULAR PRECIPITATION

It has been shown in binary systems that the addition of a third element can have an effect on the occurrence of discontinuous cellular precipitation, i.e. the reaction is either favoured or suppressed[50]. The mechanism whereby the addition of a third element affects discontinuous cellular precipitation is two-fold:[50] the addition of a third element can change the characteristics of the precipitate as well as affect the boundary mobility of the precipitate cell[50]. The effect of a third element is complex and again published observations are often specific to particular alloy systems.

Chromium nitrides that form both discontinuously and continuously in high nitrogen steels, often contain elements in addition to chromium, which make up the metallic constituent of the precipitate[41]. The addition of elements such as niobium or vanadium to the base composition of a high nitrogen steel alloy can result in the formation of precipitates with the same metal:interstitial ratio as precipitates associated with the base composition, but possess a different composition. A change in the precipitate composition causes a change in the lattice parameter(s) of the precipitate and hence a corresponding change in the misfit between the precipitate and the matrix, which can affect the occurrence of discontinuous cellular precipitation[78].

Ternary elements can also affect the structure of the grain boundary, which in turn affects boundary mobility and precipitate nucleation[50]. The presence of solute atoms segregated to the grain boundary is known to decrease the velocity of the boundary or interface migration by solute drag[79]. A boundary or interface that contains solute atoms will migrate a short distance, leaving behind the solute atoms. The solute atoms that prefer to settle on the grain boundary will exert an attractive force on the grain boundary, pulling it back to its original position, thus slowing down or even preventing boundary or interface motion[80].

The efficiency of techniques that are available to measure the solute segregation of atoms to the grain boundaries is limited. A grain boundary is assumed by many authors to be approximately 0.5 nm in width or one atomic distance. Clearly the measurement of a concentration of atoms from such a small area is complicated[79-81]. The most well known method of measuring grain boundary segregation is by Auger Electron Spectroscopy, which measures the trace elements on the boundary surface. However, this method relies on exposed grain boundaries, which are difficult to obtain in ductile or tough materials, such as high nitrogen steels, for which other techniques are necessary.

Suehiro *et al* proposed thermodynamic parameters that predict the segregation potential of a particular element in an alloy system[82,83]. Using a series of calculations and relevant models, Suehiro *et al* were able to derive the Gibbs energy of segregation for a particular element in a specific alloy system[83]. In a different publication, Suehiro *et al* used this parameter to determine the degree of segregation of niobium in a low carbon steel alloy, in order to predict the solute drag effect of niobium on recrystallisation[84]. It was shown that during recrystallisation the boundary velocity decreased with increasing niobium additions over a range of temperatures. In addition, calculations showed that as the niobium content was increased, the fraction of the driving force for boundary migration dissipated by solute drag, increased dramatically above a particular niobium concentration. This niobium concentration was termed the critical niobium concentration for solute drag[84]. Suehiro also compared the effect of grain boundary pinning by small niobium precipitates with the effect of solute drag[84]. It was argued that the pinning force of precipitates is dominant when the driving force for boundary migration is small[84]. Discontinuous cellular precipitation is largely dependent on boundary or interface migration, thus both solute drag and grain boundary pinning have a significant effect on the occurrence of this form of precipitation[50].

Bauman and Williams showed that discontinuous cellular precipitation was suppressed successfully in Cu-Be alloys by the addition of zirconium to the binary system[85]. Zirconium additions lead to the formation of zirconium rich precipitates on the grain boundaries, which might have caused a grain boundary pinning effect, thus slowing down boundary motion and preventing discontinuous cellular precipitation[85]. Further, it was proposed that zirconium additions caused a solute drag effect on the grain boundaries, however the authors report no measurements of zirconium concentrations at grain boundaries. The authors concluded that if boundary migration was hindered by solute drag, then their results show that segregation is the result of limited atomic solubility, rather than atomic size mismatch, which was suggested by other authors[85].

2.2.3 NIOBIUM AND VANADIUM NITRIDE PRECIPITATION

Niobium, vanadium, and titanium are frequently added to stainless steels to stabilise the steel, thereby preventing the formation of chromium carbonitride precipitates, which are known to sensitise the steel[2]. Stabilised grades of stainless steel would then form carbides or nitrides rich in niobium, vanadium or titanium, which do not result in sensitisation[2,3]. Further, the formation of these precipitates is often used to improve the creep resistance of stainless steels during high temperature service[2,3]. Niobium, vanadium, and titanium have also been used in high strength low alloy (HSLA) steels to favour the formation of fine dispersions of nitrides, carbides and carbonitrides during thermomechanical processing. These precipitates have a precipitation hardening effect and are partly responsible for the remarkable strength of these alloys[86]. It is the aim of the current work to improve the strength of a high nitrogen steel alloy in a similar way.

Little work has been conducted on niobium and vanadium nitride precipitation in high nitrogen steels, but the work on stainless steels and HSLA steels is reviewed since the characteristics of the precipitates are likely to be similar. The characteristics of these precipitates will first be discussed with reference to their composition, crystallography and their thermodynamics of formation so that they can be easily identified in high nitrogen steels. In addition, the tendency for the precipitates to coarsen will also be discussed, since the precipitate size will certainly affect the mechanical properties. Finally, the formation of carbonitrides during solidification of steel will also be discussed since the persistence of these precipitates after solution treating will affect the behaviour of the steel during subsequent ageing treatments.

2.2.3.1 *COMPOSITION AND CRYSTALLOGRAPHY*

When elements such as niobium, vanadium and titanium are added to steels, carbides or nitrides of these elements form because of the affinity that these elements have for both nitrogen and carbon. These precipitates have an MX stoichiometry where M represents the metallic constituent of the precipitate and X represents the interstitial constituent. The symbol, MX is illustrative of a metal:interstitial ratio of 1:1 for the precipitate[2,3,41]. When niobium, vanadium or titanium are added individually to steels containing either nitrogen or carbon, one would expect a simple binary precipitate to form, for example NbN[41,87,88]. The composition of MX precipitates is frequently more complex, since steels generally contain more than one precipitate forming element and significant levels of both carbon and nitrogen. In such cases, the metallic constituent of the MX precipitate will be a solid solution of more than one element, for example niobium and vanadium, and in some cases may include a third element, such as titanium[41,87,88]. The metallic constituent might also contain small amounts of other matrix elements present in the steel such as iron, manganese and chromium[87]. The X constituent of the precipitate can similarly be a solid solution of both carbon and nitrogen atoms, depending on the composition of the steel. MX-type precipitates possess an NaCl FCC crystal structure, such that the precipitate is made up of a metallic FCC sublattice with nitrogen and carbon in the octahedral interstitial sites of the metallic lattice[89]. Binary precipitates of the elements niobium vanadium and titanium with either carbon or nitrogen, viz. NbN, NbC, VN, VC, TiN, TiC, have the same crystal structure with similar lattice parameters, which facilitates the solid solution of more than one precipitate forming element in the metallic constituent of the precipitate[41].

Chromium is able to form a similar type of precipitate with a CrN stoichiometry, NaCl FCC crystal structure and a comparable lattice parameter to the niobium and vanadium rich MX precipitates. These precipitates have been noted in steels with nitrogen additions greater than 1 wt% and have been discussed in section 2.2.1[42]. Table 2.2.1 shows the lattice parameters of pure MX-type precipitates, ie. only one element makes up the metallic constituent, M and only one element makes up the interstitial constituent, X[41].

Carbonitrides of niobium, vanadium and titanium with an MX stoichiometry are isomorphous and because of the similarity of their lattice parameters are miscible with each other. As a consequence of the miscibility of these precipitates, stacking faults are frequently observed in the precipitate together with other defects such as vacancies and impurity atoms[41]. A further consequence is that the composition of the precipitates depends on the duration and temperature of the ageing treatments of the alloy[87,90,91]. Further, precipitates are often under-stoichiometric with regard to the interstitial levels, which has a significant effect on the crystallography of the precipitate. It has been shown that the NaCl FCC crystal structure is stable up to interstitial levels of 0.5 at%-1.0 at%[41,87,89,91]. When the interstitial levels are below this range the stoichiometry changes to an M_2X type precipitate, which in most cases possesses an HCP crystal structure (table 2.2.1)[41].

Table 2.2.1 The lattice parameters and crystallography of stoichiometric niobium and vanadium nitrides after Goldschmidt[41].

Stoichiometry	***Crystal Structure***	***Lattice Parameter (Å)***
VN	NaCl FCC	a = 4.066 (N = 0.72) a = 4.139 (N = 1.0)
V_2N	HCP	a = 2.823, c = 4.545 (N= 0.48) a = 2.839, c = 4.560 (N = 0.50)
NbN	NaCl FCC	a = 4.381 (N = 0.9) a = 4.392 (N = 1.0)
Nb_2N	HCP	a = 3.056, c = 4.957
TiN	NaCl FCC	a = 4.22 (N = 0.45) a = 4.24 (N = 1.0)
Ti_2N	Tetragonal	a = 4.9452, c = 3.0342
CrN	NaCl FCC	a = 4.149 (N = 1.0)
Cr_2N	HCP	a = 4.759, c = 4.438 a = 2.748, c = 4.4380* *After Sandaraman *et al*[43]

2.2.3.2 PRECIPITATE COARSENING

It is not uncommon that during precipitate coarsening, changes in composition, and in some cases, crystal structure occur. In the case of a 17 wt% Cr-12 wt% Ni steel alloyed with nitrogen, niobium and vanadium additions, it was shown that prolonged ageing treatments resulted in precipitates with a rod-like morphology[87]. This morphology is said to be uncommon for MX precipitation in austenite and might have been the result of a change in crystal structure[87]. Electron diffraction studies showed that the rod-like precipitates possessed a tetragonal crystal structure with a = 3.04 Å and c = 7.39 Å. The composition of the precipitate also changed from (NbV)N to NbCrN and the authors, Karlsson *et al*, concluded that the precipitate had transformed to the z-phase[87]. The z-phase is closely related to the NbN precipitate and is loosely described as a distorted NaCl type precipitate, lacking half of the nitrogen atoms[87,92]. It is a more complex nitride, with different metal atoms structured in layers along the c-direction of the precipitate, such that metallic atoms A and B are arranged AABBAABB. It has a stoichiometry which is considered to be (AB)N, where A is either Cr, Fe or Mn and B is Nb, Mo or Ta. Thus it is an ordered precipitate and is considered to form during the later stages of ageing when ordering has had time to occur within the precipitate[87]. Another argument for the formation of the z-phase is the interfacial energy benefit associated with the shape of such a precipitate. A fine NbN could reduce the interfacial energy between the precipitate and the matrix by extending along the c-axis, which causes the precipitate to alter its crystallography from NaCl FCC to tetragonal. This is accompanied by a change from the more common cuboidal or spherical morphology to a rod-like precipitate[87].

The tendency for MX-type precipitates to be non-stoichiometric has also been used to explain the inability of titanium to stabilise an 18 wt% Cr-12 wt% Ni stainless steel after prolonged ageing[90]. Similar results have been observed in an 18-10 austenitic stainless steel, with negligible nitrogen levels, and carbon levels below 0.12 wt%[37]. Titanium could not prevent chromium carbide ($M_{23}C_6$) precipitation after extended exposure (of the order of 1000hrs) to high temperatures[93]. Increased titanium additions only prolonged the time for $M_{23}C_6$ precipitates to form, and the already existing titanium carbides simply provided nucleation sites for the $M_{23}C_6$ precipitates[93]. Andrén *et al* proposed that these observations were the result of a change in composition of MX-type precipitate during precipitate coarsening[90]. When the carbon content of a TiC type precipitate decreases and the chromium replaced the titanium in the precipitates, the lattice parameter of the precipitate decreases. A decrease in the lattice parameter of the precipitate will result in a decrease in the misfit between the precipitate and matrix, which is energetically favourable[90]. Andrén *et al* explained that it is expected that a driving force would exist for the precipitates to alter their composition and thus lower the interfacial energy between the precipitate and the matrix, which would then favour a transformation from TiC to the less desirable $M_{23}C_6$ precipitate[90].

It has also been shown in an 18-10 stainless steel that that niobium was most effective at preventing $M_{23}C_6$ precipitation when the niobium levels exceeded 0.7 wt%, but at lower niobium levels $M_{23}C_6$ precipitation did occur. Vanadium additions to the same steel accelerated $M_{23}C_6$ precipitation and also resulted in formation of an V_2C precipitate rather than the expected MX or VC type precipitate. However, when the vanadium levels were increased to greater than 1 wt%, the expected VC precipitate formed[93].

In alloy systems that contain niobium and vanadium additions, it has been shown that the first precipitate to form is the NbN, since it has the highest free energy of formation[16]. After ageing, however, the niobium is replaced with vanadium, which reduces the lattice parameter of the precipitates and hence the interfacial energy between the precipitates and the matrix[87]. This observation by Karlsson *et al*, complements the explanations given by Andrén *et al* for the change in precipitate stoichiometry during extended ageing treatments[87,90].

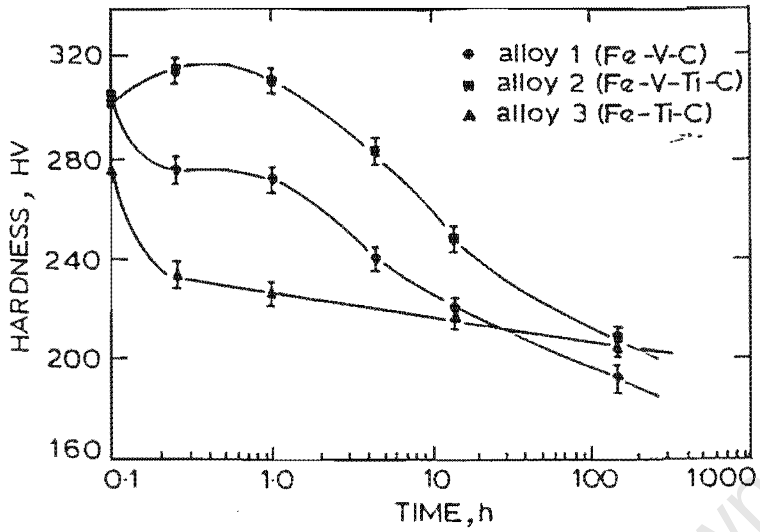

Fig. 2.2.7 Hardness as a function of ageing time for three different alloy compositions investigated by Dunlop and Honeycombe[94].

Dunlop *et al* have also shown that mixed carbonitride precipitates coarsen more slowly than simple binary MX precipitates[94]. This had a beneficial effect on the hardness of the steel; the hardness of the steel could be maintained even after longer ageing times. This effect is illustrated in figure 2.2.7, which shows the hardness of the steel as a function of ageing time. The alloy that contained both vanadium and titanium additions showed greater hardness for longer ageing times compared to the alloys with only vanadium or titanium additions[94]. The authors attributed the stability of the precipitates to the increased chemical bonding energy of the mixed precipitate, compared to the binary precipitate[94].

2.2.3.3 PRECIPITATE SIZE AND MORPHOLOGY

MX-type precipitates are very small in size, and have been reported to be between 5-500 nm in diameter, depending on the composition of the precipitate, ageing temperature and ageing time[87,90,91,93,94,95,96]. These precipitates are generally expected to form during ageing treatments at temperatures between 600°C and 1000°C for times up to 100 hours, and the precipitates do not grow to sizes larger than 500 nm, which appears to be characteristic of MX-type precipitation. Further, it has been shown that nitrogen supports finer precipitates than carbon[97]. Wen-Tai *et al* said that this observation, together with the observation that $M_{23}C_6$ precipitates coarsen very quickly compared to niobium, titanium or vanadium rich precipitates, explains why niobium and titanium nitrides are more favourable for the improvement of creep resistance than $M_{23}C_6$ precipitation[98].

In addition to the small size of niobium, vanadium and titanium carbonitride precipitates, a homogeneous distribution in the matrix is usually expected, which is favourable for the strength and toughness of the steel. These precipitates nucleate on grain boundaries, dislocations and stacking faults[87,88,90,91-98]. They have been reported to have a spheroidal morphology[95], a cuboidal morphology or in some cases a rod-like morphology[87]. The spheroidal and cuboidal morphologies would support better mechanical properties than the rod-like morphology.

2.2.3.4 PRECIPITATE FORMATION DURING SOLIDIFICATION

It has been shown, in a range of steels with niobium and nitrogen additions that large blocky precipitates, rich in niobium and nitrogen, form during solidification[99,100,101,102]. The precipitates are reported to have a NaCl FCC crystal structure, the same as that which would form in a steel with niobium additions during a solid state reaction[97,98,101]. It is proposed that during solidification, austenite is the first phase to form as a cellular dendritic structure. As the solid forms, niobium and carbon are rejected into the liquid, which eventually becomes so rich in these elements that a eutectic NbC precipitate and austenite form, leaving a colony of large blocky precipitates embedded in the eutectic austenite[101]. Du Pont, who modelled the solidification path of steels with niobium additions, confirmed this explanation[103]. Du Pont also showed that depending on the alloy composition, the enriched dendritic liquid either solidifies as a Laves phase or as a NbC precipitate with a NaCl FCC crystal structure, together with the austenite[103].

The formation of eutectic niobium carbide precipitates, during solidification as described, indicates that microsegregation of the niobium occurs during casting[99,102]. Niobium carbide precipitates have been reported in castings regardless of the cooling rate[99]. Hannerz *et al* however showed that the amount of NbC eutectic precipitates that formed on solidification decreased with decreasing cooling rate[100]. When solidification takes place over a longer period of time, microsegregation of the alloy elements is less pronounced and this reduces the occurrence of eutectic precipitates[100].

In a study by Albarran *et al*[104] and Campillo *et al*[105], the authors showed that HSLA steels that contain niobium, nitrogen additions favour the formation of precipitates during solidification. This conclusion was drawn from the observation that steels with greater nitrogen levels contained a larger volume fraction of blocky precipitates after solidification. Du Pont also showed that as the carbon content was increased, the formation of the eutectic niobium carbide was favoured; however as the niobium content increased, the niobium-rich Laves phase + austenite eutectic reaction was favoured[103]. Heikkinen *et al* also showed that small amounts of the eutectic NbC occur even at very low levels of niobium (0.02 wt%) and the volume fraction of the eutectic niobium carbide that formed increased with the niobium level in the steel[99].

Other eutectic precipitate reactions have also been reported during solidification of different steels. Large blocky precipitates have been observed in a Hadfield's steel as a result of titanium additions[106]. Wen Tai *et al* showed that in a stainless steel, with an approximate composition of Fe-25 wt%Cr-20 wt%Ni, large blocky precipitates of the form M_7C_3 formed eutectically in the interdendritic regions and on the grain boundaries, which later transformed to $M_{23}C_6$ precipitates during high temperature exposure[97]. Similar steels stabilised with niobium, titanium and zirconium formed blocky precipitates rich in these elements on solidification[98]. Boothby showed that niobium carbide precipitates formed with M_6C precipitates during solidification in a similar steel, however the precipitates that were observed were fine and formed on austenite/ferrite boundaries[88]. The small size of the precipitates that formed on casting, as opposed to the large blocky precipitates observed in other alloys, can probably be attributed to the low carbon and nitrogen levels in the steel that was investigated.

The formation of eutectic precipitates during solidification has also been observed in high nitrogen steels[42]. It has been shown that during solidification, when the nitrogen levels were greater than 0.6 wt%, austenite was the primary solidification phase to form in all alloys, followed by chromium nitrides of the form CrN in the interdendritic regions[42]. Simmons *et al* proposed that as the primary austenite forms the remaining liquid is enriched in nitrogen and chromium, which was supported by the observation that no nitrides were observed in the primary austenite[42]. The enriched liquid results in the eutectic formation of CrN, which forms as dendrites with a rod-like morphology. These observations contradict the theory that the nitrogen solubility in the solid Fe-Cr-Ni austenite is greater than in the liquid[42]. CrN dendrites were also observed in high nitrogen steel castings with lower nickel levels and high manganese levels in later work, together with the solid state Cr_2N precipitation on cooling[107].

Eutectic precipitation of niobium carbonitrides represents a considerable waste of the niobium additions to the steel, which would then not be available for precipitation hardening during subsequent ageing treatments[104,105]. Itman predicted that up to 40% of the alloy elements are lost due to eutectic precipitation[102].

Heikkinen *et al* showed that eutectic NbC precipitates did not dissolve at ordinary reheating temperatures[99]. Campillo *et al* showed that after long solution treatments at temperatures of 1250°C, larger precipitates simply grew at the expense of the smaller ones[108]. The inability of the precipitates to dissolve at appropriate solution treatment temperatures has led to much work on the solubility of such precipitates in HSLA steels.

Equations have been proposed for the solubility of niobium nitride, niobium carbide, vanadium nitride and vanadium carbide and mixed niobium and vanadium carbo-nitride precipitates, and have been used to predict the solubilities of each of these precipitates[109,110]. Figure 2.2.8 shows the solubility products determined for niobium nitride, niobium carbide, vanadium nitride and vanadium carbide as a function of temperature. The graph shows that the solubility of niobium nitride is the lowest, followed by niobium carbide, vanadium nitride and then carbides of both niobium and vanadium[111]:

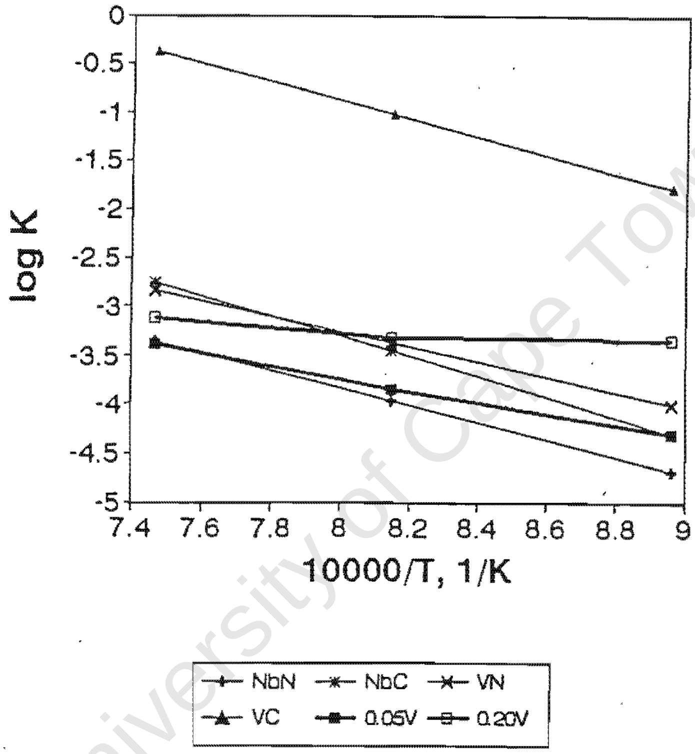

Fig. 2.2.8 The solubility products of NbN, NbC, VN and VC as a function of temperature, after Xiaodong et al[111].

Other authors have confirmed the result shown in figure 2.2.8 using solubility product calculations[109,111,112]. Further, the solution treatment temperature for the dissolution of mixed (NbV)N precipitates was shown to be increased as niobium replaces vanadium in the precipitate[113]. Figure 2.2.9 shows a set of HSLA steel alloys with different carbon and nitrogen levels. The graph plots the solution treatment temperature for the carbonitride precipitates in each alloy as a function of the niobium content in a mixed niobium and vanadium rich carbonitride.

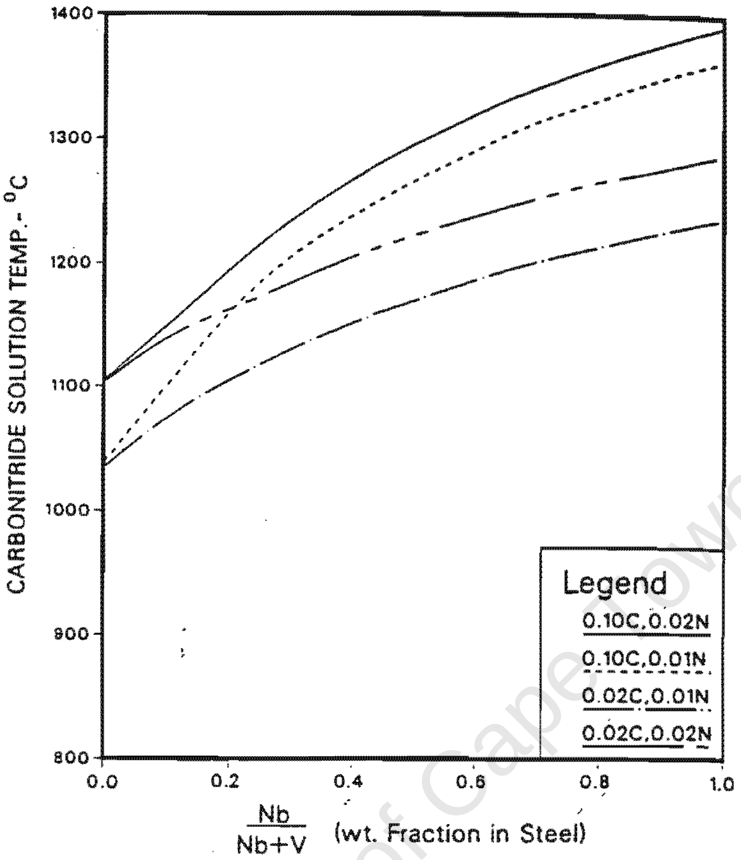

Fig. 2.2.9 Dissolution temperature for mixed (NbV)N precipitates as a function of niobium percentage of the combined niobium and vanadium level in the precipitate after Speer et al[113].

Vodopivec *et al* showed that the dissolution kinetics of niobium carbonitride precipitates that form during solidification are quite slow and that the solubility product alone was not sufficient to determine the stability of the niobium carbonitride in austenite[101]. After solution treatments at temperatures between 1250°C and 1300°C, a niobium concentration gradient adjacent to the precipitate was detected, which is evidence of niobium diffusing out of the precipitate. The authors attributed the stability of the niobium carbonitride precipitate in austenite to the slow diffusion rate of niobium in austenite[101].

The formation of eutectic blocky precipitates is favoured by the addition of elements such as niobium, vanadium, titanium etc to HSLA[102,104,105,108] steels, stainless steels[88,98] and mild steels[99,100,101]. Once these precipitates are present in the solid state, their solubility in the austenite is low and they are not expected to dissolve[108,113]. The niobium rich precipitates have been shown to be the most insoluble in steels[113]. Further, even if niobium rich eutectics were to dissolve it has been shown that the kinetics of dissolution is slow[101]. Thus the addition of appreciable levels of precipitate forming elements, especially niobium to steels, must be carefully considered in view of the influence of this element on the solidification behaviour of the steel.

2.3 MECHANICAL PROPERTIES FOR WEAR RESISTANCE

Wear by abrasion can be defined as the sliding of an abrasive particle over a distinctly softer base material at a high pressure, resulting in consequent material removal from the surface. The abrasive particles break through the covering layers and asperities of the base material and cause it to be grooved[114,115]. Two types of abrasive wear are commonly observed, two-body abrasive wear, which is the result of a harder surface sliding against a softer surface, and three-body wear, which is the result of two surfaces sliding against one another with hard particles in between[115].

The mechanism of wear (or material removal) during abrasion can be either plastic or brittle[116]. The plastic wear mechanism involves material removal from the surface by plastic deformation. The wear surface is characterised by either cutting or ploughing, which involves grooves with characteristic shear lips[116]. For materials that wear in a plastic manner the wear rate is said to be approximately inversely proportional to the hardness of the material[116]. Although the importance of hardness to wear resistance cannot be ignored, the ability of the material to accumulate plastic strain also becomes important during later stages of abrasion[117,118].

In order to optimise the properties of a metallic material for improved wear resistance, some understanding of the wear process during abrasion of metallic materials is required. The wear process in reasonably ductile metals occurs by an initial accumulation of strain or plastic deformation to some threshold value, followed by microfracture and finally failure[117,118]. Consequently, a wear resistant material should plastically deform to high levels of strain, and allow for a large accumulation of strain before microfracture occurs. Thus the initial material hardness, the work hardening rate and the total plastic work capacity of a material are important in determining the wear resistance of a material.

Ball *et al* proposed that it is the high work hardening exponent of materials such as the AISI 201, 301 and 304 steels that accounts for the superior wear performance of these steels[117]. Mills and Knutsen compared the abrasive wear resistance of three steels, viz. a Hadfield steel, a high nitrogen Cr-Mn steel and also an AISI 304 steel[119]. It was shown that increased yield strength was insufficient to improve the wear resistance, but where microfracture and material removal could be postponed to higher levels of plastic strain, abrasion resistance was greatest. Lenel and Knotts investigated the wear performance of a similar range of steels[120]. The authors showed that steels with greater work hardening ability show better wear performance. Basak *et al* have also confirmed the influence of work hardening rate on improved wear performance and showed that alloys with higher nitrogen and manganese levels, and associated increased work hardening rates, show better wear performance than those with lower nitrogen and manganese levels[121]. The best results were obtained when fine titanium carbonitrides, which have a greater hardness than the matrix, formed in the austenite[121].

It has been shown that the formation of particles in steels affects the hardness, yield strength, elongation to failure and work hardening ability. During ageing treatments, the precipitates in the steel grow resulting in particles of different sizes and distributions, which affect the tensile properties of the steel differently[122]. This is illustrated in figure 2.3.1, which shows the effect on precipitate formation on the tensile properties as a function of ageing treatments and thus particle size distribution[122]. In attempts to improve the wear resistance by particle distribution in the matrix, ie carbides or nitrides in the case of steels, care should be taken to optimise the size and distribution of the particles such that the work hardening ability is maintained along with an increase in hardness[1].

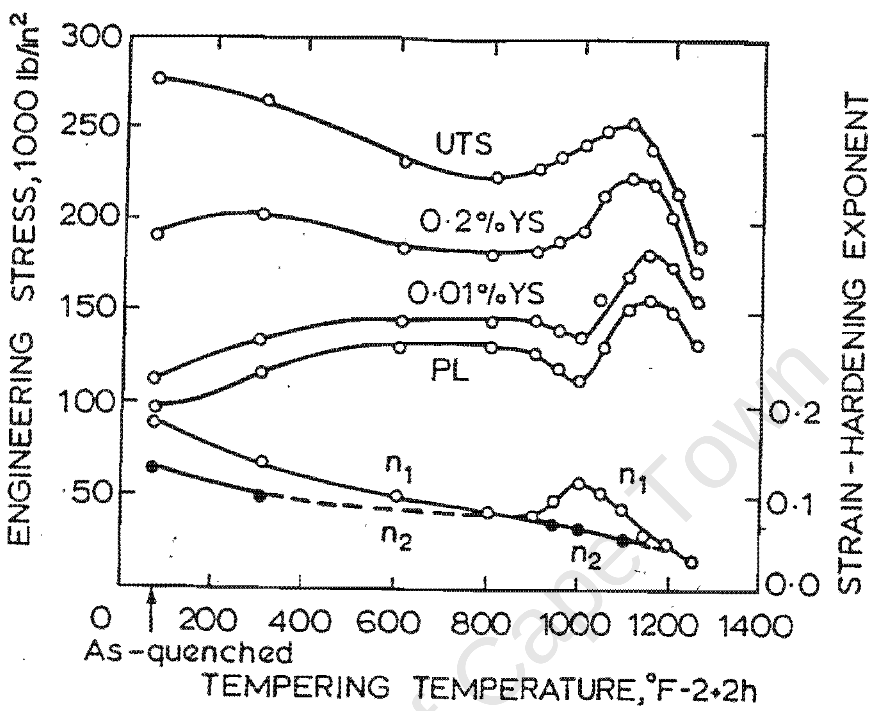

Fig. 2.3.1 The effect of heat treatment and consequently particle distribution on the tensile properties of a steel after Nicholson[122].

The wear mechanism during abrasive wear can also be brittle in nature[116]. In such cases the impact of abrasive particles on the wear surface causes microfracture and consequent material removal[116]. This mechanism occurs in materials with low fracture toughness. For this reason ceramic materials, with low fracture toughness exhibit a lower abrasive wear resistance than cast irons, even though they have the same level of hardness[116].

High nitrogen steels are known for their excellent work hardening ability and toughness as a consequence of the high nitrogen levels and in many cases the high manganese levels. Since good work hardening ability and toughness are beneficial to the wear resistance of metallic materials, these properties should not be decreased dramatically with the formation of precipitates that would potentially increase wear resistance by increasing the hardness.

2.3.1 THE EFFECT OF CHROMIUM NITRIDE PRECIPITATION ON MECHANICAL PROPERTIES

In a series of papers, Rawers and co-workers considered the effect of chromium nitride precipitation on the mechanical and corrosion properties of austenitic stainless steels[107,123,124]. The formation of Cr_2N precipitates increased the hardness and the yield strength of the high nitrogen steel to a small degree[107,123,124], but had a far more dramatic effect on the fracture toughness and plasticity of the steel[107,124]. Increased amounts of cellular Cr_2N precipitation reduced both the elongation to failure and the reduction in area during tensile tests. In addition, the results of Charpy tests also showed a decrease in the toughness of the steel with increased volume fraction of discontinuous cellular precipitation of Cr_2N[124,107]. This collection of data is shown in figure 2.3.2 (a) and (b)[107]. Figure 2.3.2 (a) which shows that increased volume fractions of discontinuous cellular precipitation of Cr_2N, represented by ageing time reduces the toughness of the steel, represented by impact energy in Joules. Figure 2.3.2 (b) shows that the yield strength is not improved by the presence of Cr_2N precipitate cells and the reduction in area during tensile testing is also reduced with ageing. In both figures 2.3.2 (a) and (b), the influence of discontinuous cellular precipitation of Cr_2N on the mechanical properties represented is more pronounced at 900°C, because of the increased kinetics of precipitation at this temperature[107,124].

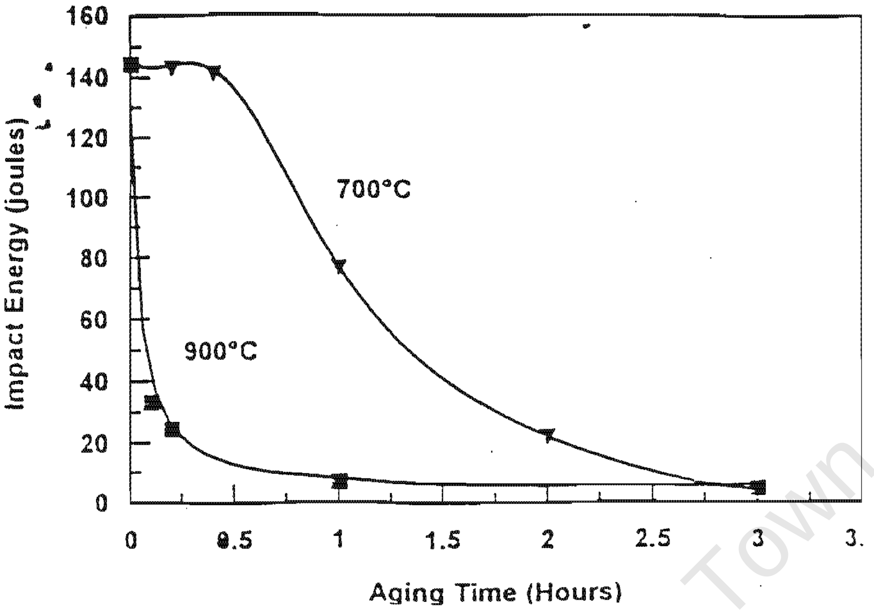

Fig 2.3.2 (a)

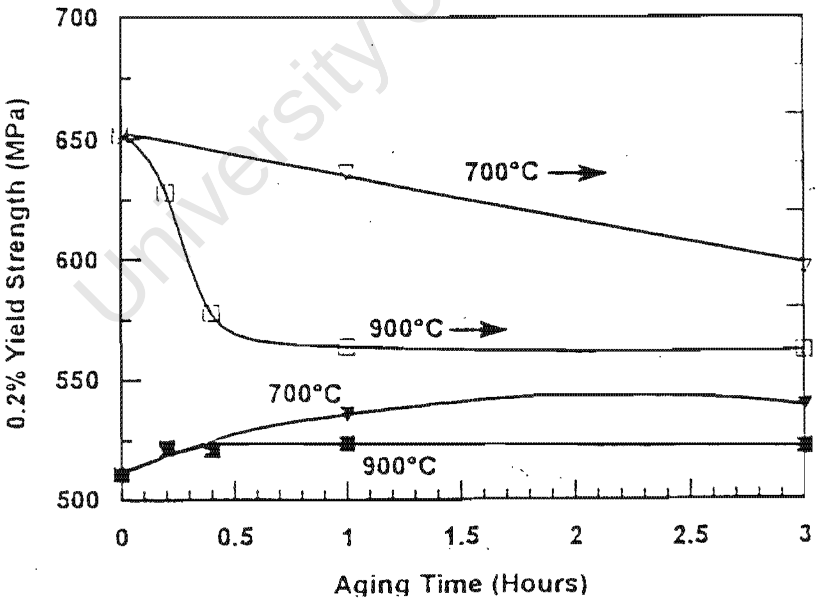

(b)

Fig.2.3.2 The influence of ageing time on the toughness of a nitrogen alloyed steel (a) and the tensile properties of the same steel (b), after Hawk et al[107].

The wear resistance of stainless steels alloyed with low levels of both manganese and nickel, showed an increased wear resistance with increased volume fraction of Cr_2N and CrN precipitation. The improvement in wear resistance was the greatest for the CrN type of precipitates, which formed during solidification and were large (approximately 10μm in diameter) with a blocky type of morphology[107]. It was proposed that the addition of niobium and vanadium might lead to the formation of similar nitride precipitates which could improve the wear resistance further because niobium and vanadium nitrides, with an MX stoichiometry are harder than CrN precipitates[107]. In a similar set of alloys, the formation of discontinuous precipitate cells caused a reduction in wear resistance and this was attributed to extensive microfracture that occurred in the regions of the cells[107]. Further observations in high nitrogen steel alloys with slightly different alloy compositions, viz manganese additions instead of nickel, showed that the formation of discontinuous cellular precipitation of Cr_2N also resulted in a considerable decrease in the toughness of the steel, although accompanied by small increases in yield strength and hardness[125,126].

Finally, Simmons *et al* showed that the formation of Cr_2N type precipitates in low manganese and low nickel steels with additions of 0.69 wt% nitrogen resulted in the sensitisation of the steel[126]. An AISI 316 steel however, showed a greater tendency to sensitise than the high nitrogen steel, when the carbon content in the AISI 316 steel was high because increased carbon levels favour the formation of $M_{23}C_6$ precipitates. The Cr_2N precipitates that form in high nitrogen steels remove less chromium from solid solution and hence do not result in the same degree of sensitisation as is associated with the formation of the $M_{23}C_6$ precipitates. When the carbon content was reduced, then the AISI 316 steel showed better resistance to sensitisation than the high nitrogen steel, since there was less evidence of precipitate formation in the AISI 316 steel than in the high nitrogen steel[126]. The sensitisation behaviour of a high nitrogen steel, an AISI 316 steel with low carbon levels and an AISI 316 steel with high carbon levels is shown in figure 2.3.3, which illustrates the observations discussed above[126].

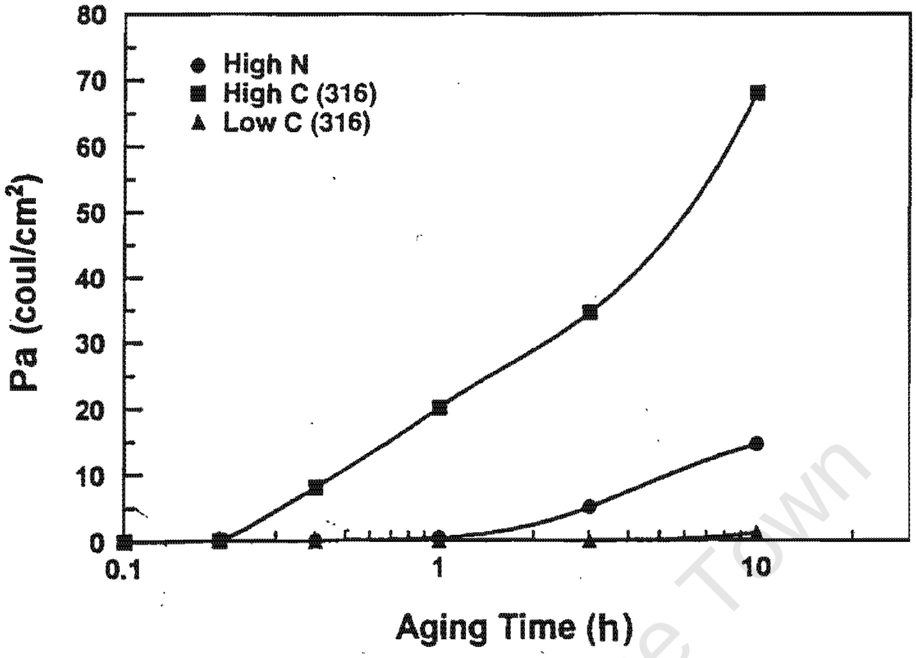

Fig. 2.3.3 A comparison of the sensitisation behaviour of a high nitrogen steel, a AISI 316 steel, with low carbon content and a AISI 316 with a higher carbon content, after Simmons et al[126]

2.3.2 THE EFFECT OF NIOBIUM AND VANADIUM NITRIDES ON MECHANICAL PROPERTIES

2.3.2.1 PRECIPITATE FORMATION DURING AGEING

The addition of niobium, vanadium and titanium to stainless steels has been known to improve the creep resistance of steel because MX-type precipitates, rich in these elements, form in preference to chromium carbides or chromium nitrides[93,98,95,127].

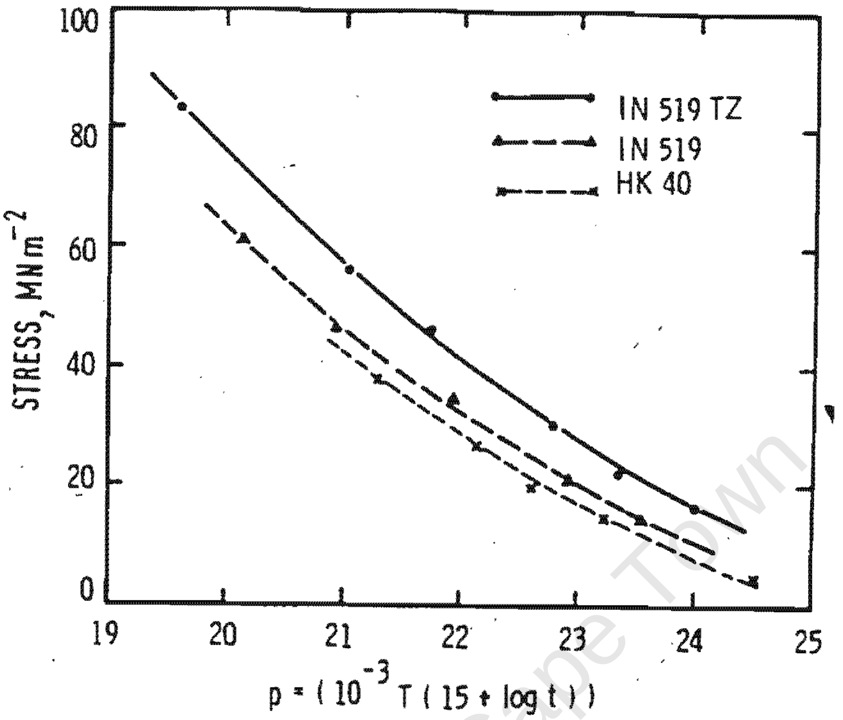

Fig. 2.3.4 A comparison of the creep rupture strength of stainless steels alloyed with niobium (IN519), niobium, titanium and zirconium (IN 519 TZ), and without any precipitate forming elements (HK 40)[98].

The chromium rich precipitates usually coarsen more quickly than the niobium or vanadium rich MX-type precipitates[95,97,98]. The MX precipitates are therefore more effective than chromium rich precipitates at improving the creep resistance of the steel because they are finer than the chromium nitride precipitates[98]. Figure 2.3.4 shows that steels with niobium, titanium and zirconium (alloy IN 519 TZ) and those with niobium additions (IN 519) show better creep resistance than an alloy with the same base composition, without the addition of precipitate forming elements (alloy HK 40)[98].

In spite of the improved creep resistance of steels with MX-type precipitates, these steels often exhibit lower fracture toughness than steels with no precipitation[95].

Miyahara *et al* have proposed that the alloy composition of stainless steels with regard to precipitate forming elements such as titanium, vanadium, and tantalum, must be carefully balanced to produce precipitates of the correct size distribution so that the hardness is improved while retaining some toughness[95]. Their work on titanium, vanadium and tantalum additions to a 12 wt%Cr – 15 wt%Mn steel showed that steels with a large volume fraction of very fine vanadium nitride precipitates exhibited the greatest hardness and the lowest Charpy toughness. Precipitates that were coarser, as a result of tantalum additions, exhibited better toughness although hardness was reduced[95]. Figure 2.3.5 shows that the greatest level of hardness was achieved in alloys 2C1NWV and 1C2NWV and was the result of alloying with vanadium and tungsten[95]. The hardness of these alloys was greater than the alloy with tantalum additions, 1C2NWVTiTa.

It has been observed that the formation of titanium nitrides in a Fe-20 wt%Cr-25 wt%Ni steel improved the wear resistance of the steel considerably[128]. The titanium nitrides were introduced into the steel by a complex powder metallurgy process. A fine distribution of small particles formed in the steel, with a cuboidal/spheroidal shape. Although the yield strength was significantly increased when compared to commercial high nitrogen steels, the elongation to failure decreased significantly. The wear resistance however, of the steel still proved to be better than the AISI 321 steel[128].

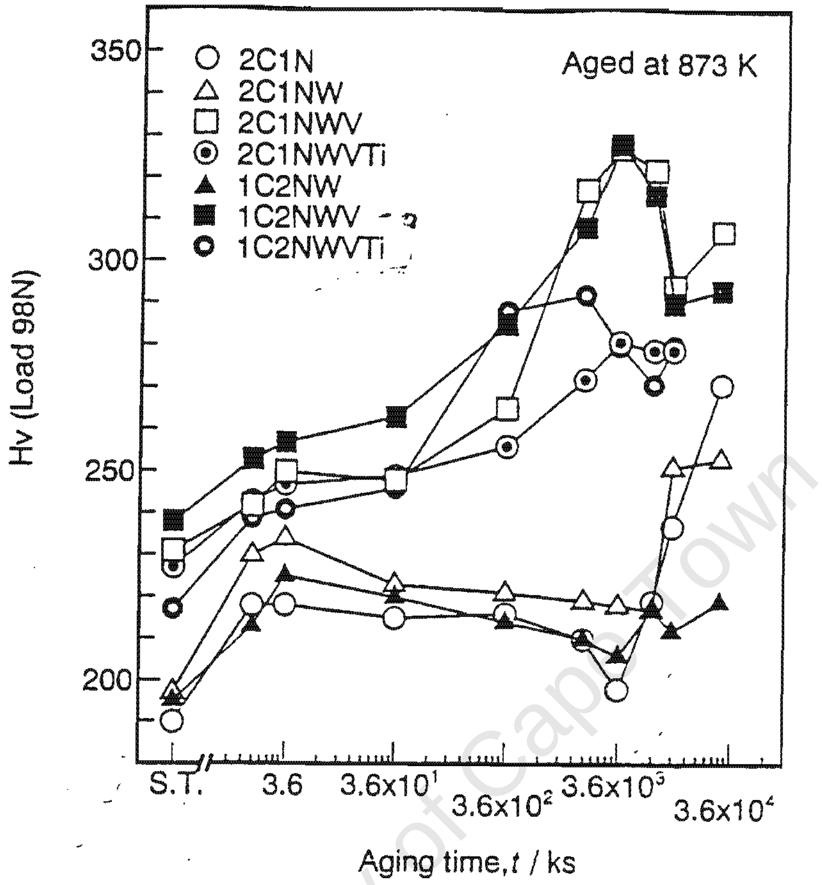

Fig.2.3.5 Vickers hardness as a function of ageing time for a range of Fe-12wt%Cr-15wt%Mn alloys with vanadium, titanium and tantalum additions after Miyahara et al[95].

2.3.2.2 THE EFFECT OF EUTECTIC PRECIPITATES ON MECHANICAL PROPERTIES

Large eutectic niobium carbide precipitates that formed during solidification have been reported to reduce Charpy V-notch toughness and the elongation to failure of mild steels[99,100]. In contrast, Wen Tai *et al* showed that the formation of eutectic $M_{23}C_6$ precipitates and niobium, titanium and zirconium rich eutectics in a Cr-Ni stainless steel improved the creep resistance of the steel[98]. It was proposed that the precipitates hinder crack propagation and grain boundary sliding[98].

The formation of eutectic precipitation is not expected to show favourable results for the wear resistance of materials, because the brittleness associated with these materials could lead to premature microfracture during abrasive wear. Should the addition of precipitate forming elements for the purpose of hardening during a solid state reaction, result in eutectic precipitates, their influence on the wear performance must be carefully considered. The overall effect of the addition of precipitate forming elements might not turn out to be beneficial because of the associated formation of eutectic precipitates.

3. EXPERIMENTAL APPROACH

3.1 MATERIALS

The purpose of the project was to investigate the influence of niobium and vanadium additions on high nitrogen steel alloys with a base composition of 20 wt%Cr-18 wt%Mn-1 wt%N. Columbus Stainless currently produces similar steels for commercial purposes, with the trade name CROMANITE™. The alloy compositions investigated were chosen so that the individual effect of the addition of niobium and vanadium on the microstructure and mechanical properties could be evaluated. Further, the alloy compositions were selected so that the combined effect of both niobium and vanadium could be investigated at different levels of each element. The eight alloys that were selected for experimental investigation are shown in table 3.1.1.

Alloy C contains low levels of both niobium and vanadium, and is thus representative of the base composition of the high nitrogen steel alloy. Alloy D contains 1 wt% niobium and represents the influence of niobium additions to the base composition; likewise alloy E is representative of the influence of vanadium. Alloy F represents the combined effect of both niobium and vanadium, at 1 wt% addition of each. Other alloys were selected with intermediate levels of both niobium and vanadium, which include alloys A and H with more niobium than vanadium, and alloys B and G contain more vanadium than niobium.

Table 3.1.1 The alloy compositions chosen for the current investigation.

Element (wt%)	**Alloy A**	**Alloy B**	**Alloy C**	**Alloy D**	**Alloy E**	**Alloy F**	**Alloy G**	**Alloy H**
Fe	Bal	Bal	Bal	Bal	Bal	Bal	Bal	Bal
Cr	23.88	24.65	24.06	24.43	23.5	23.11	22.99	23.69
Mn	18.79	18.32	17.5	17.45	18.29	14.84	18.42	18.43
N	1.02	1.145	1.03	1.02	1.168	0.98	1.129	1.125
C	0.11	0.14	0.077	0.11	0.13	0.23	0.12	0.14
Nb	**0.62**	**0.29**	**0.04**	**1.17**	**0.04**	**0.92**	**0.29**	**0.40**
V	**0.45**	**0.75**	**0.20**	**0.11**	**1.18**	**0.94**	**0.47**	**0.22**
Trace Elements								
S	*0.006*	*0.006*	*0.004*	*0.007*	*0.004*	*0.006*	*0.006*	*0.004*
P	*0.002*	*0.021*	*0.023*	*0.002*	*0.02*	*0.03*	*0.02*	*0.02*
Si	*0.48*	*0.30*	*0.25*	*0.28*	*0.28*	*0.47*	*0.5*	*0.45*
Cu	*0.05*	*0.08*	*0.09*	*0.06*	*0.07*	*0.08*	*0.07*	*0.06*
Co	*0.01*	*0.02*	*0.01*	*0.02*	*0.03*	*0.01*	*0.02*	*0.02*
Ti	*0.008*	*0.003*	*0.003*	*0.005*	*0.003*	*0.008*	*0.007*	*0.005*
Mo	*0.003*	*0.030*	*0.080*	*0.110*	*0.020*	*0.920*	*0.020*	*0.030*
Ni	*0.21*	*0.21*	*0.48*	*0.48*	*0.20*	*3.36*	*0.21*	*0.22*

3.2 EXPERIMENTAL PROCEDURE

3.2.1 HEAT TREATMENTS

Sections of material were cut from the ingots and then heat treated in a vacuum furnace in an argon atmosphere. Samples were placed in the vacuum furnace and a vacuum of 0.0133 Pa was obtained, following which argon was bled into the furnace to a pressure of 40000 Pa at room temperature. During the heating to the required heat treatment temperature the pressure increased to values of approximately 13000 Pa, because of the heating up of the furnace, and the heat treatment was completed at this pressure. After the required time at the heat treatment temperature, argon was bled into the vacuum furnace to atmospheric pressure, so that the furnace could be opened and the specimens could be drop quenched into water. Water quenching of the samples ensured that the high temperature microstructure was frozen in and could then be investigated using standard metallographic techniques described in section 3.2.2.

Fig 3.2.1 The vacuum furnace used for heat treatments for the work presented in this thesis.

The vacuum furnace that was used for the heat treatments is shown in figure 3.2.1. The furnace was specifically designed for drop quenching from elevated temperature. The specimen is suspended at (a) inside the furnace on a pin and the furnace tube is closed and is sealed at (b), (c) and (d). The vacuum system is on the left-hand side of the photograph and consists of a rotary pump for roughing (e) and an oil diffusion pump for backing (f) and both are used to obtain the required vacuum in the tube (the roughing pump cannot be seen because it is behind the diffusion pump). It is the oil diffusion pump that is able to achieve vacuums of better than 0.0133 Pa. Argon is bled into the furnace before heating at (g) to the required argon pressure and after the heat treatment, argon is bled in to atmospheric pressure, so that the gate valve at (c) can be opened. A bucket of water (h) is placed under the furnace tube (i) and a lever is pushed at (a) so that the basket holding the specimen falls off the pin on which it is suspended and into the water. This ensures that it is quenched quickly to room temperature from elevated temperature. An S-type thermocouple is suspended in the furnace at (b) and care is taken so that the specimen is at the same level as the tip of the thermocouple where temperature measurements are recorded (j). A EUROTHERM temperature controller (k) is responsible for the heating cycles during the heat treatments and is connected to a series of eight elements which are placed around the furnace tube inside the aluminium housing (j). The furnace tube is a 99.7 % purity alumina tube, which is able to resist temperatures of 2000°C and also has good vacuum integrity. The photograph was taken at elevated temperature, which explains the orange glow of the alumina tube.

Samples of the alloys were first solution treated before they were aged at different temperatures. Initial investigations for an appropriate solution treatment showed that there was little difference in the microstructure after two, five and ten hour solution treatments at 1250°C and 1300°C. A solution treatment of two hours at 1300°C was therefore selected as a standard treatment for all of the alloys prior to ageing. This treatment ensured that the specimens from the castings were homogenised and that maximum dissolution of precipitates that formed during casting had been achieved.

Following the solution treatment at 1300°C for two hours, specimens of the eight alloys were aged at three different temperatures. Various authors have shown that precipitation occurs in high nitrogen steel alloys between 500°C to 1200°C and different forms of precipitation have been reported in this temperature range[31,33,38,42,107],. For a complete investigation of precipitate formation in the eight high nitrogen steel alloys temperatures of 800°C, 1000°C and 1100°C were selected.

For an initial investigation of the influence of ageing treatments on microstructural evolution, specimens were first aged for 2 hours. Following this study, consideration was given to the feasibility of an investigation of longer and shorter ageing times for each alloy and for each ageing temperature. Where necessary, some of specimens were aged for times of 0.5 hours, 5 hours, 10 hours and 100 hours. After each ageing treatment the specimens were water quenched, again to freeze in the high temperature microstructure for further analysis.

3.2.2 METALLOGRAPHY

After heat treatments, specimens were sectioned so that any surface effects due to heat treatment would be eliminated. The specimens were then mounted in resin and polished using a STRUERS automatic polisher to a 0.25 μm finish. The mounted samples were electro-polished, when necessary, in a chromic acid solution with the composition given below, at 20 V for up to 60 seconds at room temperature.

25g CrO_3
133ml acetic acid
7ml distilled water

The same solution was used for etching, but the voltage was decreased to 10 V and the samples were etched for approximately 20 seconds. Niobium and vanadium precipitates were not preferentially attacked by the chromic acid solution, during electro-polishing and etching, which left the precipitates standing proud on the matrix surface. Chromic acid however, did attack chromium rich precipitates preferentially, leaving behind holes. The etching procedure did however produce good results for light microscopy, and any further analysis of the precipitates was completed either in backscattered mode on the scanning electron microscope, or in the transmission electron microscope.

Light microscopy was carried out using a REICHERT Me3A light microscope using Nomarski interference contrast. The images obtained from this microscope showed the distribution of the precipitates and volume fraction of the precipitates. In some cases the morphology of the precipitates could be characterised. Light micrograph images were captured using a LEICA digital camera.

3.2.3 COMPOSITIONAL ANALYSIS

Polished sections of the alloys after various heat treatments were imaged using a LEICA 440 scanning electron microscope (SEM). In most cases, images were acquired using backscattered electron mode, but the microscope was also used in secondary electron mode. The primary purpose for the use of the LEICA 440 SEM was to obtain compositional information from the precipitates, in the form of x-ray maps.

X-ray maps show the change in concentration of an element across a field of view of the sample, in terms of a change in colour. For the current investigation, red indicates a high concentration of the element detected and blue represents a low concentration. X-ray maps were acquired successfully from bulk samples when the precipitates of interest were at least 1μm in diameter. In this case, an accelerating voltage of 20 kV was used with a probe current of 2 nA. X-rays were collected from each data point for approximately 70 ms, and the size of the maps was 256x256 pixels. The area of the sample that was scanned depended on the magnification selected.

X-ray maps from precipitates smaller than 1 μm could not be acquired successfully from bulk samples. The interaction volume of the electron beam in a bulk sample produced x-rays from the small precipitate as well as the matrix below. Consequently the x-rays from the interaction volume masked any difference in composition at the surface and the compositional change in the precipitate could not be detected. Instead of bulk samples, thin foil samples were mounted on cylindrical stubs and placed in the SEM. X-ray maps generated from these samples successfully showed the compositional differences between the precipitate and the matrix, since the foils reduced the interaction volume associated with bulk samples. The x-ray maps generated from the thin foils were acquired using the same instrument settings as those that were acquired from the bulk samples. As a consequence a qualitative description of the composition of precipitates approximately 50-100 nm in diameter or width could be obtained.

3.2.4 X-RAY DIFFRACTION

X-ray diffraction (XRD) data was collected to determine the lattice parameter of the austenite in selected alloys. This data was used so that the austenite could be used as a standard for electron diffraction studies of precipitates in the austenite matrix. In addition, XRD data was used to identify second phases in the alloys when necessary. A computer interfaced PHILIPS x-ray diffractometer was used to collect x-ray data using a copper tube, which generates x-rays with a wavelength of 1.54 Å. X-rays were collected over a 2-theta range of 30° to 100° at an increment of 0.01°, and the x-rays at each increment were collected for 10 s. The voltage was set at 40 kV and the current at 25 mA.

3.2.5 ORIENTATION MAPPING

Microstructural maps based on orientation measurements were acquired using two different systems. At the Electron Microscope Unit at the University of Cape Town the HKL TECHNOLOGY electron backscattered diffraction (EBSD) system attached to a CAMBRIDGE S200 SEM was used. At the University of Manchester and UMIST, the HKL TECHNOLOGY EBSD system was attached to a field emission gun SEM, which was capable of higher resolution than the CAMBRIDGE S200 SEM. In both cases the scanning electron microscopes were operated at 20kV and the beam current was optimised for good pattern quality. Both the beam scan mode and the stage scan mode were employed, depending on the microstructural features that were analysed.

Typical step size values for the beam scan mode were 1 μm and for the stage scan mode, 15μm. The beam scan mode was used for the analysis of fine microstructural features, of the order of 1μm and the stage scan mode was used for coarser microstructural features such as grain sizes of 10 μm. The orientation data was processed using a custom written program, VMAP 6[129]. The orientation images were produced as Euler colour maps. These maps are 256 colour maps in which the strengths of the primary colours are proportional to the three Euler angles. In many cases, regions of similar orientation have similar colours. However, this is not always the case because of discontinuities in Euler space, but this complication did not create any confusion for the purposes of the current investigation.

3.2.6 DIFFRACTION STUDIES

The transmission electron microscope (TEM) was required for imaging of very fine precipitates that could not be resolved in the light microscope, to characterise their size and morphology. In addition, diffraction information generated by the TEM was used to determine the crystal structure of the precipitates, to calculate the lattice parameters and to establish the orientation relationship between the precipitate and the matrix.

3.2.6.1 SPECIMEN PREPARATION

Discs 3 mm in diameter were punched from a mechanically thinned square of material approximately 200 μm thick. The discs were further thinned mechanically until they were 80-100 μm thick. Finally the discs were electrochemically thinned to perforation, using a STRUERS TENUPOL jet electropolisher with the following polishing solution:

10% perchloric acid
20% glycerol
70% methanol

Samples were polished between 15 V-17 V and at temperatures between –10°C and 0°C, using an approximate flow rate setting of 4.5 on the instrument.

3.2.6.2 *Selected Area Diffraction vs Convergent Beam Electron Diffraction Techniques*

A JEOL 200CX transmission electron microscope was used at the beginning of the project for the analysis of the precipitates. In many cases the precipitates that were studied were less than 100 nm in diameter or width. Further, the precipitates frequently possessed a lamellar structure, which led to complicated selected area diffraction (SAD) patterns, as a result of double diffraction effects[130]. Selected area diffraction studies on the JEOL 200CX gave limited diffraction information, which then motivated for the use of an electron microscope with convergent beam electron diffraction (CBED) capabilities.

A PHILIPS CM 12 electron microscope was used for diffraction studies and later when this microscope was no longer available, a PHILIPS 420 electron microscope was used. The CM 12 microscope is more modern than the EM 420, however both microscopes are designed with the patented Twin Lens system by PHILIPS[130]. The design includes an auxiliary lens that is placed above the upper objective lens pole piece. The prefield of the upper objective lens pole piece acts together with auxiliary lens and creates a telefocal lens effect. This enables the microscope to generate both a parallel beam for selected area diffraction studies and also allows the user to focus the beam onto the sample to allow CBED[130].

Both selected area diffraction and CBED methods were used to obtain diffraction information from the precipitates in the TEM samples. Selected area diffraction techniques are limited however, since the size of selected area aperture on a TEM cannot be reduced indefinitely in order to limit the diffraction information to a small areas on the specimen[44]. The smallest area that can be selected for SAD is approximately 500 nm[44]. As the aperture size is decreased, the errors that occur in the diffraction pattern, as a result of spherical aberration effects, increase significantly[44]. In cases where diffraction information cannot be collected from the precipitates because they are small in relation to the matrix that is exposed by the selected area aperture, CBED techniques can be used. The beam can be focussed to a fine probe on the sample, which in the case of the PHILIPS 420 and CM12 microscopes is a minimum of 40 nm in diameter, in the microprobe mode. This allowed CBED information to be obtained directly from the very fine precipitates that were commonly found in the Cromanite alloys.

The diffraction pattern that is obtained using convergent beam electron diffraction (CBED) techniques is different to that obtained by SAD; instead of the fine spots generated by SAD, discs of intensity are seen that correspond to the convergent diffracted beams[44]. When the C2 aperture setting is between 10-50 μm (aperture diameter) the Kossel-Möllenstedt (K-M) conditions are satisfied and a K-M pattern is generated[44]. The K-M pattern consists of discs of intensity that do not overlap, but when the diameter of the aperture is increased then the diffraction discs overlap[44]. Figures 3.2.2 and 3.2.3 show the ray for the electron beam associated with each technique and how spots in the case of SAD are generated and discs in the case of CBED are generated.

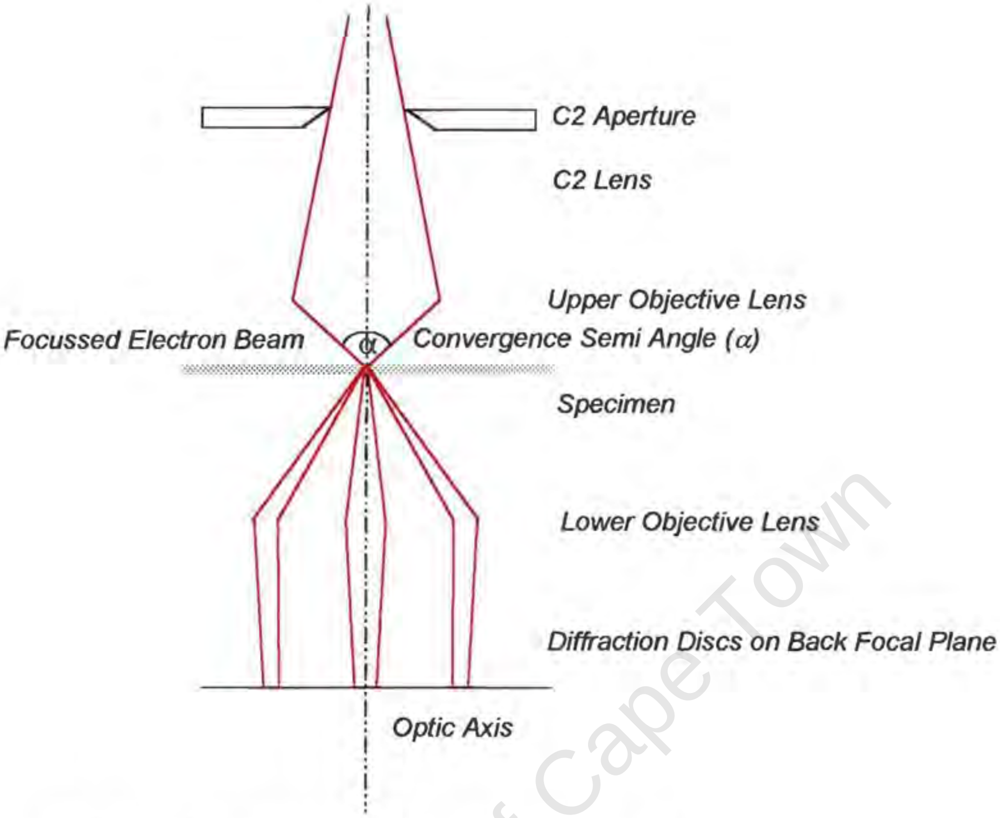

Fig 3.2.2 Ray diagram for a CBED pattern, after Williams and Carter[44].

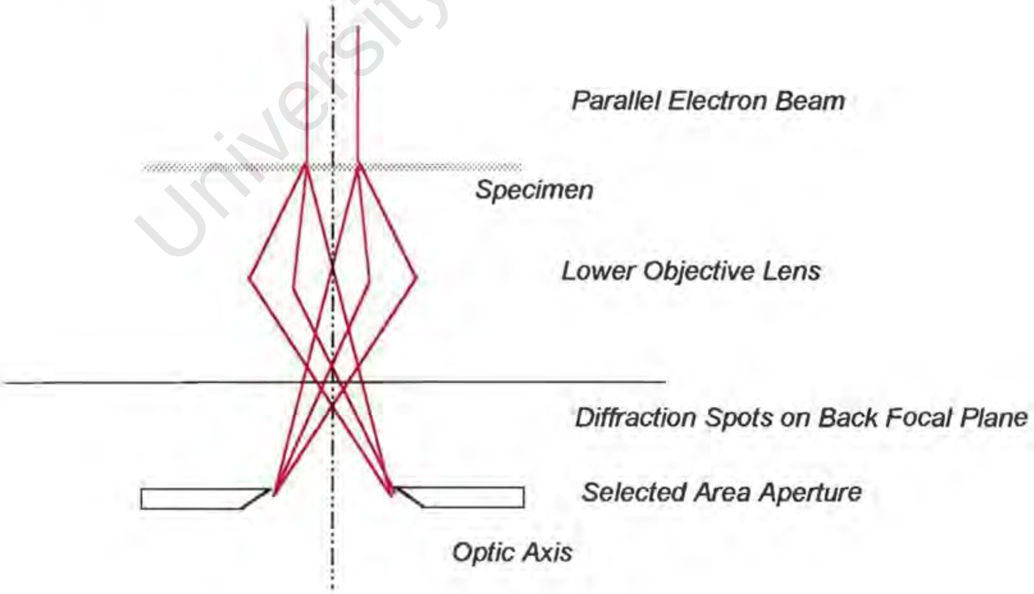

Fig 3.2.3 Ray diagram for typical SAD patterns after Williams and Carter[44].

The variables associated with CBED are, like selected area diffraction, the camera length and focus of the pattern. CBED, however, introduces a further variable, which is the convergence semi-angle (α) and is dependent on the size of the C2 aperture[44]. For small C2 apertures, the diffraction discs are small, but if the C2 aperture is increased, the diffraction discs also increase in size and can overlap, in which case it is possible to obtain Kikuchi line diffraction patterns from the sample[44]. The K-M diffraction pattern obtained using CBED techniques with a small C2 aperture, ie a small convergence semi-angle (α), can be indexed in the same way as a spot pattern obtained by SAD techniques; the difference is that the area analysed in the case of CBED is much smaller. Thus the two diffraction patterns can be compared with each other. A further variable for CBED is the spot size or the size of the probe. A change in spot size does not change the distance between the spots in the diffraction pattern, but decreases the area and volume from which diffraction information is obtained.

A large amount of information can be obtained from a CBED diffraction pattern. Specimen thickness can be determined from the fringes that are observed in diffraction discs, for the relevant C2 aperture setting. Further, since CBED patterns can show reflections for the zero order laue zones, as well as higher order laue zones, the symmetry of the crystal that is analysed can be determined. For the purposes of the current work, in each case the zero order Laue zone was recorded and analysed. The purpose of the CBED studies was to generate diffraction information from small precipitates, of the order of 50 nm in diameter, and distinguish their crystal structure as either NaCl FCC or HCP.

3.2.6.3 *INSTRUMENT SETTINGS*

In the case of the PHILIPS CM12 a camera length of 770 mm was used, and in the case of the PHILIPS 420, 660mm was used. In analysis of the diffraction pattern the camera constant, $L\lambda$, was determined using the austenite spots, knowing that the lattice parameter of the austenite is 3.6 nm, (calculated from x-ray diffraction results).

In addition a standard sample of pure aluminium was also used to confirm the results of the calculation for Lλ. For the CBED work a C2 aperture setting of 2 was used and this translates to a size of 50 μm, and resulted in diffraction patterns with small discs that did not overlap, ie the Kossel-Möllenstedt conditions were satisfied. This type of diffraction pattern is sometimes termed a microdiffraction pattern. In this thesis K-M type patterns have been generated to identify the phases in the high nitrogen steel alloys and are referred to as CBED patterns.

3.2.7 THERMODYNAMIC CALCULATIONS USING THERMOCALC

Thermocalc is a software package used for various types of thermodynamic calculations. In particular Thermocalc can be used for phase diagram calculations for binary systems, ternary systems, quaternary systems and most pertinent, multicomponent systems. Isopleth diagrams can be generated for multicomponent systems for different conditions. For example, a diagram can be generated to show how a difference in temperature and the addition of an element to a base composition changes the phase stability of the system. Another example could be diagrams that show how the phase stability of the system changes with the addition of two elements at a particular temperature. This sort of diagram is a type of 'ternary diagram' and has been used extensively in the current work, but is more correctly termed an isopleth diagram.

The thermodynamic calculations that are generated by Thermocalc require comprehensive databases that describe the binary, ternary and quaternary systems relevant to the multicomponent systems. A number of databases have been developed for specialised applications, such as light alloys, steels, those for geological applications and also aqueous solutions, to name a few. The database that was used during the current investigation is called FEDATA, and has been developed especially for steels. The accuracy of isopleth diagrams that are generated for multicomponent systems depends on the accuracy of the assessments made of the binary, ternary and quaternary systems stored in the database that are relevant to the multicomponent system.

Thermocalc was used at the beginning of the project to assist with an initial investigation of the phases that were expected to form in the range of high nitrogen steel alloys. For this investigation, a base composition of Fe-24 wt%Cr-18 wt%Mn-1 wt%N-0.1 wt%C was used to generate isopleth diagrams for 1300°C, 1100°C, 1000°C and 800°C, which correspond to the different heat treatment temperatures in the experimental matrix. The diagrams show two axes, the x-axis varies niobium from 0 to 1wt% and the y-axis varies vanadium from 0 to 1wt%, and iron takes up the compositional balance in each case.

Following some experimental investigation, minor discrepancies were found between the results predicted by Thermocalc and those found by experiment. Thermocalc predicts that ferrite should be stable in all of the alloys through a range of temperatures, and this was not observed experimentally. Secondly, the temperature at which some precipitation reactions were predicted to occur could not be verified by the experiments. The most critical parameters, which determined the ferrite/austenite phase balance in the current high nitrogen steel alloy system were those that described the interactions between Fe-Mn-N and Cr-Mn-N. These interaction parameters were not well described in the database for the high levels of these alloy additions in the high nitrogen steel system[131]. This problem was investigated further, and some tentative changes were made that gave better predictions for the austenite/ferrite balance for the high nitrogen steel alloy system[131]. Any permanent changes to the database however, require a more rigorous assessment of the relevant binary and ternary diagrams for the alloy levels relevant to the current high nitrogen steel alloy system.

The discrepancies associated with the temperatures at which different precipitation reactions occurred was also remedied to some degree. Comparison of the experimental results with the predictions made by Thermocalc motivated careful study of the factors that affect the phase balance in this alloy system. It was found that the silicon levels in the high nitrogen steel alloys affected the stability of the M_2X phase, but the silicon levels were not included in the initial calculations. The calculations were then repeated, for niobium and vanadium additions to a base composition of Fe-24 wt%Cr-18 wt%Mn-1 wt%N-0.1 wt%C-0.5 wt%Si, and these calculations gave better predictions of the phase balance at the four temperatures that were investigated. It is this set of diagrams that have been presented in the current work.

The isopleth diagrams that were finally generated by Thermocalc resulted from an iteration between the evaluation of experimental results and communication with the Royal Institute of Technology, Stockholm, Sweden where the Thermocalc software is developed. The final product is a convenient map of the phase balance as a function of niobium and vanadium additions, which aids the understanding of the influence of these elements on the microstructural evolution. These diagrams represent the best possible prediction that Thermocalc can make for these alloy systems. The discrepancies that have been discovered might be addressed in the future by the developers of the software and the assessment of the database that is required for better predictions is beyond the scope of the current work.

Thermocalc was also used to generate Scheil-Gulliver simulations of solidification for the alloys to determine the influence of niobium and vanadium on the nature of solidification. These simulations helped to explain the microstructural evolution of the alloys observed in the solution treated condition. Such simulations assume that local equilibrium is established at the transformation front. Further, for Scheil-Gulliver solidification, the solid that has formed at the solid liquid interface is removed from the system and then the calculation proceeds to the next step. Complete mixing in the liquid is assumed, but the back diffusion in the solid is ignored. The Scheil-Gulliver simulation of solidification is a type of a macro, which makes use of both the Thermocalc software and the relevant databases and for the current project the

FEDATA database was used for the Scheil-Gulliver solidification simulations. The discrepancies that were found for the isopleth diagrams as a result of using the FEDATA database were also found for the Scheil-Gulliver simulations. There was no evidence that ferrite formed during solidification in all of the current alloys, contrary to predictions by Thermocalc, however the Scheil-Gulliver simulations were primarily used to predict the eutectic formation of MX precipitates in some of the alloys, for which satisfactory results were obtained.

3.2.8 MECHANICAL TESTS

In order to characterise the mechanical behaviour of the current system, as a function of microstructural evolution four different mechanical tests were employed. These tests were selected so that the wear performance of the samples investigated would be properly evaluated. Tensile tests were used to determine the yield strength, ultimate tensile strength and the ability of the material to plastically deform; properties that are pertinent to the wear resistance of a material. Charpy V-notch tests were used to determine the response of the steel to high strain rate conditions and thereby evaluate the toughness. Finally abrasion tests were performed to characterise the abrasion resistance of the steel, since the high nitrogen steel alloys were intended for applications that require superior abrasion resistance.

3.2.8.1 TENSILE TESTS

The first objective of the tensile tests was to determine the effect of precipitate type, dependent on both alloy composition and heat treatment, on the tensile properties of the steel. Secondly the aim of the tensile tests was to determine the influence of ageing time on tensile properties. The ageing time and alloy compositions that were selected for this evaluation were those that showed promising microstructural results for improved wear resistance.

Samples were machined from bulk material, to a diameter of 5.04 mm and a gauge length of 25.2 mm, according to the ASTM 8E standard. The specimens were tested at a strain rate of 10^{-3} s^{-1} and force (N) vs elongation (mm) data was generated by a ZWICK tensometer with corresponding ZWICK software.

3.2.8.2 CHARPY V-NOTCH TESTS

Substandard Charpy V-notch specimens were machined from the ingots following the appropriate heat treatments. The dimensions of the substandard Charpy V-Notch specimen are shown in figure 3.2.4. The samples were tested and the toughness of the material was measured by the amount of energy (Joules) required to fracture the specimen.

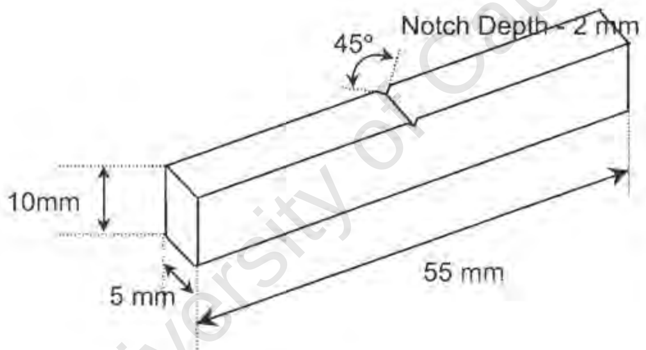

Fig. 3.2.4 Dimensions of the sub-size Charpy V-notch specimens used for testing of the toughness of selected specimens.

3.2.8.3 WEAR TESTS

Abrasion tests on selected high nitrogen steel alloys were performed on a converted Rockwell belt sandblaster shown in figure 3.2.5. The tests were of the pin-on-belt type and the specimen that was used in each case was the shoulder of a tensile test specimen. The abrasive belt runs at a constant velocity and the machine has been designed so that the specimen moves across the abrasive belt at a constant velocity.

An especially designed holder for the tensile specimen shoulder holds the specimen firmly in place and owing to the design of the rig, the specimen is always exposed to fresh abrasive on the belt. Before the commencement of each test, the sample is first 'run-in' so that a steady state material loss regime can be achieved during the test. After each 2.4 m abrasion run the specimen is weighed to an accuracy of 0.1 mg and the mass loss of each sample is plotted as a function of abrasion distance, in 2.4 m increments. The test conditions used for the evaluation of the abrasive wear resistance of the material are shown in table 3.2.1.

Table 3.2.1 Conditions employed for the abrasive wear test

Description	***Test Condition***
Specimen Area	50.2 mm^2
Abrasion Speed (forward)	260 $mm.s^{-1}$
Abrasion Speed (transverse)	2.2$mm.s^{-1}$
Load	15 N
Abrasive Particles	80 grit alumina on an abrasive belt
Abrasive Path Increment	2.4 m
No of increments	5

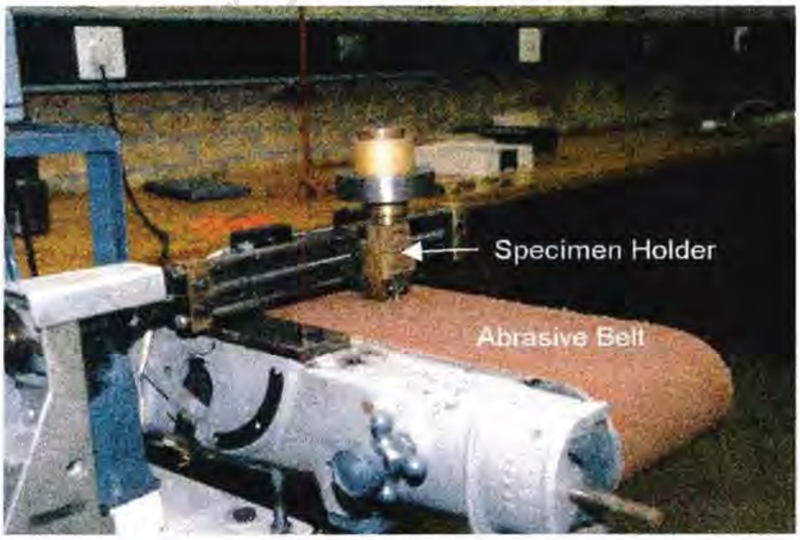

Fig 3.2.5 Rockwell belt sandblaster converted for two body abrasive wear tests of the pin-on-belt type.

4. RESULTS

4.1 THE SOLUTION TREATED CONDITION

All of the eight alloys in the current investigation were first solution treated at 1300°C for two hours and water quenched, prior to any further ageing treatments. The microstructural evolution during ageing will develop from the microstructure in the solution treated condition, thus proper characterisation of the influence of ageing treatments on the alloys first requires a study of the alloys in the solution treated condition. Such a study allows the precipitates that have formed during ageing to be distinguished from those that were already present in the solution treated condition. This follows through to the influence of precipitation on the mechanical properties. It is necessary to determine the effect of niobium and vanadium additions on the mechanical properties of the alloys in the solution treated condition, so that any changes in mechanical performance as a result of ageing can be distinguished.

4.1.1 ISOPLETH DIAGRAM

The results of the thermodynamic calculations using the Thermocalc software with the FEDATA database are shown in figure 4.1.1. This diagram represents the equilibrium phase balance that is expected for each of the eight alloys at 1300°C as a function of both niobium and vanadium levels, represented on the x and y axis respectively. Alloys C, D, F and E represent the boundary conditions of the current investigation with regard to composition. Those alloys that mark the centre of the phase diagram represent the intermediate compositional conditions.

Thermocalc predicts that alloy C should contain both austenite and ferrite, whereas all of the other alloys should consist of austenite, ferrite and MX precipitates. Further examination of the isopleth diagram shows that niobium is more effective than vanadium at promoting MX precipitation, since only 0.1 wt% niobium is required for

MX precipitation but MX precipitation is absent up to levels of 0.8 wt% vanadium. This observation is supported by the metallographic studies of the alloys after solution treatment, which follow. These predictions are accordingly consistent with the microstructural investigation of the alloys. The only discrepancy is the prediction that ferrite should be present at this temperature in all of the alloys, whereas it was only observed in alloy D. The reason for this discrepancy is explained in section 3.2.7.

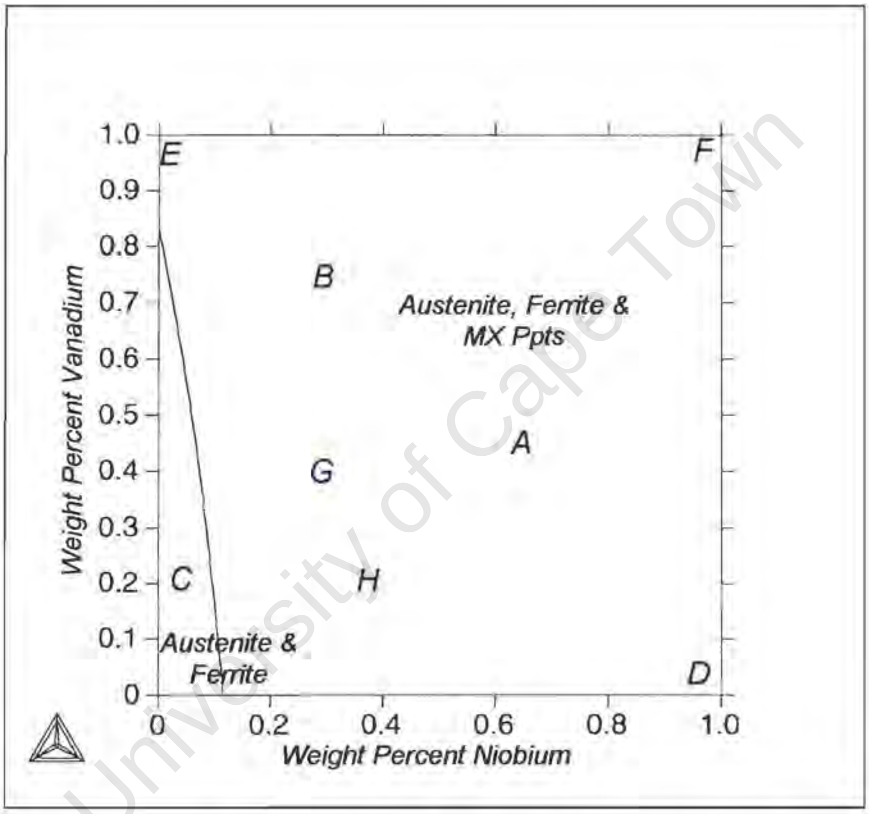

Fig.4.1.1 Section of an isopleth diagram at 1300 ℃ for a base composition of Fe-20 wt%Cr-18 wt%Mn-1 wt%N-0.1 wt%C-0.5 wt%Si. Niobium and vanadium are plotted on the x and y axis respectively and iron makes up the third axis. The diagram shows the influence of niobium and vanadium levels on the phase balance in the high nitrogen steel alloys, marked A-H on the map at 1300℃.

4.1.2 PHASE IDENTIFICATION

4.1.2.1 METALLOGRAPHY

Figures 4.1.2 (a)–(d) show the microstructure of each of alloys C, D, E and F after the solution treatment. These alloys represent the compositional limits of the alloys investigated, as shown in figure 4.1.1. The microstructure of alloy C in figure 4.1.2 (a) shows that alloy C (the base composition) consists of a single phase microstructure with large grains, probably resulting from the casting process. The microstructure of alloy E after the solution treatment is similar to alloy C in the solution treated condition and is shown in figure 4.1.2 (b). In contrast, the microstructure of alloy D, shown in figure 4.1.2 (c) consists of large blocky precipitates and a second metallic phase in the austenite matrix. No evidence of a second metallic phase was observed in alloy F, which represents the addition of 1 wt% of both niobium and vanadium. Large blocky precipitates are observed embedded in the matrix of alloy F, similarly to alloy D, as shown in figure 4.1.2 (d).

To confirm that the matrix phase in alloys C, E, D and F was austenite and to identify the second metallic phase observed in alloy D, X-ray diffraction (XRD) studies were conducted on these four alloys. The XRD plot in figure 4.1.3 (a) is representative of the results obtained from alloys C, E and F, and the plot in figure 4.1.3 (b) is representative of alloy D. As was expected, the XRD plots show that alloys C and E are fully austenitic. The matrix in alloy F is austenite and the second metallic phase in alloy D is ferrite. The identity of the precipitates is confirmed later in section 4.1.2.2 by the results of x-ray maps and electron diffraction studies.

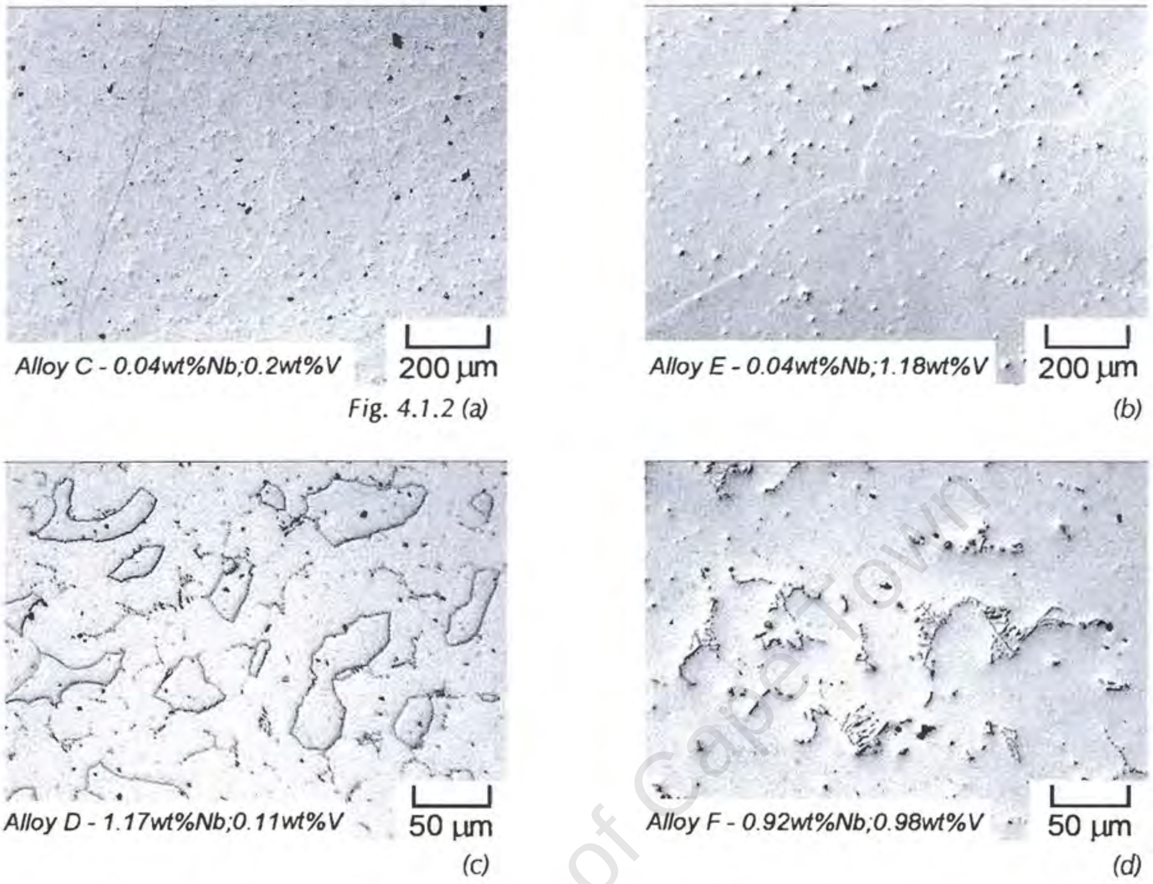

Figure 4.1.2 (a)-(d) Alloys C, E, D & F respectively showing the different volume fractions of blocky precipitates in each of the alloys after the solution treatment.

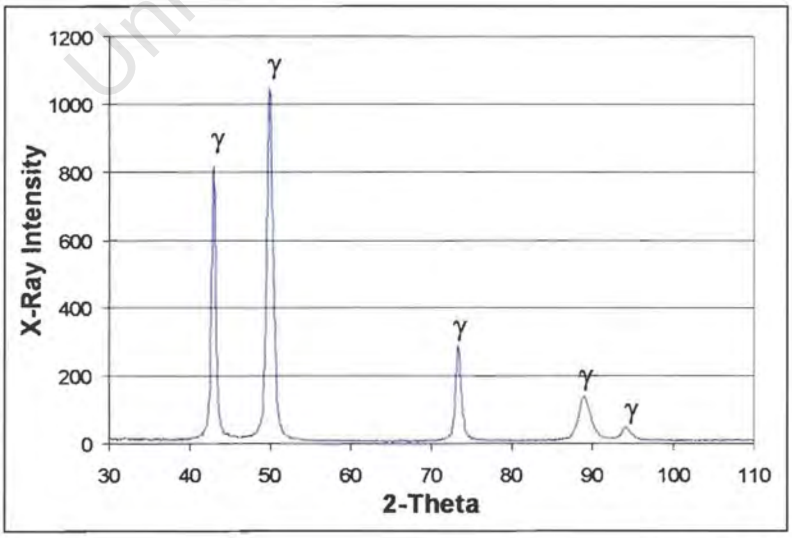

Fig. 4.1.3 (a)

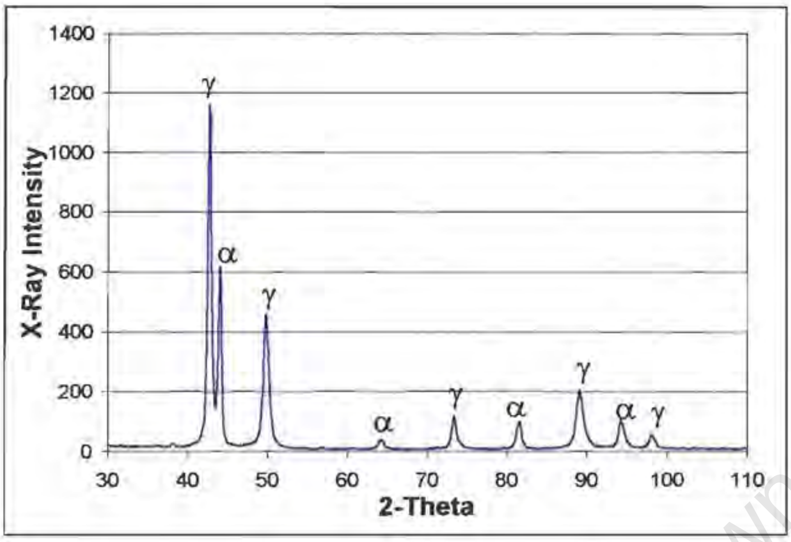

(b)

Fig. 4.1.3 XRD plots representative of (a) alloy C, E and F showing the x-ray peaks for austenite, (b) alloy D showing the x-ray peaks for both austenite and ferrite.

Figures 4.1.4 (a)-(d) show the microstructure of alloys A, B, G and H after the solution treatment. Alloys A, B, G and H each contain unequal amounts of niobium and vanadium, at levels of less that 1 wt% of each. After the solution treatment, all of these alloys are observed to contain blocky precipitates embedded in the austenite matrix, similar to the blocky precipitates in alloys D and F. Alloys A and H, which contain more niobium than vanadium exhibit a greater volume fraction of blocky precipitates. Conversely, alloys B and G contain more vanadium than niobium and exhibit a lower volume fraction of blocky precipitates. None of the alloys A, B, G and H show the presence of the ferrite phase after the solution treatment.

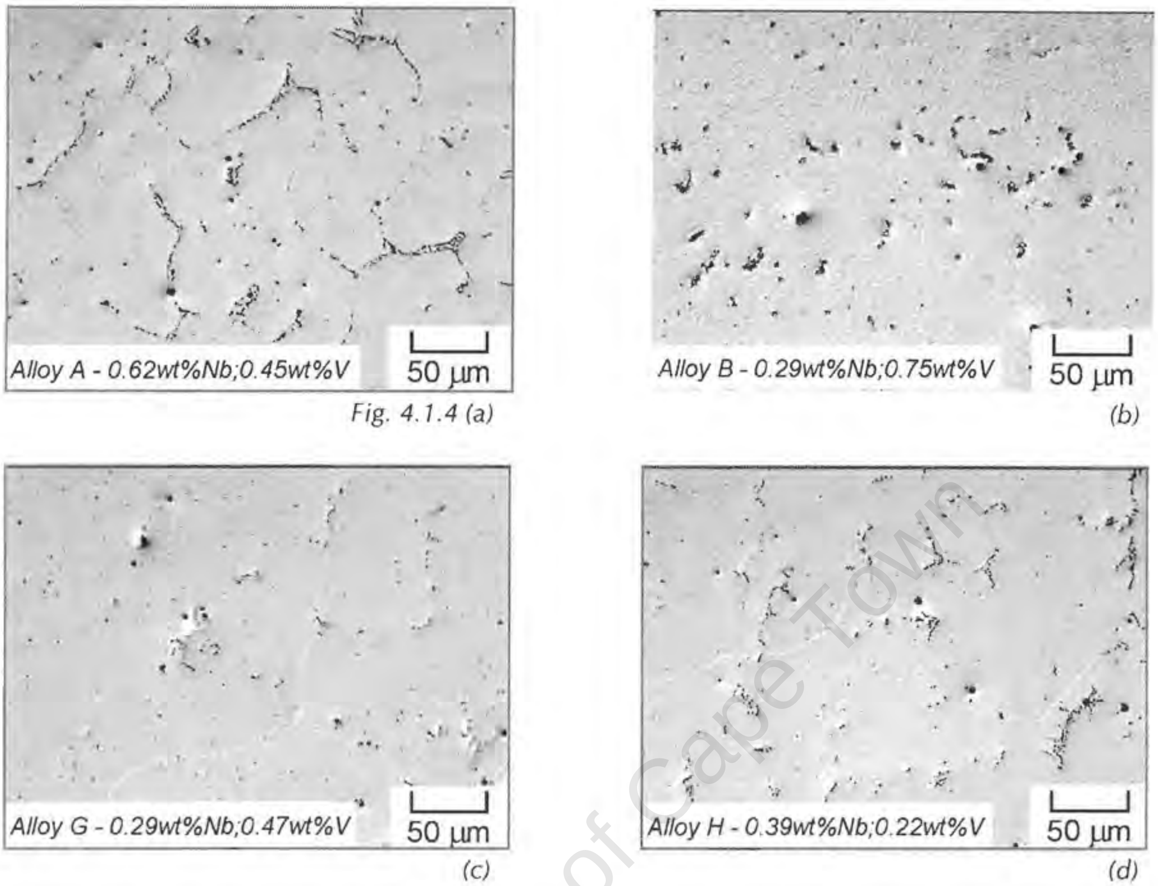

Fig. 4.1.4 (a) *(b)* *(c)* *(d)*

Figure 4.1.4 (a)-(d) Alloys A, B, G & H respectively, showing the different volume fractions of blocky precipitates in each of the alloys after the solution treatment.

4.1.2.2 COMPOSITIONAL AND CRYSTALLOGRAPHIC ANALYSIS

Alloys A, D and F were chosen for further characterisation of the blocky precipitates that were observed in alloys A, B, D, F, G, H using x-ray mapping techniques and electron diffraction studies. These alloys were chosen so that the effect of niobium and vanadium additions on the composition and crystallography of the precipitates could be determined. Alloy D was selected because this alloy represents the influence of niobium on precipitate characteristics. Alloy A was chosen so that the influence of both niobium and vanadium additions at intermediate levels on the composition and crystallography could be characterised. Alloy F was selected because this alloy represents the influence of both niobium and vanadium at 1 wt% of each alloy element (levels greater than alloy A) on the precipitate characteristics.

The x-ray maps for alloy D in figure 4.1.5 (b)-(d) show that the large blocky precipitates in the backscattered electron image in figure 4.1.5 (a) are rich in niobium and nitrogen, and depleted in iron and manganese. In alloys containing vanadium together with niobium, ie alloys A and F, the blocky precipitates are rich in niobium, vanadium and nitrogen, and depleted in iron and manganese. The x-ray maps taken from alloys A and F together with the secondary electron image for the field of view from which the maps were taken are shown in figures 4.1.6 (a)-(f) and 4.1.7 (a)-(g) respectively.

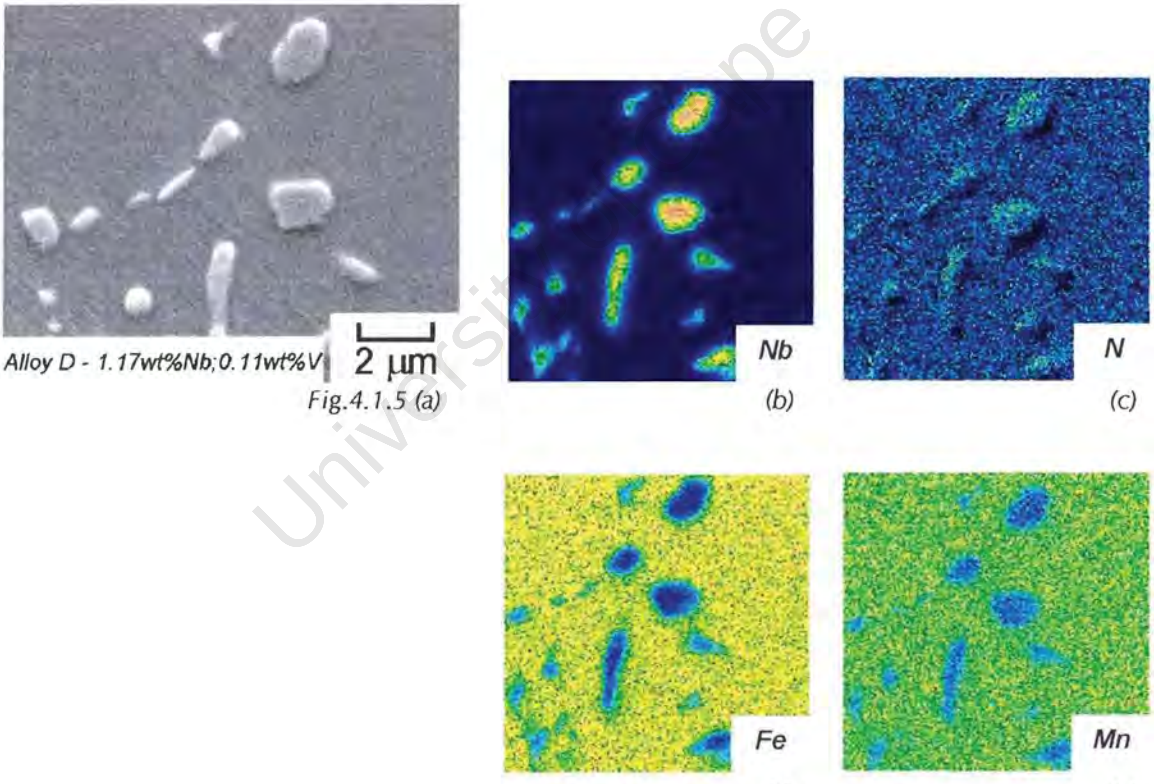

Fig.4.1.5 (a) *(b)* *(c)*

(d) *(e)*

Fig.4.1.5 (a) SEM (secondary electron) image of the blocky precipitates in alloy D, together with x-ray maps for (b) niobium, (c) nitrogen, (d) iron and (e) manganese, showing that the blocky precipitates in alloy D are rich in niobium and nitrogen and depleted in iron and manganese.

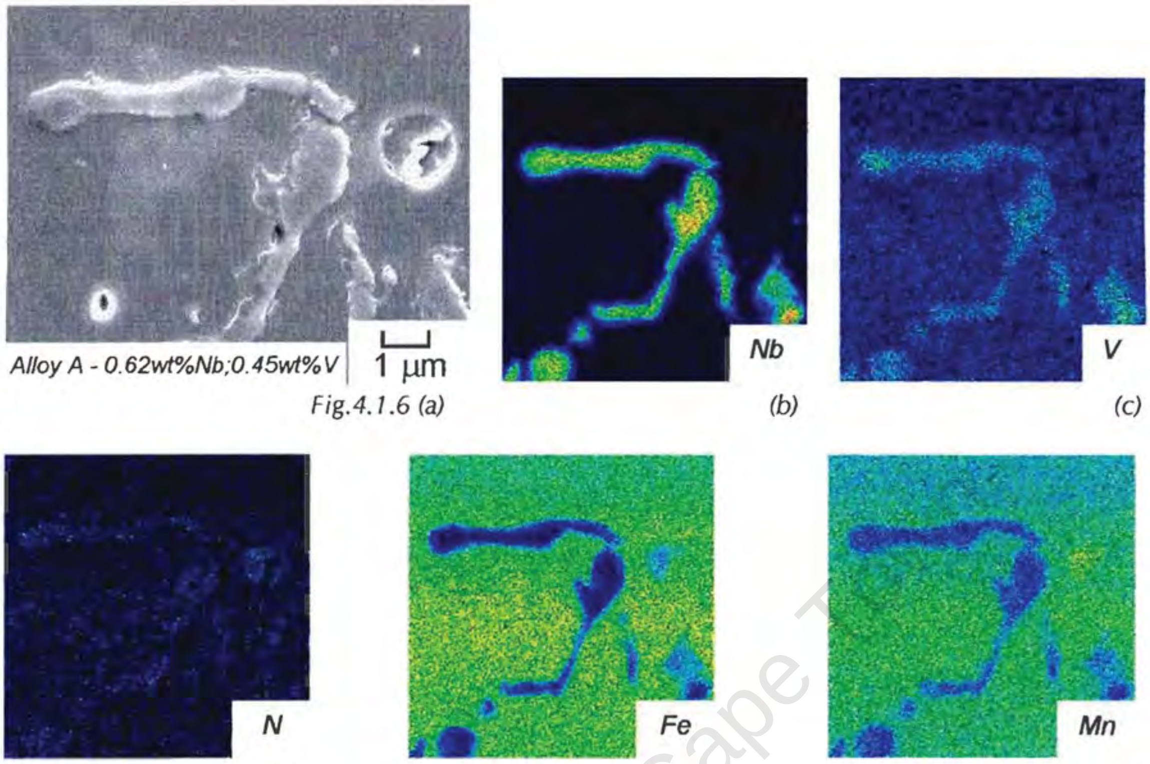

Fig.4.1.6 (a) *(b)* *(c)*

(d) *(e)* *(f)*

Fig.4.1.6 (a) SEM (secondary electron) image of the blocky precipitates in alloy A, together with x-ray maps for (b) niobium, (c) vanadium, (d) nitrogen, (e) iron, (f) manganese, showing that the precipitates in are rich in niobium, vanadium and nitrogen and are depleted in iron and manganese.

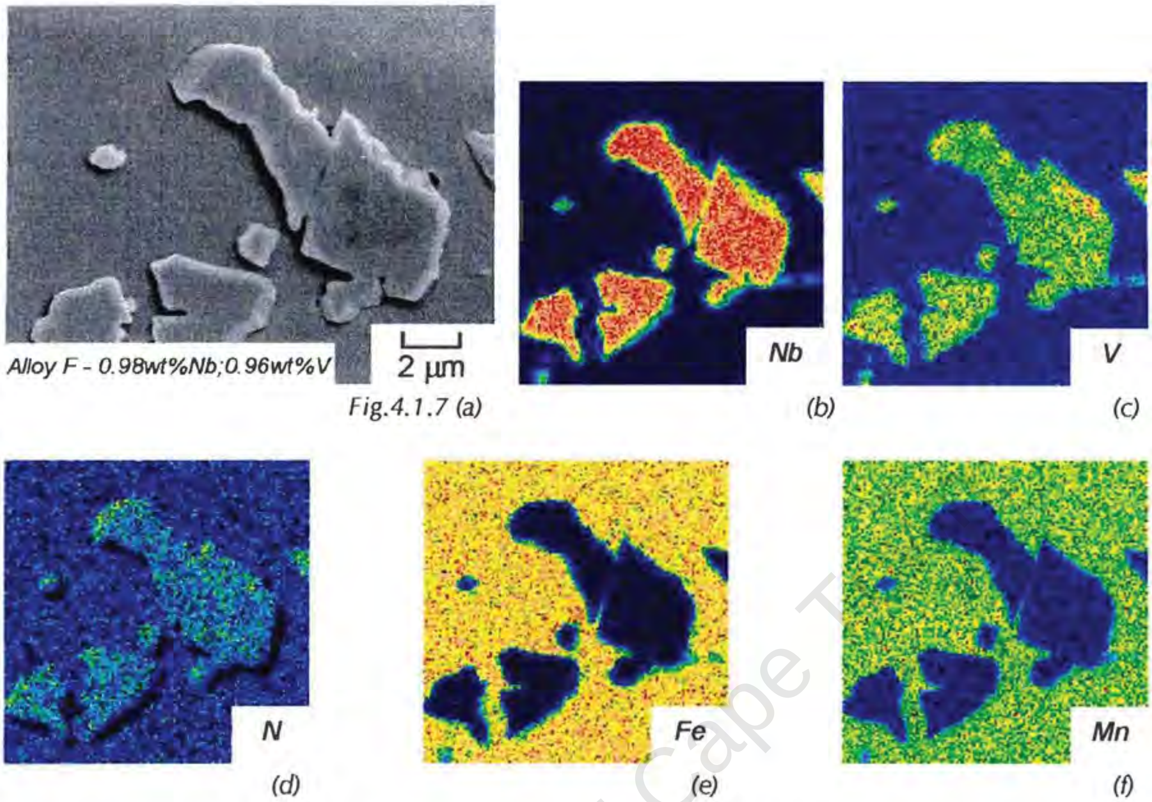

Fig. 4.1.7 (a) SEM (secondary electron) image of the blocky precipitates in alloy F together with x-ray maps of the precipitates for (b) niobium, (c) vanadium, (d) nitrogen, (e) iron, (f) manganese, showing that the precipitates are rich in niobium, vanadium and nitrogen and depleted in iron, and manganese.

The information from the x-ray maps together with the phase diagram generated by Thermocalc suggest that the blocky precipitates in alloys A, D and F are MX precipitates, typical of those found in alloys with nitrogen, niobium and vanadium additions[40,41]. This was confirmed by convergent beam electron diffraction (CBED) studies on the blocky precipitates in alloys A, D and F. Figure 4.1.8 (a) shows the [001] zone axis diffraction pattern for austenite taken from alloy A, and figure 4.1.8 (b) shows the [001] zone axis diffraction pattern for a blocky precipitate in alloy A. On comparing the two diffraction patterns it was observed that the crystal structure is the same (FCC), but the lattice parameter of the precipitate is larger than the austenite. This is also observed for alloys D and F, which have different levels of niobium and vanadium compared to alloy A. Figure 4.1.9 (a) shows the [011] zone axis for the austenite in alloy D and figure 4.1.9 (b) shows the [011] zone axis for the blocky precipitate. Similarly figure 4.1.10 (a) and (b) shows the [112] zone axis for austenite and the [112] zone axis for the blocky precipitate in alloy F. The feint maxima between the bright spots in figure 4.1.8 (b) might represent superlattice reflections associated with the FCC NaCl crystal structure, common to niobium and vanadium nitrides[41]. The indexing of the diffraction patterns, shown in figures 4.1.8–4.1.10 is shown in figures 4.1.11 (a)-(c).

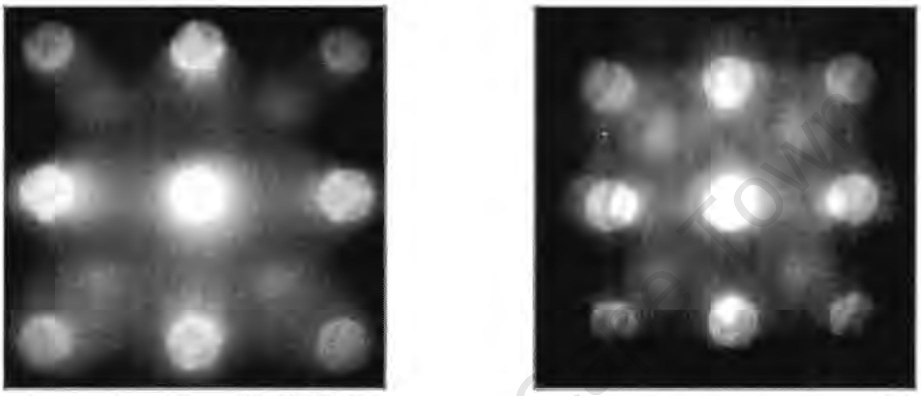

Fig. 4.1.8 (a) *(b)*

*Fig.4.1.8 (a) CBED pattern of the austenite matrix in **alloy A (0.62 wt%Nb;0.45 wt%V)** showing the [001] zone axis, (b) CBED pattern of a blocky precipitate in alloy A that corresponds to the [001] zone axis for the FCC system, showing that it has a FCC crystal structure.*

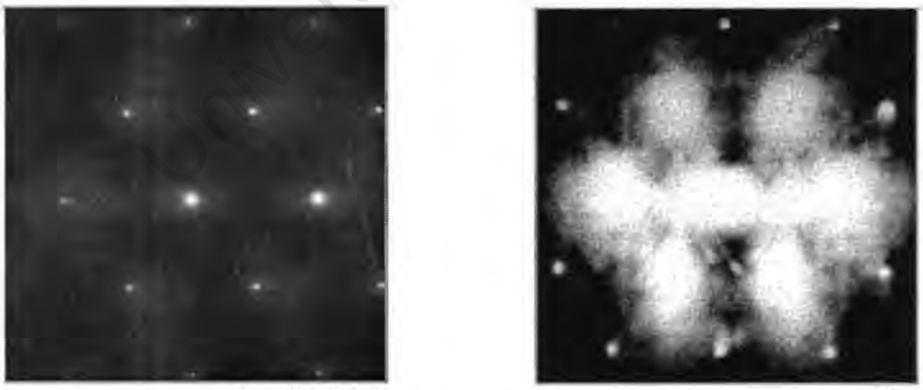

Fig. 4.1.9 (a) *(b)*

*Fig.4.1.9 (a) SAD pattern of the austenite matrix in **alloy D (1.17 wt%Nb;0.11 wt%V)** showing the [011] zone axis, (b) CBED pattern of a blocky precipitate in alloy D that corresponds to the [011] zone axis for the FCC system, showing that it has a FCC crystal structure.*

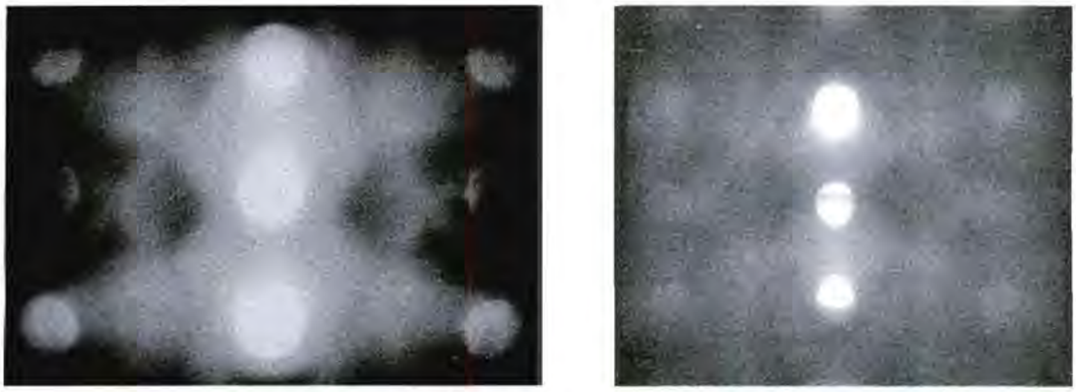

Fig. 4.1.10 (a) (b)

Fig.4.1.10 (a) CBED pattern of the austenite matrix in **alloy F (0.92 wt%Nb;0.98 wt%V** showing the [112] zone axis, (b) CBED pattern of a blocky precipitate in alloy F that corresponds to the [112] zone axis for the FCC system, showing that it has a FCC crystal structure.

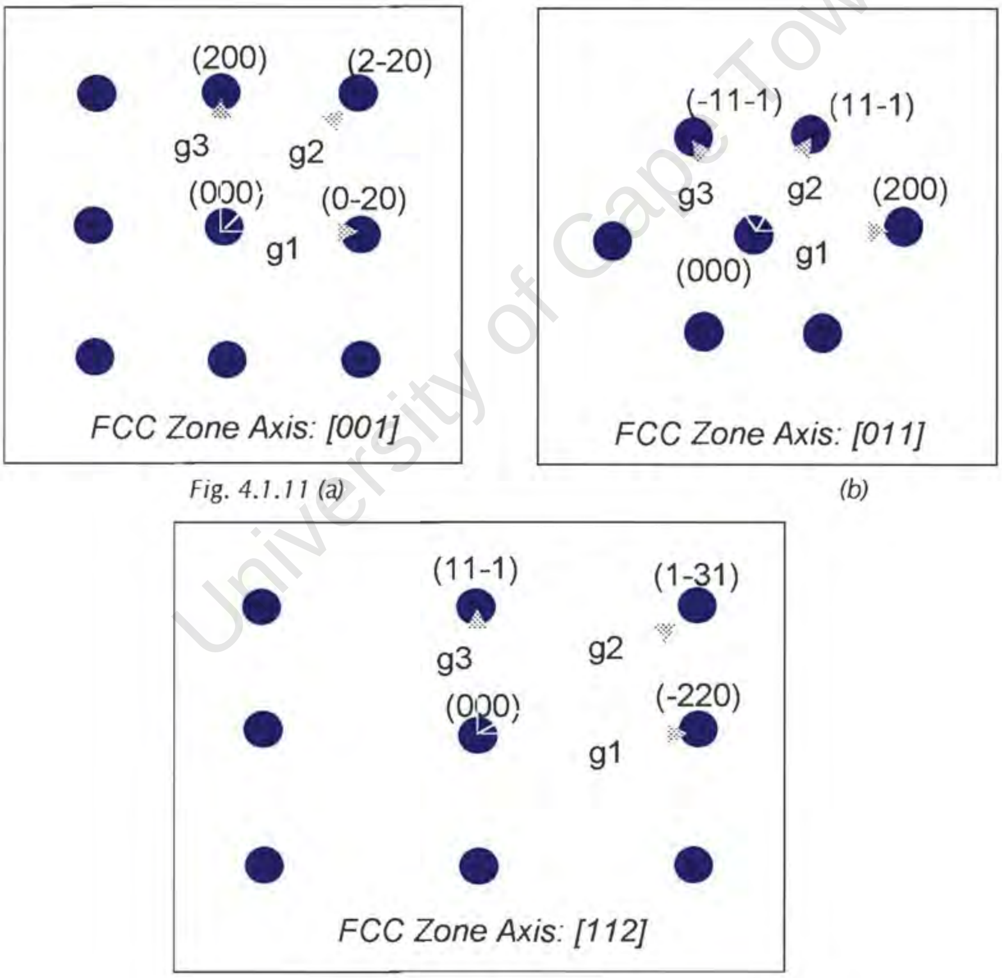

Fig. 4.1.11 (a) (b)

(c)

Fig. 4.1.11 Schematics of the diffraction patterns from the blocky precipitates in (a) alloy A showing the indexing of the [001] zone axis, (b) alloy D showing the indexing of the [011] zone axis and (c) alloy F showing the indexing of the [112] zone axis diffraction patterns.

The lattice parameters were calculated for the precipitates in each of the alloys from the diffraction patterns. The results of the calculations are shown in table 4.1.1, together with the published values for pure niobium and vanadium nitrides with a M:X stoichiometry of 1:1 by Goldschmidt[41]. The published lattice parameter values and the calculated lattice parameter values are in good agreement with each other.

*Table 4.1.1 Lattice parameters of blocky precipitates calculated for alloys A,D and F, together with the published values *by Goldschmidt[41].*

	a(Å)
Niobium Nitride (NbN)*	**4.38-4.39**
Vanadium Nitride (VN)*	**4.07-4.14**
Alloy A [001]	4.36-4.38
Alloy D [011]	4.24-4.32
Alloy F [112]	4.20-4.38

4.1.3 ALLOY SOLIDIFICATION

In order to determine the origin of the large blocky precipitates observed in alloys A, B, D, F, G and H after the solution treatments, Scheil-Gulliver simulations of solidification using the Thermocalc software with the FEDATA database were conducted. Figures 4.1.12 (a)-(d) and figures 4.1.13 (a)-(d) show the results of the simulations on alloys C, E, D and F, together with a micrograph of each of these four alloys in the as-cast condition (figures 4.1.12 (b), (d) and figures 4.1.13 (b) and (d)).

The Scheil-Gulliver simulation of alloy C in figure 4.1.12 (a) shows that no MX precipitation is expected to form during solidification, which is confirmed by the micrograph in figure 4.1.12 (b). Figure 4.1.12 (b) shows that a small amount of lamellar precipitates have formed during cooling from the solidus temperature. The solidification path for alloy E in figure 4.1.12 (c), shows that when vanadium is added to the base composition, MX precipitates form during stages 2, 3 and 4 during the

Scheil-Gulliver simulation of solidification. If these precipitates have formed they were not resolved in the light microscope. The Scheil-Gulliver simulation for alloy E also predicts that $M_{23}C_6$ precipitates will form last during solidification. The simulation does represents equilibrium conditions, which are probably not achieved in practice and this might account for the absence of $M_{23}C_6$ precipitates and even the MX precipitates in the as-cast condition. A larger amount of discontinuous cellular precipitation is observed in alloy E in the as-cast condition than alloy C. These are probably chromium nitrides (Cr_2N) which formed during cooling from the solidus temperature and have dissolved during the solution treatment. Further discussion on the discontinuous precipitation of chromium nitrides follows in subsequent sections and will not be discussed further in this section.

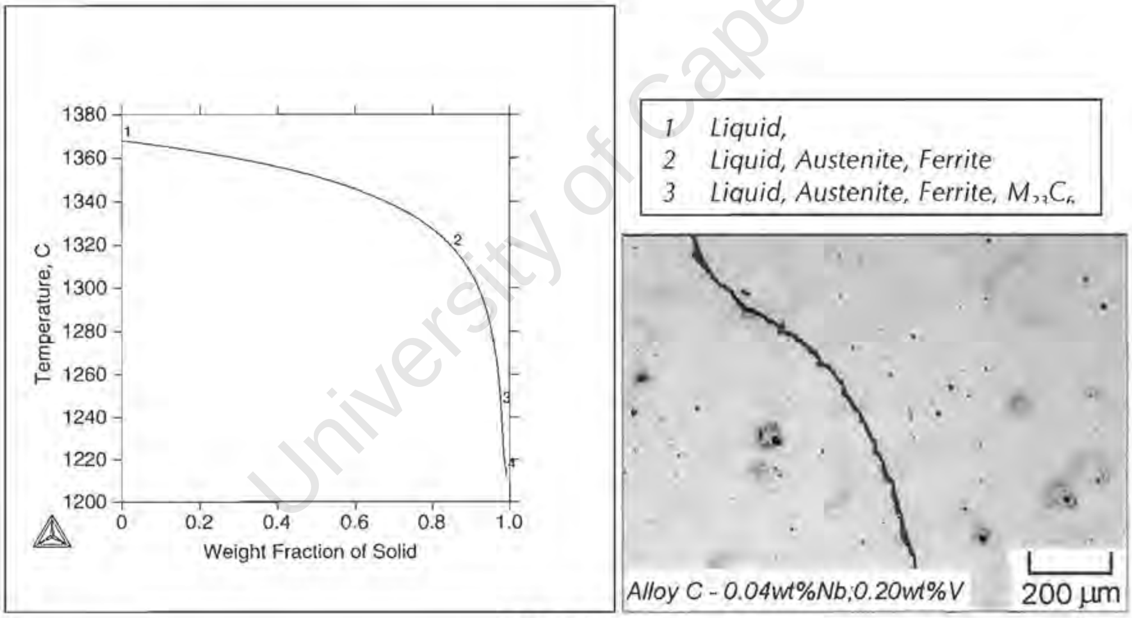

4.1.12 (a) *(b)*

Fig. 4.1.12 (a) Scheil-Gulliver simulation of solidification for alloy C, (b) Alloy C in the as-cast condition showing a single phase austenitic structure and a small amount of precipitation on the grain boundary.

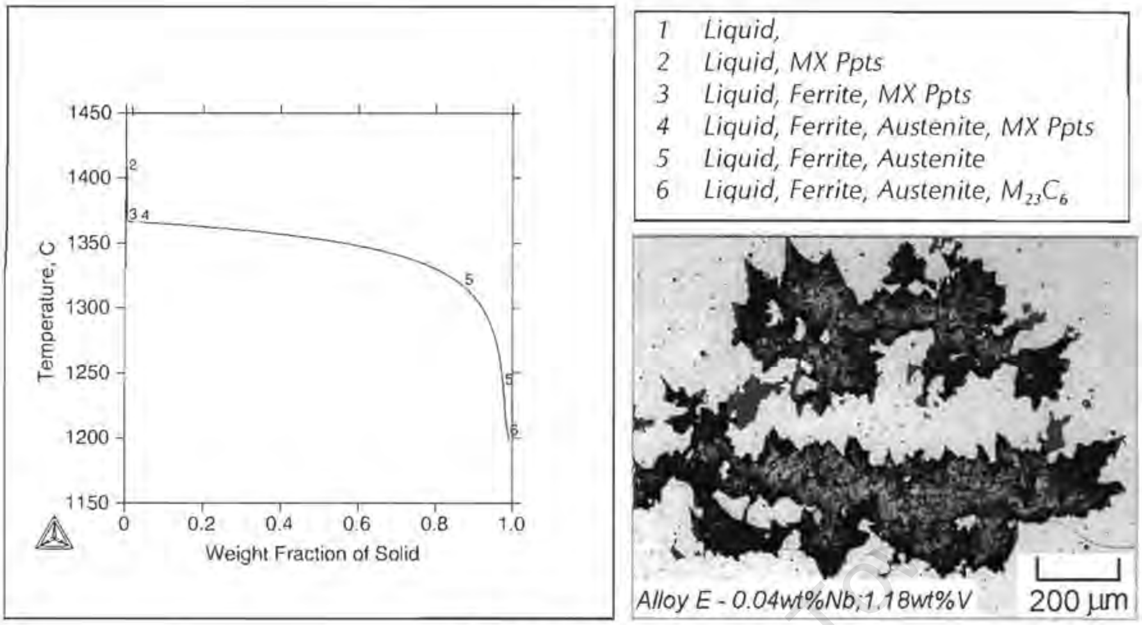

Fig. 4.1.12 (c) *(d)*

Fig. 4.1.12 (c) Scheil-Gulliver simulation of solidification for alloy E, (d) Alloy E in the as-cast condition, showing discontinuous cellular precipitation in the austenite matrix.

The Scheil-Gulliver simulation of alloy D, in figure 4.1.13 (a) represents different solidification behaviour as a consequence of niobium addition to the base composition. MX precipitates form in the liquid during stages 3, 4 and 5 shown in the Scheil-Gulliver simulation of solidification. Stage 5 of the solidification path indicates that MX precipitates form as a type of eutectic reaction with the remaining austenite. The micrograph of alloy D in the as-cast condition (figure 4.1.13 (b)) shows that the blocky MX precipitates are surrounded by austenite and have not formed in the ferrite. Stage 5 of the solidification path therefore, accounts for the formation of MX precipitates with a blocky morphology in alloy D. MX precipitation is not predicted to form during the last stage of solidification in alloy E or alloy C and no blocky precipitates are observed in these alloys. HCP precipitates are predicted to form by the simulation but are not observed in the as-cast condition of alloy D shown in figure 4.1.13 (b). As in the case of alloy E, the Scheil-Gulliver simulation, represents equilibrium conditions that are probably not the case in practice.

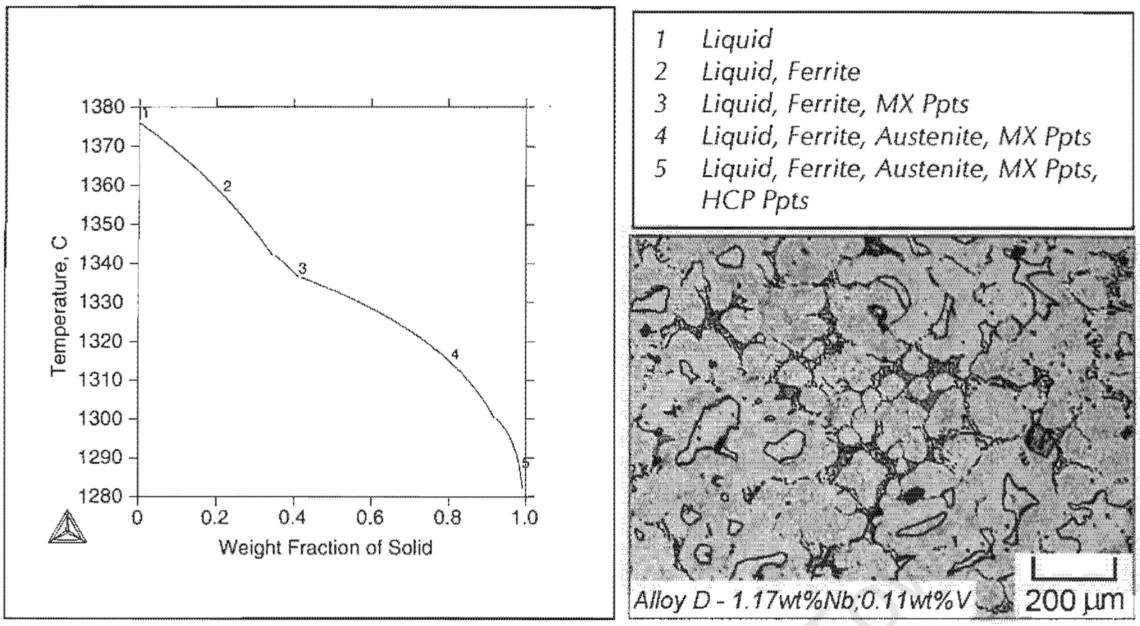

Fig. 4.1.13 (a) *(b)*

Fig. 4.1.13 (a) Scheil-Gulliver simulation of solidification of alloy D, (b) Alloy D in the as-cast condition, showing the large blocky precipitates embedded in the austenite, together with islands of ferrite in the austenite.

The solidification behaviour of alloy F is representative of both the influence of niobium and vanadium additions, and shows solidification having characteristics of both alloys E (figure 4.1.12 (c)) and D (figure 4.1.13 (a)). MX precipitates form during stages 2, 3 and 4 during the Scheil-Gulliver simulation of solidification. MX precipitates in alloy F from during the first stages of solidification (figure 4.1.13 (c)), as in the case of alloy E (figure 4.1.12 (c)), and during the last stages similar to alloy D (figure 4.1.13 (a)). No ferrite is observed in this alloy, and the blocky precipitates are embedded in the austenite matrix. This observation indicates that a large portion of the blocky MX precipitates have formed eutectically during stage 4 with the austenite.

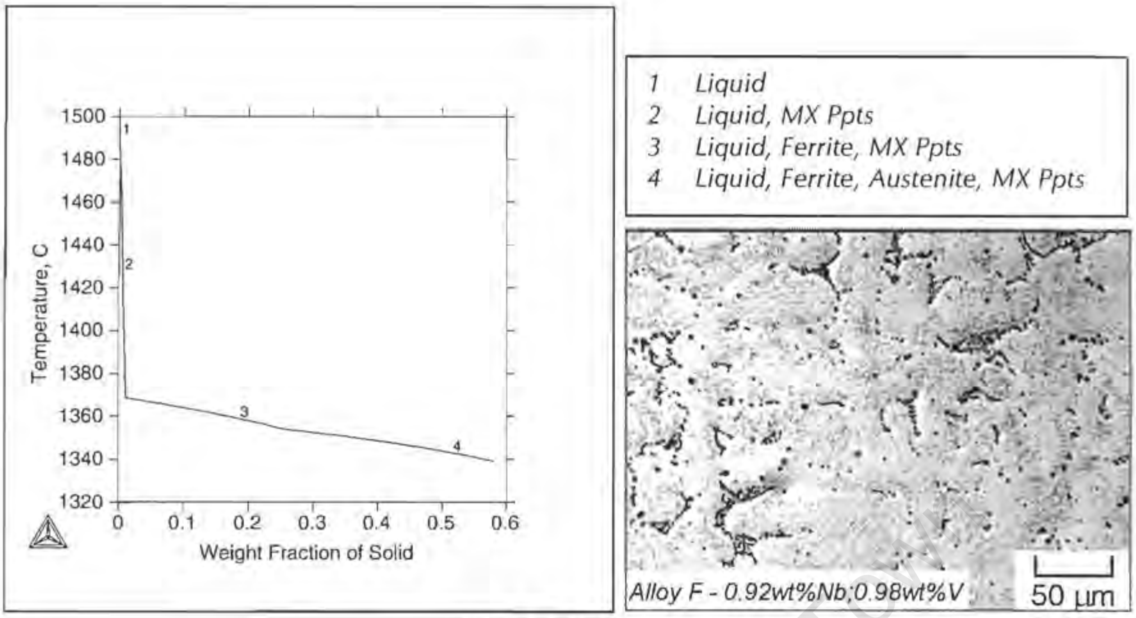

Fig. 4.1.13 (c) *(d)*

Fig. 4.1.13 (c) Scheil-Gulliver simulation of solidification of alloy F, (d) Alloy F in the as-cast condition, showing the blocky precipitates embedded in the austenite matrix.

4.1.4 MECHANICAL PROPERTIES

4.1.4.1 TENSILE TESTS

The tensile properties of six of the alloys, A, C, D, E, F and H, were investigated in order to determine the influence of the blocky precipitates, observed in alloys A, D, F and H, and not in alloys C and E, on the yield strength, ultimate tensile strength and elongation to failure. The results of tensile tests on alloy C were used to compare the influence of microstructural differences observed in the other alloys on the tensile behaviour. Further, the results of the tensile tests of these six alloys in the solution treated condition are used as a comparison for the results obtained from the same alloys after ageing treatments. Any changes in mechanical behaviour which are a consequence of exposure to a particular ageing temperature can then be easily identified.

The results of the tensile tests on alloys A, C, D, E, F and H are shown in figure 4.1.14. The data for all of the alloys is shown on the same set of axes for purposes of comparison. Table 4.1.2 lists each of the properties that were calculated from the tensile data, together with the results of Vickers hardness tests. It should be noted that alloy D contains some ferrite, which compromises direct comparison with the other alloys. However, this alloy has been included so that an understanding of the mechanical behaviour of this alloy can be established.

Figure 4.1.14 shows that alloy C has the greatest elongation to failure of up to 63%, but the lowest yield strength and ultimate tensile strength. Alloys A, D, F and H have higher strength than alloy C and also decreased elongation to failure. The loss of elongation to failure corresponds to the formation of the blocky precipitates in alloys A, D, F and H. Alloy H has the lowest volume fraction of blocky precipitates and the smallest loss in elongation to failure, followed by alloy A and then alloys D and F, which have the lowest elongation to failure and the largest volume fraction of blocky precipitates. Alloy E has the same yield strength as alloy C, but reduced elongation to failure. There is no explanation for this behaviour when studying the microstructure in the solution treated condition since it is similar to that of alloy C, and therefore it is expected that these alloys should have similar mechanical behaviour.

The tensile test results suggest that the blocky precipitates do not decrease the capacity for plastic work significantly. The tensile tests however, represent low strain rate conditions and do not give an indication of the materials' fracture toughness. In order to determine the effect of the blocky precipitates on the toughness of the steel Charpy V-notch tests were completed on the six samples, again using alloy C for comparative purposes.

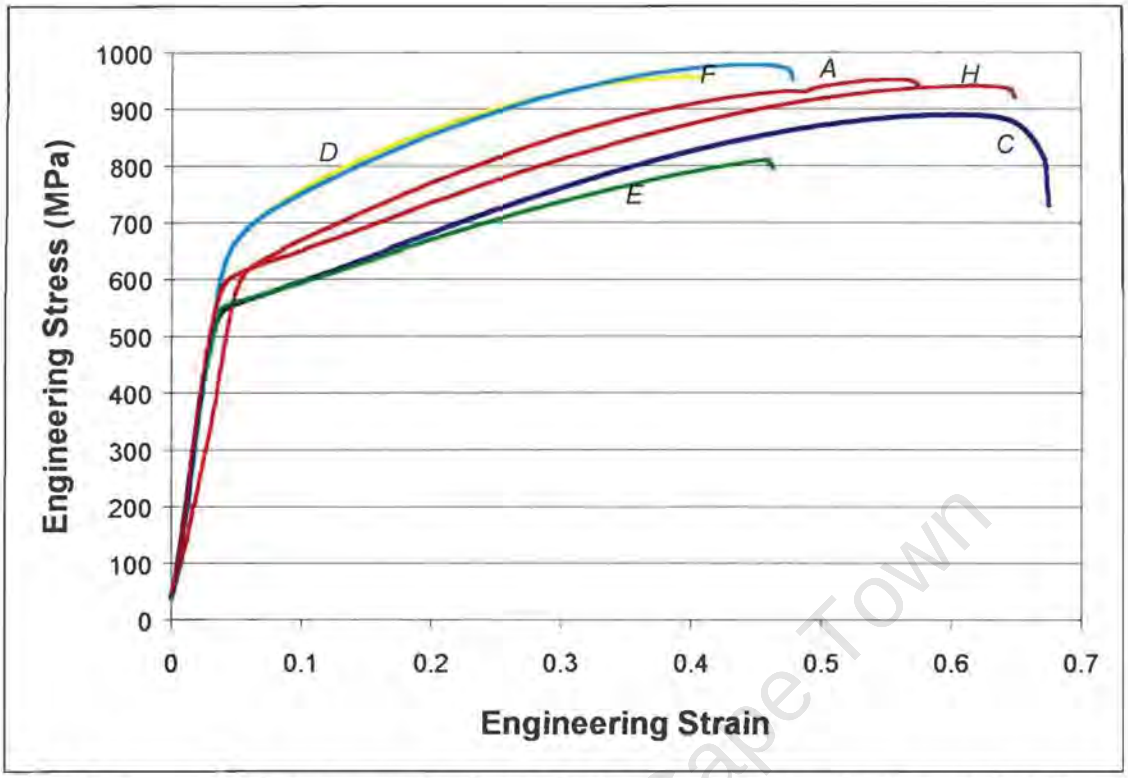

Fig. 4.1.14 Tensile test results on alloys A, C, D, E, F and H in the solution treated condition.

Table 4.1.2 List of tensile properties and hardness for alloys A, C, D, E, F and H, in the solution treated condition

Alloy	**Yield Strength (MPa)**	**Ultimate Tensile Strength (MPa)**	**Total Elongation to Failure (%)**	**Plastic Elongation to Failure (%)**	**Hardness (Vickers)**
A	600	952	58	53	272
C	548	889	68	63	270
D	625	957	42	37	290
E	548	811	46	42	298
F	624	978	46	43	295
H	589	941	65	61	290

4.1.4.2 CHARPY V-NOTCH TESTS

The results of the Charpy V-notch tests on alloys A, C, D, E, F and H are shown in table 4.1.3. Two specimens of each alloy were tested, but there was still much variability in the results, which can be attributed either to porosity associated with cast materials or inclusions which are often observed in the alloys. In spite of these variations, the results show consistently that the presence of blocky precipitates in alloys A, D, F and H resulted in a dramatic decrease in toughness when compared to alloy C. The results show that alloy C has a Charpy V-notch toughness of between 69 and 114 Joules and all of the other samples exhibit a toughness of below 10 Joules. Blocky precipitates were not observed in alloy E; however the Charpy V-notch toughness is also below 10 Joules.

Table 4.1.3 Charpy V-Notch Energy for alloys A, C, D, E, F and H after solution treating, showing that the blocky precipitates reduce the fracture toughness of the steel

Alloy	***Charpy V-Notch Energy (Joules) Test 1***	***Charpy V-Notch Energy (Joules) Test 2***
A	7	3
C	114	69
D	5	7
E	7	3
F	10	8
H	3	3

The fracture surfaces of the Charpy V-notch specimens were examined in the scanning electron microscope. Figures 4.1.15 (a) and (b) show the fracture surfaces of alloys C and F respectively and illustrate that the failure mode of alloy C is a classic cup and cone type failure. This is indicative of a ductile failure mode, which accounts for the high Charpy energy value in table 4.1.3. The fracture surface of alloy F is characterised by facetted islands, which are the same size as the blocky precipitates in alloy F shown in figure 4.1.2 (d). The cleavage planes in the blocky precipitate can be seen in the micrograph, which have induced a brittle type failure mode in this alloy and probably the others that contain blocky precipitates.

The fracture surface of the Charpy specimen of alloy E is shown in figure 4.1.15 (c). The fracture surface shows straight cleavage lines, which resemble first and second order twin planes or slip bands. High nitrogen steels are known to exhibit brittle fracture when crack propagation occurs along deformation twin planes[29,30]. This provides a possible explanation for the brittle failure mode of this alloy and consequently the low fracture toughness exhibited by alloy E.

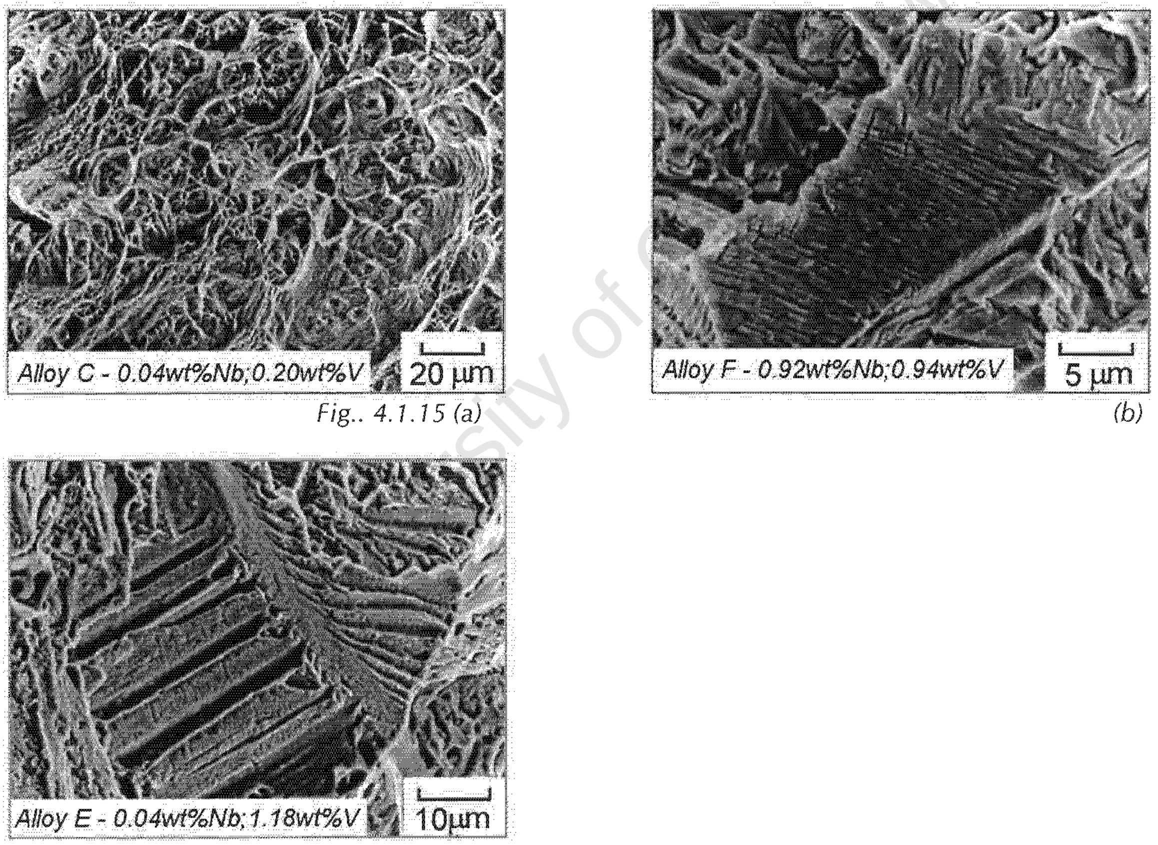

Fig.. 4.1.15 (a)

(b)

(c)

Fig. 4.1.15 SEM (secondary electrons) image of the fracture surface of the Charpy V-notch specimens showing (a) the ductile fracture surface of alloy C and (b) cleavage planes on the blocky precipitate in alloy F, (c) fracture along possible twin planes in alloy E.

4.1.4.3 *ABRASIVE WEAR TESTS*

The results of abrasive wear tests on alloys A, C, D, E and H are shown in figure 4.1.16. Alloys C and E, which have no blocky precipitates in the austenite, show the best wear performance of all five alloys. Alloys C and E also show the lowest yield strength. Alloys C and H have similar plastic elongation to failure, but alloy C shows superior wear performance to alloy H, which contains blocky precipitates. This result suggests that the presence of blocky precipitates in alloys A, D and H has a more profound effect on the wear resistance of the alloys than the differences in tensile properties. The total mass loss over an abrasive path length of 12 m is plotted in figure 4.1.17 for alloys A, C, D, E and H. This chart shows the difference in wear performance of the alloys tested and indicates that alloys A, D and H show poorer wear performance than alloys C and E.

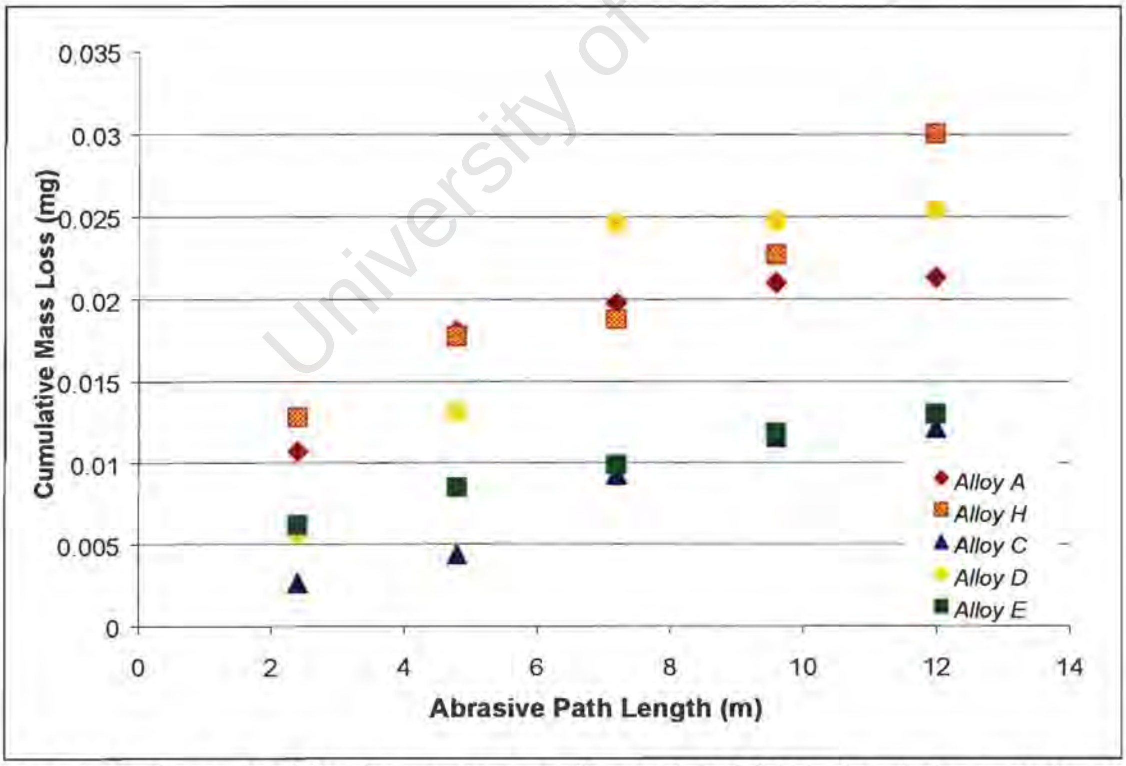

Fig. 4.1.16 The results of abrasive wear tests on alloys A, C, D, E & H in the solution treated condition.

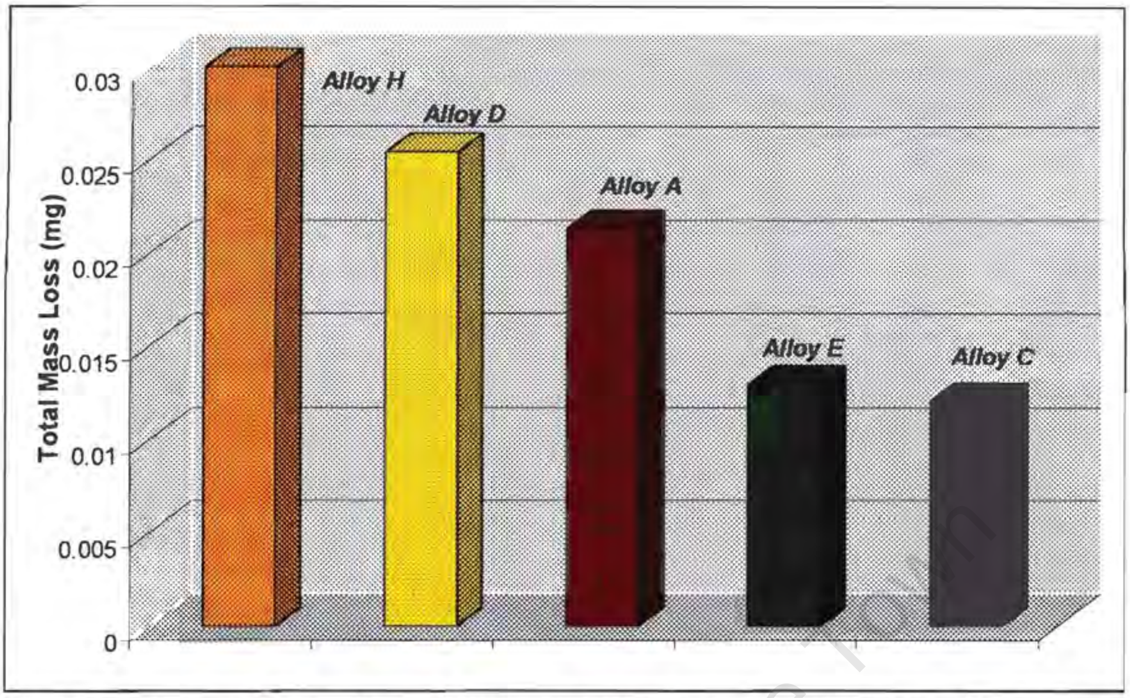

Fig. 4.1.17 Total mass loss after an abrasive path of 12 m for alloys A, C, D, E & H in the solution treated condition, showing the relative wear performance of the alloys tested.

Following the abrasive wear tests, the wear surfaces of alloys A and C were examined in the SEM. Figure 4.1.18 (a) shows the abrasive wear surface of alloy C after an abrasive path length of 12 m. There is evidence of work hardened shear lips, common to ductile type materials exposed to abrasive wear. In contrast, figure 4.1.18 (b) shows islands of brittle regions on the wear surface of alloy A. These islands are the same size as the blocky precipitates in alloy A and show that the action of the abrasive wear particles causes the precipitates to fracture, thus adversely affecting the wear resistance of the alloy.

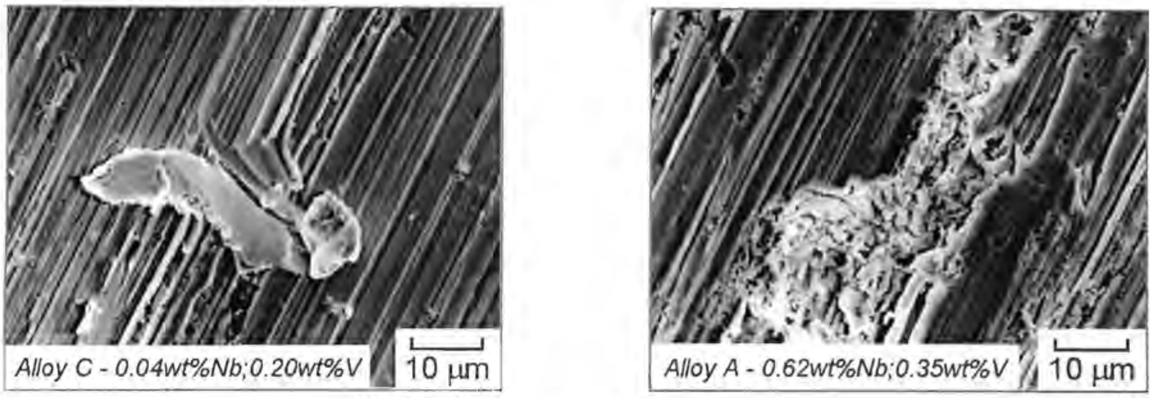

Fig. 4.1.18 (a)

(b)

Fig. 4.1.18 SEM (secondary electron) image of the abrasive wear surfaces of alloys C and A in the solution treated condition showing, (a) work hardened lips on the surface of alloy C and (b) fracture of a blocky precipitate on the surface of alloy A.

4.1.5 SUMMARY: THE SOLUTION TREATED CONDITION

A microstructural characterisation of the alloys shows that niobium and vanadium influence the formation of large blocky precipitates during solidification. These blocky precipitates do not dissolve during the solution treatment, whereas lamellar precipitates that have also formed during cooling from the solidus temperature do dissolve. The blocky precipitates are rich in niobium in the case of alloy D, but when the alloy also contains vanadium, then the precipitates are rich in both niobium and vanadium. Niobium additions to the base composition favour the formation of MX precipitates as a type of eutectic reaction with the austenite during solidification. Vanadium additions to the base composition did not show the same effect, but when both elements were added to the steel, then the eutectic type reaction was observed. The isopleth diagram shown in figure 4.1.1 which predicts the phase stability of the eight high nitrogen steel alloys at 1300°C does correspond to some degree to the experimental results in terms of the precipitation reactions, but not in terms of the presence of ferrite. If the information regarding the presence of ferrite is not considered then this isopleth diagram represents a good summary of the microstructural results of the alloys in the solution treated condition. The isopleth diagram also predicts that MX precipitates should be present in all of the alloys at 1300°C. No blocky precipitates were detected however in alloy E in the solution treated condition, thus the MX precipitates that were predicted by Thermocalc might have been fine precipitates and were not detected. As a summary of the microstructural results at 1300°C, figure 4.1.19 shows a map of the phase stability of the eight alloys, on the same axes as the isopleth diagram in 4.1.1. This figure is not an attempt to propose a more accurate isopleth diagram, but rather a summary of experimental observations made in the current investigation. The alloys that are circled by the yellow ring represent those that contain large blocky precipitates in the solution treated condition. The red labels indicate the phase stability that was observed experimentally of the eight alloys and are different to the predictions made by Thermocalc.

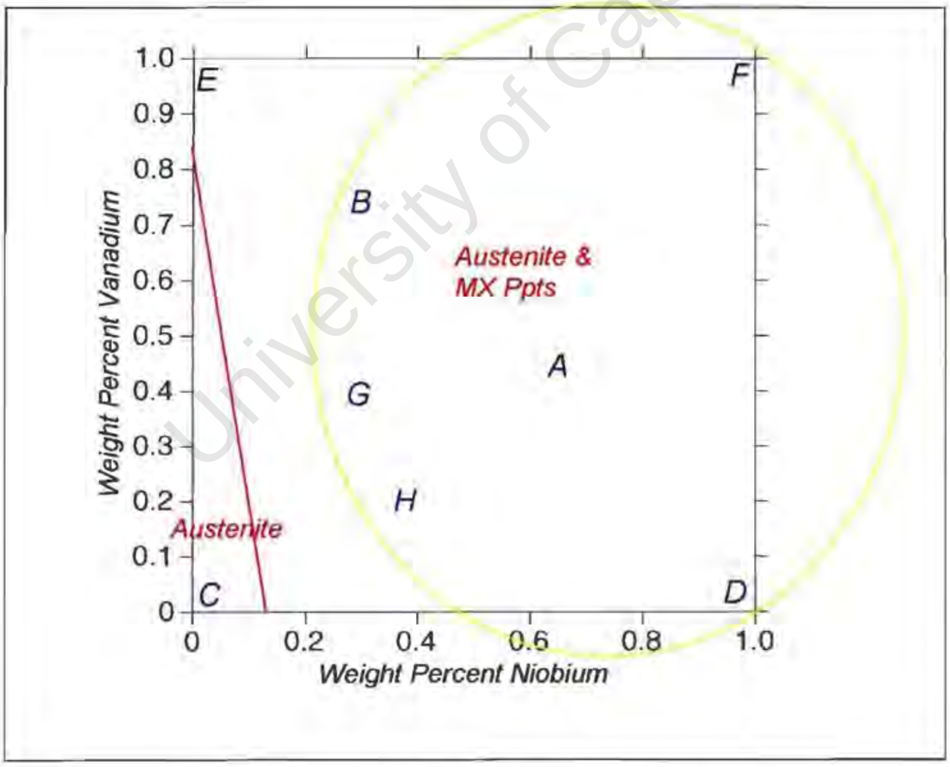

Figure 4.1.19 Summary of the microstructural characterisation after the solution treatment at 1300 °C.

The presence of the blocky precipitates reduced the elongation to failure of the alloys to some degree but had a more profound effect on the toughness of the steel. The toughness of the steel was reduced considerably by the presence of blocky precipitates compared to alloy C, which contained no blocky precipitates. No significant increase in strength could be associated with the blocky precipitates and the wear performance of the steel was severely reduced as a consequence of these large precipitates. These results characterise the mechanical behaviour of the alloys in the solution treated condition, and are used as a basis of comparison to detect any changes in mechanical properties that result from ageing treatments.

4.2 AGEING TREATMENTS AT 1100°C

All eight alloys were first solution treated as described in section 4.1 and then aged at 1100°C for two hours and water quenched, for an initial investigation. Alloy composition played an important role in the development of the microstructure during ageing. Ageing treatments at 1100°C resulted in the precipitation of fine MX precipitates in alloys A, D and H. These precipitates are of greatest interest to the improvement of the wear properties of the steel. M_2X precipitation also occurred during ageing at 1100°C, both by discontinuous cellular precipitation and continuously in alloys B, E, F, G. The results of ageing treatments at 1100°C show that these two reactions (MX precipitation and M_2X precipitation) compete with one another, the niobium and vanadium balance favouring either one or the other reaction. These two precipitation reactions influence the mechanical performance differently, and the effect of both reactions on tensile properties and abrasion resistance is characterised.

4.2.1 ISOPLETH DIAGRAM

The isopleth diagram in figure 4.2.1 shows the influence of niobium and vanadium on the phase balance expected in the eight high nitrogen steel alloys at 1100°C. Thermocalc predicts that three phases are stable in this alloy system at this temperature, namely austenite, ferrite and MX precipitates. Alloy C is predicted to be fully austenitic at this temperature and an addition of less than 0.1 wt% niobium is sufficient to stabilise the ferrite phase. Approximately 0.1 wt% niobium is required to stabilise the MX precipitates. Thermocalc thus predicts that alloy D should contain austenite, ferrite and MX precipitates. In comparison, vanadium additions stabilise the MX precipitates at approximately 0.1 wt%, but the formation of ferrite occurs only at 0.25 wt% vanadium. Similarly to alloy D, alloy E should also contain austenite, ferrite and MX precipitates. Thus both vanadium and niobium additions result in MX precipitation at similar levels. The other alloys, A, B, F, G and H are predicted by

Thermocalc to contain austenite, ferrite and MX precipitates. The isopleth diagram cannot give an indication of the volume fraction of each phase in each of the alloys, but rather maps out the phase stability of each of the alloys.

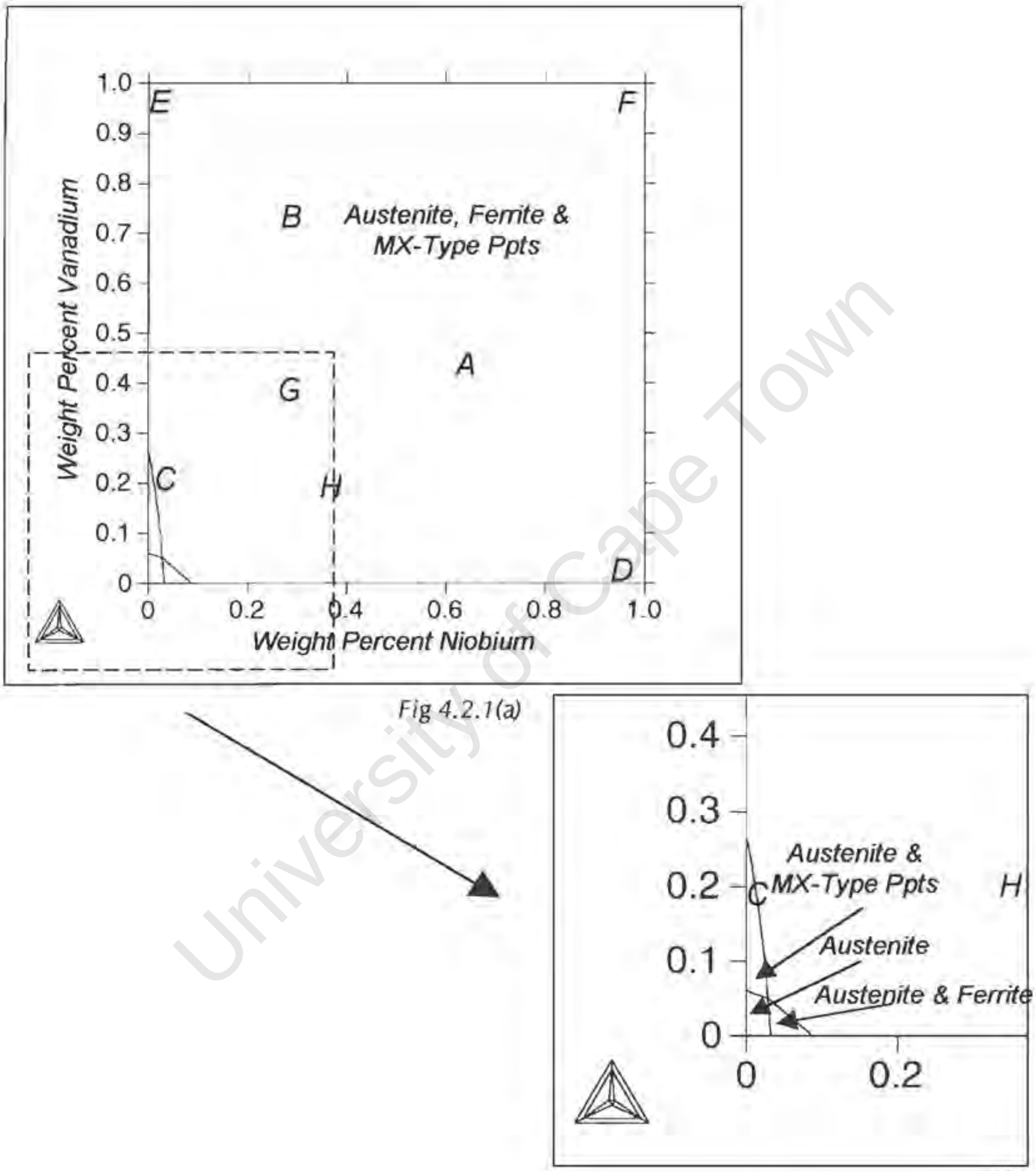

Fig 4.2.1(a)

(b)

Fig 4.2.1 (a) Isopleth diagram for the high nitrogen steel alloys for 1100 °C, showing the phase balance in each of the eight alloys as a function of the niobium and vanadium level, (b) an enlargement of the region of the diagram marked in (a) by the grey square.

4.2.2 PHASE IDENTIFICATION

4.2.2.1 METALLOGRAPHY

The microstructures of alloys C, E, F, B and G after ageing for two hours at 1100°C are shown in figures 4.2.2 (a)-(h). No precipitation was observed in alloy C after ageing for two hours at 1100°C. Figure 4.2.2 (a) shows that this alloy consists only of austenite, similarly to the solution treated condition. This is consistent with the predictions made by Thermocalc, in figure 4.2.1. Ageing alloy E at 1100°C results in a significant volume fraction of lamellar precipitates observed in figure 4.2.2 (b) and (c). Although lamellar precipitation has occurred most extensively in alloy E, this form of precipitation is also observed in alloys B, F and G as shown in figures 4.2.2 (d)–(i). Careful study of the precipitate colonies in each of these four alloys shows that the colonies have originated from the grain boundaries and the lamellae are bounded by a migration front, marked by the arrows in figure 4.2.2 (c), (e), (g) and (i). The precipitate lamellae never protrude further than the migration front and in some cases the migration front has extended ahead of the lamellae. These observations indicate that the lamellar precipitates observed in these four alloys have formed by a discontinuous cellular precipitation reaction, which is associated with the formation of a precipitate colony behind a migrating boundary. Further investigation of the discontinuous cellular precipitation reaction in the current alloy system follows in section 4.3. Further observations that are associated with discontinuous cellular precipitation in these alloys is the formation of twins within the precipitate cells. This can be seen in figure 4.2.2 (i), a higher magnification image of the precipitate cell in alloy G. Similar observations were made as a consequence of discontinuous cellular precipitation at 1000°C and 800°C and an extensive investigation of this phenomenon follows in section 4.3.3.

The precipitates in alloys E and F have a typical lamellar morphology, whereas those in alloys B and G are often broken and have a more particulate nature. This is illustrated by the TEM micrographs in figures 4.2.3(a) and (b), which show the nature of the precipitates that have formed discontinuously in alloys E and B respectively. In addition to lamellar precipitation in alloys B, E, F and G, fine precipitates have formed continuously in these alloys. These precipitates are not immediately apparent in the light microscope but can be observed in the TEM. Figure 4.2.4 (a) shows the plate-like precipitates that have formed in alloy E and figure 4.2.4 (b) shows the precipitates that have formed in alloy B, with a different morphology to those in alloy E. Further analysis of these precipitates to determine whether they were the same as those that have formed discontinuously follows in section 4.2.2.2.

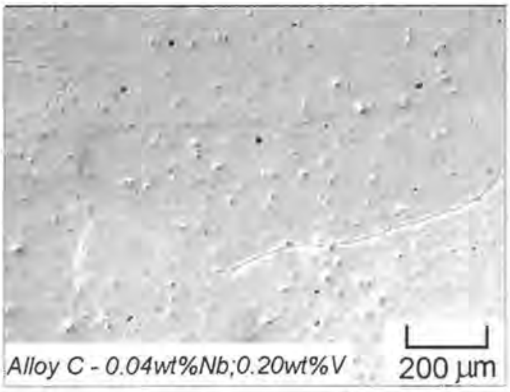

Fig. 4.2.2 (a)

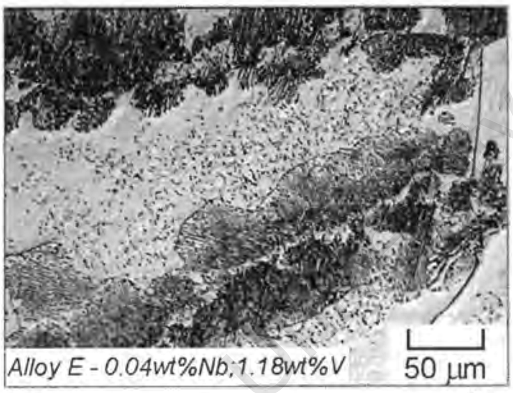

(b)

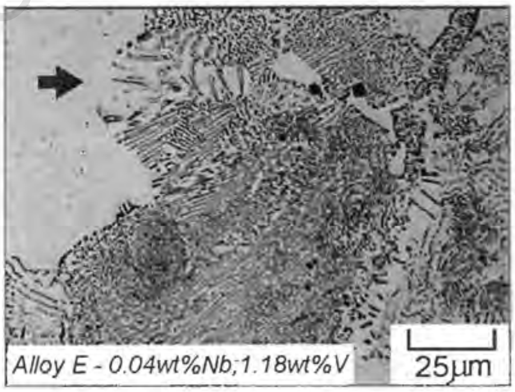

(c)

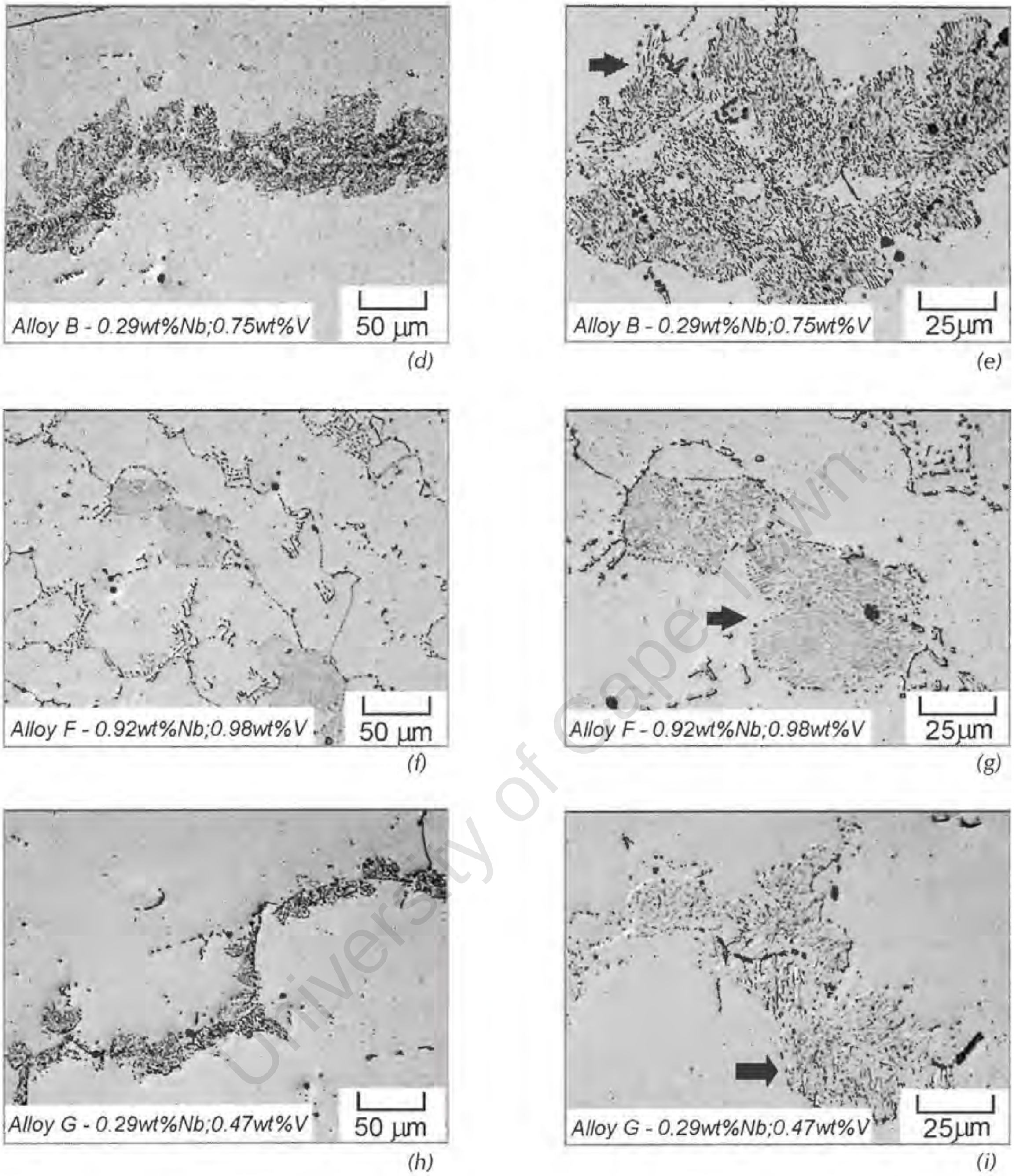

Fig 4.2.2 Alloys C, E, F, B and G after ageing for two hours at 1100°C showing (a) no precipitation in alloy C and a fully austenitic structure, (b) & (c) lamellar precipitates in alloy E that have formed discontinuously, (d) & (e) particulate precipitates in alloy B that have formed discontinuously, (f) & (g) lamellar precipitates in alloy F that have formed discontinuously, (h) & (i) particulate precipitates in alloy G that have formed discontinuously.

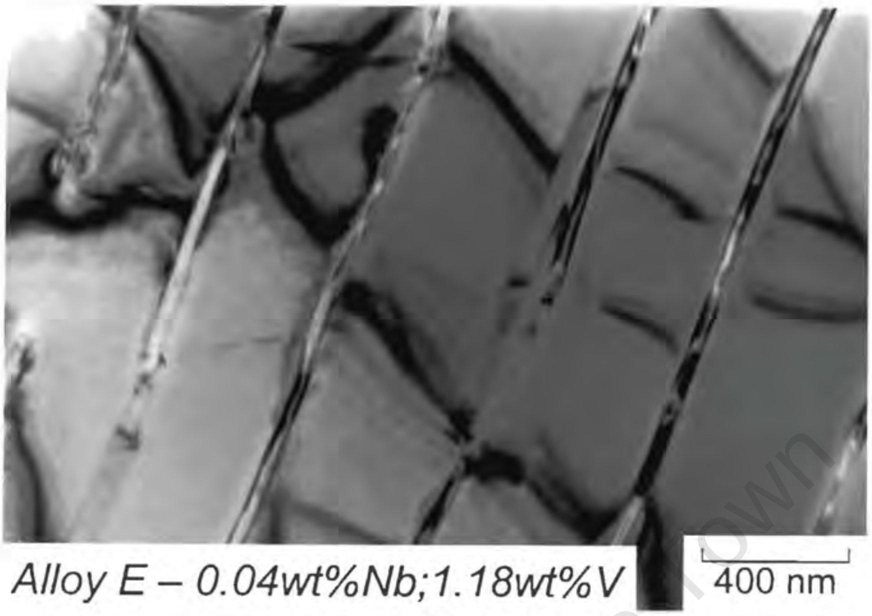

Fig. 4.2.3 (a)

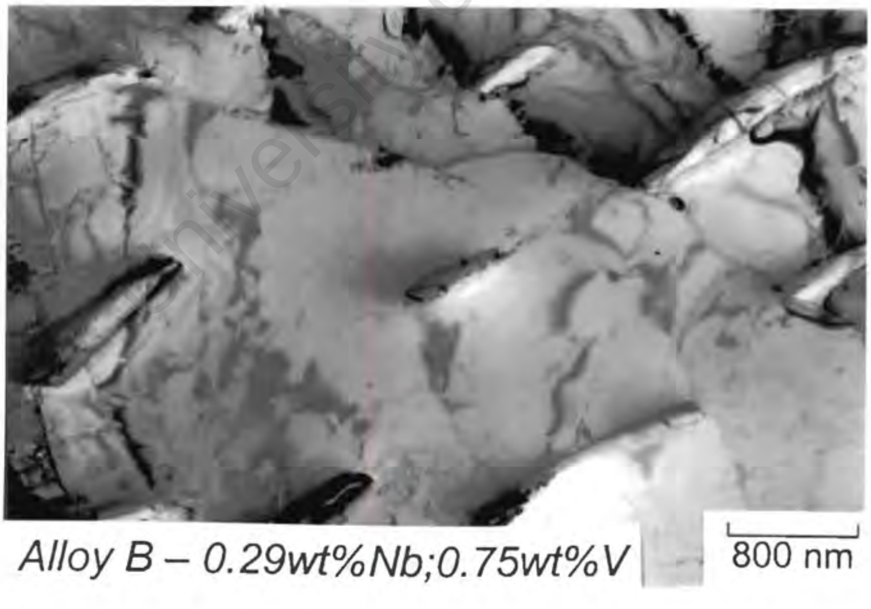

(b)

Fig. 4.2.3 TEM micrographs of alloys E and B after ageing at 1100 °C for two hours showing, (a) the lamellar precipitates in the discontinuous cell colonies in alloy E, (b) the particulate nature of the discontinuous precipitates in alloy B.

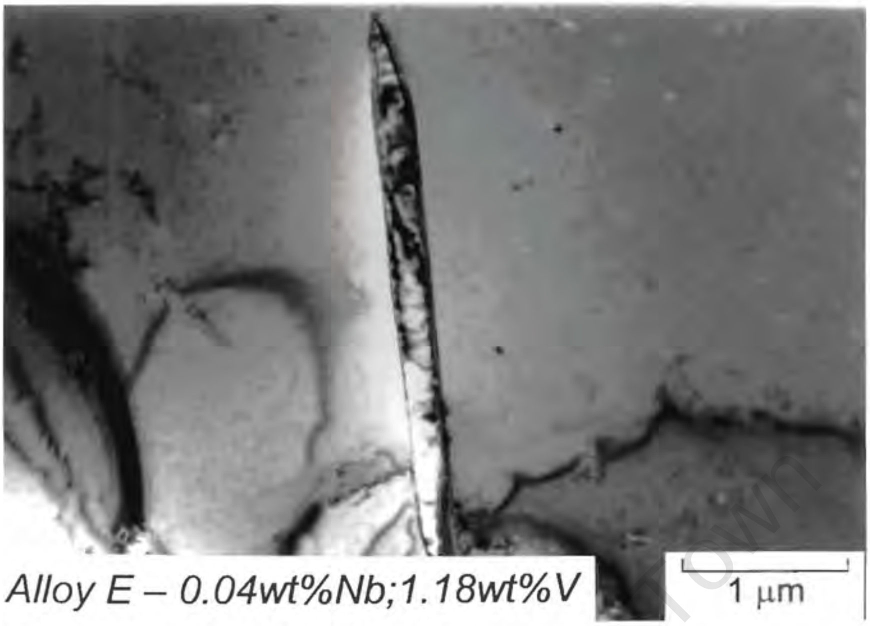

Fig 4.2.4 (a)

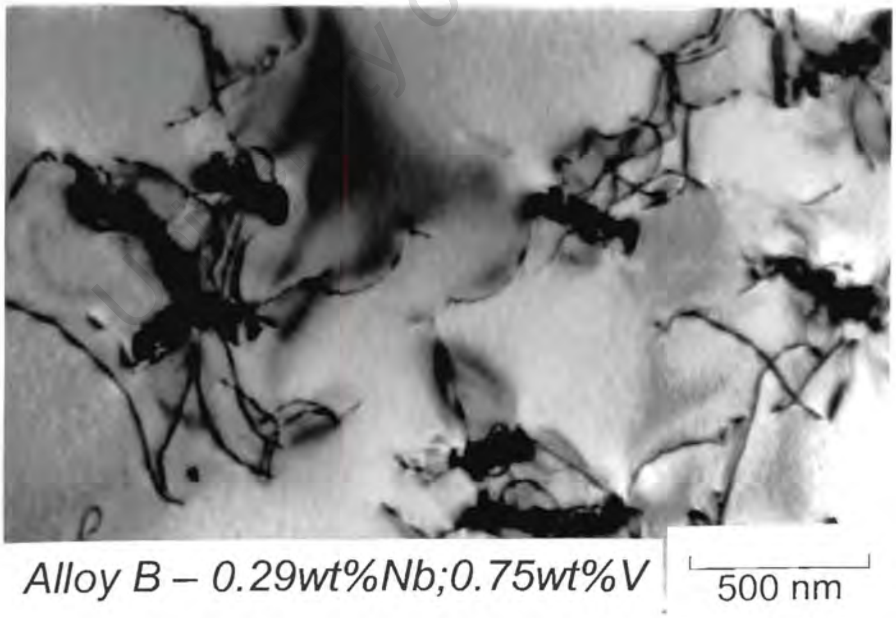

(b)

Fig 4.2.4 TEM micrographs of alloys E and B after ageing at 1100℃ for two hours showing (a) the plate-like precipitates in alloy E that have occurred continuously and (b) the continuous precipitates in alloy B.

The results of ageing treatments on alloys A, D and H in figures 4.2.5 (a)-(c) show the influence of niobium additions to the high nitrogen steel base composition. No lamellar precipitation was observed in these alloys after ageing at 1100°C for two hours and instead fine precipitates have formed both on the grain boundaries and within the grains. These precipitates could not be resolved in the micrographs in figures 4.2.5 (a)-(c) and were therefore imaged in the TEM. Figures 4.2.6 (a) and (b) show the TEM micrographs of the fine precipitates in alloys A and D, which show the prolific distribution of the precipitates in each case. Alloy D contains a larger quantity of finer precipitates, while alloy A shows a more sparse distribution of larger precipitates. Figures 4.2.6 (c) and (d), show the typical size and morphologies of the precipitates associated in alloys A and D; alloy D supports smaller, spherically shaped precipitates, while those in alloy A are larger with both spherical and cuboidal morphology. Finally, the presence of ferrite is also observed in alloy D after ageing at 1100°C for two hours, as islands in the austenite matrix shown in figure 4.2.5 (b).

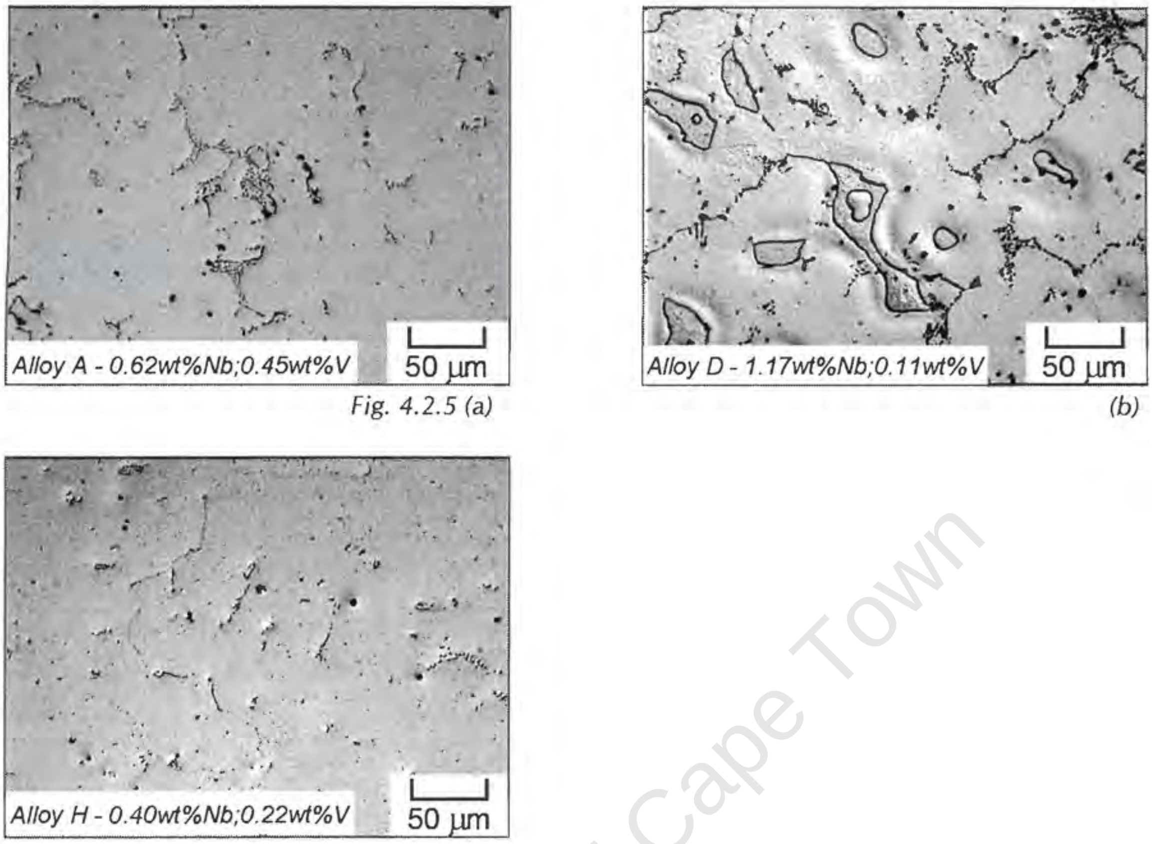

Fig. 4.2.5 (a)

(b)

(c)

Fig. 4.2.5 (a)–(c) Alloys A, D & H after ageing at 1100 ℃ for two hours, showing that no lamellar precipitates have formed in these alloys after this heat treatment.

Fig. 4.2.6 (a)

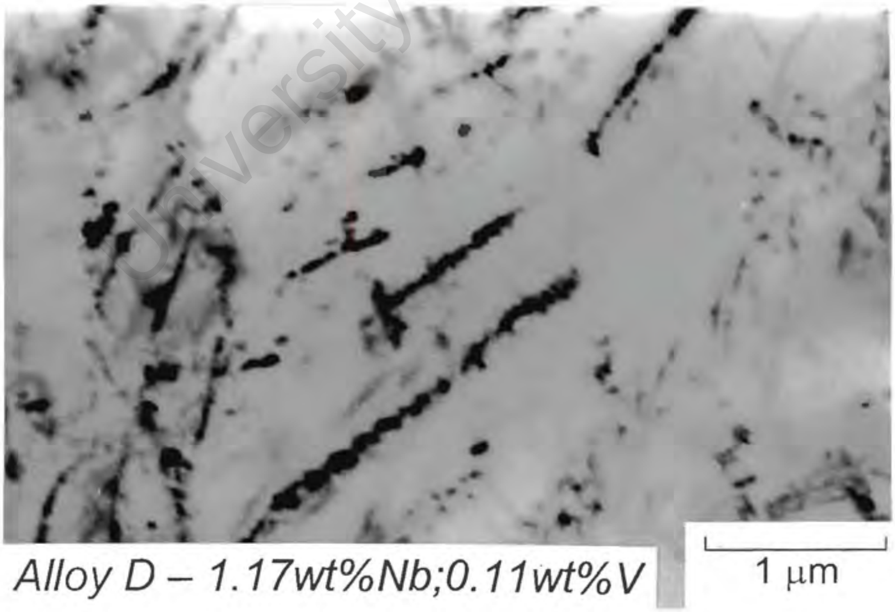

(b)

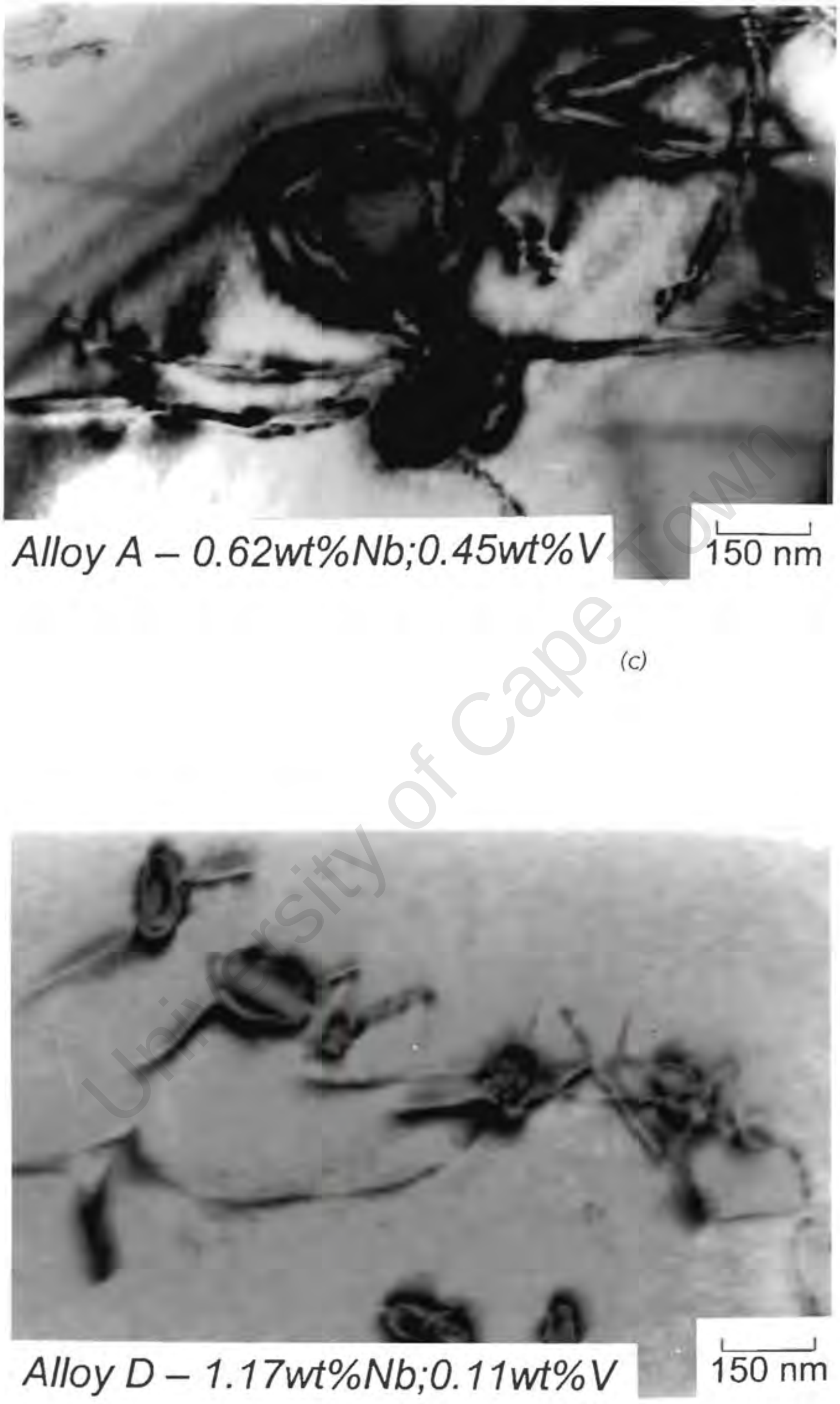

(c)

(d)

Fig. 4.2.6 TEM micrographs of the fine precipitates in alloys A and D that formed after ageing for two hours 1100 °C, showing, (a) & (b) the distribution of precipitates in alloys A and D respectively, (c) & (d) the difference in size and morphology of the precipitates in alloys A and D respectively.

Although no lamellar precipitation was observed in alloys A, D and H after ageing for two hours, it was suspected that lamellar precipitates might form in alloys A, D and H after longer ageing times. These alloys were therefore aged for 5 hours, 10 hours and 100 hours at 1100°C to determine whether lamellar precipitates would occur in these alloys after extended ageing at 1100°C. Figures 4.2.7 (a)-(c) show the results of ageing treatments on alloys A, D and H at 1100°C for 100 hours; no evidence of discontinuous cellular precipitation of lamellar precipitates was observed. Fine precipitates have formed extensively instead of the lamellar precipitates and again these precipitates are more clearly viewed in the TEM. The TEM micrographs in figures in 4.2.8 (a)-(d) show the distribution of the precipitates in alloys A and D as well as the size and morphological differences between the precipitates in alloy A and those in alloy D after ageing for 100 hours at 1100°C.

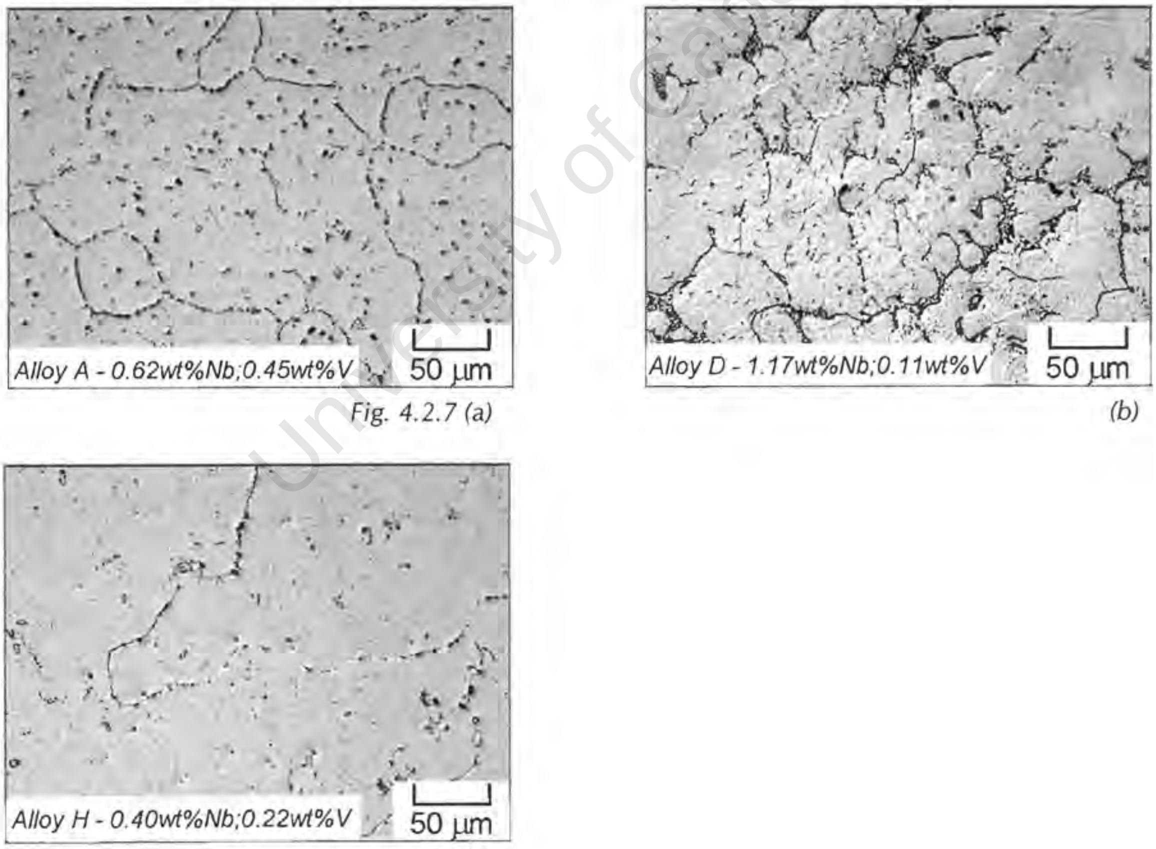

Fig. 4.2.7 (a)

(b)

(c)

Fig. 4.2.7 (a)-(c) Alloys A, D, & H showing the absence of lamellar precipitation in these alloys after ageing for 100 hours at 1100℃. Instead, fine precipitates can be observed in each of these alloys after this ageing treatment.

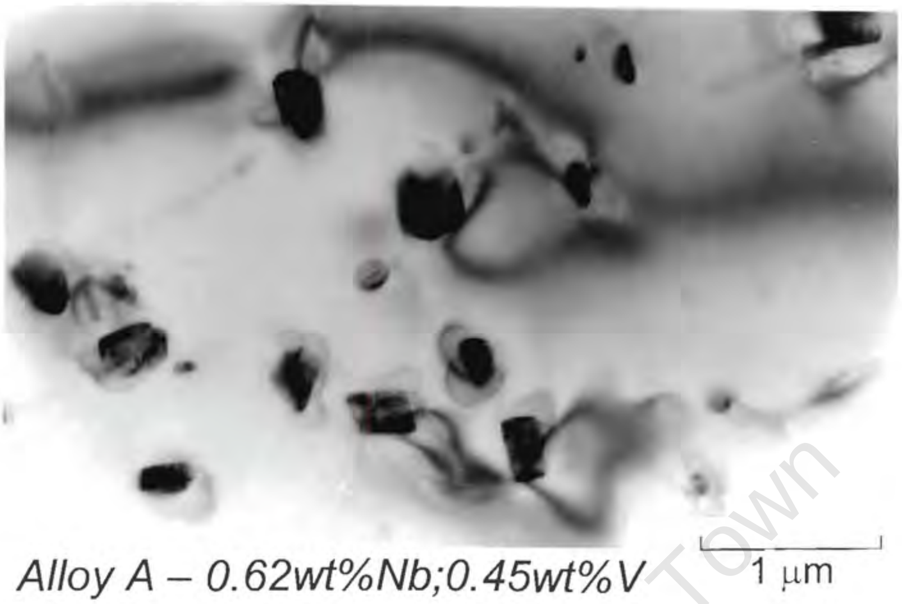

Fig. 4.2.8 (a)

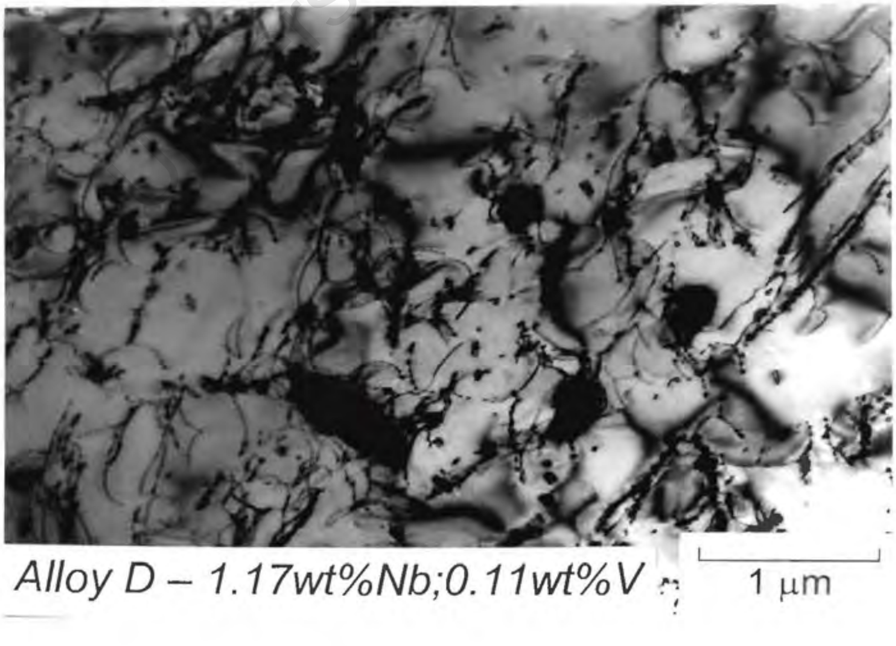

(b)

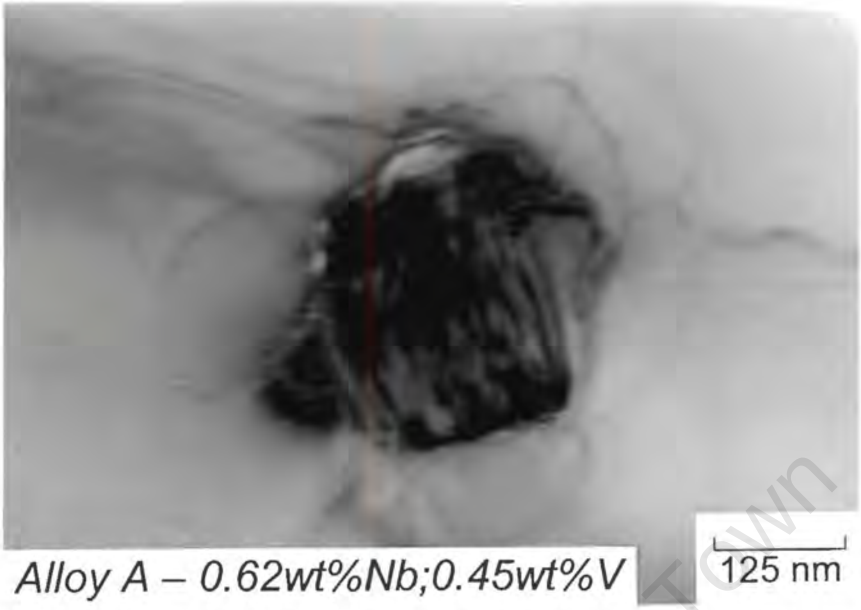

(c)

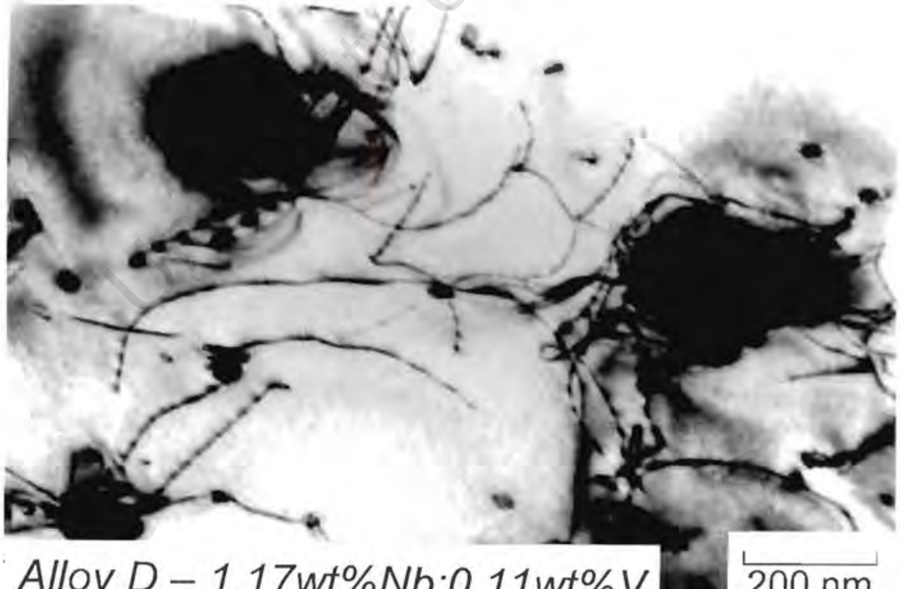

(d)

Fig. 4.2.8 TEM micrographs of the fine precipitates in alloys A and D that formed after ageing for 100 hours showing, (a) & (b) the distribution of precipitates in alloys A and D respectively, (c) & (d) the difference in size and morphology of the precipitates in alloys A and D respectively.

4.2.2.2. COMPOSITIONAL AND CRYSTALLOGRAPHIC ANALYSIS

The morphology of the lamellar precipitates in alloys B, E, F, and G suggests that the precipitates are chromium nitrides (Cr_2N) which occur in high nitrogen steels, typically with a lamellar structure. These precipitates have a HCP crystal structure and an M_2X stoichiometry. Thermocalc did not predict that M_2X precipitation was stable at this temperature, only that MX precipitates were stable. MX precipitates have been noted to form discontinuously in other alloy systems, thus the identification of the precipitates that formed discontinuously in alloys B, E, F and G could not be based solely on their morphology. Accordingly, x-ray maps were acquired from the cell colonies and electron diffraction studies were conducted on the lamellar precipitates in order to determine their composition and crystal structure.

X-ray maps show that the lamellae in alloys B and E are rich in both chromium and vanadium and depleted in iron. Figure 4.2.9 (a) shows a backscattered electron image of a precipitate colony in alloy E, showing the lamellae within the cell and figures 4.2.9 (b)-(d) show the x-ray maps for chromium, vanadium and iron, for the same field of view. Likewise, figure 4.2.10 (a) shows a backscattered image of a precipitate colony in alloy B and the corresponding x-ray maps are in figures 4.2.10 (b)-(d).

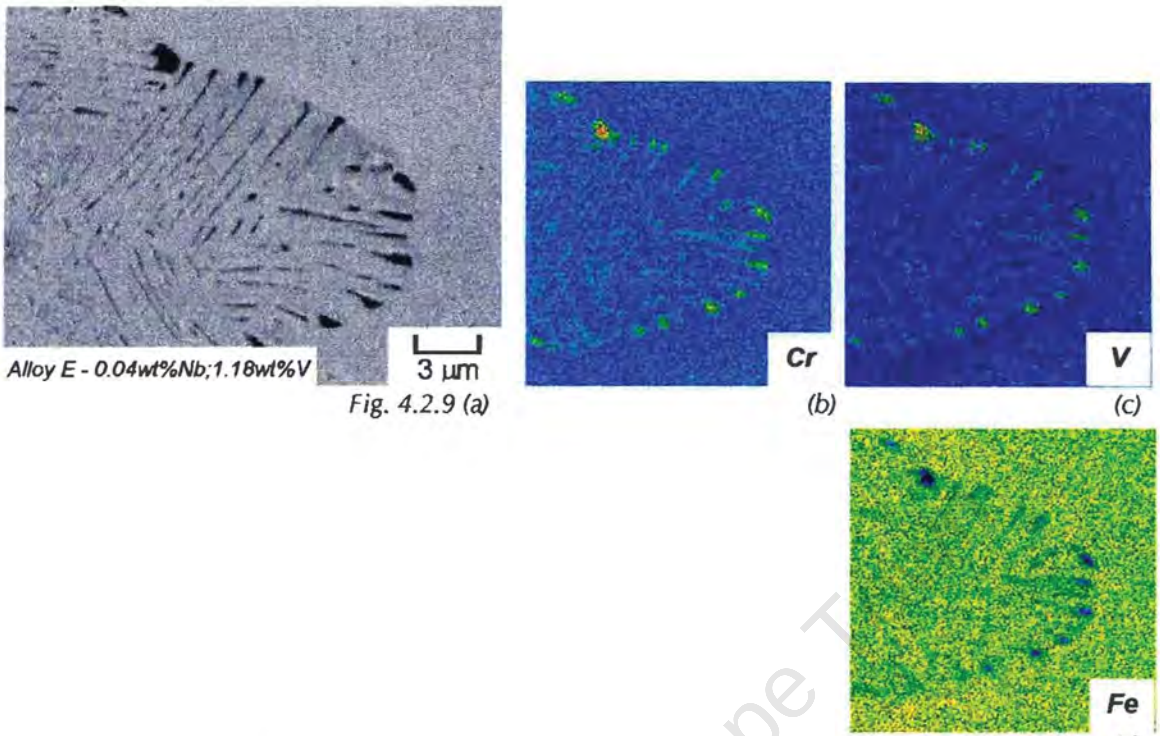

Fig. 4.2.9 (a) *(b)* *(c)* *(d)*

Fig. 4.2.9 (a) SEM (backscattered electron) image of lamellar precipitates in alloy E after ageing at 1100 °C for two hours, together with x-ray maps of the same field of view for (b) vanadium, (c) chromium and (d) iron, showing that the lamellar precipitates are rich in vanadium and chromium and depleted in iron.

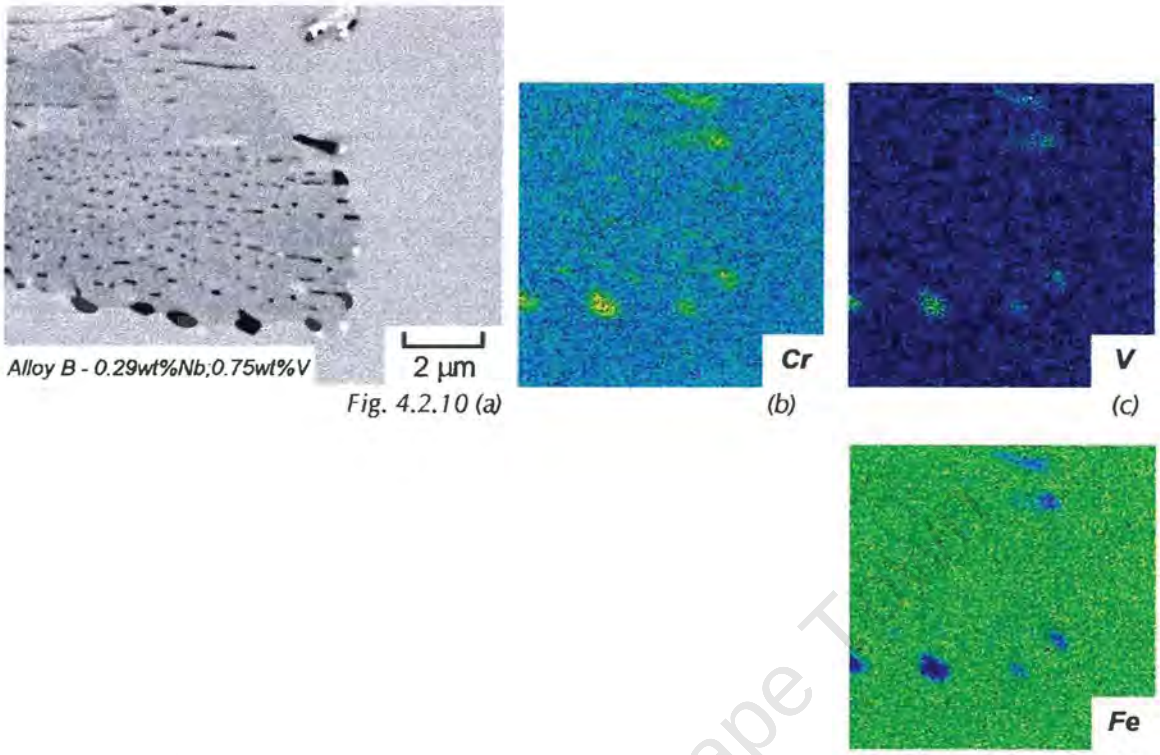

Fig. 4.2.10 (a) (b) (c)

(d)

Fig. 4.2.10 (a) SEM (backscattered electron) image of lamellar precipitates in alloy B after ageing at 1100 °C for two hours, together with x-ray maps of the same field of view for (b) vanadium, (c) chromium and (d) iron, showing that the plate-like precipitates are rich in vanadium and chromium and depleted in iron.

X-ray maps were also acquired from the plate-like precipitates in alloy E that occurred continuously at 1100°C. Figure 4.2.11 (a) shows a backscattered image of these precipitates and the x-ray maps of the same field of view follow in figures 4.2.11 (b)-(d), for chromium, vanadium and iron. These x-ray maps show that the composition of the continuous precipitates in alloy E is similar to the discontinuous lamellar precipitates in alloy E (figures 4.2.9 (a)-(d)). The precipitates that formed continuously in alloy B were much finer that those in alloy E and a sample of alloy B was aged for 10 hours so that the continuous precipitates would be larger. Figure 4.2.12 (a) shows a backscattered image of a string of precipitates on a grain boundary, selected because the precipitates were larger in this region; the x-ray maps for chromium, vanadium and iron are shown in figures 4.2.12 (b)-(d). This set of x-ray maps show that the composition of the continuous precipitates in alloy B is similar to the lamellar precipitates that formed discontinuously in alloy B (figure 4.2.10 (a)-(d)).

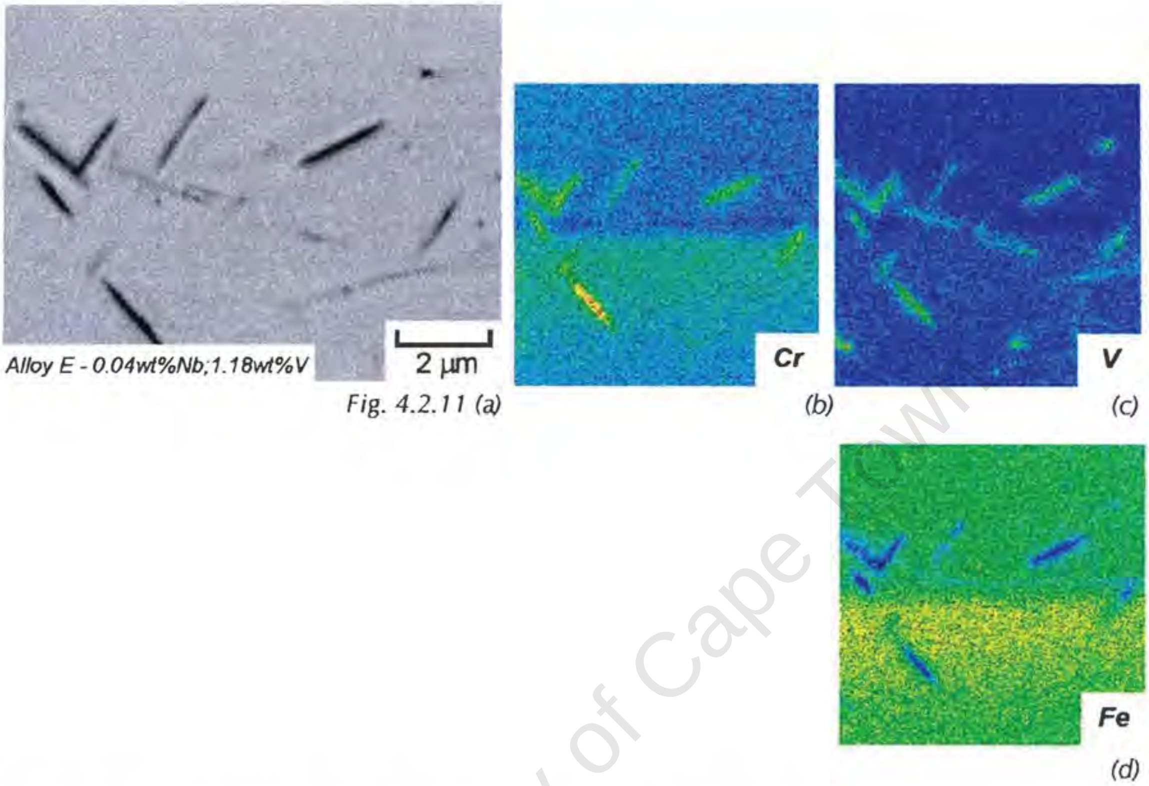

Fig. 4.2.11 (a) SEM (backscattered electron) image of lamellar precipitates in alloy E after a solution treatment and ageing at 1100 °C for two hours followed by a water quench, together with x-ray maps for (b) vanadium, (c) chromium and (d) iron, showing that the plate-like precipitates are rich in vanadium and chromium and depleted in iron.

The x-ray maps for the lamellae and the continuous precipitates in alloys B and E show that both forms of precipitation in these alloys have a similar composition and therefore suggest that they are the same type of precipitate, which has formed via a different mode. Electron diffraction studies of both forms of precipitation in these two alloys show that in the case of alloy E; the discontinuous cellular precipitates and the continuous plate-like precipitates both have a hexagonal close packed structure and the same orientation relationship with the austenite. Diffraction studies of the continuous precipitates in alloy B were not as simple since the precipitates were very fine, even after prolonged ageing. It could be established however, that the lamellar precipitates in alloy B had an HCP crystal structure with the same orientation relationship as the lamellar precipitates in alloy E.

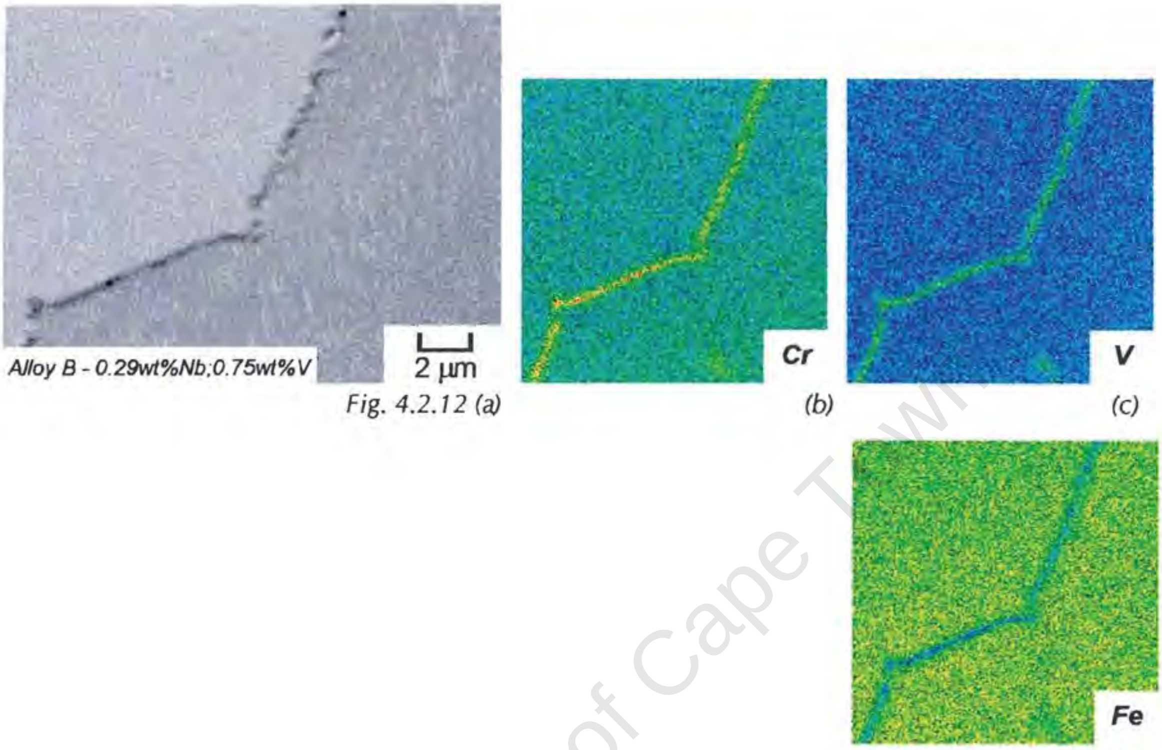

Fig. 4.2.12 (a) *(b)* *(c)*

(d)

Fig. 4.2.12 (a) SEM (backscattered electron) image of the continuous precipitates on the grain boundary in alloy B after ageing at 1100 °C for 10 hours, together with x-ray maps for (b) vanadium, (c) chromium and (d) iron, showing that the plate-like precipitates are rich in vanadium and chromium and depleted in iron.

A series of electron diffraction patterns is shown in figures 4.2.13 (a)-(e), which were taken from regions including the austenite and a precipitate lamella in alloy E. Figure 4.2.13 (a) shows the selected area diffraction pattern for the [1-10] austenite zone axis, taken from a region including both a precipitate lamella and the austenite matrix, where reflections for the FCC phase can be seen together with extra reflections from the precipitate lamella. When the beam diameter is reduced and focussed onto the precipitate, a CBED pattern can be obtained from the precipitate, which eliminates diffraction information from the austenite matrix, shown in figure 4.2.13 (b). Both of these diffraction patterns were indexed and it was calculated that the precipitate reflections belong to the [1-210] HCP zone axis. The (0001) reflection in the [1-210] HCP zone axis pattern is forbidden by the structure factor, but might appear if double diffraction conditions are achieved[132]. Since the lamellae are very closely spaced it is not unreasonable to expect double diffraction effects[41]. As a consequence the [-1101] reflection can be re-diffracted into the position of the [0001] reflection. Figures 4.2.13 (c)&(d) show selected area diffraction patterns of the [11-2] austenite zone axis, taken from regions including one lamella and the austenite matrix. Both of these SAD patterns show extra reflections that originate from the precipitate lamella but figure 4.2.13 (d) shows more reflections for the precipitate than figure 4.2.13 (c). The d-values calculated for the extra reflections in figure 4.2.13 (d) are larger than those that are expected for the M_2X-type precipitate, while those for figure 4.2.13 (c) matched d-values of this phase. These reflections, which are just inside of the matrix spots, correspond to the d-values associated with reflections in the [10-10] HCP zone axis. The extra precipitate reflections in figure 4.2.13 (d) with greater d-values than those for the M_2X phase, probably arise from a superlattice structure, a phenomenon that is not uncommon to this form of precipitation. Figure 4.2.13 (e) shows a CBED pattern taken from a precipitate lamella, in which both the matrix reflections and the precipitate reflections can be seen. These precipitate reflections belong to the [0001] HCP zone axis, while the matrix reflections belong to the [111] FCC zone axis.

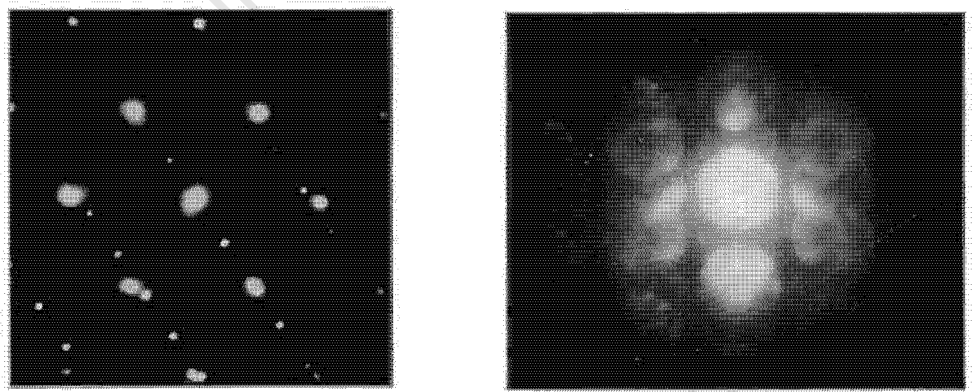

Fig. 4.2.13 (a)

(b)

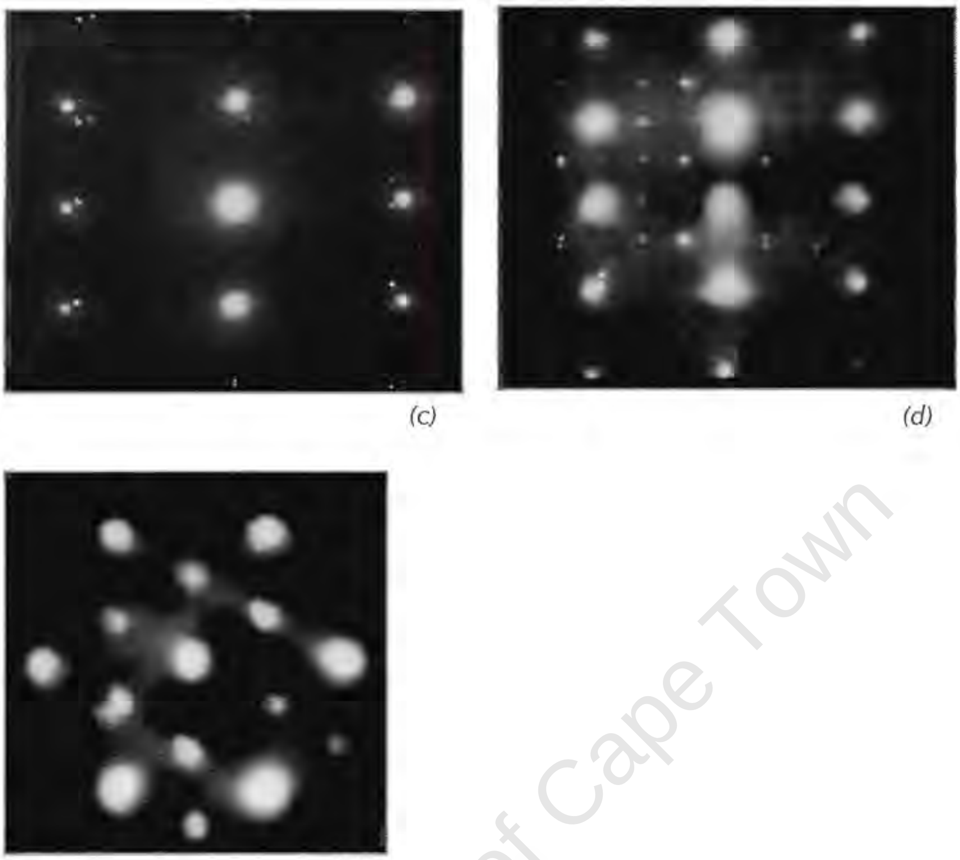

(c) (d)

(e)

Fig.4.2.13 Diffraction Patterns taken from the precipitate lamellae in ***alloy E (0.04wt%Nb;1.18wt%V)*** *after ageing for two hours at 1100°C, showing (a) SAD pattern for the [1-10] austenite zone axis with extra spots for the [1-210] zone axis of the HCP precipitates, (b) CBED pattern taken from the precipitate lamellae, for the [1-210] HCP zone axis, (c) SAD pattern for the [11-2] austenite zone axis with extra spots for the [10-10] HCP zone axis, (d) SAD pattern for the [11-2] austenite zone axis with extra spots for the [10-10] HCP zone axis, and extra spots for a superlattice, (e) CBED pattern taken from the austenite and the precipitate lamellae showing reflection for the [111] austenite zone axis and the [0001] HCP zone axis.*

The indexing of the diffraction patterns shown in figures 4.2.13 (a)-(e) is shown in a series of schematics shown in figures 4.2.14 (a)-(c). From this analysis it could be concluded that the precipitates have the following orientation relationship with the matrix:

$$(111)\gamma//(0001)M_2X;[-110]\gamma//[1-210]M_2X$$

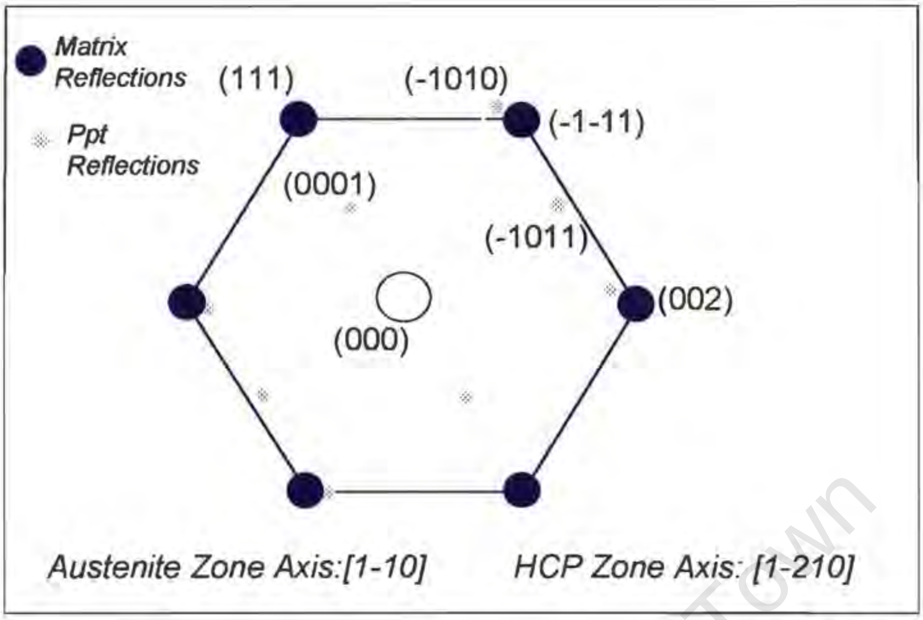
Matrix Reflections
Ppt Reflections
(111)
(-1010)
(-1-11)
(0001)
(-1011)
(002)
(000)
Austenite Zone Axis:[1-10]
HCP Zone Axis: [1-210]

Fig. 4.2.14 (a)

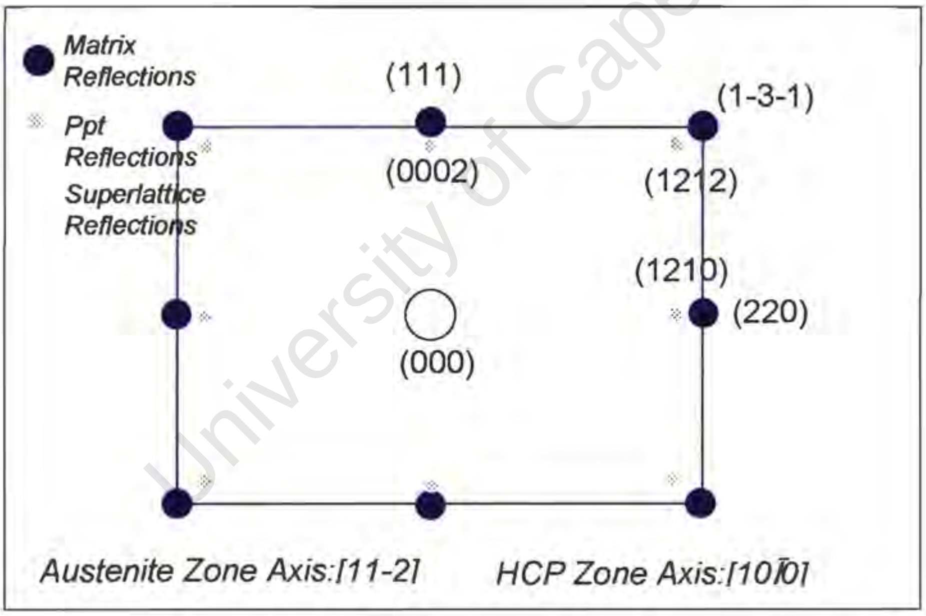
Matrix Reflections
Ppt Reflections
Superlattice Reflections
(111)
(1-3-1)
(0002)
(1212)
(1210)
(220)
(000)
Austenite Zone Axis:[11-2]
HCP Zone Axis:[10$\bar{1}$0]

(b)

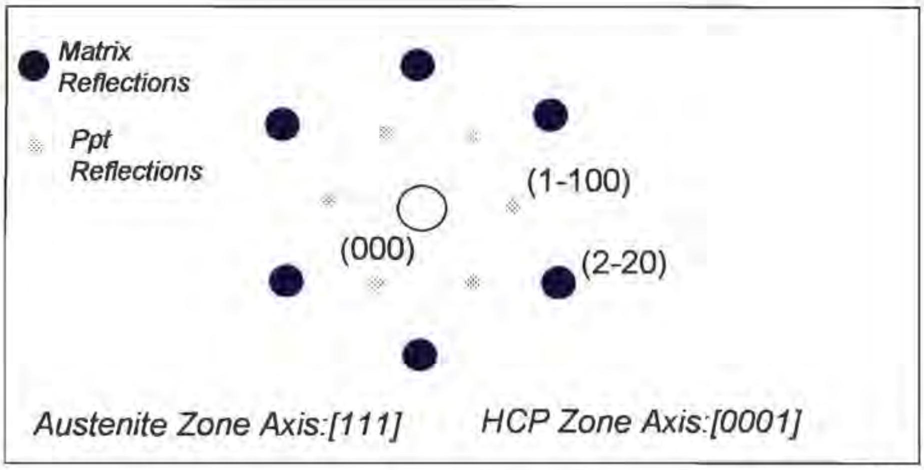

(c)

Fig. 4.2.14 Schematic diagrams showing the indexing of (a) the SAD [1-10] austenite zone axis, with the extra spots for the precipitates for the [1-210] zone axis, (b) the [11-2] austenite zone axis, together with the extra reflections for the precipitate, which belong to the [10-10] zone axis and those that belong to the superlattice, (c) the [111] austenite zone axis with the extra reflections for the precipitate, which belong to the [0001] HCP zone axis.

Diffraction patterns similar to those in figures 4.2.13 (a)-(e) were obtained for the lamellar precipitates in alloy B and the continuous precipitates in alloy E, and are shown in figures 4.2.15 (a)–(d)-4.2.16 (a)-(c). These diffraction patterns were indexed in the same way as shown in the series of schematics in figures 4.2.14 (a)-(c). This shows that the lamellar precipitates in alloy B also have an HCP structure, as do the continuous precipitates in alloy E. Superlattice reflections for the continuous precipitates in alloy E were observed in the SAD pattern for the [11-2] austenite zone axis, and were also evident in the CBED pattern taken from the precipitate (figure 4.2.15 (c) & (d)). These reflections were not observed in the [11-2] austenite zone axis pattern taken from the lamellae in alloy B. Reflections that corresponded to the [10-10] HCP zone axis did appear consistently with the [11-2] austenite zone axis patterns for the lamella in alloy B and the continuous precipitates in alloy E.

Finally, each of the diffraction patterns shown in figures 4.2.15-4.2.16 were indexed in the same way as illustrated in figure 4.2.14. From this analysis, the lattice parameters for the lamellae in alloys B and E and the continuous precipitates in alloy parameters for the lamellae in alloys B and E and the continuous precipitates in alloy E were determined for each of the zone axis diffraction patterns and the results of these calculations are shown in table 4.2.1. The calculated values are in good agreement with the published values by Goldschmidt[41]. In each case the experimental values fall in a range between those given for V_2N and those for Cr_2N, which can be expected since these precipitates are rich in both vanadium and chromium.

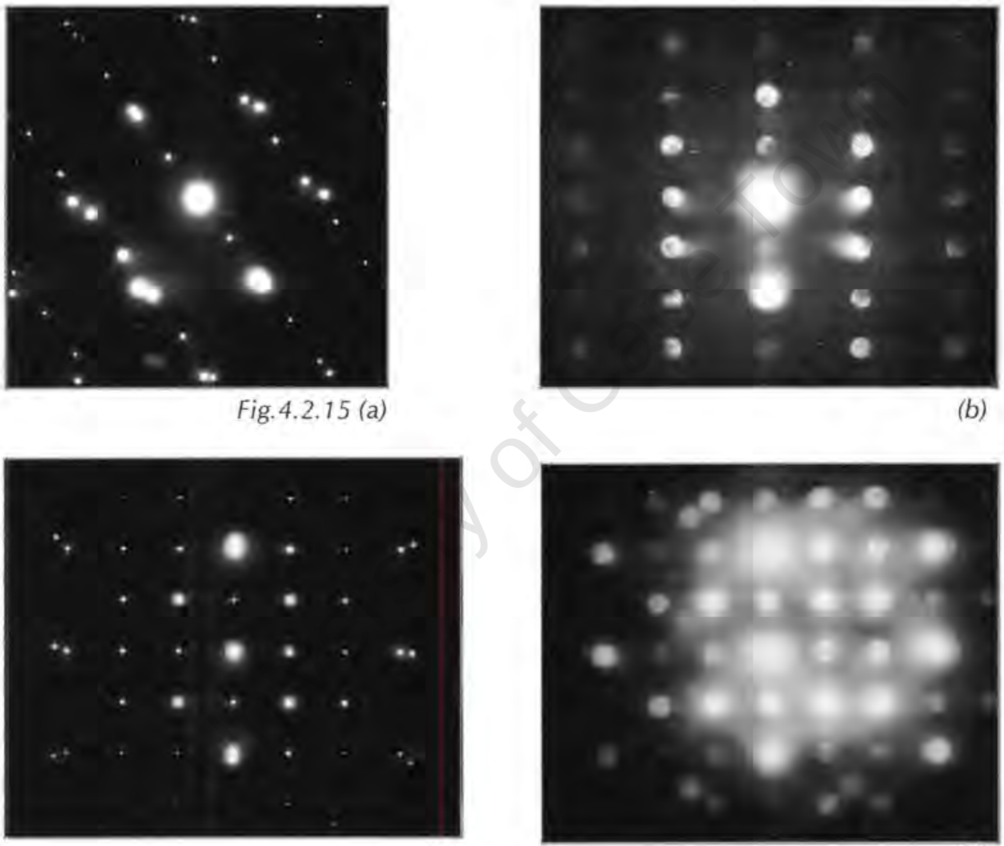

Fig.4.2.15 (a) (b)

(c) (d)

Fig. 4.2.15 Diffraction Patterns taken from the continuous plate-like precipitates ***in alloy E (0.04wt%Nb;1.18wt%V)*** *after ageing for two hours at 1100℃, showing (a) SAD pattern for the [1-10] austenite zone axis with extra spots for the [1-210] zone axis of the HCP precipitates, (b) CBED pattern taken from the precipitate lamellae, for the [2110] HCP zone axis, (c) SAD pattern for the [11-2] austenite zone axis with extra spots for the [10-10] HCP zone axis and extra spots for a superlattice, (d) CBED pattern taken from the precipitate lamellae showing reflections for the [10-10] HCP zone axis as well as superlattice reflections.*

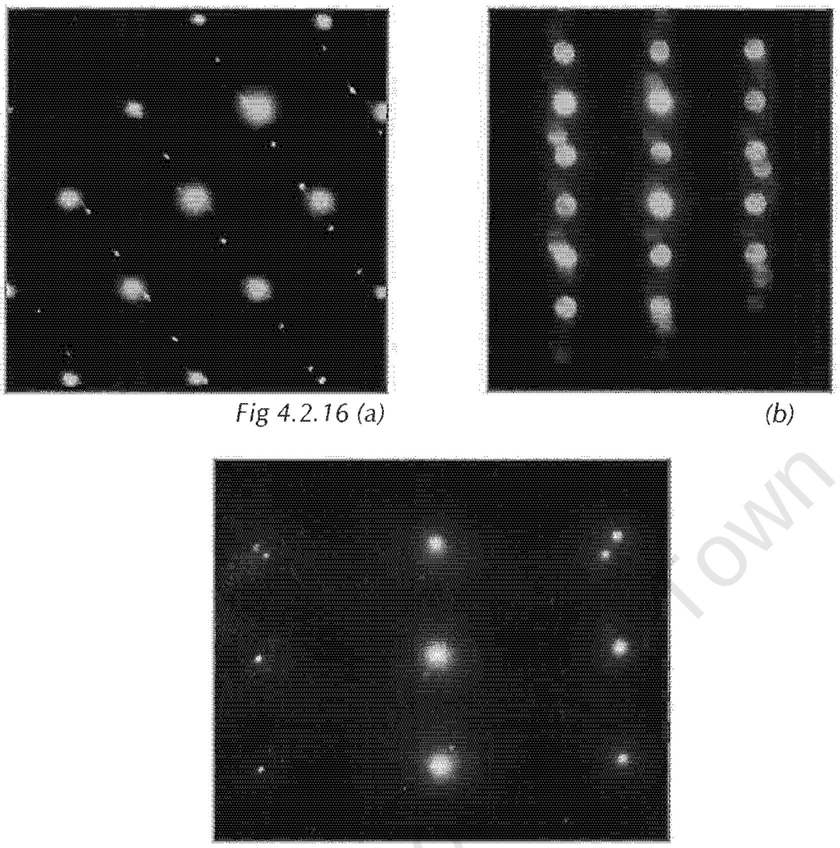

Fig 4.2.16 (a)

(b)

(c)

Fig. 4.2.16 Diffraction Patterns taken from the precipitate lamellae in ***alloy B (0.29wt%Nb;0.75wt%V)*** *after ageing for two hours at 1100℃, showing (a) SAD pattern for the [1-10] austenite zone axis with extra spots for the [1-210] zone axis of the HCP precipitates, (b) CBED pattern taken from the precipitate lamellae, for the [1-210] HCP zone axis, (c) SAD pattern for the [11-2] austenite zone axis with extra spots for the [10-10] HCP zone axis*

Table 4.2.1 Lattice parameters for the lamellar precipitates and continuous precipitates, calculated from the diffraction patterns.

	a (Å)	*c (Å)*
Chromium Nitride (Cr_2N)	**2.75**	**4.44**
Vanadium Nitride (V_2N)	**2.82**	**4.54**
Alloy E *(lamella) – [1-210]*	2.57	4.57
Alloy E *(lamella) – [10$\bar{1}$0]*	2.76	4.28
Alloy E *(lamella) – [0001]*	2.58	-
Alloy E *(continuous) – [1-210]*	2.84	4.48
Alloy E *(continuous)– [10$\bar{1}$0]*	2.81	4.52
Alloy B *(lamella) – [1-210]*	2.75	4.61
Alloy B *(lamella) – [10$\bar{1}$0]*	2.84	4.66

The continuous precipitates in alloy B were very fine and difficult to analyse using diffraction techniques. Many attempts were made to obtain a diffraction pattern from the precipitates, but only one was successful and is shown in figure 4.2.17. The diffraction pattern shows extra spots that belong to the [001] zone axis for the FCC system and show that this precipitate is a MX precipitate, with a cube-cube orientation relationship with the matrix, and a lattice parameter of 4.3 Å. This diffraction pattern can be indexed in the same way as the [001] zone axis pattern for the MX precipitate that formed during solidification in alloy A, shown in section 4.1. The x-ray map data from the continuous precipitates in alloy B (figures 4.2.12 (a)-(d)) suggested that they were chromium and vanadium rich M_2X precipitates, but the diffraction information from the continuous precipitates in alloy B (figure 4.2.17) suggests that the precipitates are MX type precipitates. Thus the indications are that both M_2X and MX precipitates formed continuously in this alloy after ageing for 10 hours at 1100°C.

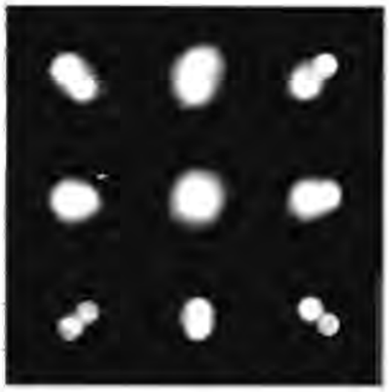

Fig. 4.2.17 CBED pattern taken from a continuous precipitate in alloy B, showing reflections for the austenite matrix and the precipitate showing that the precipitate has an FCC crystal structure.

An analysis of the fine precipitates (figures 4.2.6 (a) and (b)) in alloys A and D was conducted to determine their composition, crystal structure and orientation relationship with the matrix. The small size of the precipitates made it difficult to obtain diffraction information or compositional information from them. Specimens of these alloys were therefore aged for 10 hours so that compositional and diffraction analysis could be carried out on the larger precipitates that had grown during prolonged ageing.

Figure 4.2.18 (a) shows a backscattered image of the precipitates that have grown from a grain boundary in alloy A, after a 10 hour ageing treatment at 1100°C. The x-ray maps for niobium, vanadium and iron in figures 4.2.18 (b)-(d) show that the particles are rich in both niobium and vanadium and depleted in iron. Similarly figure 4.2.19 (a) shows the fine precipitates that have formed in alloy D after ageing for 10 hours at 1100°C. These precipitates are rich only in niobium, and contain no vanadium, which was expected since alloy D has low vanadium additions.

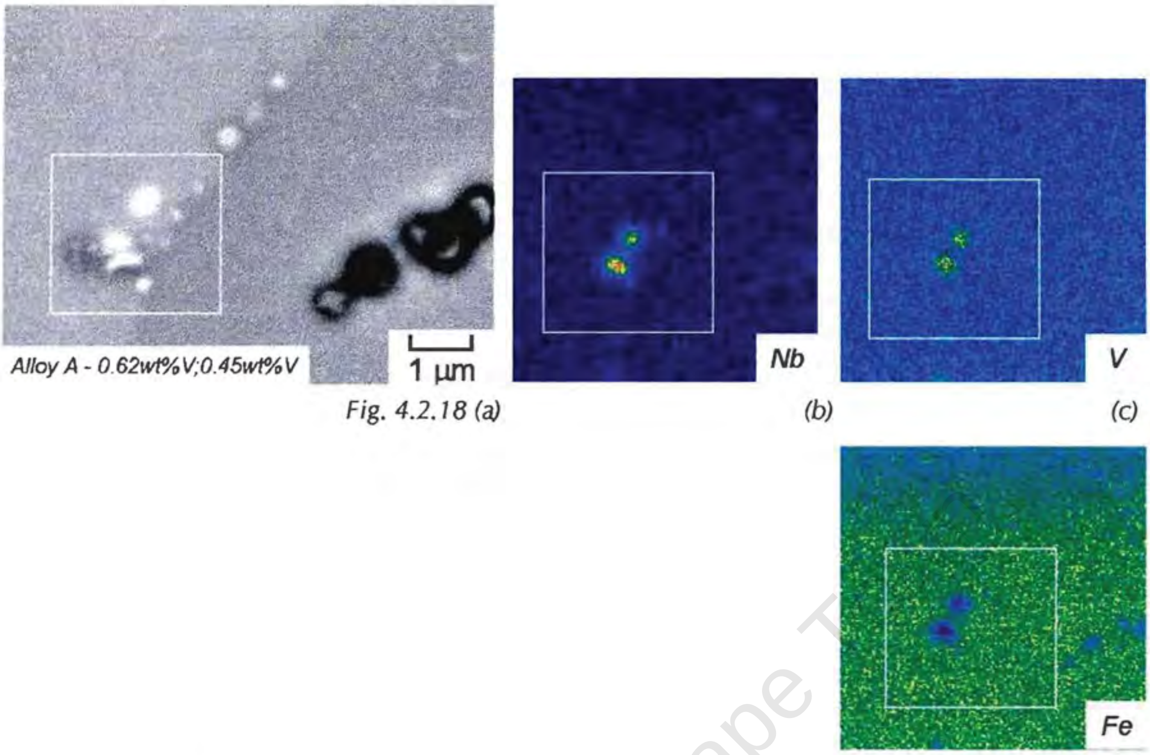

Fig. 4.2.18 (a) *(b)* *(c)*

(d)

Fig. 4.2.18 (a) SEM (backscattered electron) image of fine precipitates in alloy A after ageing for 10 hours at 1100 °C, showing the field of view from which the x-ray maps were taken, with x-ray maps for (b) vanadium, (c) chromium, (d) iron, showing that the precipitates are rich in niobium and vanadium and depleted in iron.

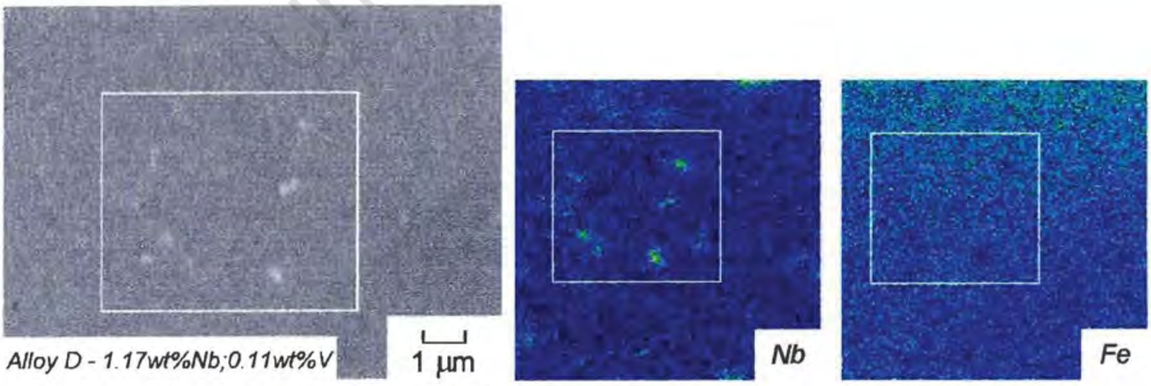

Fig 4.2.19 (a) *(b)* *(c)*

Fig 4.2.19 (a) SEM (backscattered electron) image of the fine precipitates in alloy D after ageing for ten hours at 1100 °C, showing the field of view from which the x-ray maps were taken, with x-ray maps for (b) niobium and (c) iron, showing that are rich in niobium and depleted in iron.

Electron diffraction studies show that the precipitates in both alloys A and D have a FCC crystal structure. Figures 4.2.20 (a) & (b) show the CBED patterns taken from the precipitates in alloy A at the same tilt and rotation as the [001] austenite zone axis and the [112] austenite zone axis respectively. These two sets of diffraction patterns show that the fine precipitates in alloy A have a cube-cube orientation relationship with the austenite, which is typical for a precipitate with a FCC crystal structure.

A similar set of diffraction patterns was recorded for alloy D, which leads to the same conclusion. Figures 4.2.21 (a) and (b) show the [011] and [112] zone axis for the FCC structure taken from the fine precipitates. These diffraction patterns were taken at the same tilt and rotation as the corresponding austenite [011] and [112] zone axis patterns, which indicates that the precipitate has a cube-cube orientation relationship with the matrix.

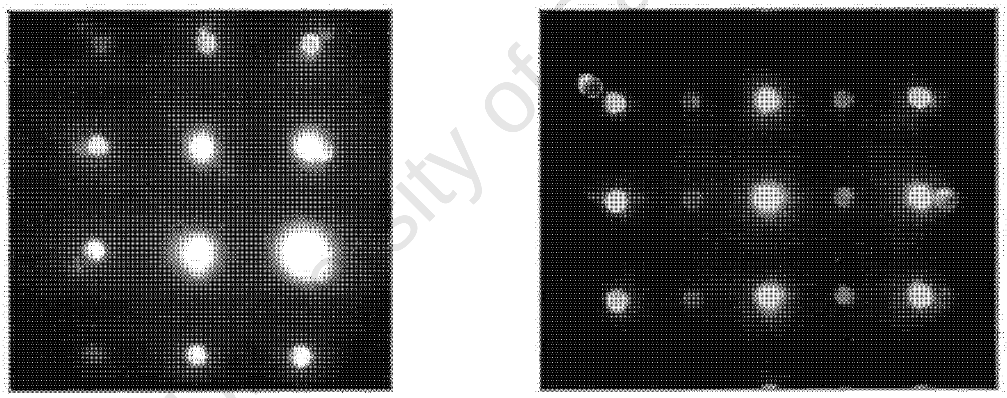

Fig. 4.2.20 (a) *(b)*

*Fig. 4.2.20 CBED patterns for the fine precipitates in **alloy A (0.62wt%Nb;0.45wt%V)** after ageing at 1100°C showing (a) the [001] zone axis for the MX precipitate & (b) the [11-2] zone axis for the MX precipitate.*

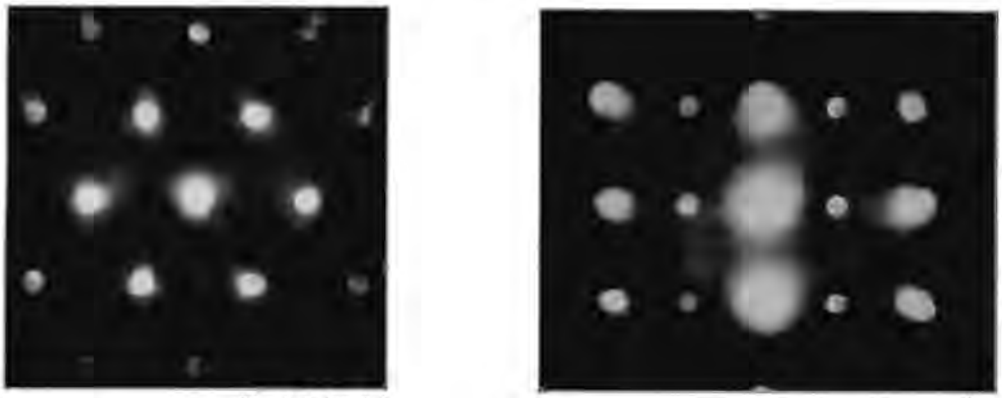

Fig 4.2.21 (a) (b)

Fig. 4.2.21 CBED patterns from the fine precipitates in ***alloy D (1.17wt%Nb;0.11wt%V)*** *after ageing at 1100°C showing, (a) the [011] zone axis for the MX precipitate, (b)the [112] zone axis for the MX precipitate.*

The faint spots that are observed in the [112] zone axis diffraction patterns taken from the precipitates in alloys A and D in figures 4.2.20 (b) and 4.2.21 (b) can be indexed as precipitate superlattice reflections, since d-values for the reflections are greater than those for the FCC precipitate. This indicates that the precipitates have an ordered NaCl FCC crystal structure, typical of MX precipitates[132].

The lattice parameters for the precipitates in alloys A and D were calculated from the diffraction patterns and the results of these calculations are shown in table 4.2.2. The values agree, with some variability, with the published values given for pure niobium and vanadium nitrides with an exact 1:1 MX stoichiometry.

*Table 4.2.2 Lattice parameters for the fine precipitates in alloys A and D calculated from the corresponding diffraction patterns, together with the published values *after Goldschmidt*[41]*.*

	a(Å)
Niobium Nitride (NbN)*	**4.38-4.39**
Vanadium Nitride (VN)*	**4.07-4.14**
***Alloy A** [001]*	4.3
***Alloy A** [112]*	4.2
***Alloy D** [011]*	4.2
***Alloy D** [112]*	4.4

There are some discrepancies between the predictions made by Thermocalc and the experimental results. M_2X precipitates were not predicted at this temperature for any of the alloys, however this form of precipitation was observed in alloys B, E, F and G. The predictions did however agree with the microstructural observations for alloys A, C, D and H, where in the case of alloy C no precipitation was predicted or observed and in alloys A, D and H, MX precipitation was observed as predicted by Thermocalc. Ferrite was not observed in any of the alloys except alloy D, although it was predicted to be present in all the alloys, except alloy C. The reasons for these discrepancies were discussed in section 3.2.7.

4.2.3 MECHANICAL TESTS

The results of tensile tests on alloys A, D, E & H, illustrate the effect of the two different forms of precipitation that occur at 1100°C on the mechanical behaviour of the steel. The results from alloys A, D and H after ageing treatments at 1100°C show the influence of MX precipitate formation on the tensile properties, whereas the results of alloy E show the influence of lamellar precipitation. Alloy C in the solution treated condition was included for comparison purposes since the purpose of the current investigation was to determine the influence of precipitation reactions, as a consequence of niobium and vanadium additions on the mechanical performance of the high nitrogen steel base alloy. The tensile results of alloys A, D, E and H after ageing at 1100°C for two hours were therefore compared with alloy C. This comparison is limited to some degree because of the presence of the blocky precipitates in alloys A, D and H that have some effect on the tensile behaviour of the steel. The tensile results from alloys A, D and H were selected for a more detailed study of ageing time on the tensile properties. The effect of ageing time on the tensile properties of these alloys was compared with the solution treated counterparts so that the influence of the fine precipitates could be established. The aim of this study was twofold: first to find the best combinations of yield strength and elongation to failure for each alloy as a function of ageing time and second to determine the peak aged, under aged and over aged conditions for each alloy, A, D and H. The aged alloys with the best product of yield strength and elongation to failure were then selected for abrasive wear tests.

4.2.3.1 TENSILE TESTS

Figure 4.2.22 shows the tensile test curves for alloys A, D, E and H after ageing for two hours together with alloy C in the solution treated condition. Table 4.2.3 shows the tensile properties for each of the alloys. The tensile results of alloy E show that the lamellar colonies that have formed after ageing at 1100°C have a significant effect on the strength of the steel, without a large reduction in elongation to failure. This is better illustrated in figure 4.2.23, where the tensile results of alloy E after ageing for two hours at 1100°C can be compared with alloys E and C in the solution treated condition. After ageing at 1100°C for two hours, the yield strengths of alloys A, D and H are lower than alloy E, but similar to each other. Comparison with alloy C in the solution treated condition suggests that the MX precipitates do cause some strengthening and this is further illustrated in figures 4.2.24-4.2.26 where the tensile results of each of the alloys after ageing treatments at 1100°C are compared with the solution treated counterpart.

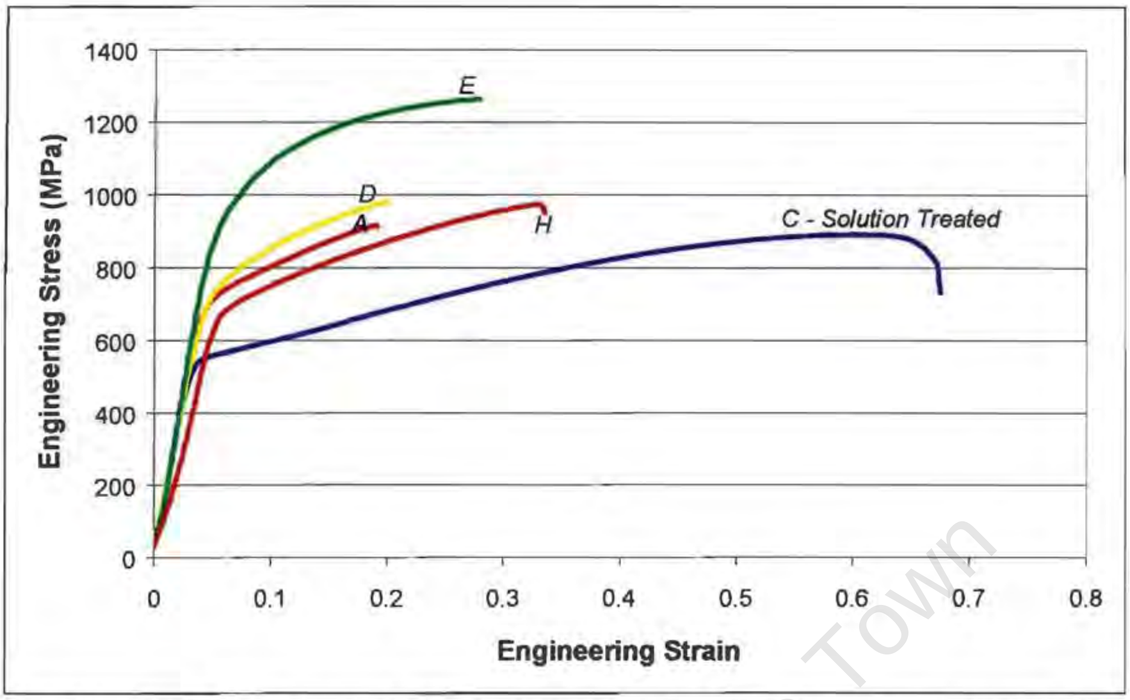

Fig. 4.2.22 Tensile test results of alloys A, D, E and H after ageing for two hours at 1100 ℃ together with alloy C in the solution treated condition for comparative purposes.

Table 4.2.3 Tensile properties of alloys A, D, E and H after ageing for two hours at 1100 ℃, together with alloy C in the solution treated condition.

Alloy	***Yield Strength (MPa)***	***Ultimate Tensile Strength (MPa)***	***Total Elongation to Failure (%)***	***Plastic Elongation to Failure (%)***
A	658	913	19	15
C	587	914	68	63
D	676	979	20	16
E	886	1262	28	23
H	662	970	33	28

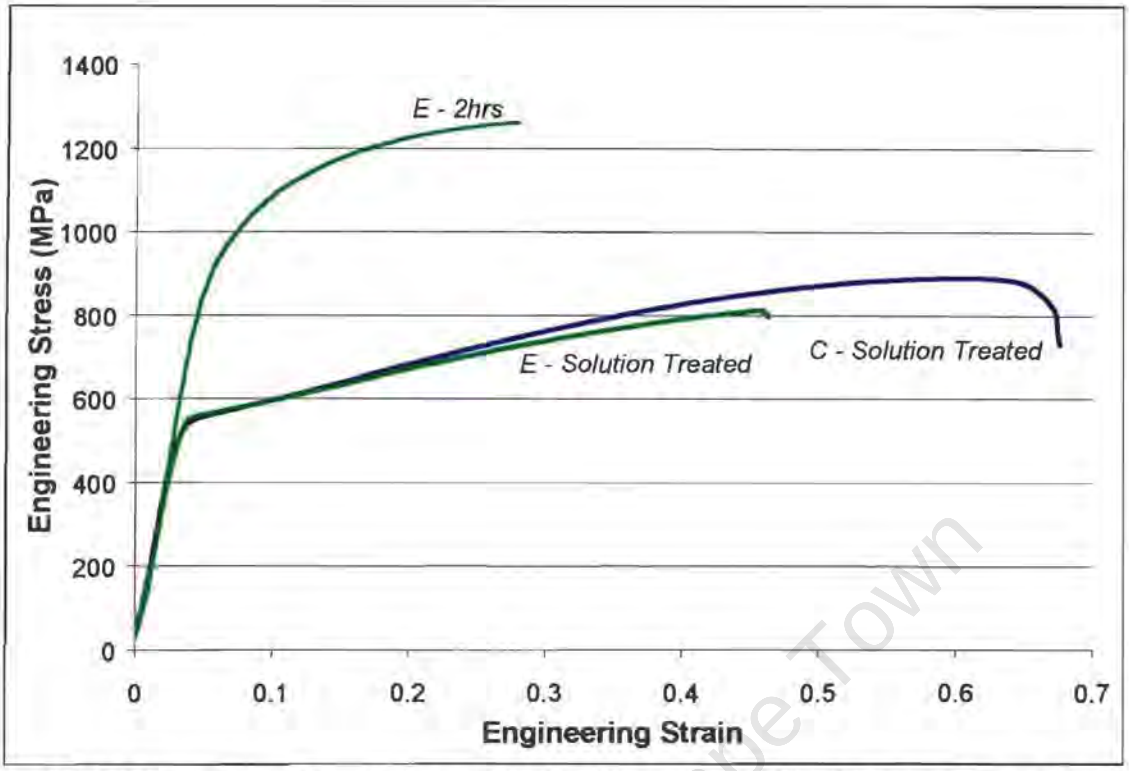

Fig. 4.2.23 Comparison of tensile test results of E after ageing at 1100 °C for two hours with alloys C and E in the solution treated condition.

The effect of ageing time at 1100°C on alloy A is illustrated by the collection of tensile test curves in figure 4.2.24, which shows the results of ageing treatments for 0.5, 2, and 5 hours. Similarly the tensile test results for alloys D and H after ageing at 1100°C for 0.5, 2, 5 and 10 hours are shown in figures 4.2.25 and 4.2.26. The results have been plotted so that the difference in yield point and plastic elongation to failure can be compared for each specimen more clearly, since both of these properties should be optimised for improved wear performance. For each set of data the corresponding solution treated alloy is included for comparative purposes. The numerical results of the tests, for the three alloys after the four different ageing times, is shown in table 4.2.4 together with the results in the solution treated condition for comparative purposes.

The tensile results for alloy A (figure 4.2.24) show that the yield strength is greatest after a 2 hour ageing treatment, and as expected the elongation to failure is also the lowest. The yield strength is lower and the elongation to failure greater after ageing for 0.5 hours and 5 hours. After all three heat treatments, the yield strength is greater than the solution treated condition and the elongation to failure lower. The results of ageing for 10 hours were dubious, since the ultimate tensile strength and elongation to failure are low, and suggest that failure occurred as a consequence of inclusions or porosity in the castings. A second test in the same condition showed similar results and the limited availability of material prevented further testing of alloy A after ageing at 1100°C for 10 hours. A reliable tensile result for alloy A after ageing for 10 hours could not be obtained and the data that was acquired has been omitted.

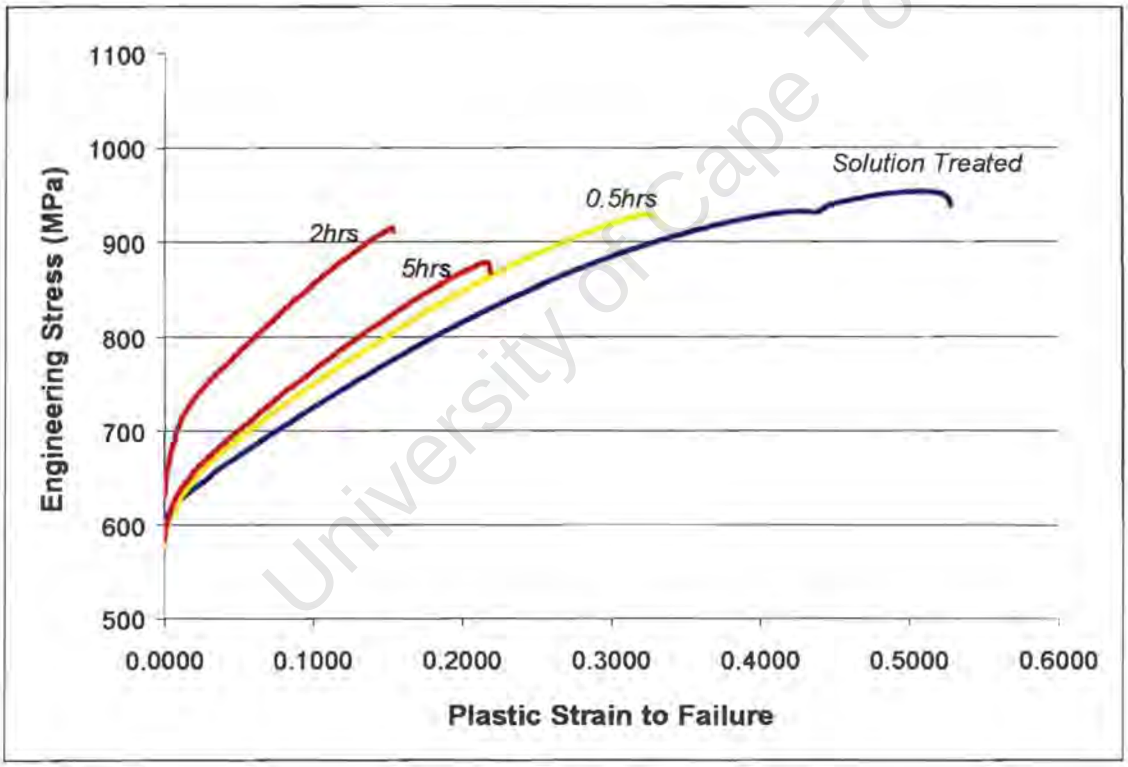

Fig. 4.2.24 The effect of ageing time at 1100 °C on the tensile properties of alloy A

The tensile results of the ageing treatments at 1100°C for 0.5, 2, 5 and 10 hours on alloy D in figure 4.2.25 show that the tensile properties vary with ageing time. The maximum yield strength occurs after 0.5 hours of ageing, but the elongation to failure in this alloy only reaches a minimum after 2 hours of ageing. The yield strength of alloy D decreased after 5 hours of ageing compared to the 0.5 hour ageing treatment and after 10 hours, the yield strength was similar to the solution treated condition. The elongation to failure after ageing at 1100°C was a minimum after ageing for 2 hours and was greater after ageing for 0.5, 5 and 10 hours at 1100 °C.

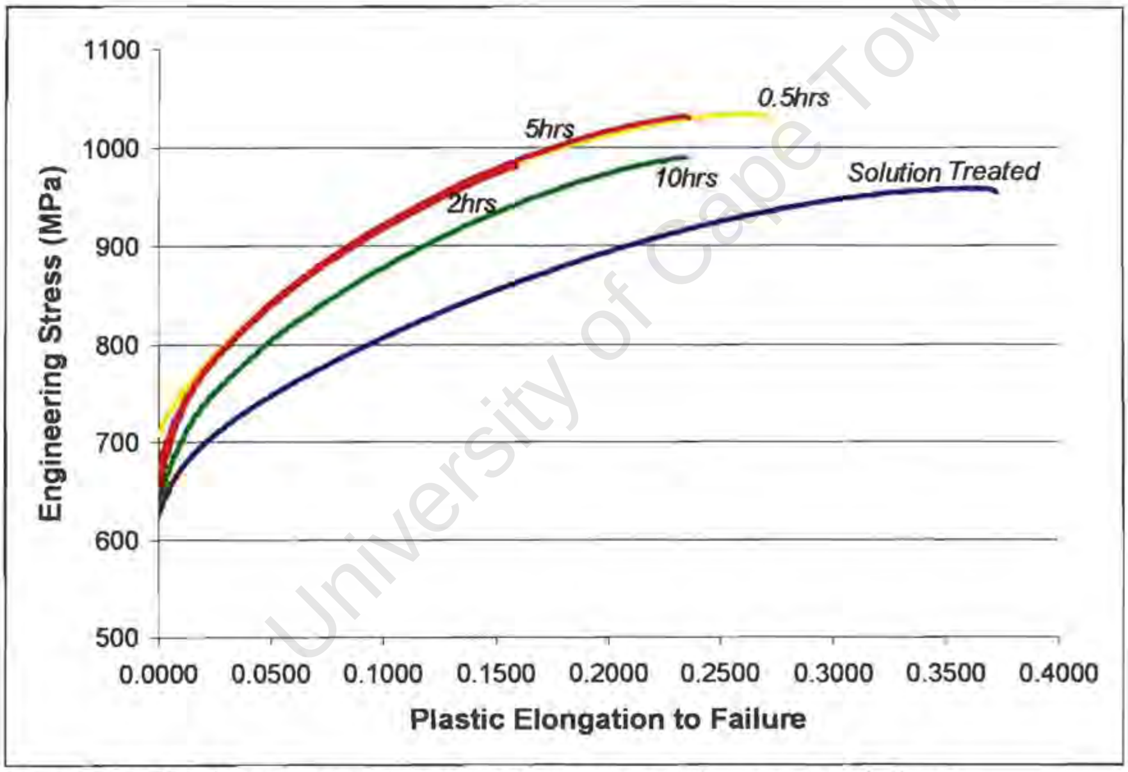

Fig. 4.2.25 The effect of ageing time at 1100 °C on the tensile properties of alloy D.

The difference in yield strength and elongation to failure for alloy H (figure 4.2.26) after different ageing times at 1100°C is not as marked as for alloys A and D. Alloy H shows maximum strength after ageing for 2 hours at 1100°C and a minimum after ageing for 0.5 hours and 10 hours. The elongation to failure after ageing at 1100 °C decreased compared to the solution treated condition, but did not show any obvious minimum value.

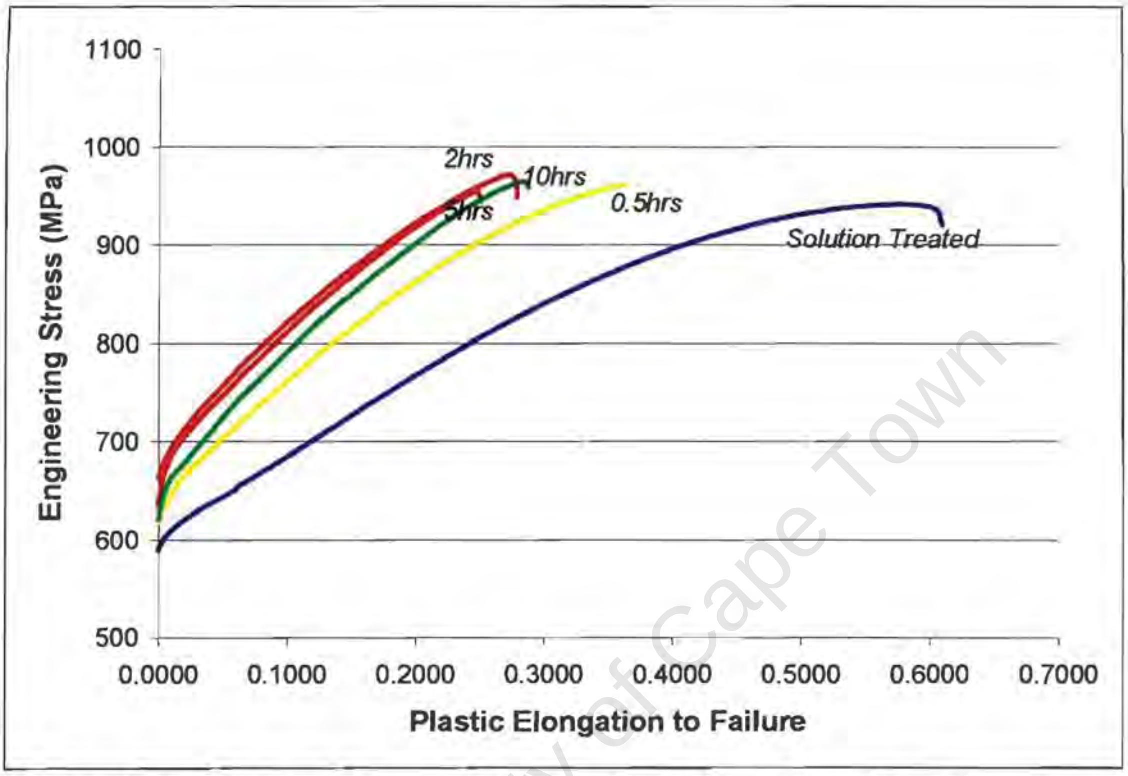

Fig. 4.2.26 The effect of ageing time at 1100 °C on the tensile properties of alloy H.

Table 4.2.4 *Tensile properties of alloys A, D and H after ageing treatments at 1100℃ at different times together with the tensile properties of each alloy in the solution treated condition.*

(Time in hours)	***Yield Strength (MPa)***	***Ultimate Tensile Strength (MPa)***	***Total Elongation to Failure (%)***	***Plastic Elongation to Failure (%)***
Alloy A				
Solution Treated	600	952	58	53
0.5	576	928	36	32
2	658	913	19	14
5	607	877	25	21
10	541	696	12	9
Alloy D				
Solution Treated	625	957	42	37
0.5	707	1032	31	27
2.0	676	979	18	16
5.0	648	1029	27	23
10.	628	988	27	23
Alloy H				
Solution Treated	589	940	65	61
0.5	618	960	40	36
2.0	662	970	34	28
5.0	636	950	30	25
10.0	618	964	33	29

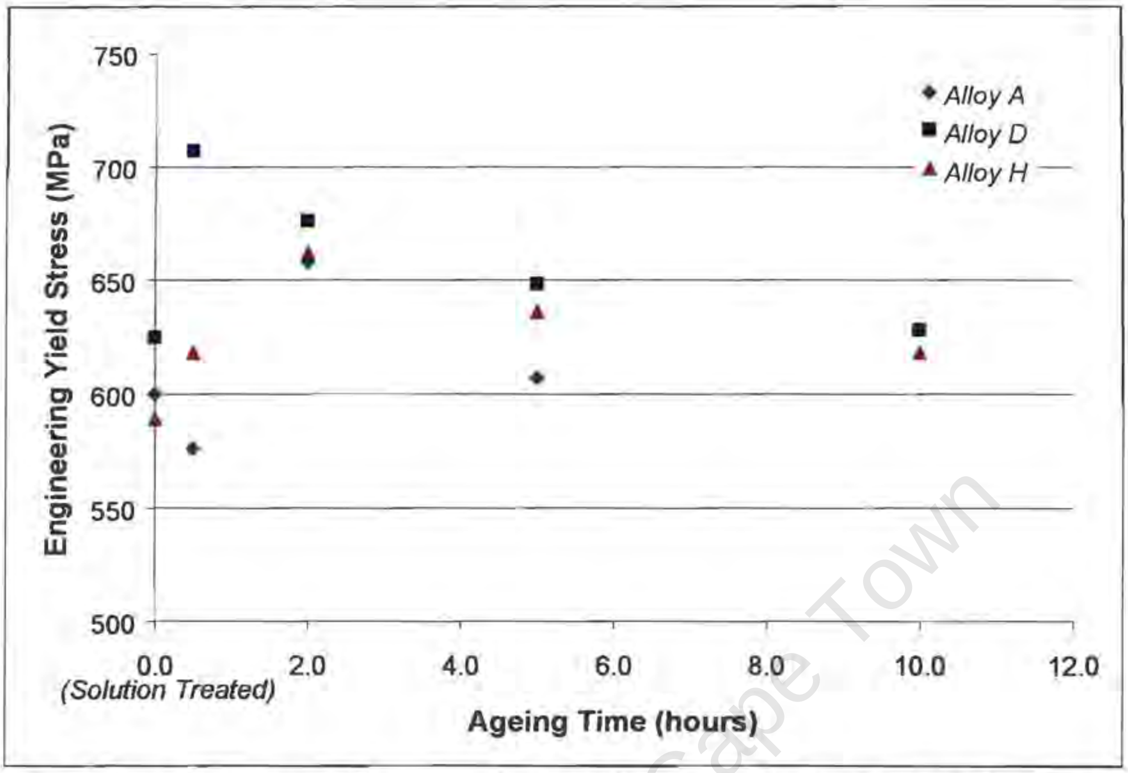

Fig. 4.2.27 (a) Engineering yield stress as a function of ageing time for alloys A, D, H showing the peak aged condition for each of these alloys at 1100 °C.

Table 4.2.4 shows the numerical results of the tensile properties for alloys A, D and H after the four different ageing times, together with the tensile results of these alloys in the solution treated condition. The results of these tests are summarised in figures 4.2.27 (a) and (b), which show the yield strength and plastic elongation as a function of ageing time respectively. Figure 4.2.27 (a) shows that a maximum in the yield strength is reached as a function of ageing time and figure 4.2.27 (b) shows that the elongation to failure decreases after ageing treatments at 1100 °C.

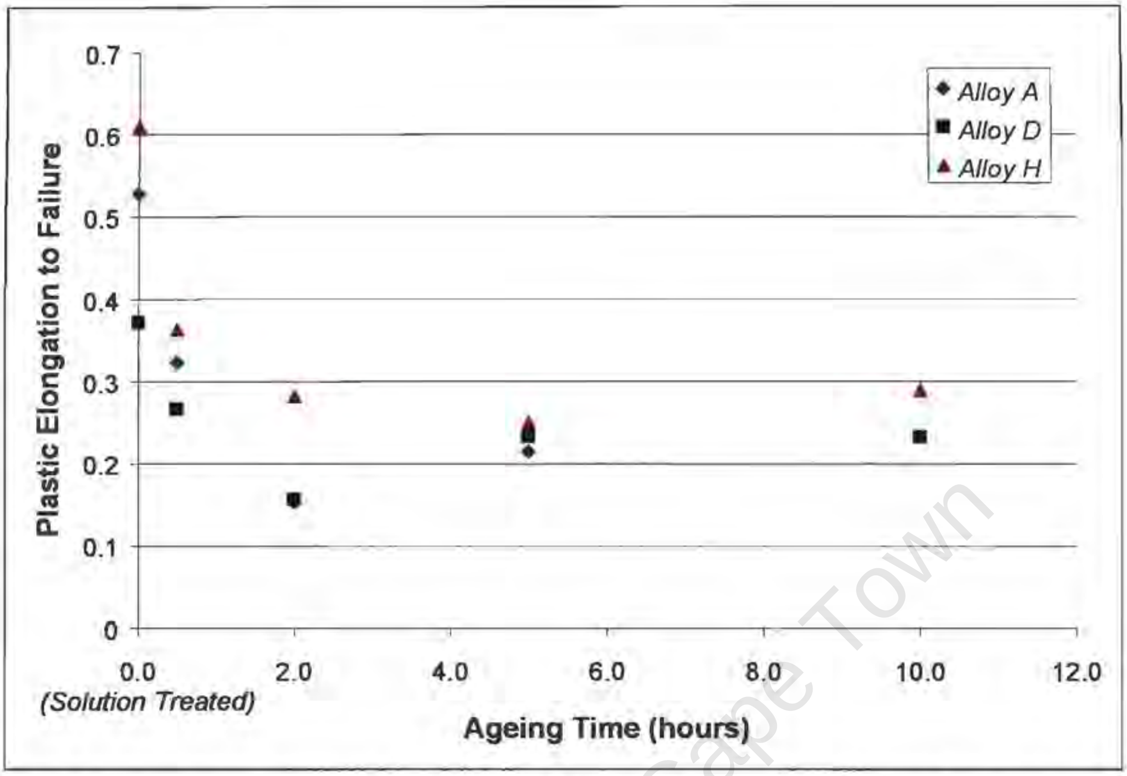

Fig. 4.2.27 (b) Plastic elongation to failure as a function of ageing time for alloys A, D, H showing the peak aged condition for each of these alloys at 1100 °C.

4.2.3.2 CHARPY V-NOTCH TESTS

Alloys A, D, E and H all showed reasonable levels of ductility during the low strain rate conditions of the tensile test. These alloys were therefore tested to determine their toughness under high strain rate conditions. Two specimens of each of alloys A, D, E and H were machined for Charpy V-notch tests after solution treating and ageing for 2 hours at 1100°C. The results of the Charpy V-notch tests are shown in table 4.2.5 together with alloy C in the solution treated condition. These tests show that the toughness of alloys A, D, E and H is low compared to alloy C in the solution treated condition. The low fracture toughness of these alloys probably arises from the blocky precipitates in alloys A, D, and H (table 4.1.3) since these alloys were shown to have low fracture toughness in the solution treated condition. The influence of ageing at 1100°C on the toughness of alloys A, D and H could not be established and further tests to determine the influence of ageing time on the fracture toughness of these alloys was not considered useful. The fracture toughness of alloy E was also low in the solution treated condition therefore the low fracture toughness of this alloy after ageing at 1100°C could not be attributed to the lamellar precipitates observed in this alloy. The results of the Charpy V-notch tests are shown in table 4.2.5.

Table 4.2.5 The results of Charpy V-notch tests for the selected alloys.

Alloy	***Charpy V-Notch Energy (Joules)Test 1***	***Charpy V-Notch Energy (Joules)Test 2***
C		
Solution Treated	114	69
A	2	2
D	10	3
E	2	4
H	4	2

4.2.3.3 ABRASIVE WEAR TESTS

The specimens of alloys A, D and H with the best combination of yield strength and plastic elongation to failure that were chosen for abrasive wear tests are tabulated in table 4.2.6 together with the Vickers hardness for each specimen. Abrasive wear tests were also performed on alloy E after ageing for two hours, since this alloy showed exceptionally high yield strength and an elongation to failure comparable to the specimens selected from the heat treatments on alloys A, D and H. The results of abrasive wear tests on Alloy C in the solution treated condition were included for comparative purposes.

Table 4.2.6 Specimens selected for abrasive wear tests together with the Vickers hardness of each specimen.

Alloy	**Ageing Treatment at 1100°C (hours)**	**Vickers Hardness**
A	2	325
	5	338
D	0.5	359
	2	328
H	2	333
	5	305
C	2	287
E	2	372

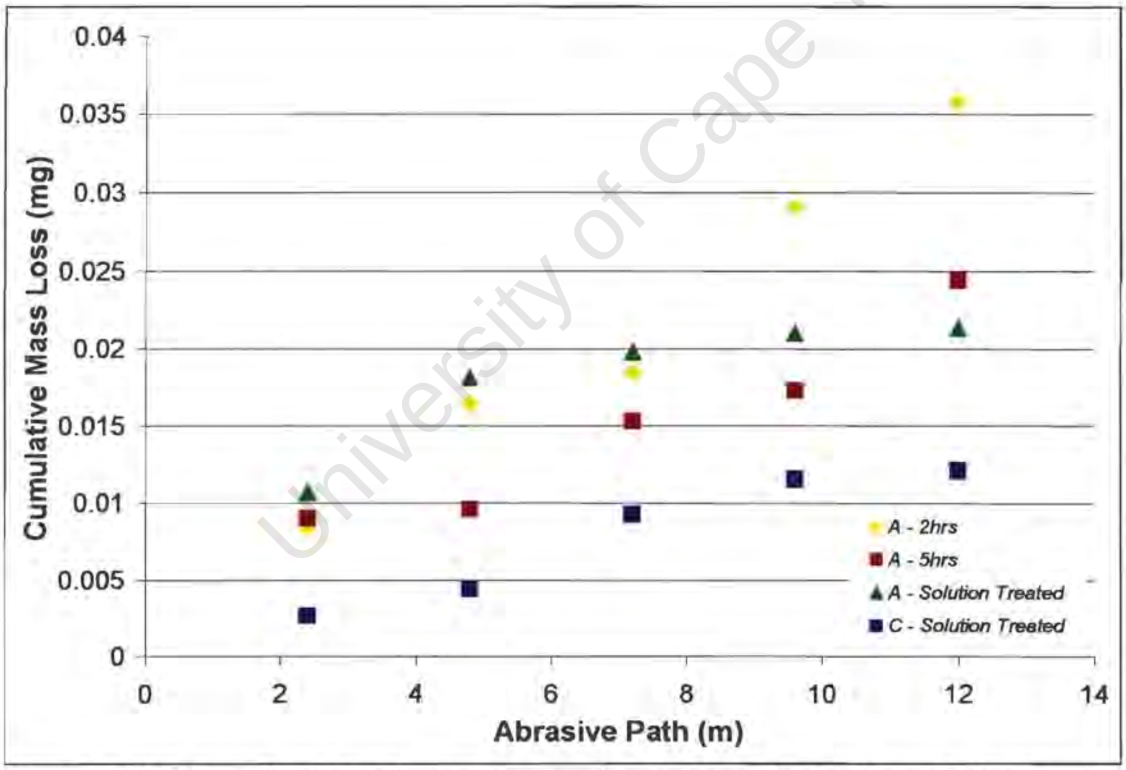

Fig. 4.2.28 (a) The results of abrasive wear tests on alloy A after ageing for 2hrs and 5hrs, together with alloy A and C in the solution treated condition for comparative purposes.

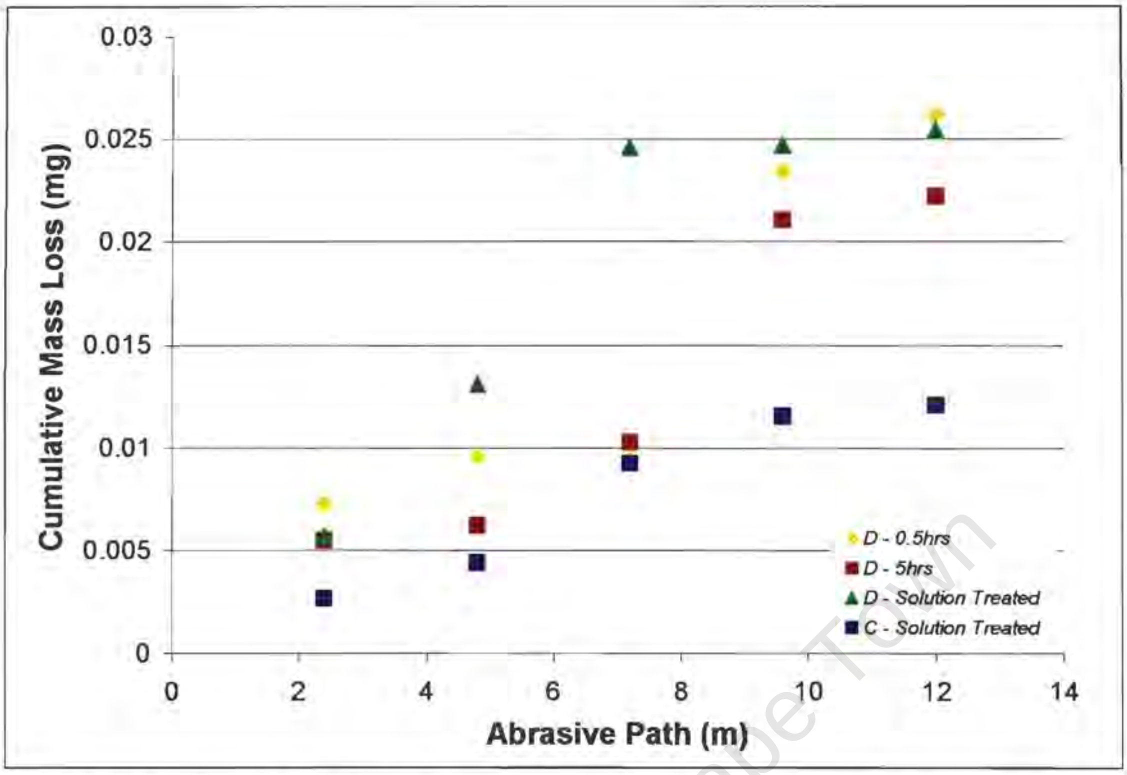

Fig. 4.2.28 (b) The results of abrasive wear tests on alloy D after ageing for 0.5hrs and 5hrs, together with alloys A and C in the solution treated condition for comparative purposes.

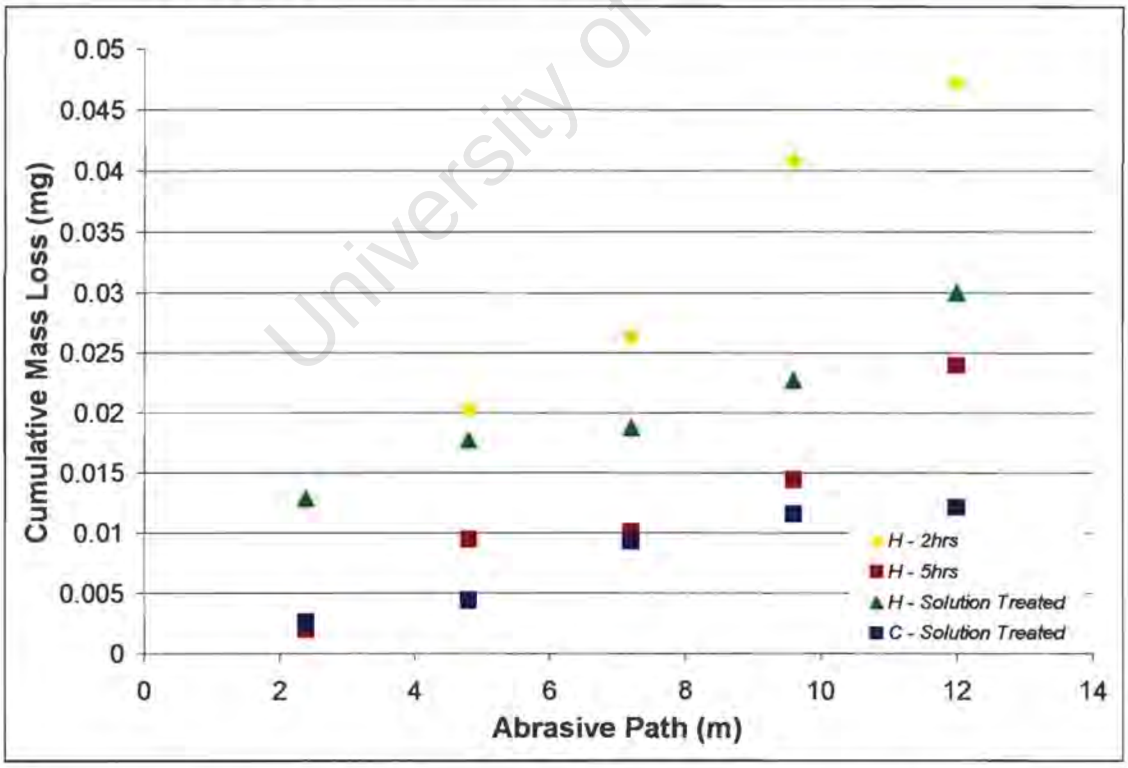

Fig. 4.2.28 (c) The results of abrasive wear tests on alloy H after ageing for 2hrs and 5hrs, together with alloys A and C in the solution treated condition for comparative purposes.

The results of wear tests on alloy A are shown in figure 4.2.28 (a) and show that the wear resistance of each of the specimens of alloy A is inferior to alloy C in the solution treated condition. Ageing for two hours at 1100°C shows the poorest abrasive wear performance of all four specimens shown on the graph. Ageing of alloy A for 5 hours results in better wear resistance over the abrasive path length tested than after ageing for 2 hours. Further, the results show that the wear resistance of alloy A aged for 5 hours decreases in comparison to alloy A in the solution treated condition after extended abrasion.

The abrasive wear resistance of specimens of alloy D, after ageing treatments for 0.5 and 5 hours and in the solution treated condition also show poorer wear performance than the solution treated specimen of alloy C, as illustrated in figure 4.2.28 (b). Ageing alloy D for 5 hours results in an improvement in the wear resistance of the alloy compared to the same alloy in the solution treated condition. In contrast, the wear resistance after ageing for 0.5 hours is inferior to the wear resistance in the solution treated condition. Figure 4.2.28 (c) shows the abrasive wear test results for the selected specimens of alloy H together with alloy C. The wear resistance of alloy H is improved by ageing at 1100°C for 5 hours, compared to the same alloy in the solution treated condition. Further, the wear resistance of alloy H after ageing for two hours shows the poorest wear performance of all the specimens represented in the graph. Once again, none of the specimens of alloy H show superior wear performance to alloy C in the solution treated condition.

In spite of the superior tensile properties of alloy E after ageing for two hours at 1100°C, this alloy shows significantly poorer wear resistance than either alloy C or alloy E in the solution treated condition. Figure 4.2.29 shows the abrasive wear results of these three specimens.

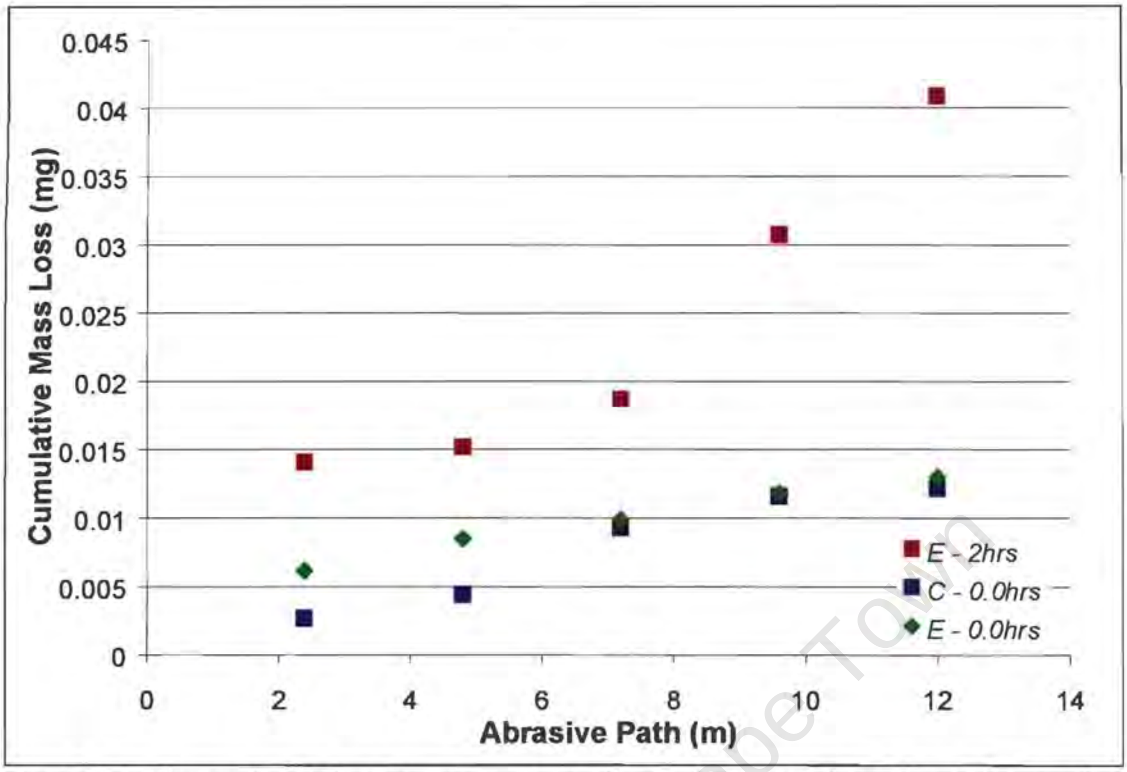

Fig. 4.2.29 The results of abrasive wear tests on alloy E after ageing for 0.0hrs, 2 hrs together with alloy C in the solution treated condition for comparative purposes.

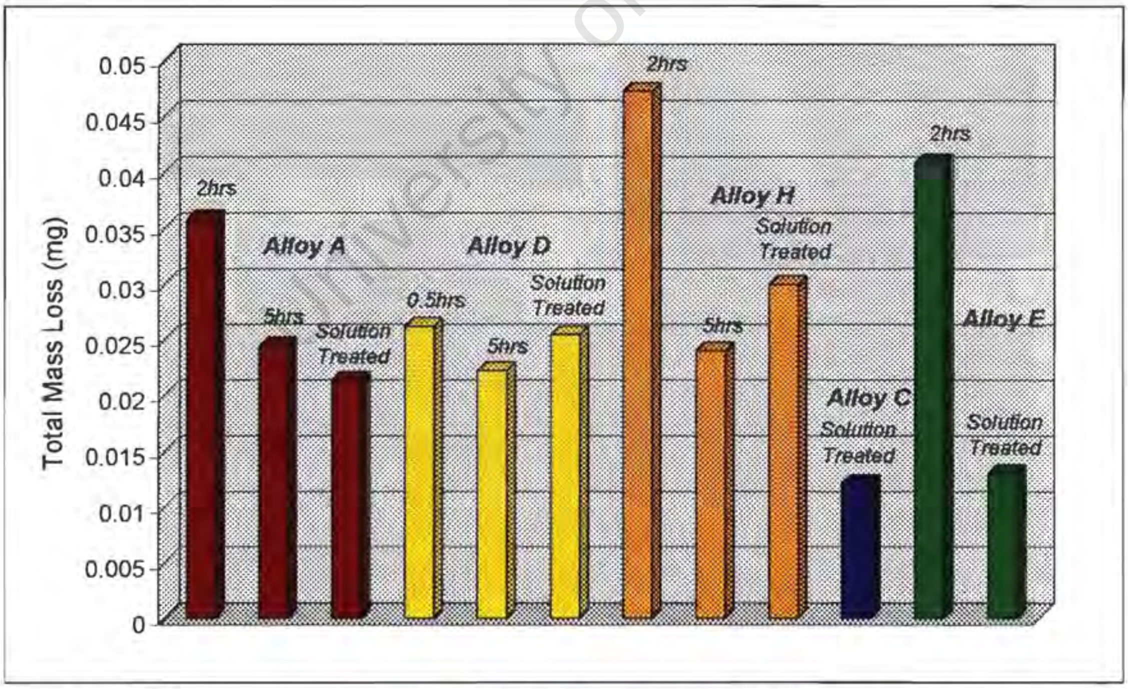

Fig. 4.2.30 Chart showing the results of abrasive wear tests of all the specimens tested after solution treating and after ageing at 1100 ℃ for various times, showing the differences in total mass loss for each specimen represented.

The cumulative mass loss for each of the specimens tested after an abrasive path of 12 m is shown in figure 4.2.30. This chart compares the overall wear performance of all of the specimens tested after ageing at 1100°C, together with the respective alloys in the solution treated condition. The results for alloys D and H aged for 5 hours show better wear resistance than the solution treated counterpart. The decrease in wear resistance of alloy A after ageing for 5 hours compared to the solution treated condition is less than 2 hour aged condition. The wear performance of alloy E after ageing at 1100°C for 2 hours was inferior to all of the other alloys, except for alloy H after ageing for two hours. Thus the improved tensile strength of alloy E as a consequence of ageing at 1100°C for two hours did not improve the wear performance of the steel. None of the specimens represented on the chart showed better wear performance as a consequence of precipitate formation when compared to alloy C in the solution treated condition.

4.2.4 SUMMARY: AGEING TREATMENTS AT 1100°C

The results of ageing treatments at 1100°C show that the type of precipitation reaction that occurs at this temperature is dependent on the niobium and vanadium balance in the alloy. No precipitation is observed in alloy C after ageing at 1100°C, thus any precipitation reaction at this temperature is the result of niobium and vanadium additions. MX precipitates are observed in alloy D, as a result of niobium additions, whereas M_2X precipitates are observed in alloy E as a result of vanadium additions. Combined additions result in either the formation of MX precipitates or M_2X precipitates. M_2X precipitation is observed in alloys B, F and G, while MX precipitates are observed in alloys A, D and H. The M_2X precipitate that forms in alloys B, E, F and G is typical of chromium nitrides that form in high nitrogen steels but is rich in both chromium and vanadium. These precipitates have formed discontinuously during the initial stages of precipitate formation, but after extended exposure at 1100°C, the precipitation mode changes from discontinuous to continuous.

The experimental results can be summarised with the aid of figure 4.2.31, which shows a map of the phase stability observed for the eight alloys. The tie lines that have been drawn in red are simply estimates based on experimental observations, as are the red labels for the phase fields bounded by the tie lines. The positions of the tie lines by no means suggest absolute positions for these tie lines. Figure 4.2.31 simply serves to map out the precipitation reactions that are observed in the eight high nitrogen steel alloys on ageing at 1100°C.

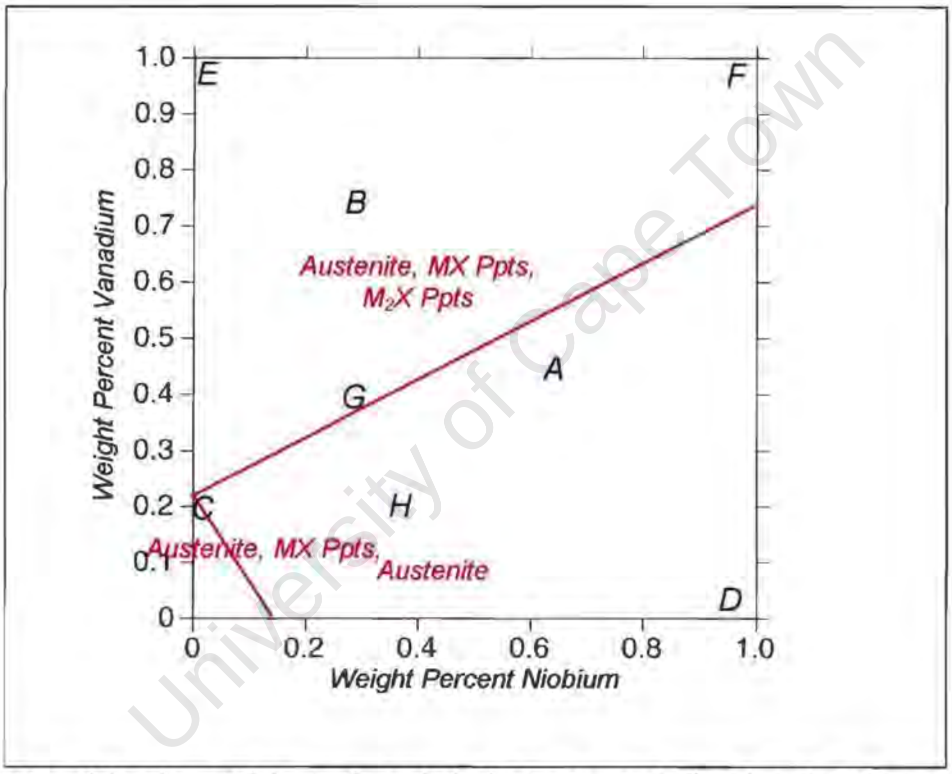

Fig. 4.2.31 Map of the phase stability in the eight high nitrogen steel alloys based on the experimental results.

M_2X precipitates and MX precipitates affect the mechanical properties differently. MX precipitates have resulted in some strengthening, and it has been shown that the degree of strengthening is dependent on ageing time for all three alloys A, D and H. M_2X precipitation has also resulted in strengthening, as observed in alloy E. The wear performance of alloy E was however the poorest of all the alloys. The formation of MX precipitates shows some potential for improved wear performance.

4.3 AGEING TREATMENTS AT 1000°C

All eight alloys were first solution treated as described in section 4.1 and then aged at 1000°C for various times and water quenched. Discontinuous cellular precipitation of lamellae, similar to that observed at 1100°C, was common to all of the alloys, except alloy D after ageing treatments at this temperature. The purpose of an investigation of the microstructural evolution in the eight high nitrogen steel alloys at 1000°C is to characterise the influence of niobium and vanadium additions on the discontinuous cellular precipitation reaction. An investigation of the nucleation and growth characteristics of discontinuous cellular precipitation in the current system is discussed. Finally, the influence of this form of precipitation on the mechanical properties is evaluated.

4.3.1 ISOPLETH DIAGRAM

The isopleth diagram generated by Thermocalc for a base composition of Fe-24 wt%Cr-18 wt%Mn-1 wt%N-0.1 wt%C- 0.5 wt%Si at 1000°C is shown in figure 4.3.1. The diagram maps out the phase stability expected for the system at 1000°C as a function of niobium and vanadium content. Thermocalc predicts that alloy C (the base composition) should contain austenite and M_2X precipitates at 1000°C. Thermocalc predicts that the addition of niobium and vanadium causes MX precipitates to be stable in alloys A, B, E, F, G and H at 1000°C together with M_2X precipitates, austenite and ferrite. Different behaviour is predicted for alloy D: no M_2X precipitation is predicted to form in alloy D, but only MX precipitates together with austenite and ferrite. Examination of the change in phase stability along the niobium and vanadium axes of the isopleth diagram reveals the predicted influence of niobium and vanadium on the different precipitate phases observed at this temperature. Increased levels of niobium to the base composition are predicted to suppress the M_2X precipitate phase and at levels greater than 0.3 wt% only MX precipitates are predicted to occur. As the vanadium levels are increased in the base composition, the M_2X phase remains stable and MX precipitates become stable at levels greater than 0.4 wt% together with the M_2X precipitate phase.

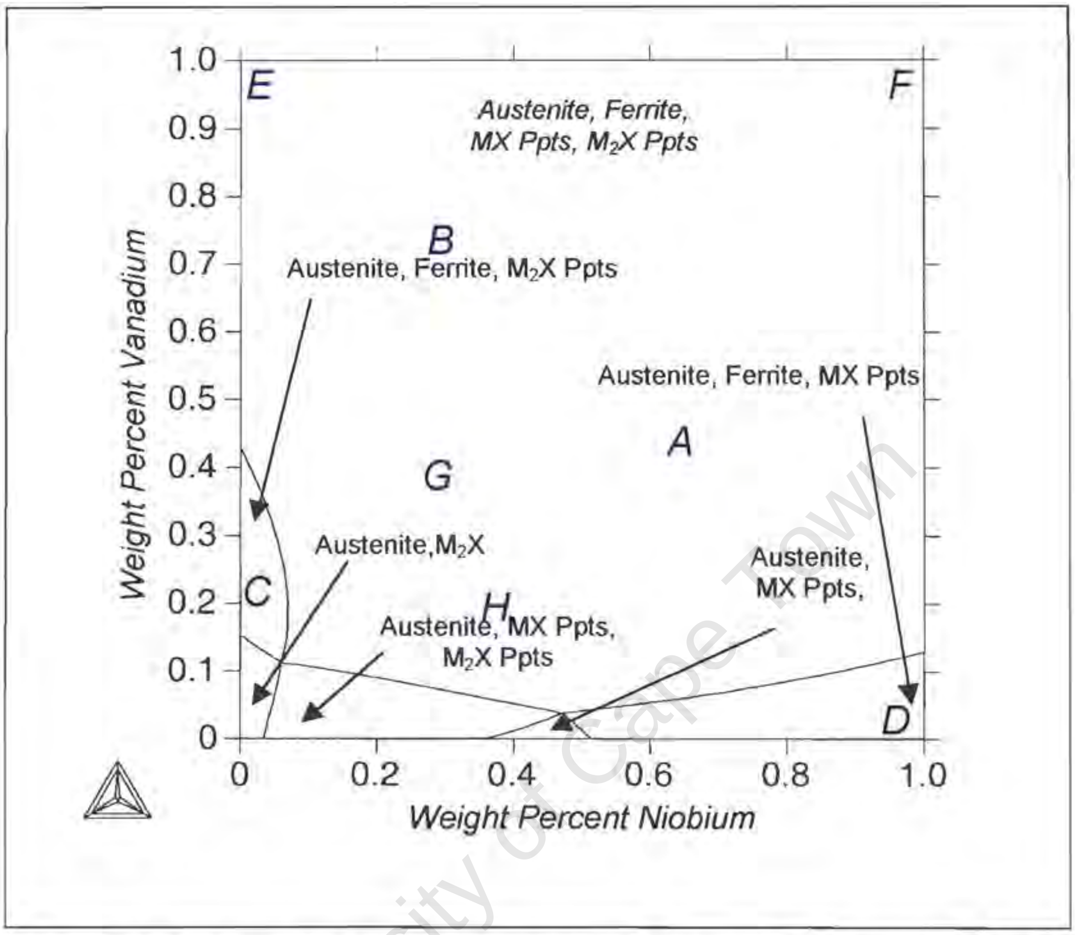

Fig. 4.3.1 Isopleth diagram for the high nitrogen steel alloys at 1000 °C, showing the phase balance in each of the eight alloys as a function of niobium and vanadium level.

4.3.2 PHASE IDENTIFICATION

4.3.2.1 METALLOGRAPHY

Figures 4.3.2 (a) to (n) show the results of two hour ageing treatments at 1000°C on all of the eight alloys. Discontinuous cellular precipitation of lamellar precipitates was observed in alloy C, shown in figure 4.3.2 (a). The individual lamellae are resolved in figure 4.3.2 (b) together with the migration front associated with the discontinuous cellular reaction. The lamellae have nucleated on the grain boundary and grown into the grain behind the migration front, with the interlamellar spacing decreasing with increased growth. A significantly greater volume fraction of lamellar precipitation was observed in alloy E after the same ageing treatment, as shown in figures 4.3.2 (c) and (d). The characteristic growth front can be observed, but the interlamellar spacing is finer than in alloy C.

Combined additions of niobium and vanadium to the base composition influenced the volume fraction of lamellar precipitates in these alloys. The effect of a 1 wt% addition of niobium together with a 1 wt% vanadium addition on the microstructure is illustrated by the result of ageing treatments at 1000°C on alloy F, in figures 4.3.2 (i) and (j). A lower volume fraction of discontinuous precipitation is observed in this alloy than in alloy C and the lamellae have grown round the large blocky precipitates that were present in the solution treated condition (figure 4.3.2 (j)). Similar observations were made in alloys A, B, G and H (figures 4.3.2 (e)-(h) & (k)-(n)) which contain niobium and vanadium additions. Lower volume fractions of lamellar precipitation occurred in these alloys after two hour ageing treatments at 1000°C than in alloy C. The characteristic migration front and evidence that the lamellae nucleated from the grain boundaries were observed in each case.

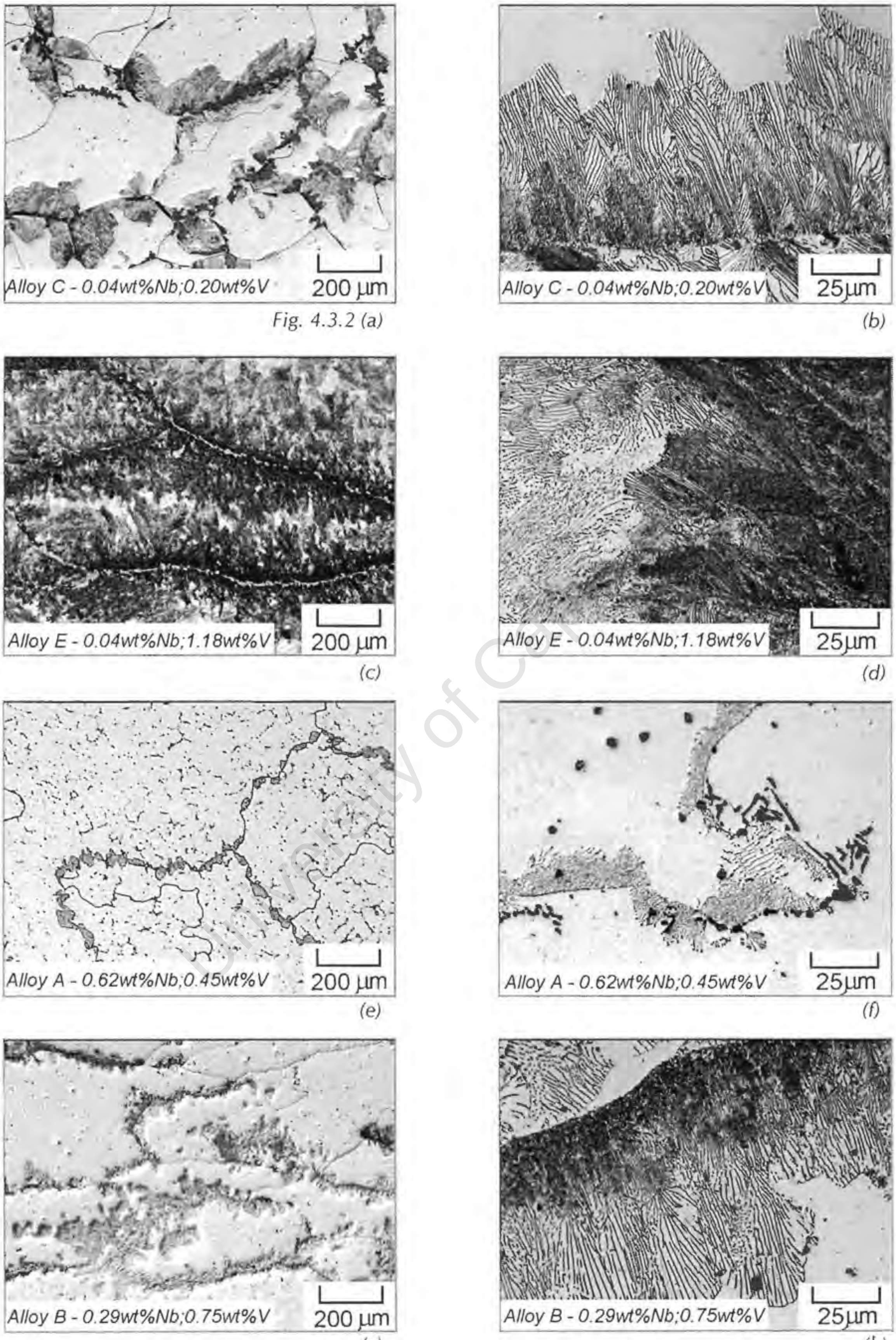

Fig. 4.3.2 (a)

(b)

(c)

(d)

(e)

(f)

(g)

(h)

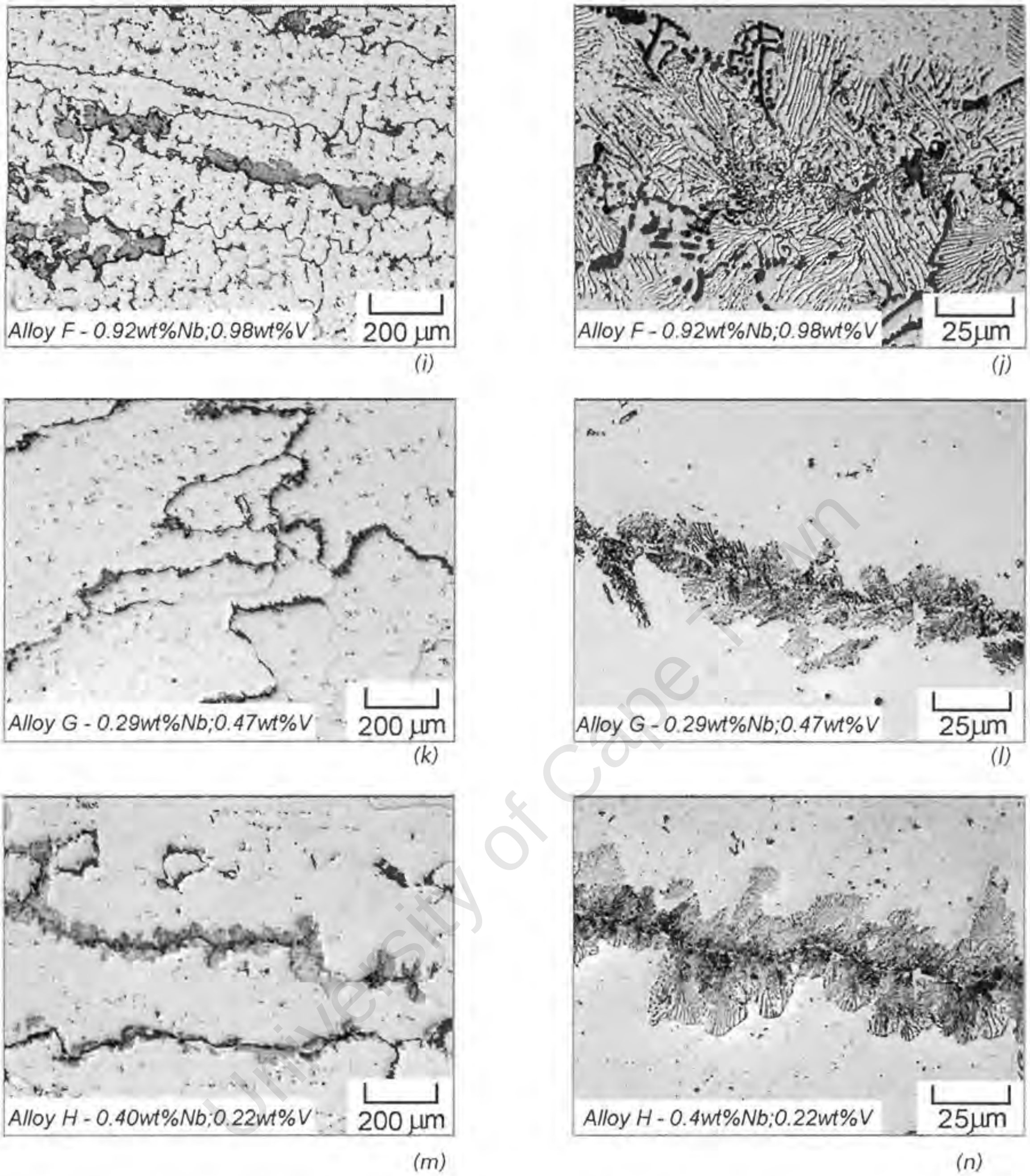

Fig. 4.3.2 (a)-(n) Alloys C, E, A, B, F, G & H after ageing at 1000°C for two hours, showing that discontinuous cellular precipitation is observed all these alloy and that the volume fraction is greatest in alloy E, followed by alloy C and then alloys A, B, F, G and H.

The influence of niobium addition on the microstructure of the high nitrogen steel alloys after ageing at 1000°C is shown in figures 4.3.3 (a) and (b). No lamellar precipitates are observed in alloy D, where instead fine spheroidal precipitates have formed and are better imaged in the TEM. Ferrite islands are observed in alloy D in the austenite and there is evidence the ferrite islands decomposed during ageing at 1000°C. Figure 4.3.4 shows a TEM micrograph of fine spheroidal precipitates that have formed both on the grain boundary and within the grain in alloy D after ageing for two hours at 1000°C.

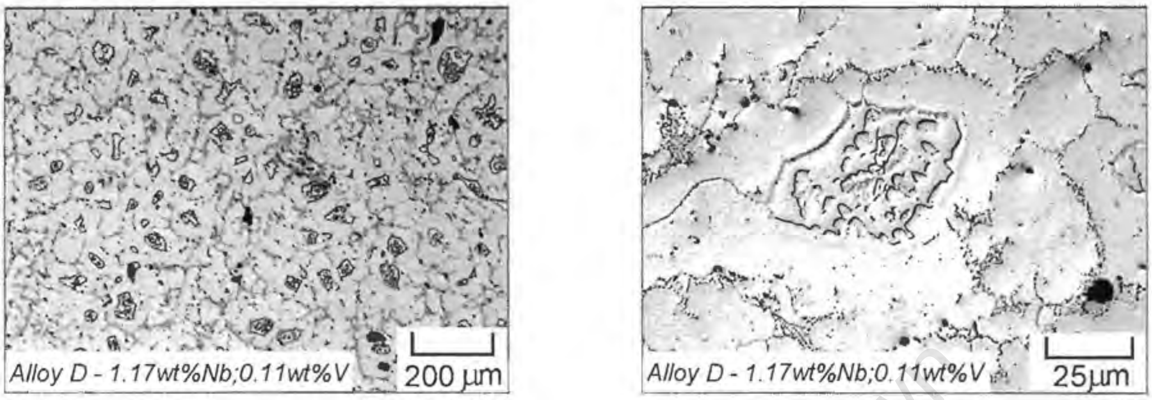

Fig. 4.3.3 (a) *(b)*

Fig. 4.3.3 (a) & (b) The microstructure of alloy D after ageing for two hours at 1000°C showing the absence of lamellar precipitates and the decomposition of ferrite which occurred during ageing.

Fig. 4.3.4

Fig. 4.3.4 TEM micrograph of alloy D after ageing for two hours at 1000°C showing the fine spheroidal precipitates that have nucleated on the grain boundary and within the grains.

In order to establish whether or not discontinuous cellular precipitation would form in alloy D after extended ageing at 1000°C, alloy D was aged for 5, 10 and 100 hours at this temperature. After the 100 hour ageing treatment, no lamellar precipitation was observed and the fine precipitates observed after two hours of ageing had simply grown as shown in figure 4.3.5.

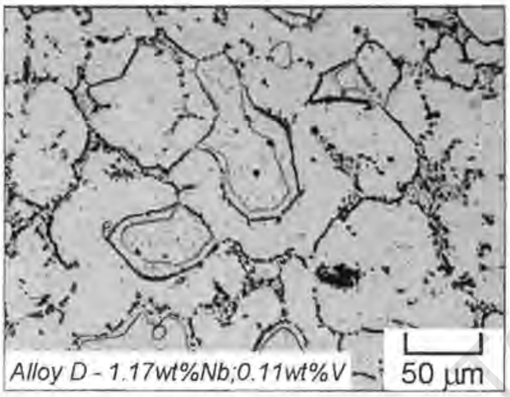

Fig 4.3.5 The microstructure of alloy D after ageing for 100 hours at 1000℃ showing the absence of lamellar precipitates and exaggerated precipitation of fine precipitates in the austenite and on the austenite/ferrite boundaries.

The other seven alloys were also aged for longer times to determine the effect of prolonged ageing on the nature of the discontinuous cellular reaction. During prolonged ageing of alloys A, B, F, G and H at 1000°C, the discontinuous cellular precipitation of lamellae stopped and plate-like precipitates formed continuously in the untransformed matrix as shown in figures 4.3.6 (a)-(e). In alloys B, F and G, the discontinuous reaction stopped between 5 and 10 hours, whereas in alloys A and H the reaction stopped between 10 and 100 hours.

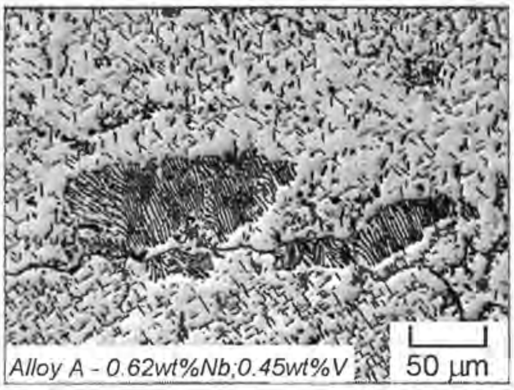

Fig. 4.3.6 (a)

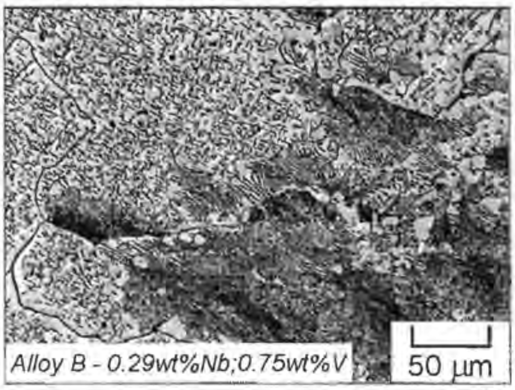

(b)

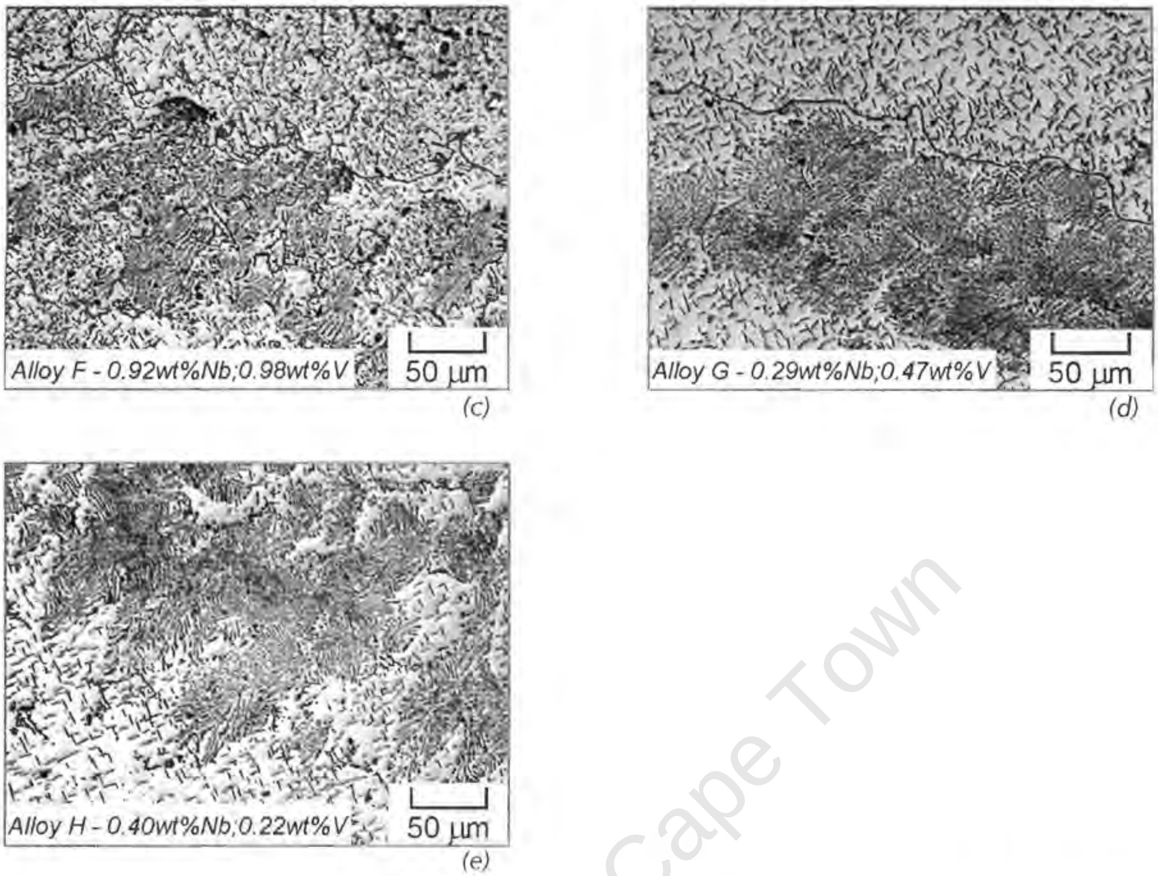

Fig. 4.3.6 (a)-(e) Alloys A, B, F, G & H after ageing at 1000℃ for 100 hours showing the presence of both lamellar precipitates and continuous precipitates that have a plate-like structure.

In contrast to alloys A, B, F G and H, the discontinuous cellular precipitation reaction did not stop in alloys C and E, even after 100 hours of ageing at 1000°C. This was evidenced by the formation of new precipitate cells with a wider interlamellar spacing in the original precipitate cell; the new cells nucleated and grew on the original precipitate cell boundaries. The results of 100 hour ageing treatments on alloys C and E are shown in figures 4.3.7 (a) and (b). The re-nucleation of new precipitate cells during prolonged ageing is more prolific in alloy E than in alloy C.

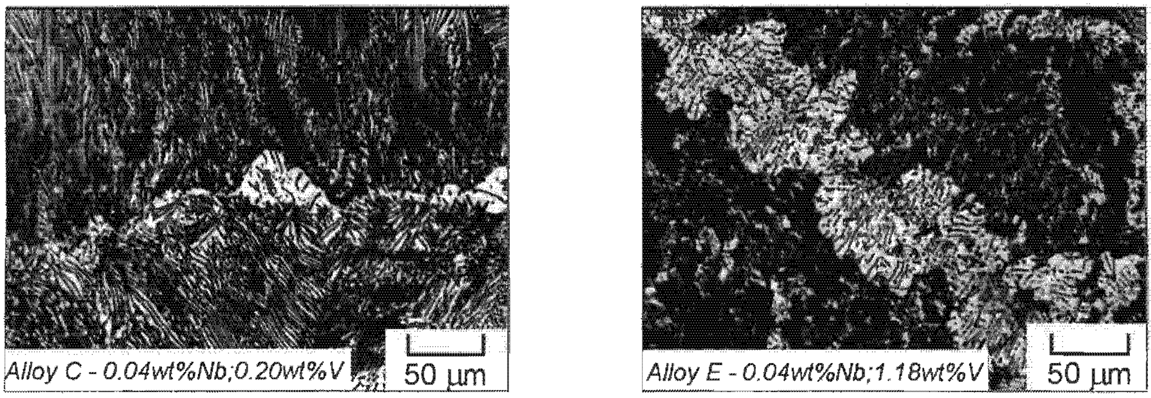

Fig. 4.3.7 (a) *(b)*

Fig.4.3.7 (a) & (b) Alloys C and E respectively after ageing for 100 hours at 1000℃, showing the formation of new precipitate cells, at the boundaries of the old cells, and that the precipitates within the cells have a greater interlamellar spacing than in the original precipitate cells.

The lamellae that formed after ageing for two hours in alloys C, E and B were imaged in the TEM, together with the plate-like precipitates that formed continuously in alloy B after further ageing at 1000°C. These microstructural features are shown in figures 4.3.8 (a)-(d). The lamellae in alloys C and E have a more uniform nature than those in alloy B, which are frequently broken and particulate in nature, similar to the lamellae that formed at 1100°C in the same alloy (figure 4.2.3 (b)). The plate-like precipitates in alloy B are more prolific after ageing at 1000°C than after the 1100°C treatment.

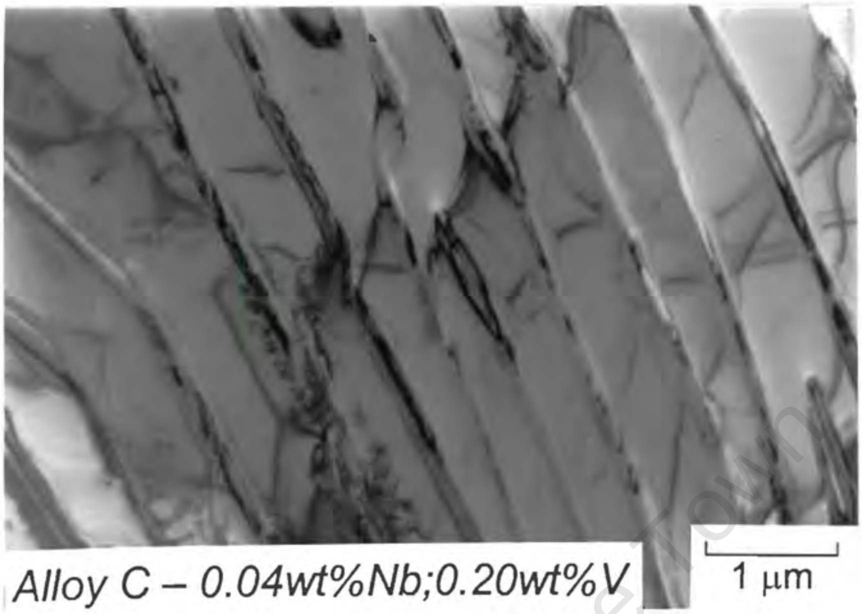

Fig. 4.3.8 (a)

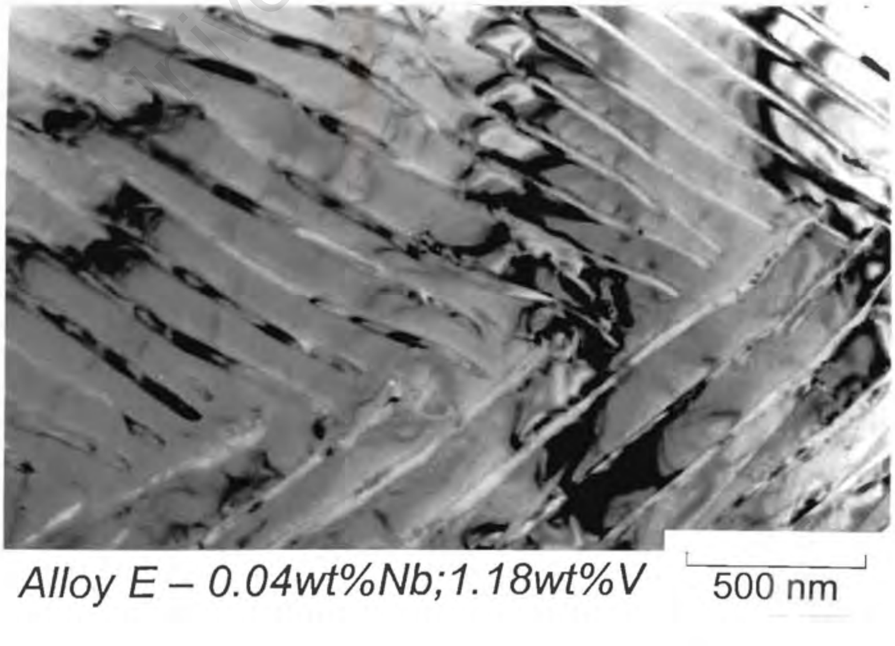

(b)

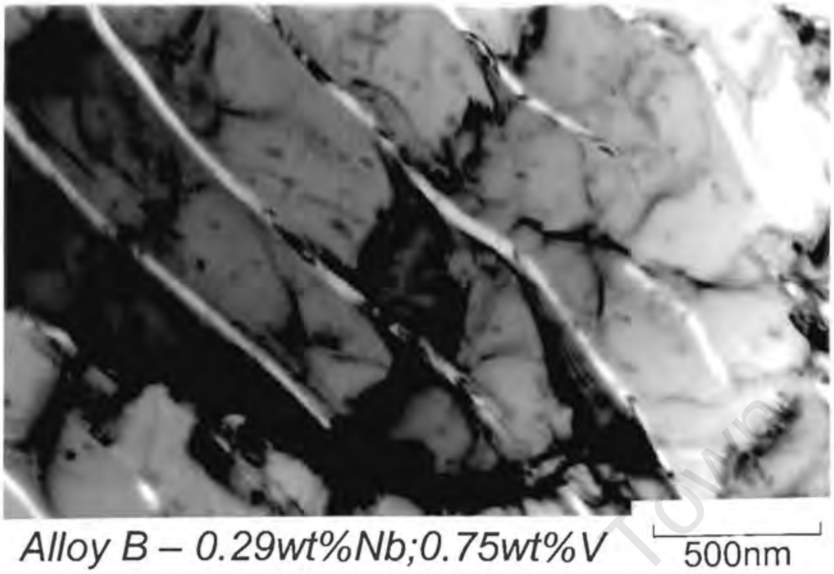

(c)

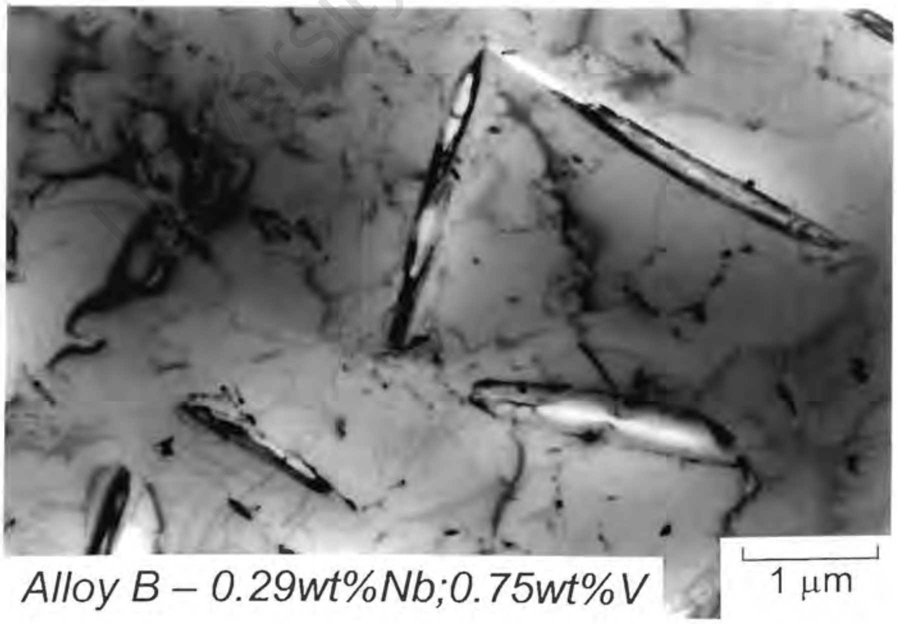

(d)

Fig. 4.3.8 TEM micrographs of alloys C, E and B, showing (a) and (b), the discontinuous lamellar precipitates in alloys C and E respectively and (c) the discontinuous lamellar precipitates in alloy B, (d) the continuous plate-like precipitates in alloy B

4.3.2.2 COMPOSITIONAL AND CRYSTALLOGRAPHIC ANALYSIS

Compositional analysis and electron diffraction studies of the lamellar precipitates in alloy C and E were conducted to determine the identity of the precipitates. The results from alloy E were compared with alloy C to determine the influence of vanadium on the composition and crystallography of the lamellar precipitates in this alloy system. The same analysis was completed on alloy B to determine the effect of both niobium and vanadium additions on the characteristics of the precipitates. Further, the plate-like precipitates in alloy B were also identified in the same way to determine if they had the same composition and crystal structure as the lamellae in alloy B.

Figure 4.3.9 (a) shows a backscattered electron image of the lamellar precipitates in alloy C and the x-ray maps that follow in figures 4.3.9 (b) and (c) show that the lamellae are rich in chromium and depleted in iron. Likewise, the lamellae in alloy E are rich in chromium and are depleted in iron, but are also rich in vanadium. These maps are shown in figures 4.3.10 (b)-(d), together with the backscattered image of the precipitate lamellae in figure 4.3.10 (a).

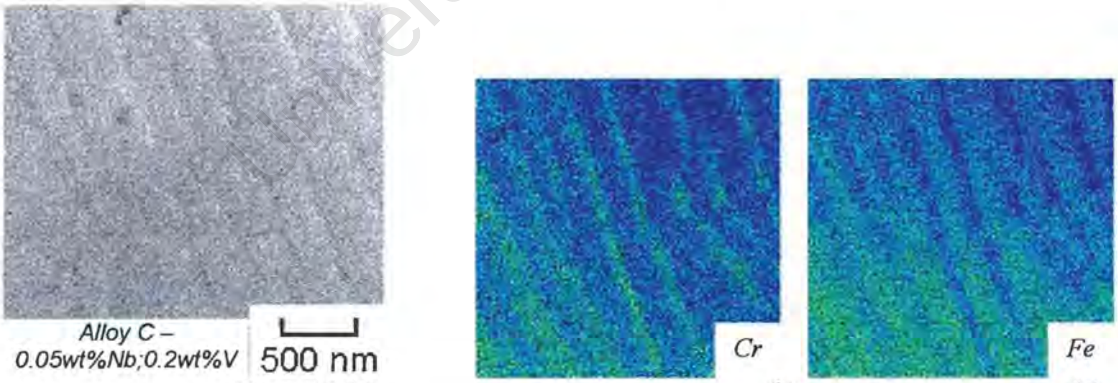

Fig. 4.3.9 (a) (b) (c)

Fig. 4.3.9 (a) SEM (backscattered electron) image of the lamellar precipitates in alloy C after ageing at 1000 °C for two hours, showing the field of view form which the x-ray maps were taken, together with the x-ray maps for (b) chromium and (c) iron, showing that the lamellae are rich in chromium, but depleted in iron.

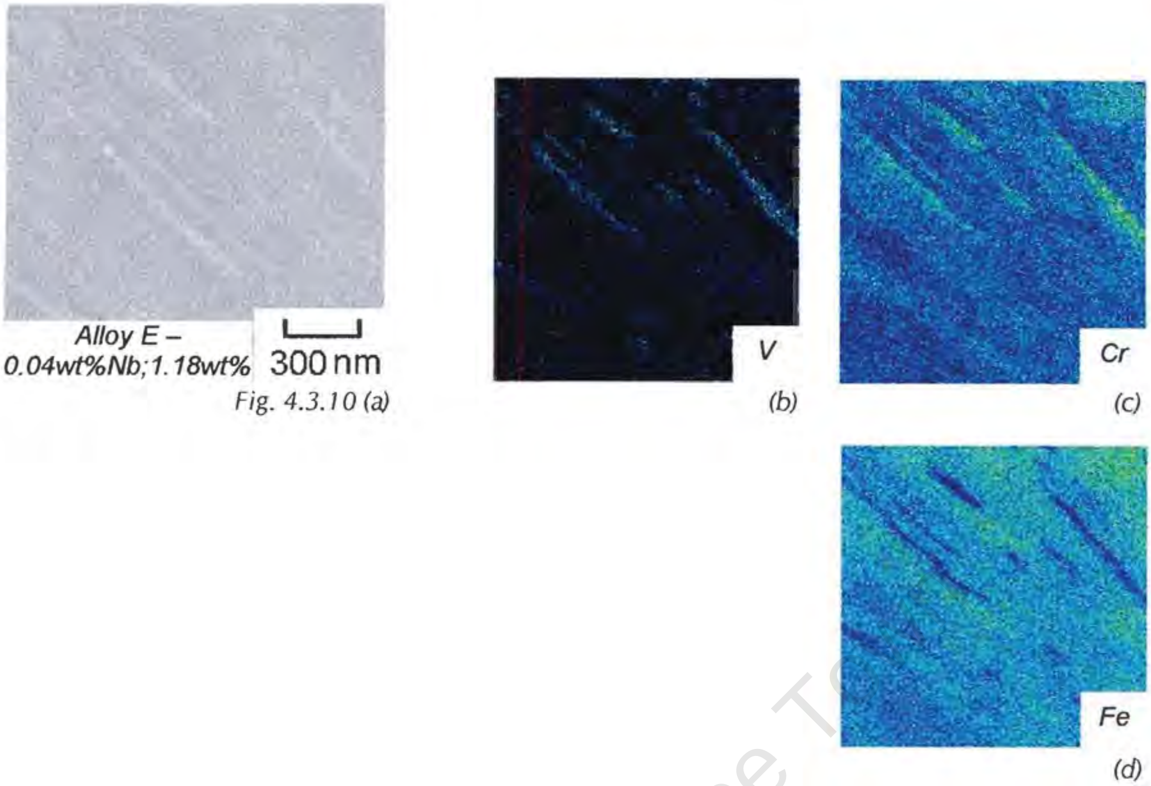

Fig. 4.3.10 (a) (b) (c) (d)

Fig. 4.3.10 (a) SEM (backscattered electron) image of the lamellar precipitates in alloy E after ageing at 1000 °C for two hours, showing the field of view from which the maps were taken together with the x-ray maps for (b) vanadium, (c) chromium and (d) iron, showing that the lamellae are rich in vanadium and chromium, but depleted in iron.

The x-ray maps taken from a lamellar colony in alloy B also show that these precipitates are rich in vanadium and chromium and depleted in iron. Figure 4.3.10 (a) shows the backscattered electron image of the lamellar colony together with the maps for chromium, vanadium and iron. The same analysis was completed on the plate-like precipitates in alloy B, which showed that they have a similar composition to the lamellar precipitates. This is shown in the series of x-ray maps for these precipitates in figures 4.3.11 (b)-(c) together with the backscattered electron image of the plate-like precipitates in figure 4.3.11 (a).

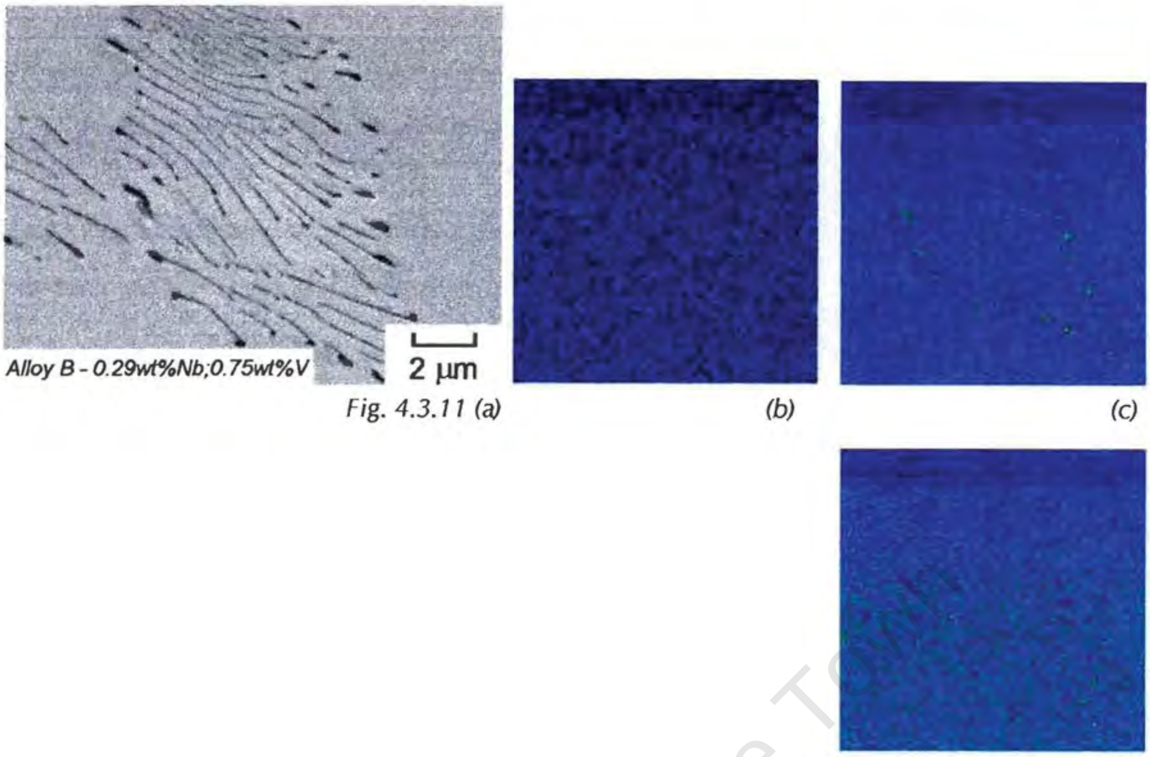

Fig. 4.3.11 (a) *(b)* *(c)*

(d)

Fig. 4.3.11 (a) SEM (backscattered electron) image of the lamellar precipitates in alloy B showing the field of view from which the x-ray maps were taken, together with the x-ray maps for (b) vanadium, (c) chromium and (d) iron, showing that the precipitates are rich in vanadium and chromium and depleted in iron.

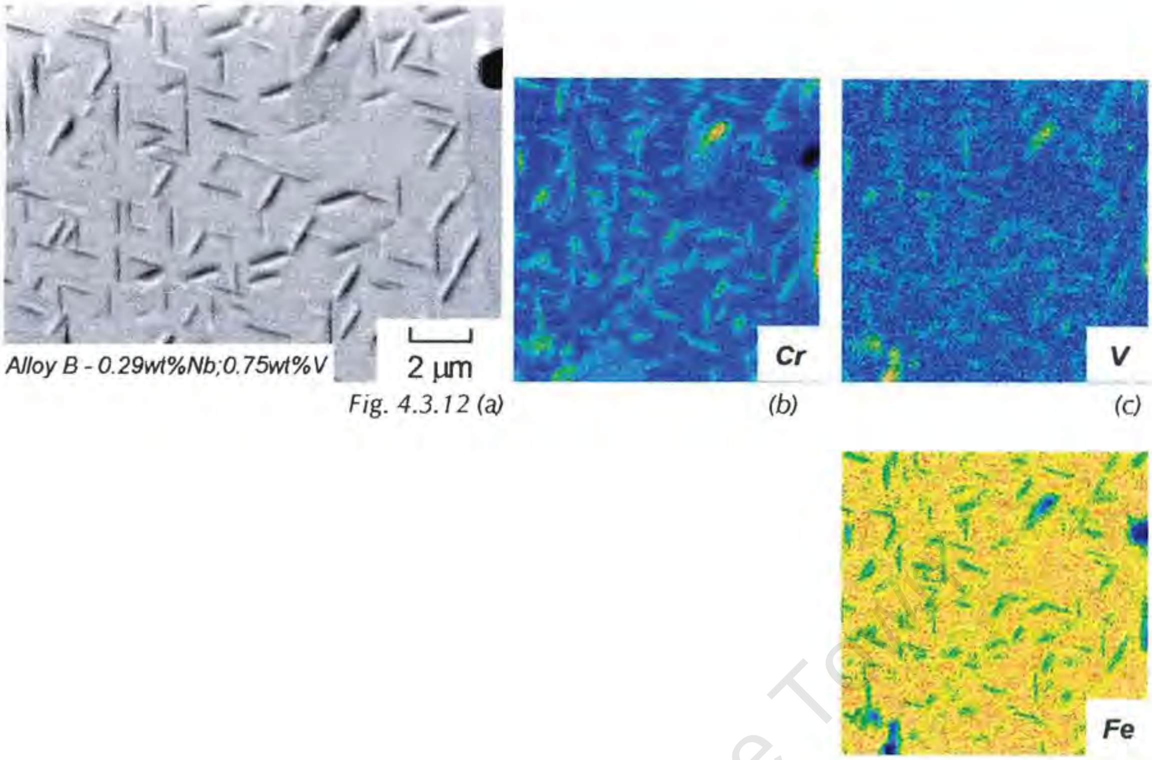

Fig. 4.3.12 (a) (b) (c)

(d)

Fig.4.3.12 (a) SEM (backscattered electron) image of the plate-like precipitates in alloy B after ageing at 1000 ℃ for two hours, showing the field of view from which the x-ray maps were taken together with the x-ray maps for (b) vanadium, (c) chromium and (d) iron, showing that the lamellae are rich in vanadium and chromium, and depleted in iron.

The results from the x-ray maps indicate that the lamellar precipitates in alloys E and B and the plate-like precipitates that formed continuously in alloy B have the same compositional characteristics. Further, it is expected from the morphology of the precipitates, that the lamellae in alloy C are the same type of precipitate as those in alloys E and B. Electron diffraction studies were completed on the four different precipitates represented in the x-ray maps (figures 4.3.9-4.3.12) to determine if they had the same crystal structure, and hence confirm that they are in fact the same precipitate type.

Figure 4.3.13 (a) shows the selected area diffraction (SAD) pattern taken from a region including austenite and a precipitate lamella in alloy C and is representative of the [1-10] austenite zone axis. The extra reflections in this diffraction pattern originate from the precipitate lamella. Similarly, figure 4.3.13 (b) shows the [11-2] austenite zone axis, with extra reflections just inside the matrix spots, which also originate from the precipitate. The [11-2] austenite zone axis pattern also shows extra reflections for the precipitate lamella in alloy C. Figure 4.3.14 (a) shows the [1-10] austenite zone axis pattern taken from a region including a precipitate lamella and the austenite matrix where reflections for both phases can be seen. Figure 4.3.14 (b) shows a CBED pattern for the [1-210] zone axis pattern for the precipitate, when the beam diameter is reduced and focussed onto the specimen. Figure 4.3.14 (c) shows the [11-2] zone axis for the austenite in alloy E and contains extra reflections from the precipitate lamella as well as superlattice reflections similar to those shown in figure 4.2.13 (d).

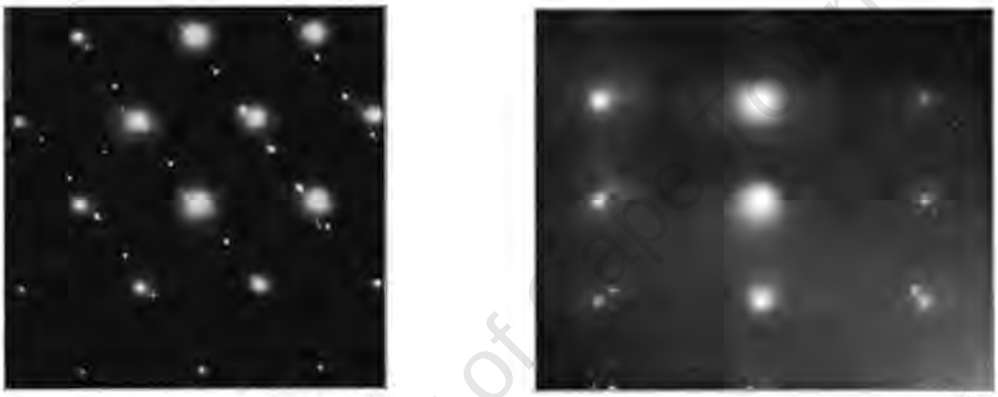

Fig. 4.3.13 (a) *(b)*

*Fig. 4.3.13 SAD patterns taken from the precipitate lamellae in **alloy C (0.04wt%Nb;0.2wt%V)** showing (a) the pattern for the [1-10] austenite zone axis showing extra reflections or the precipitate that correspond to the [1-210] HCP zone axis, (b) the pattern for the [11-2] austenite zone axis showing extra reflections for the precipitate that correspond to the [10-10] zone axis for the HCP system.*

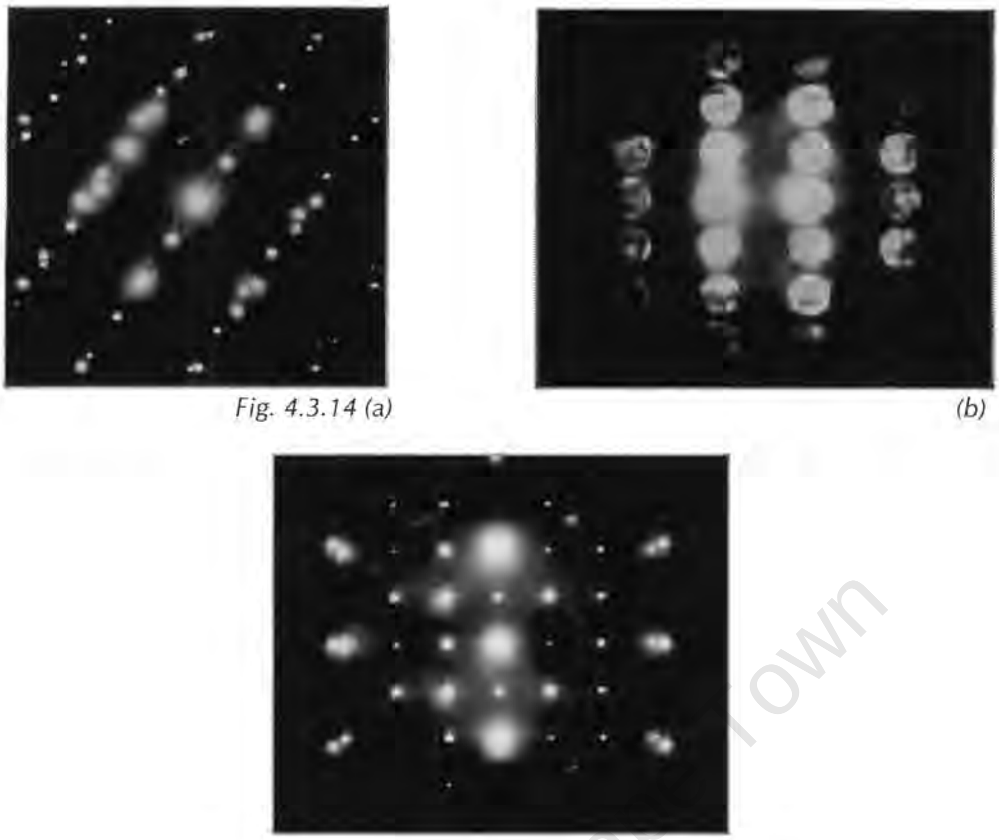

Fig. 4.3.14 (a) (b)

(c)

Fig. 4.3.14 Diffraction patterns taken from the precipitate lamellae in ***alloy E (0.04wt%Nb;1.18wt%V)*** *showing (a) SAD pattern for the [1-10] austenite zone axis, showing extra reflections for the precipitate which correspond to the [1-210] HCP zone axis, (b) CBED pattern taken directly from the precipitate showing reflection for the [1-210] zone axis for the HCP system, (c) SAD pattern for the [11-2] austenite zone axis showing extra reflections that correspond to the [10-10] HCP zone axis and superlattice reflections.*

Figures 4.3.15 (a)-(c) show a similar set of diffraction patterns taken from the lamellar colonies in alloy B, and figures 4.3.16 (a)-(c) show the diffraction patterns taken from the plate-like precipitates in alloy B. The sets of diffraction patterns shown in figures 4.3.13-4.3.16 are similar to those that were recorded for the lamellae in alloy E after ageing at 1100°C, and can be indexed in the same way as shown in the schematics in figure 4.2.14 (a) & (b). Thus the analysis that was applied to the diffraction patterns taken from the precipitate lamellae in alloy E after ageing at 1100°C was also applied to the diffraction patterns shown in figures 4.3.13-4.3.16. This analysis shows that the lamellae that formed discontinuously in alloys C and E have an HCP crystal structure with the orientation relationship given below. Likewise the lamellae in alloy B and the continuous precipitates in alloy B also have an HCP crystal structure with the same orientation relationship.

$$(111)\ \gamma//(0001)\ M_2X\ ;\ [1\text{-}10]\ \gamma//[1\text{-}210]\ M_2X$$

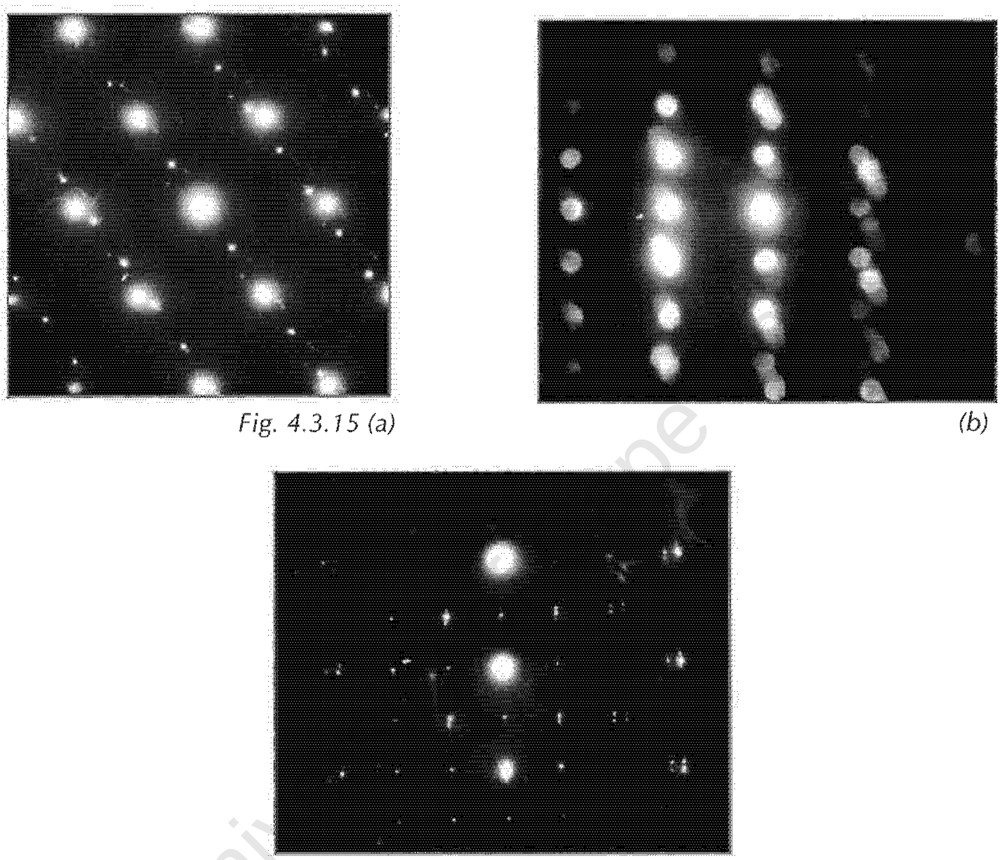

Fig. 4.3.15 (a) *(b)*

(c)

Fig.4.3.15 Diffraction patterns taken from the lamellar precipitates in ***alloy B (0.29wt%Nb;0.75wt%V)*** *showing (a) reflections for the [1-10] austenite zone axis together with extra reflections for the [1-210] HCP system from the precipitate, (b) CBED pattern taken from the precipitate showing the [1-210] HCP zone axis & (c) reflections for the [11-2] austenite zone axis together with extra reflections for the precipitate corresponding to the [10-10] zone axis.*

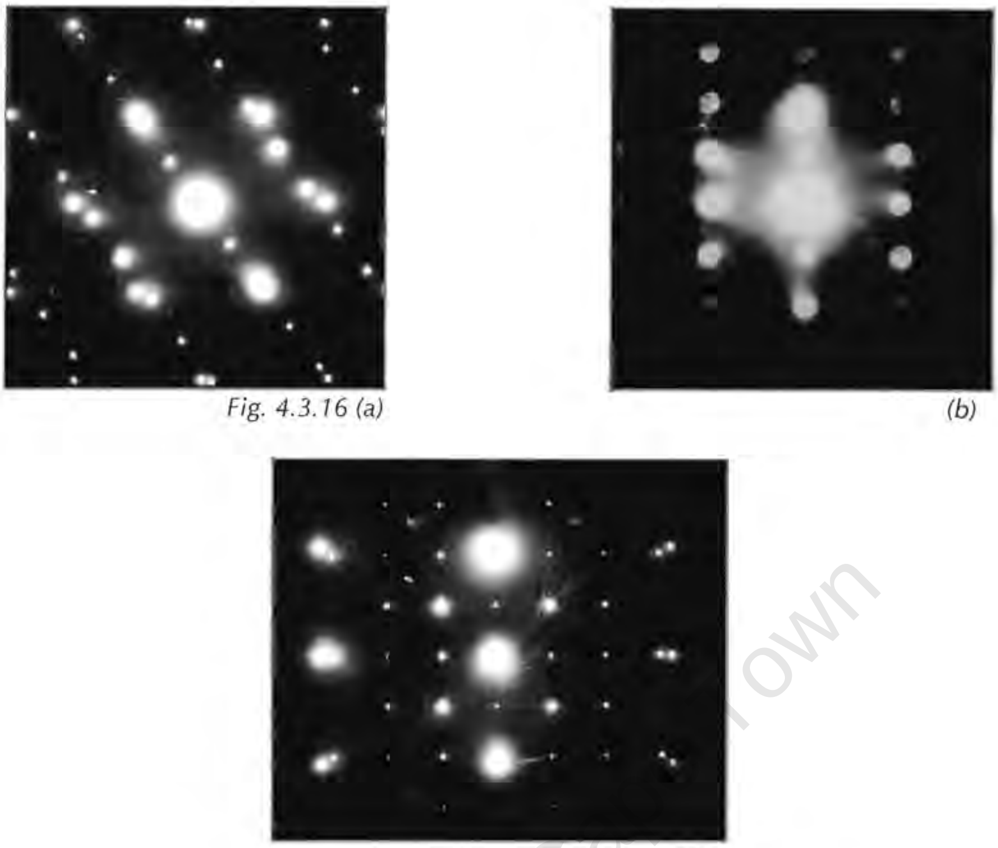

Fig. 4.3.16 (a) (b)

(c)

Fig. 4.3.16 Diffraction patterns taken from the plate-like continuous precipitates in ***alloy B (0.29wt%Nb;0.75wt%V)*** *showing (a) reflections for the [1-10] austenite zone axis together with extra reflections for the [1-210] HCP system from the precipitate, (b) CBED pattern taken from the precipitate showing the [1-210] HCP zone axis & (c) reflections for the [11-2] austenite zone axis together with extra reflections for the precipitate corresponding to the [10-10] zone axis.*

The lattice parameters for the precipitates in alloys C, E and B were also calculated from the zone axis diffraction patterns using the same analysis shown in figures 4.2.14 (a)-(c) and is shown in table 4.3.1. The published values[41] are also given for pure vanadium nitride (V_2N) and chromium nitride (Cr_2N) in table 4.3.1. The lattice parameter values for the precipitates are in good agreement with the published values.

*Table 4.3.1 Lattice parameters for the precipitates in alloy B, C and E after ageing at 1000 °C, together with the published values for Cr_2N and V_2N *after Goldschmidt*

	A (Å)	C (Å)
Chromium Nitride **$(Cr_2N)^*$**	**2.75**	**4.44**
Vanadium Nitride **$(V_2N)^*$**	**2.82**	**4.54**
Alloy C (lamellae) – *[1-210]*	2.63	4.52
Alloy C (lamellae) – *[10-10]*	2.78	4.75
Alloy E (lamellae) – *[1-210]*	2.74	4.40
Alloy E (lamellae) – *[10-10]*	2.84	4.67
Alloy B(lamellae) – *[1-210]*	2.81	4.81
Alloy B(lamellae) – *[10-10]*	2.81	4.52
Alloy B(continuous) – *[1-210]*	2.85	4.62
Alloy B(continuous) – *[10-10]*	2.85	4.62

X-ray maps of the fine precipitates in alloy D show that they are rich in niobium. Comparison with precipitates of a similar morphology that formed in alloy D after ageing at 1100°C shows that the fine precipitates in alloy D after ageing at 1000 °C are also MX precipitates rich in niobium. Figure 4.3.17 (a) shows the backscattered image of these precipitates in alloy D on a grain boundary and figures 4.3.17 (b) and (c) show the x-ray maps for these fine precipitates.

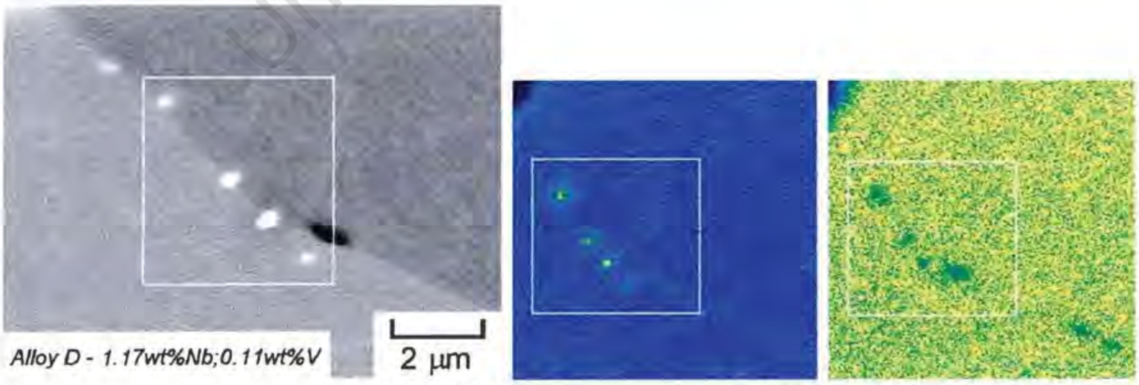

Fig. 4.3.17 (a) *(b)* *(c)*

Fig. 4.3.17 (a) SEM (backscattered electron) image of the fine precipitates that have nucleated on a grain boundary during ageing at 1000 °C, showing the field of view from which the x-ray maps were taken, together with the x-ray maps for (b) niobium and (c) iron showing that the precipitates are rich in niobium and depleted in iron.

There are some differences between the experimental results and the predictions that were made by Thermocalc for the eight alloys at 1000°C. Ferrite was only observed in alloy D, but was predicted in alloys A, B, D, E, F, G and H and the reason for this discrepancy is given in section 3.2.7. M_2X precipitation was observed in all the alloys except alloy D, where instead MX precipitation was observed as predicted by Thermocalc. MX precipitates were predicted to form together with the M_2X phase in alloys A, B, E, F, G and H but were not detected. These precipitates might have been present, but were possibly very fine and therefore not easily detected.

4.3.3 THE NUCLEATION AND GROWTH OF DISCONTINUOUS CELLULAR PRECIPITATION

Electron backscatter diffraction (EBSD) techniques were used to obtain an orientation map of the austenite within the precipitate cells in relation to the surrounding austenite matrix. No attempts were made to index the precipitates themselves since it was the relative orientation of the austenite within the cells and adjacent grains that was of interest. The purpose of orientation mapping was to understand the growth mechanisms of the precipitate colonies. Figure 4.3.18 (a) is an electron-backscattered image of alloy C showing a similar field of view that was selected for orientation mapping. The image shows three features, marked (i), (ii) and (iii) in the image, and will be discussed individually.

The feature marked (i) shows two precipitate colonies, side by side that have originated at the grain boundary. The formation of these two colonies have possibly followed a sequence shown in figure 4.3.18 (b). Before the formation of the discontinuous precipitate cell, precipitates nucleate on the grain boundary, as shown in figure 4.3.18 (b)(1). After some time the boundary begins to bow round the precipitates as shown in figure 4.3.18 (b)(2). As the boundary bows between the precipitates, the grain into which the boundary migrates is consumed by a developing precipitate cell colony. The orientation of the cell colony behind the migrating boundary takes on the orientation of the grain from which it is growing. After further growth, shown in figure 4.3.18 (b)(3), the colonies grow further and begin to impinge on one another, until finally in figure 4.3.18 (b)(4) a so called double seam develops.

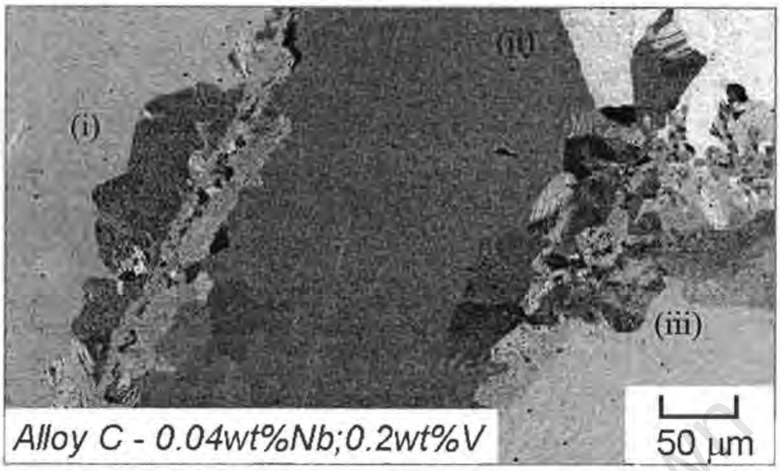

Fig. 4.3.18 (a) Electron backscattered image of the field of view from which the orientation map shown in figure 4.3.18 (c) was acquired.

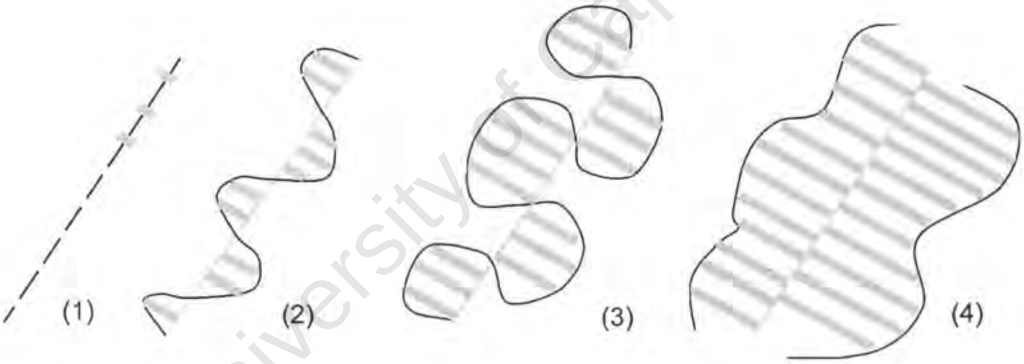

Fig 4.3.18 (b) Schematic diagrams showing the development of the double seam marked (i) in figure 4.3.18 (a).

The schematic diagrams show how the orientation of the austenite within the precipitate cells marked (i) in figure 4.3.18 (a) has developed from the parent grains. Figure 4.3.18 (c) shows the orientation map that was acquired from the field of view shown in figure 4.3.18 (a). The orientation map illustrates different orientations in Euler space in different colours, thus like orientations are represented by the same colour. The relationship between the orientation of the precipitate colonies in (i) and the parent grains either side of the double seam is more clearly seen in the orientation map.

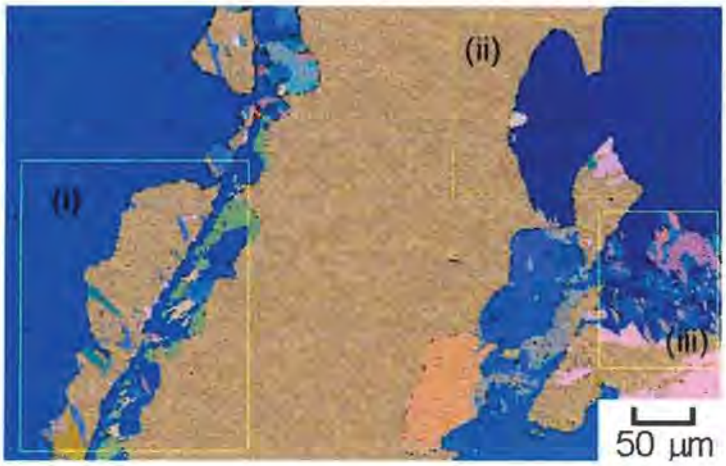

Fig. 4.3.18 (c) Orientation map for a similar field of view in (a) showing the relative orientations of the austenite within the precipitate cells compared to the parent grains.

The feature marked (ii) in figure 4.3.18 (a) can be seen more clearly in figure 4.3.18 (c). The possible evolution of this feature is shown in the series of schematics in figure 4.3.18 (d). Before the development of the precipitate cell colony, precipitates nucleate on the grain boundary (figure 4.3.18 (d)(1)). After some time the boundary bows out into the grain in the left hand side and the austenite in the precipitate colony takes on the orientation of the grain on the right hand side (figures 4.3.18 (d)(2) & (3)). Thus the precipitate colony takes on the orientation of the grain from which it is growing. This effect is more clearly shown in the orientation map in figure 4.3.18 (c), where the austenite in the precipitate colony is coloured dark blue, the same as the grain from which the colony originated.

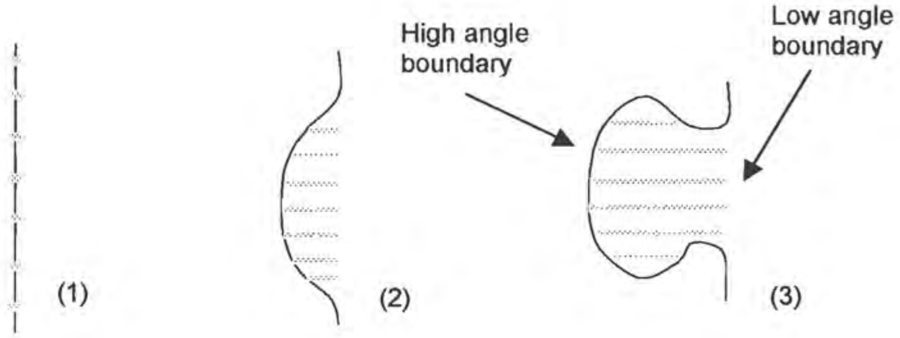

Fig. 4.3.18 (d) Schematic showing the evolution of the feature marked (ii) in figures 4.3.18 (a) and (c)

TEM studies of a similar precipitate colony show that the position where nucleation of the grain boundary precipitates occurred, marked by the arrow in figure 4.3.18 (d)(3) is decorated by a series of dislocations and is shown in figure 4.3.19 (a). Misorientation measurements across this boundary show that the dislocations mark a low angle grain boundary. The opposite side of the precipitate colony in figure 4.3.19 (a) was also imaged in the TEM and is shown in figure 4.3.19 (b). This micrograph shows that the precipitates grow behind a high angle grain boundary. This was confirmed by misorientation measurements across the boundary marked by the arrow on the left hand side in figure 4.3.18 (d)(3). These results show that as the migration front moves into an adjacent grain, the precipitate colony possesses the same orientation as the parent grain, leaving behind a low angle boundary. The migration front thus maintains the misorientation of the grain boundary where nucleation of the precipitate colony occurred.

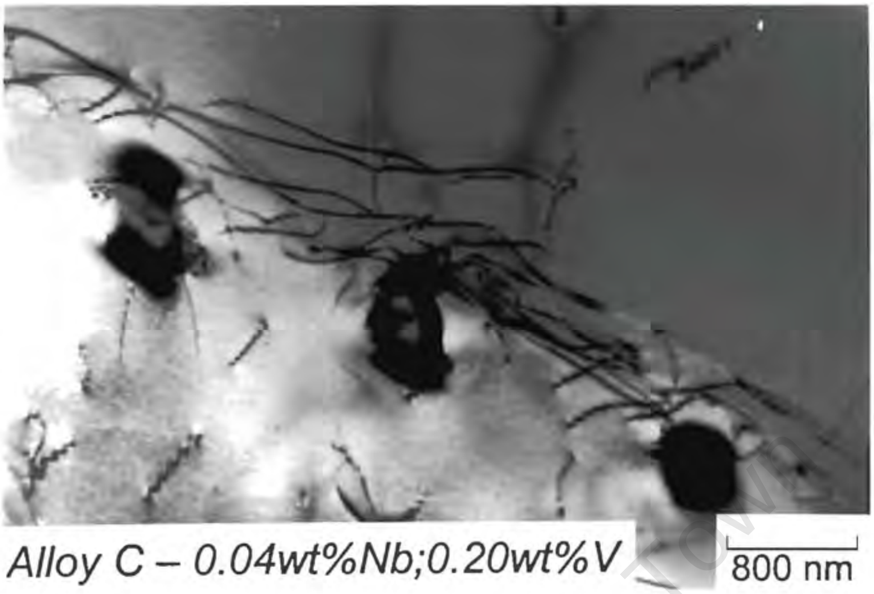

Fig. 4.3.19 (a)

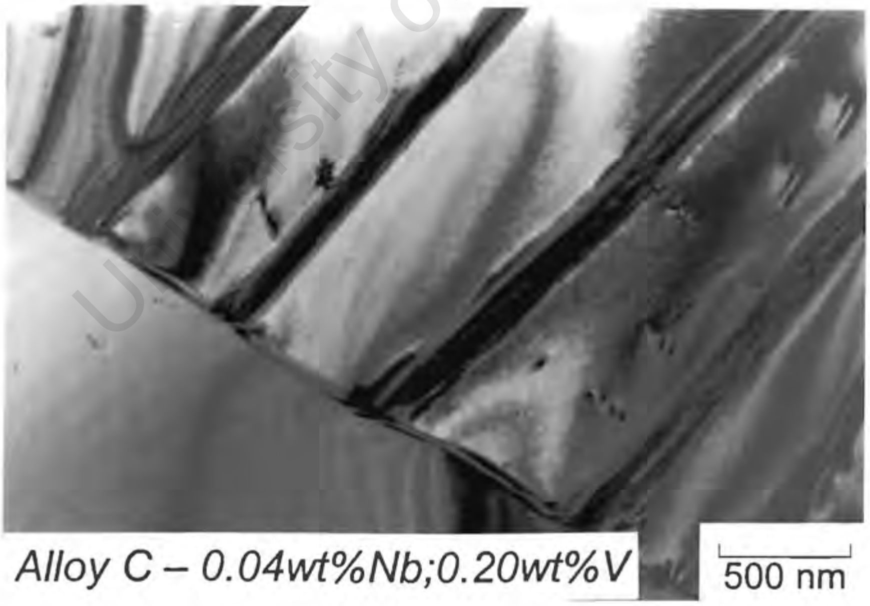

(b)

Fig. 4.3.19 TEM micrographs of alloy C after ageing at 1000 °C for 10 minutes showing, (a) a low angle boundary at the original position of the migration front where nucleation of the discontinuous precipitates occurred, (b) the high angle grain boundary or migration front with precipitate lamellae following.

Further study of the double seam feature marked (i) in figure 4.3.18 (a) together with the orientation map in figure 4.3.18 (c) shows that there are islands within the precipitate colonies that have a different orientation to the surrounding region. In the case of the precipitate colony where the orientation of the austenite is coloured brown, the islands of different orientation are coloured green. Similarly, in the precipitate colony in the double seam where the orientation is coloured blue, there are islands with a different orientation coloured green. A measurement of the misorientation across the boundary of such a region shows the area is bounded by special Σ3 boundaries with a rotation of 60° about the <111> direction, which indicates that these boundaries are twin boundaries.

The formation of twin boundaries within the precipitate cells is more clearly shown in figure 4.3.20 (a). This figure was generated from the orientation information in figure 4.3.18 (c) and represents the same field of view. Figure 4.3.20 (a) shows the twin boundaries in red and the high angle grain boundaries in black. The formation of twins is especially prolific in the region of the feature marked (iii) in figure 4.3.18 (a) shown in figure 4.3.20 (a). The twin boundaries that form within the precipitate colonies grow as the cell colonies grow. After extended ageing at 1000°C, up to 10 hours, extensive twin boundaries within the precipitate cell colonies can be resolved in the light microscope, and are more clearly observed using Nomarski interference contrast. An example of this observation is shown in figure 4.3.20 (b).

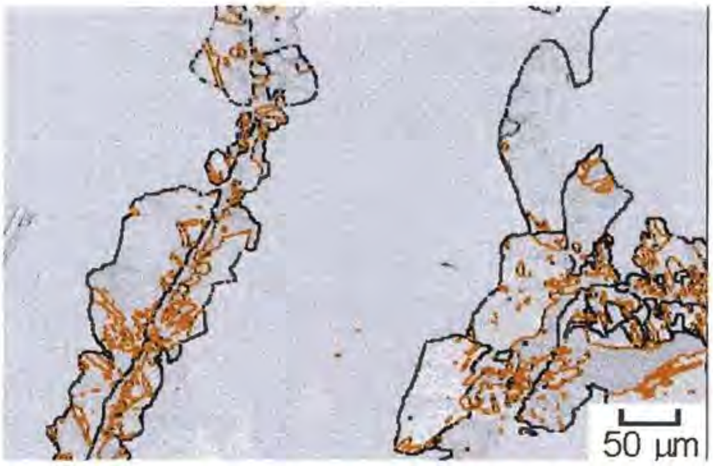

Fig. 4.3.20 (a)

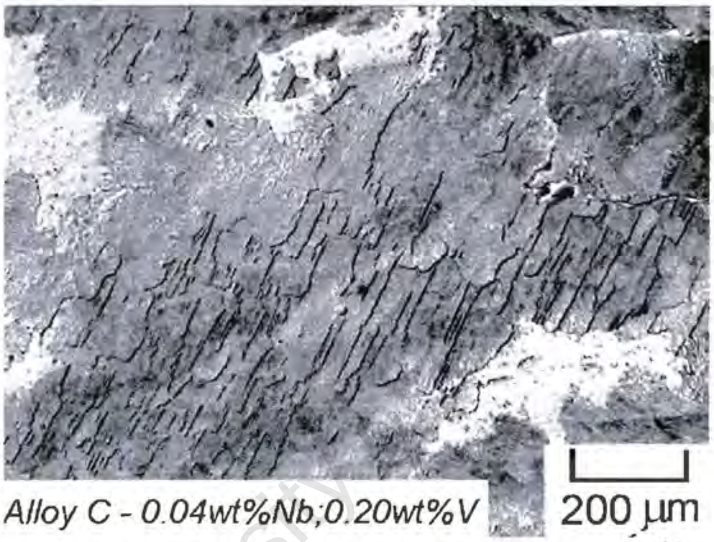

(b)

Fig. 4.3.20 (a) Image showing high angle boundaries and twin boundaries for the field of view represented by figure 4.3.18 (a) of alloy C after ageing at 1000 °C for 2 hours and (b) the presence of twins within the precipitate cells in alloy C after ageing for 10 hours at 1000 °C.

These results show that twin boundaries form within the precipitate colonies during the discontinuous precipitation reaction. It was not clear from these results if the twins in the precipitate colonies originated from boundary migration associated with the discontinuous reaction. In order to understand more about twin formation in the current system, specimens of alloy C in the solution treated condition were cold rolled in the laboratory to introduce deformation into the austenite. Specimens were cold rolled in the solution treated condition because alloy C is fully austenitic in this condition. Following cold rolling two specimens were annealed at 1100°C for 10 minutes and 30 minutes respectively.

Investigation of the microstructure of the specimen annealed for 10 minutes showed the degree of twin formation that resulted from recrystallisation and thus dislocation annihilation. The specimen annealed for 30 minutes showed the effect of grain growth on twin formation, since a fully recrystallised structure was obtained after annealing for 10 minutes, thus a further 20 minutes at 1100°C allowed the recrystallised grains to grow. A temperature of 1100°C was chosen for annealing treatments to avoid the formation of discontinuous cellular precipitates observed at 1000°C and 800°C. A qualitative description of the twin density per unit area of these two samples is shown in figure 4.3.21 (a) and (b). The figures were generated from orientation maps that were acquired using EBSD techniques in the same way as figure 4.3.20 (a) was generated from figure 4.3.18 (c). The results show that the twin density per unit area after ageing for 10 minutes (figure 4.3.21 (a)) is greater than after ageing for 30 minutes (figure 4.3.21 (b)). This shows that twin formation originates from recrystallisation rather than from grain growth.

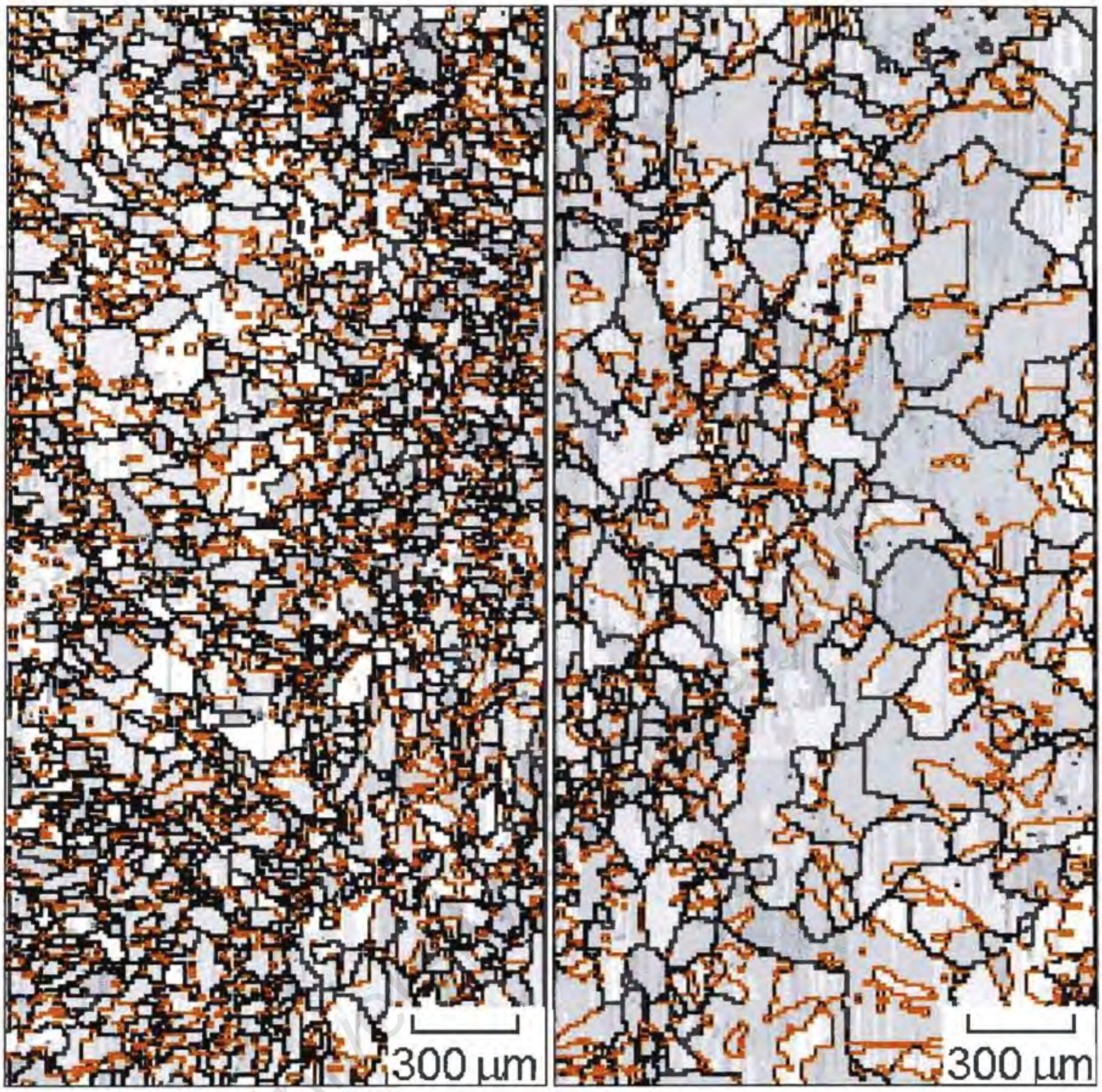

Fig 4.3.21 (a) *(b)*

Fig. 4.3.21 Alloy C after cold rolling and annealing at 1100 °C for (a) 10 minutes and (b) 30 minutes, showing the high angle boundaries in black and the twin boundaries in red and that the twin density is greater after 10 minutes of annealing than after 30 minutes.

The twin density in the precipitate colonies in alloy C after ageing at 1000°C for 10 minutes and 10 hours was determined in the same way that figures 4.3.21 (a) and (b) were acquired. The reason for this analysis was to determine the effect of boundary migration associated with the discontinuous cellular reaction on twin formation within the precipitate cells. These results show that the twin density within the precipitate cell colonies decreases with ageing time and therefore with precipitate cell growth. Figure 4.3.22 (a) shows the twin density (number of twin boundaries per unit area) within the precipitate colonies after ageing for 10 minutes at 1000°C. Figure 4.3.22 (b) shows the twin density within the precipitate colonies after ageing for 10 hours at 1000°C. It should be noted that the magnification of figure 4.3.22 (b) is lower than figure 4.3.22 (a), which means the area in figure 4.3.22 (b) is greater than figure 4.3.22 (a). These results further emphasise that the twin density after longer ageing times decreased compared to short ageing times within the precipitate colonies. This supports the results of annealing treatments shown in figures 4.3.21 (a) and (b), which show that twin density does not increase with grain growth.

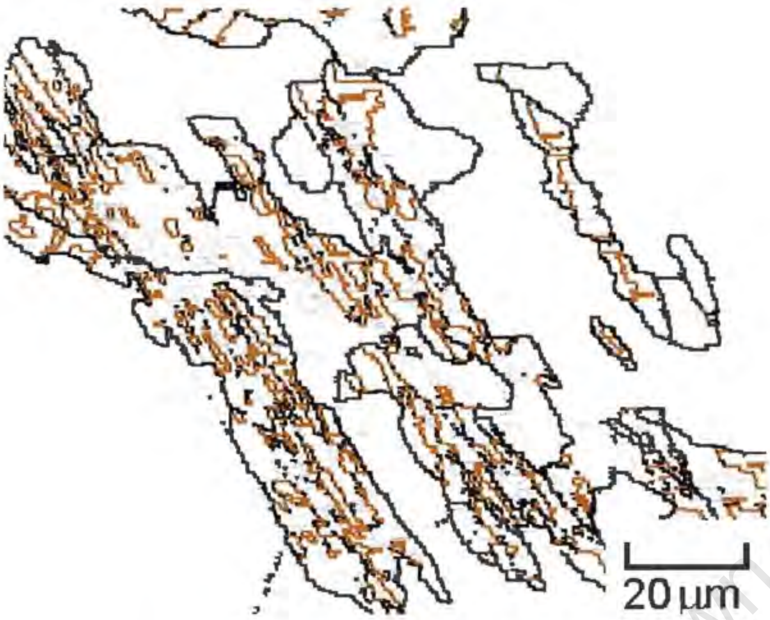

Fig 4.3.22 (a)

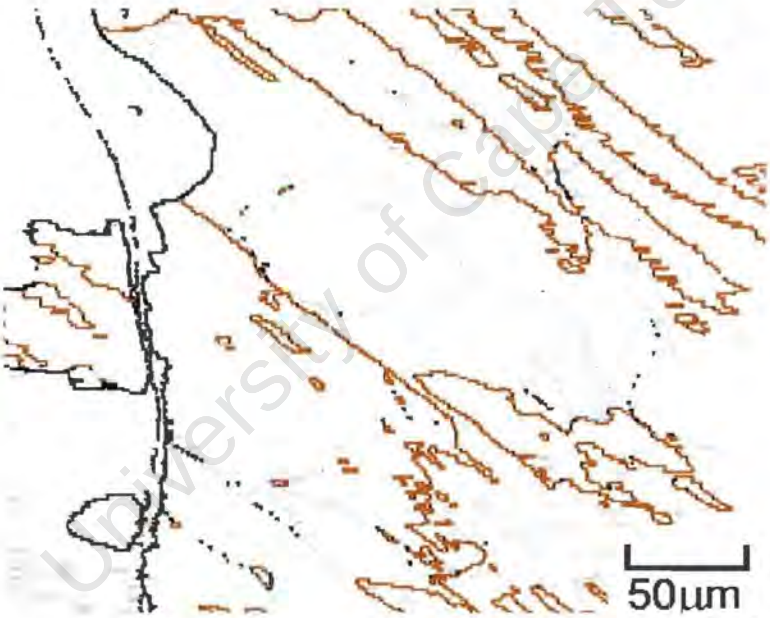

(b)

Fig.4.3.22 alloy C after ageing at 1000 °C for (a) 10 minutes and (b) 10 hours showing the special $\Sigma 3$ twin boundaries in red and the high angle boundaries in black. These figures show that the twin density within the precipitate colonies decreases with precipitate cell growth.

Figure 4.3.23 shows a TEM micrograph of alloy E after ageing at 1000 °C for two hours. The micrograph shows that stacking faults have formed in the austenite between the precipitate lamellae. In addition to stacking faults, dislocations are also observed between precipitate lamellae within the austenite in the discontinuous precipitate cell colonies. These features might account for the formation of twins within the precipitate colonies, which is discussed further in section 5.3.3.

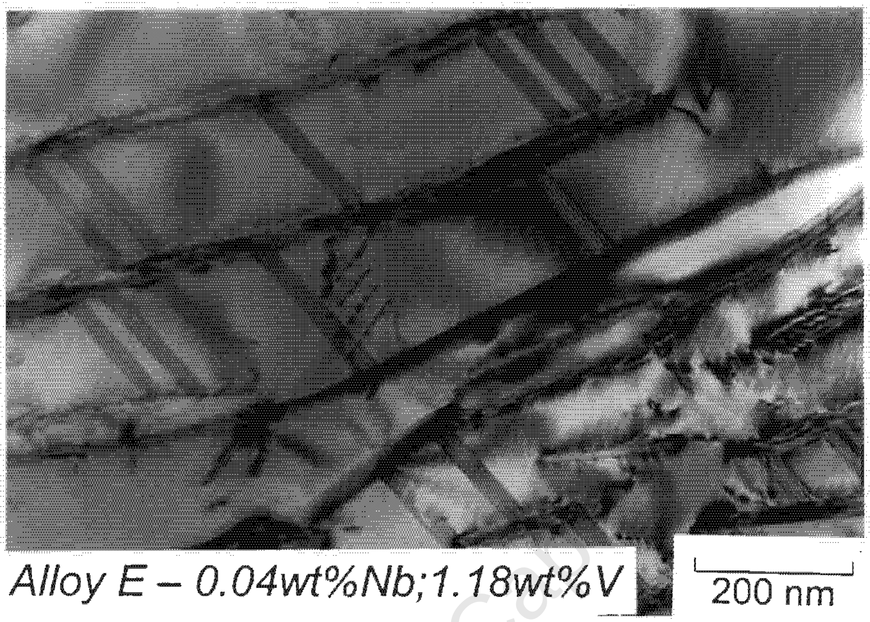

Fig. 4.3.23 TEM micrograph of stacking faults in alloy E between the precipitate lamellae after ageing at 1000°C for two hours.

The nucleation characteristics of the precipitate cells were studied by ageing specimens of alloy C at 1000°C for 5 and 10 minutes. Figures 4.3.24 (a) and (b) show the presence of precipitates on a grain boundary with the boundary bowing between the precipitates.

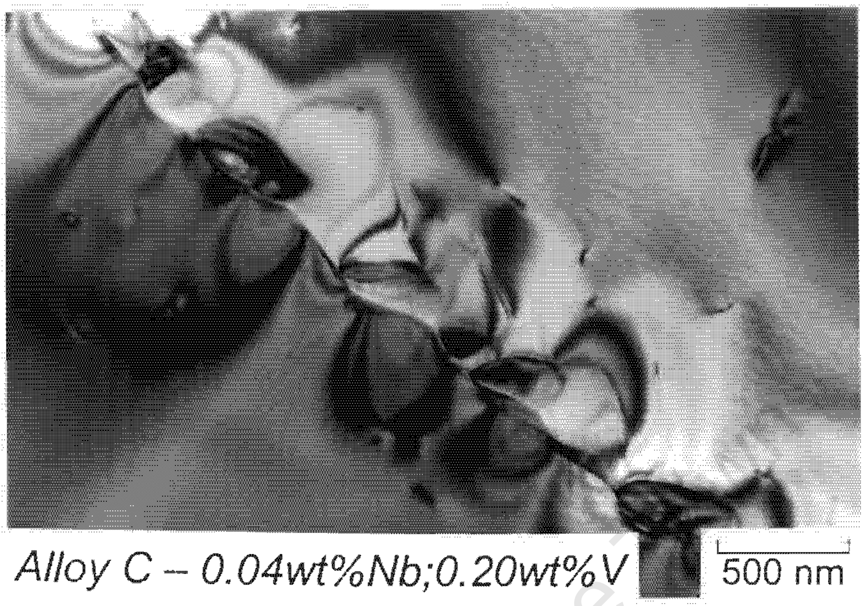

Fig. 4.3.24 (a)

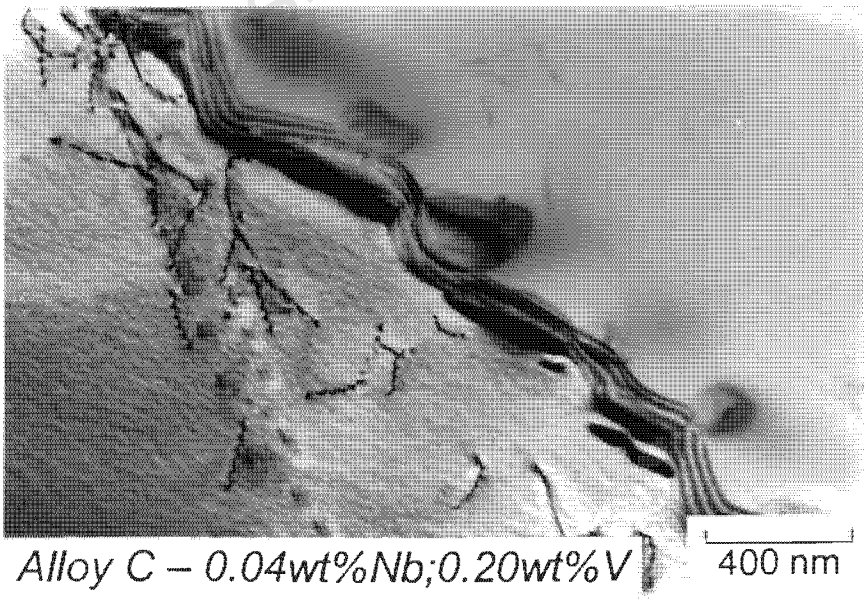

(b)

Fig. 4.3.24 (a) & (b) Alloy C after ageing for 10 minutes at 1000℃ showing the nucleation of precipitates on a grain boundary and the bowing of the boundary between the precipitates.

4.3.4 MECHANICAL BEHAVIOUR

Tensile tests were conducted for specimens of alloys A, C, D, E and H after ageing for two hours at 1000°C to illustrate the influence of different degrees of lamellar precipitation on the strength and elongation to failure of these alloys. These alloys were selected on the same basis as the alloys aged at 1100°C. Data was thus available for comparative purposes. The results of the tensile tests are shown in figure 4.3.25, together with the curve for alloy C in the solution treated condition for comparative purposes. The tensile properties calculated from the tensile data are shown in table 4.3.2. In the case of alloys A, C, E and H the elongation to failure has been reduced after ageing at 1000°C as a consequence of the formation of lamellar precipitates. The yield strength of alloys A, C and H has also been increased to levels greater than that achieved after ageing at 1100°C (figure 4.2.22). The yield strength of alloy E is similar to that after ageing at 1100°C (table 4.2.3). Alloy D shows the greatest elongation to failure of all the alloys represented in the graph, and no lamellar precipitation was observed in this alloy at ageing treatments of 1000°C. This observation offers further evidence that the decreased elongation to failure observed in alloys A, C, E and H is the result of lamellar precipitates.

Since the formation of lamellar precipitates resulted in a significant decrease in the wear resistance of alloy E after ageing at 1100°C, abrasive wear tests on alloys A, C, E and H were not considered useful. These four alloys all showed evidence of lamellar precipitation at 1000°C.

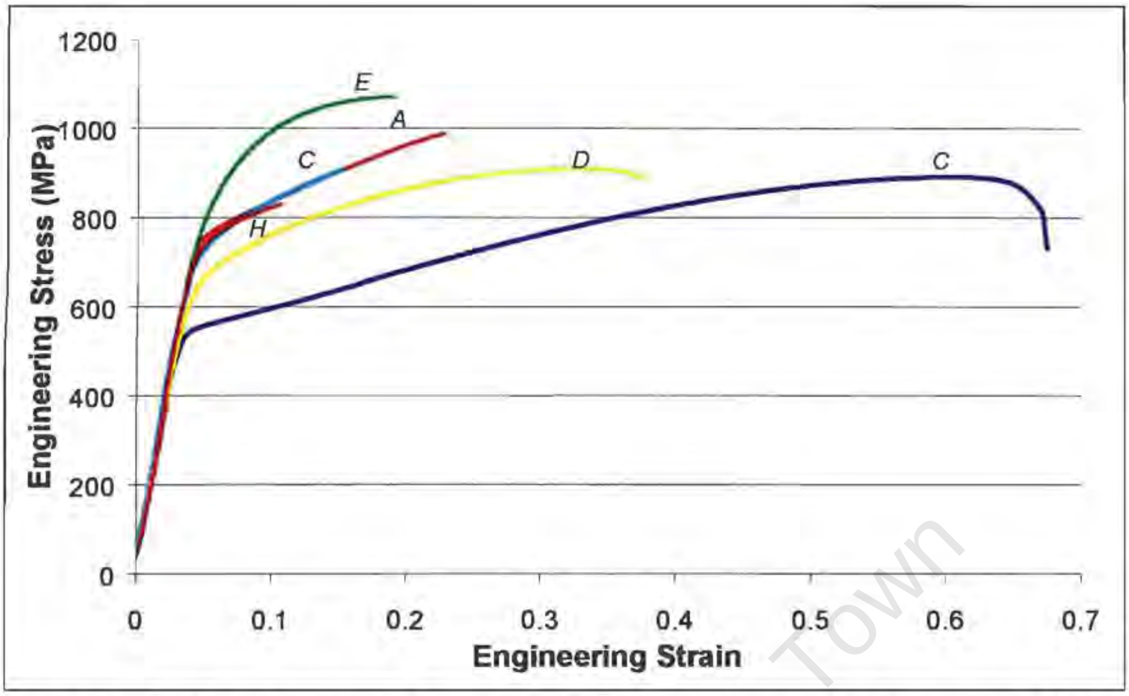

Fig. 4.3.25 Tensile test curves for alloys A, C, D, E & H after ageing for two hours at 1000 °C together with the curve for alloy C in the solution treated condition for comparative purposes.

Table 4.3.2 Tensile properties of alloys A, C, D, E & H, including alloy C in the solution treated condition for comparative purposes.

Alloy	***Yield Strength(MPa)***	***Ultimate Tensile Strength (MPa)***	***Total Elongation to Failure (%)***	***Plastic Elongation to Failure (%)***
C Solution Treated	548	889	67	63
A	746	988	23	18
C	715	906	15	12
D	638	906	37	33
E	816	1017	19	14
H	739	823	11	6

4.4.5 SUMMARY: AGEING TREATMENTS AT 1000°C

Ageing treatments at 1000°C resulted in discontinuous cellular precipitation of M_2X precipitates in alloys A, B, C, E, F, G and H. The volume fraction of lamellar precipitates that formed in these alloys was sensitive to the niobium and vanadium levels in each of the alloys. The role of niobium in suppressing discontinuous cellular precipitation in the current system was emphasised by the results of ageing treatments on alloy D, which in contrast to the role of vanadium favours the discontinuous reaction and is emphasised by the results of ageing treatments on alloy E. In the alloys that contained both niobium and vanadium additions, (alloys A, B, F, G and H) the precipitation of the M_2X phase changed from a discontinuous mode during the early stages of ageing to a continuous mode after extended ageing at 1000°C. A change in precipitation mode was not observed in alloys C and E, but rather discontinuous coarsening was observed.

The microstructural evolution of the eight high nitrogen steel alloys during ageing treatments at 1000°C is summarised by figure 4.3.26. This figure is not an attempt to predict a more accurate isopleth diagram than that shown in figure 4.3.1, but rather a map of the phase stability observed experimentally in the system at 1000°C. Careful study of figure 4.3.26 and figure 4.3.1 shows that the two diagrams are very similar except for the presence of ferrite. The red lines drawn on the diagram are approximate tie lines, based on experimental results. The alloys that have been ringed in yellow are those in which the mode of M_2X precipitation changes from discontinuous to continuous during ageing at 1000°C.

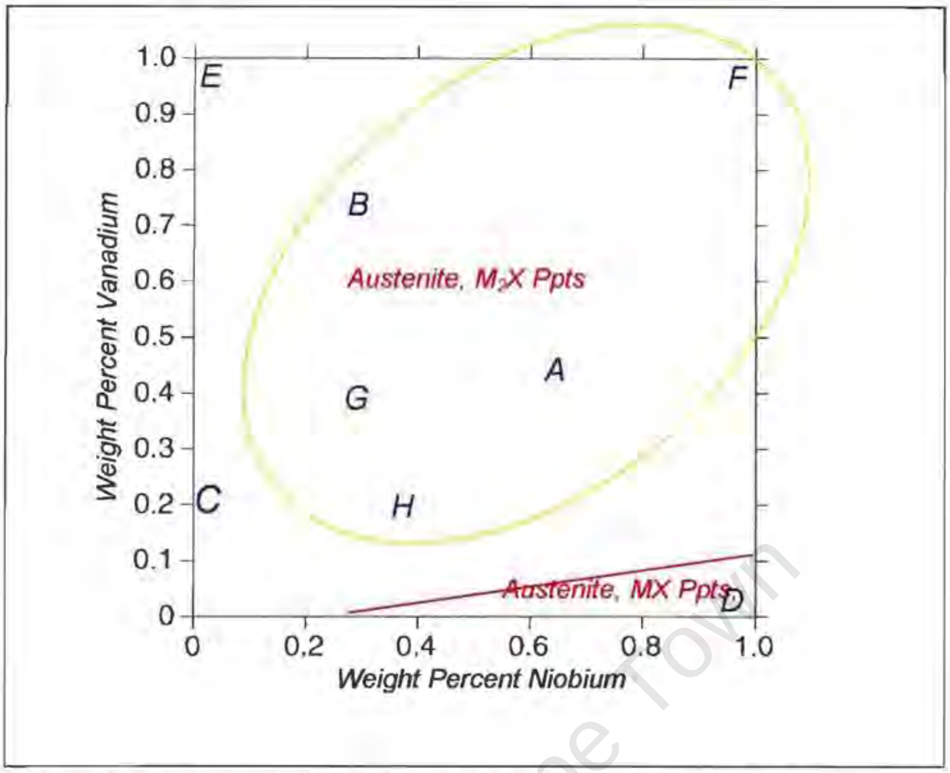

Figure 4.3.26 Map of the phase stability of the eight high nitrogen steel alloys based on experimental results.

An investigation of the discontinuous precipitate cell characteristics shows that the precipitate lamellae grow behind a migrating high angle boundary, and as the cell expands, it keeps the orientation of the grain from which it originated. Twins, stacking faults and dislocations were often observed within the precipitate lamellae. A study of twin formation during grain growth was conducted to explain the origin of twins during precipitate cell growth. In addition, an investigation of the nucleation characteristics of the precipitate lamellae and discontinuous cells reveals that the boundary on which grain boundary allotriomorphs grow bows between the precipitates during nucleation.

The formation of M_2X precipitates, regardless of the volume fraction, resulted in a significant decrease in the elongation to failure of the alloys. M_2X precipitation should therefore be avoided for improved wear performance.

4.4 AGEING TREATMENTS AT 800°C

Ageing treatments at 800°C were conducted on each of the eight alloys following the solution treatment described in section 4.1, and after each ageing treatment the alloys were water quenched to freeze in the high temperature structure for further analysis. Lamellar precipitation was observed to form discontinuously in all of the alloys after ageing treatments at 800°C. The effect of niobium and vanadium levels on the formation of discontinuous cellular precipitates at 800°C is investigated in this section. In addition, twin formation within the precipitate cells is investigated and the nucleation characteristics of the precipitate cells at 800°C is studied. Finally the influence of ageing treatments at 800°C on the mechanical properties is characterised.

4.4.1 ISOPLETH DIAGRAM

The isopleth diagram for the high nitrogen steel alloys at 800°C in figure 4.4.1 is relatively simple, with only one tie line, which indicates where the ferrite phase appears at higher levels of both niobium and vanadium. Thermocalc predicts that alloy C should contain M_2X precipitates, $M_{23}C_6$ precipitates and sigma phase in an austenite matrix. Alloys A, B, D, E, F, G and H are predicted to contain all of the phases that are stable in alloy C, as well as ferrite. Thermocalc predicts two phases to be stable at this temperature that are not stable at other ageing temperatures, viz. sigma phase and $M_{23}(CN)_6$.

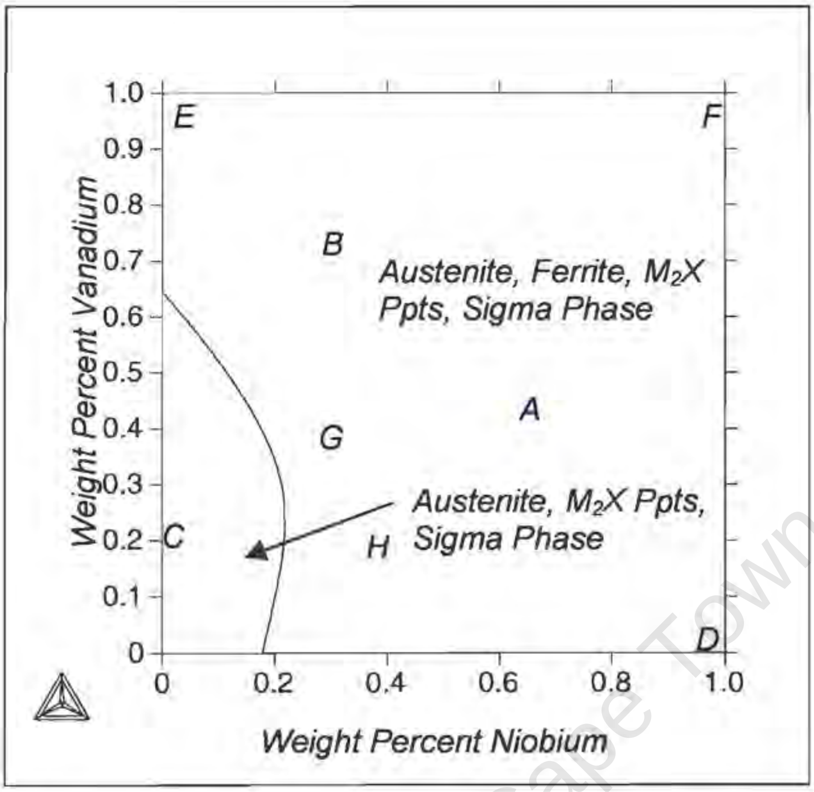

Fig. 4.4.1 Isopleth Diagram for the high nitrogen steel alloys for 800 °C, showing the phase balance in each of the eight alloys as a function of niobium and vanadium levels.

4.4.2 PHASE IDENTIFICATION

4.4.2.1 METALLOGRAPHY

Lamellar precipitation was observed in each of the eight alloys after ageing for two hours at 800°C, shown in figures 4.4.2 (a)-(c) and figures 4.4.4 (a)–(e). In each alloy, the precipitate colonies show characteristics of the discontinuous cellular precipitation reaction: the precipitate lamellae have nucleated at the grain boundaries and the colony has developed behind a migration front. Comparison of the microstructure of alloy C after ageing at 1000°C (figure 4.3.2 (a) & (b)) with the microstructure after ageing at 800°C (figure 4.4.2 (a)) shows that the interlamellar spacing within the precipitate colonies is finer in the case of the 800°C heat treatment. A greater volume fraction of discontinuous cellular precipitation is observed in alloy E than in alloy C, as shown in figures 4.4.2 (b), which was also observed after ageing at 1000°C. Examination of figure 4.4.2 (b) shows that the individual precipitate cells in alloy E after ageing at 800°C are smaller and that there is a greater number of cells than in alloy C. Further, the low magnification image suggests that the precipitate cells grow along preferential orientations in the austenite matrix. The results of a two hour ageing treatment on alloy D show a much smaller volume fraction of lamellar precipitation after ageing for two hours at 800°C (figure 4.4.2 (c)), than in alloy C. In addition to the lamellar precipitates in the austenite, precipitation has also occurred in the ferrite islands in alloy D.

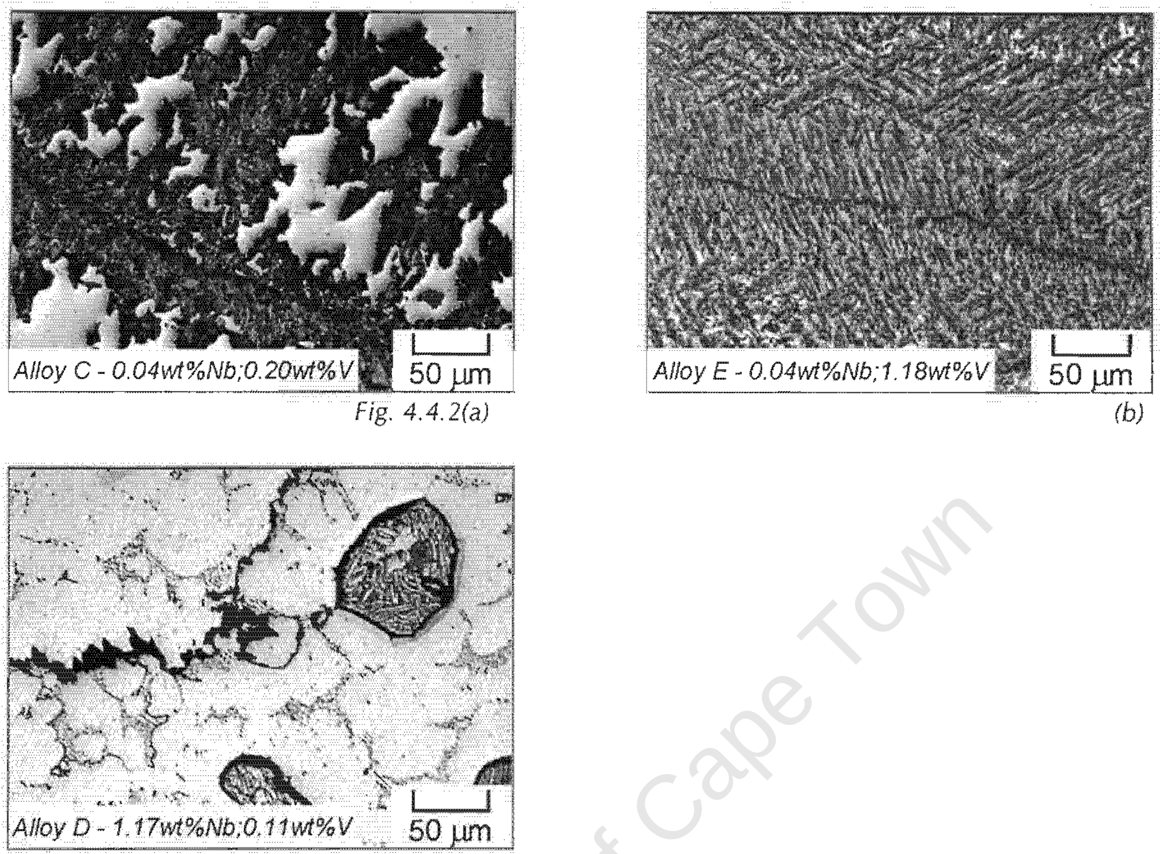

Fig. 4.4.2(a)

(b)

(c)

Fig. 4.4.2 Alloys C, E, & D after ageing for two hours at 800℃ showing (a) the lamellar precipitates in alloy C that have formed by discontinuous cellular precipitation, (b) a larger volume fraction of lamellar precipitates in alloy E, than in alloy C, (c) a smaller volume fraction of lamellar precipitates in alloy D, than in alloy C, and the presence of precipitates in the ferrite islands.

TEM studies of the lamellae in the discontinuous precipitate colonies in alloys C and E, show that the interlamellar spacing between the lamellae in alloy E is smaller than in alloy C. This is shown in figures 4.4.3 (a) and (b).

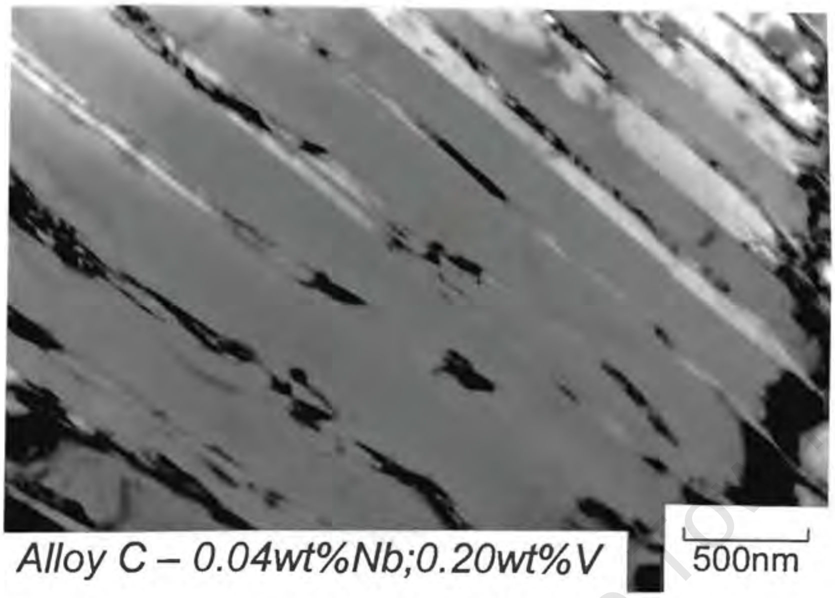

Fig. 4.4.3(a)

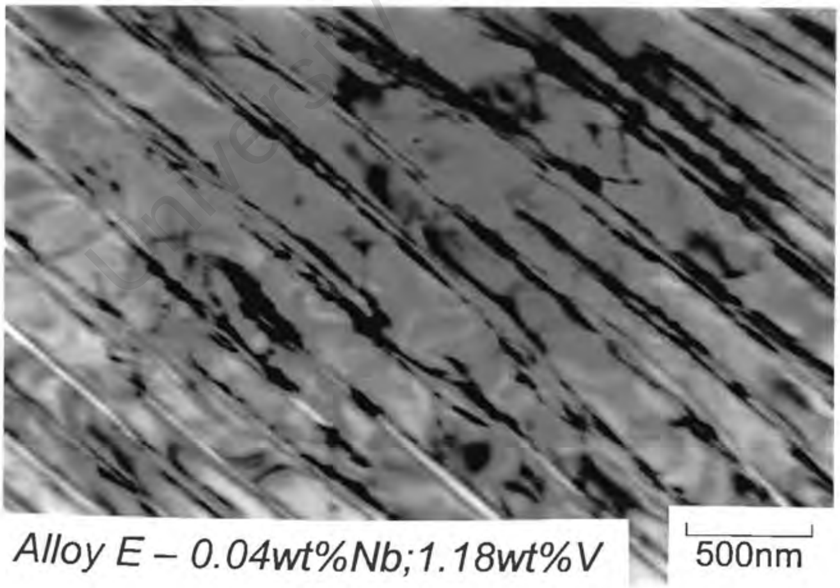

(b)

Fig. 4.4.3 TEM micrographs of the lamellar precipitates in (a) alloy C and (b) alloy E after ageing for two hours at 800 °C, showing that the interlamellar spacing in alloy E is finer than in alloy C.

Figures 4.4.4 (a)-(e) show the formation of discontinuous cellular precipitation in alloys A, B, F, G and H. The structure of the precipitate cells is consistently finer than those observed in the same alloys after ageing at 1000°C (figures 4.3.2 (e)-(n)).

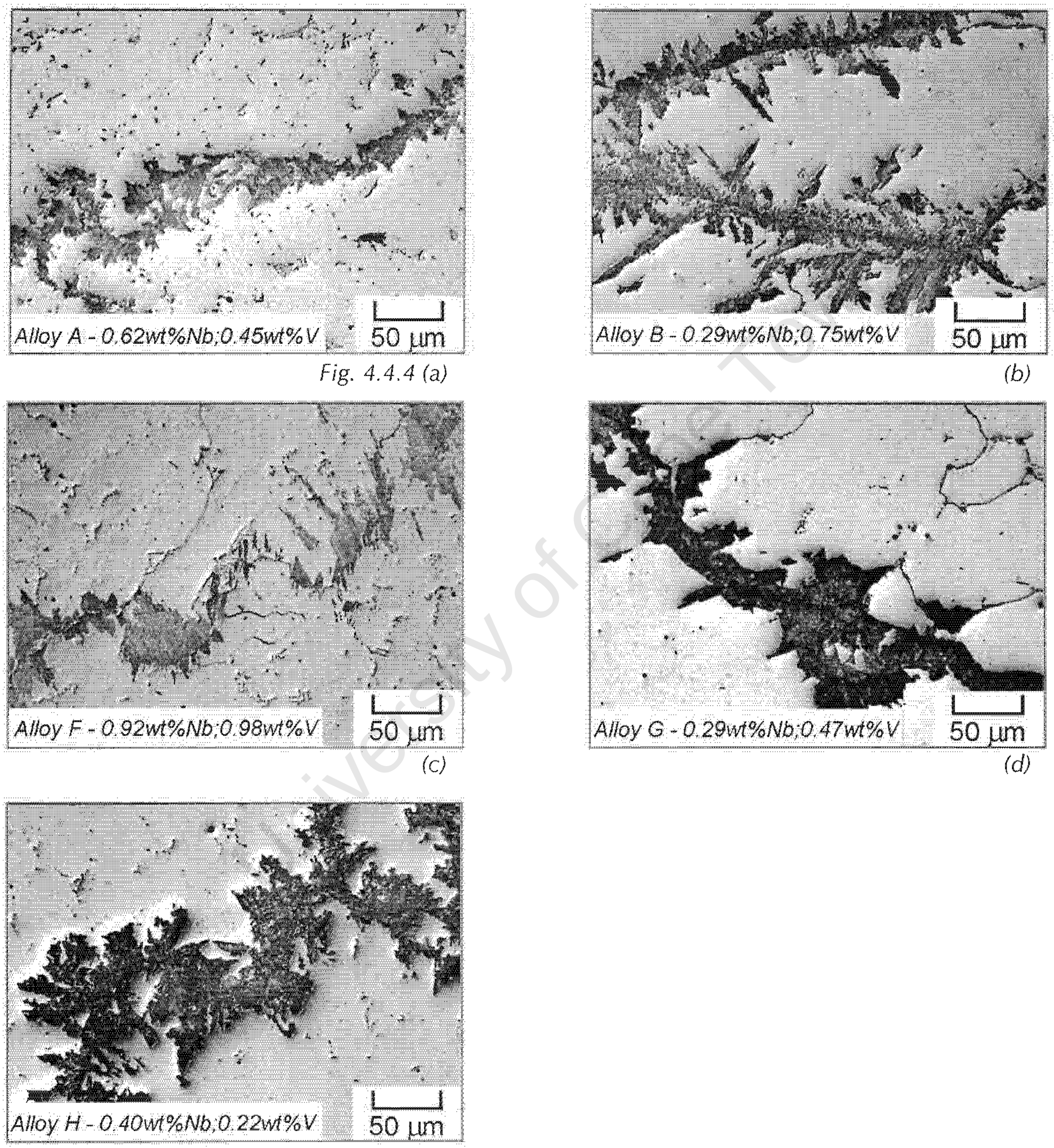

Fig. 4.4.4 (a) *(b)* *(c)* *(d)* *(e)*

Fig.4.4.4 (a)-(e) Alloys A, B, F, G & H after ageing for two hours at 800°C showing that discontinuous cellular precipitation of lamellar precipitates has occurred in all of the alloys.

Prolonged ageing treatments at 800°C for 100 hours resulted in extensive discontinuous cellular precipitation, as is shown in figure 4.4.5 (a)-(h). This observation is especially evident in alloys C and E (figures 4.4.5 (a) and (b)), where lamellar precipitates are observed to fill the whole microstructure. The increase in the volume fraction of lamellar precipitates is greater in alloy C than in alloy E, which shows a similar volume fraction after ageing for 100 hours to that after ageing for 2 hours (figure 4.4.5 (b)).

The 100 hour ageing treatment has resulted in an increased volume fraction of lamellar precipitates in alloy D shown in figure 4.4.5 (c), but the extent of discontinuous cellular precipitation in alloy D is still less than in alloy C. Alloys A and H show similar volume fractions of lamellar precipitates, whereas alloys B and G both show a greater volume fraction than alloys A and H. Alloys A and H both contain more niobium than vanadium and alloys B and G represent the opposite case. In addition, the growth of the precipitate cells in alloys A and H follow preferred crystallographic orientations, which was observed in alloy E after ageing for two hours. Finally, the microstructure of alloy F is different to the other alloys after ageing for 100 hours. In addition to the lamellar precipitate colonies, the formation of fine particles is observed in figure 4.4.5 (d).

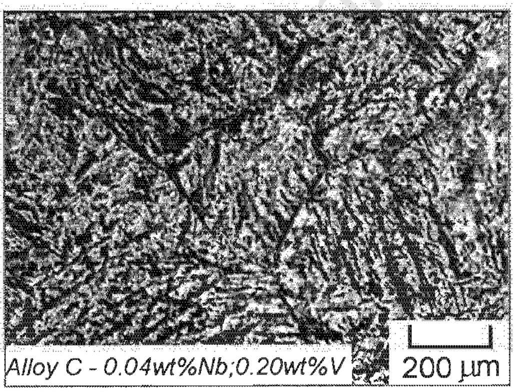

Fig. 4.4.5 (a)

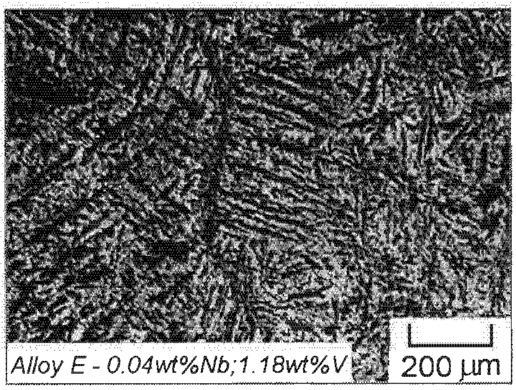

(b)

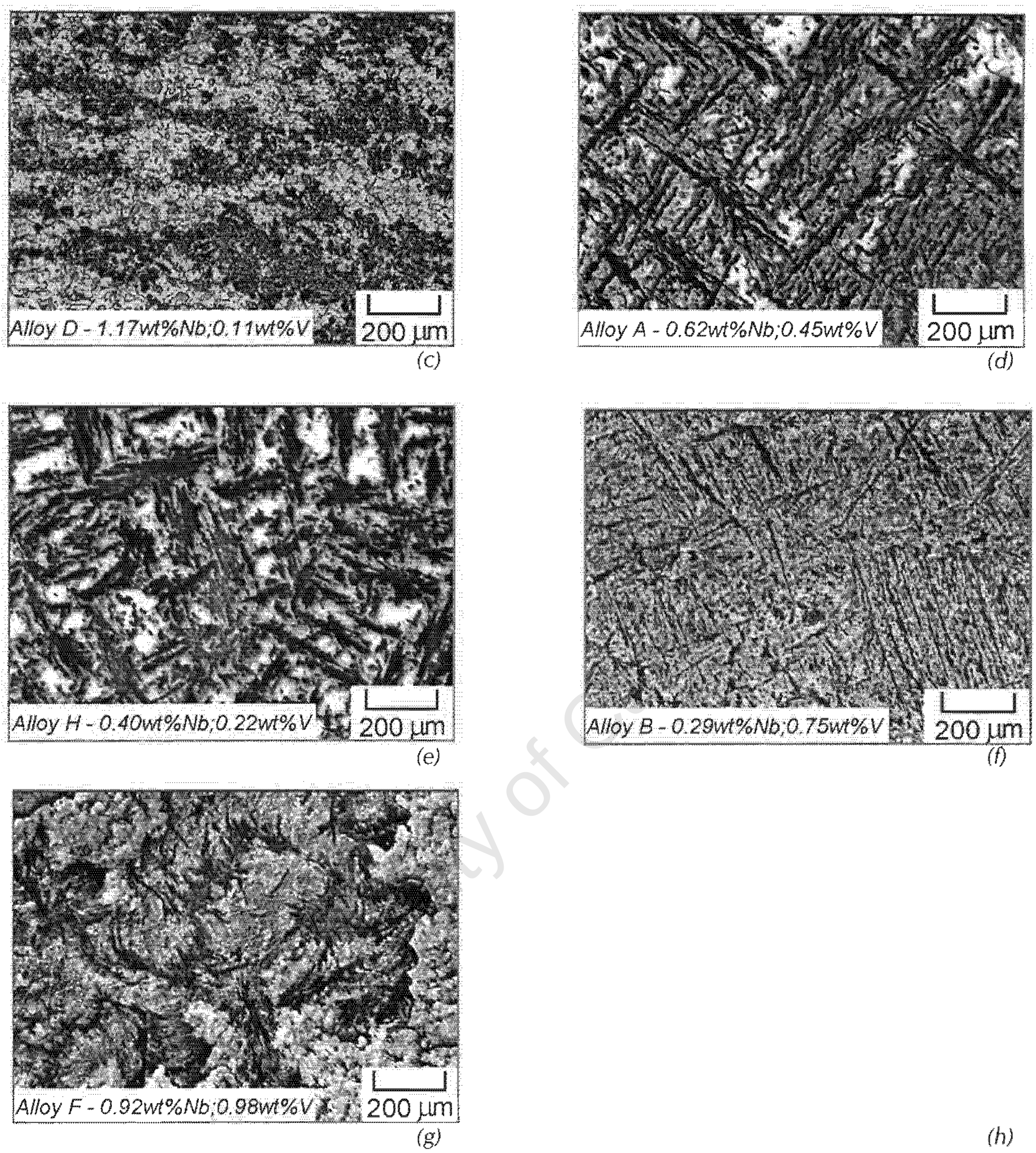

(c) (d) (e) (f) (g) (h)

Fig. 4.4.5 Alloys C, E, D, F, A, B, G and H after ageing for 100 hours at 800℃, showing the extensive coverage of lamellar precipitation in each of the alloys when compared to the set of micrographs of the same alloys after ageing for two hours

4.4.2.2 COMPOSITIONAL AND CRYSTALLOGRAPHIC ANALYSIS

Attempts were made to carry out compositional analysis of the lamellar precipitates in alloy C and in alloy E, using x-ray mapping techniques. The same success that was achieved for the analysis of the lamellae in various alloys after ageing at 1000 °C and 1100°C could not be achieved since the interlamellar spacing after ageing at 800 °C was too small. In addition the lamellae themselves were too fine for the resolution of the x-ray mapping technique. Some success however was achieved for alloy C, but only the chromium map showed any change in concentration across the field of view. The backscattered electron image of the field of view from which the x-ray map was taken is shown in figure 4.4.6 (a). The image shows colonies of precipitate cells and sigma phase (the bright phase) on the boundary of the precipitate cell. The x-ray map of this field of view for chromium is shown in figure 4.4.6 (b) and shows that sigma phase is chromium rich and the lamellar precipitates, which are just visible in the map are also chromium rich.

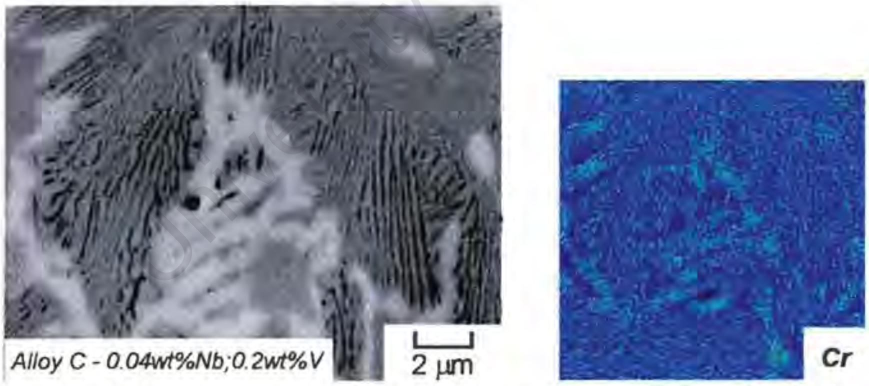

Fig. 4.4.6 (a) *(b)*

Fig.4.4.6 (a) SEM (backscattered electrons) image of a precipitate cell in alloy C after ageing for two hours at 800 °C. The precipitate lamellae can be seen together with sigma phase, which appears as the bright phase. (b) x-ray map for chromium showing that the precipitate lamellae and the sigma phase are rich in chromium.

The extent of sigma phase formation is illustrated by the lower magnification backscattered image of alloy C, shown in figure 4.4.7 (a). The influence of vanadium on the extent of sigma phase formation is illustrated by a SEM backscattered electron image of alloy E after the same ageing treatment, shown in figure 4.4.7 (b). Comparison of figure 4.4.7 (b) with figure 4.4.6 (a) shows that there is a greater volume fraction of sigma phase in alloy E than in alloy C after a 2 hour ageing treatment at 800°C.

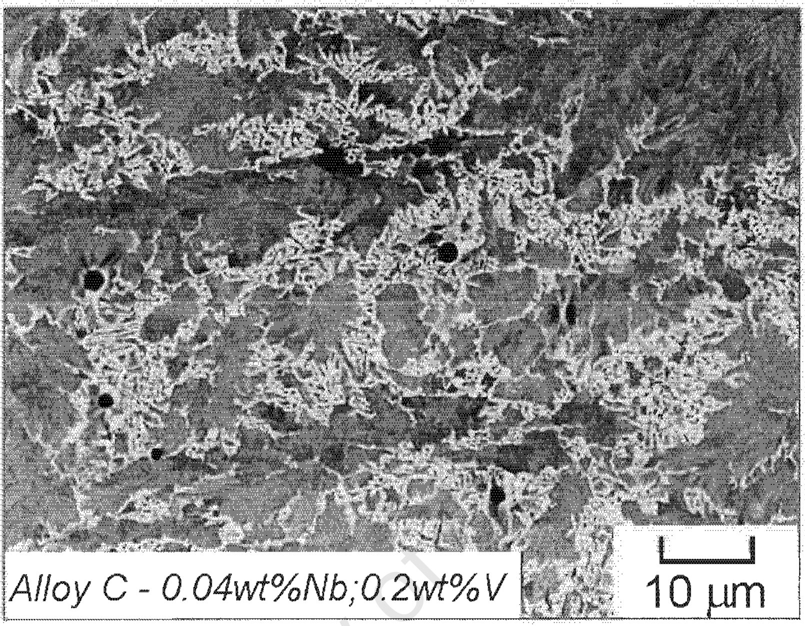

Fig. 4.4.7 (a)

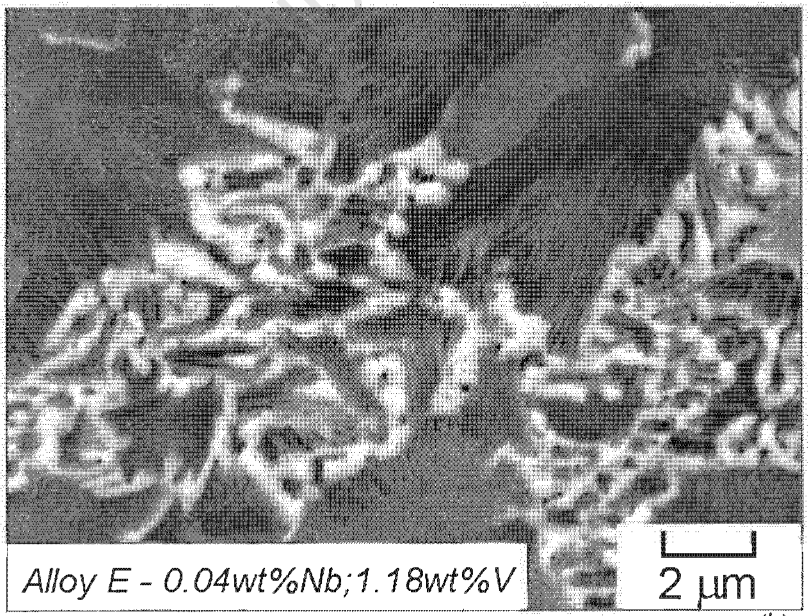

(b)

Fig.4.4.7 SEM (backscattered electrons) images showing the distribution of sigma phase after ageing at 800℃ for two hours in (a) alloy C and (b) alloy E.

Electron diffraction studies confirmed that the bright phase in the backscattered electron images in figures 4.4.6 (a) and 4.4.7 (a) and (b) is sigma phase. Diffraction patterns were taken from the sigma phase in alloy C and in alloy E to determine if the alloy composition had any effect on the crystallography of sigma phase. Figures 4.4.8 (a)-(d) show convergent beam electron diffraction (CBED) patterns of this phase taken from alloys C and E and the indexing of these patterns is shown in the schematics in figures 4.4.9 (a)-(d). From this analysis the lattice parameter values were determined for sigma phase in alloy C and alloy E and these values are shown in table 4.4.1.

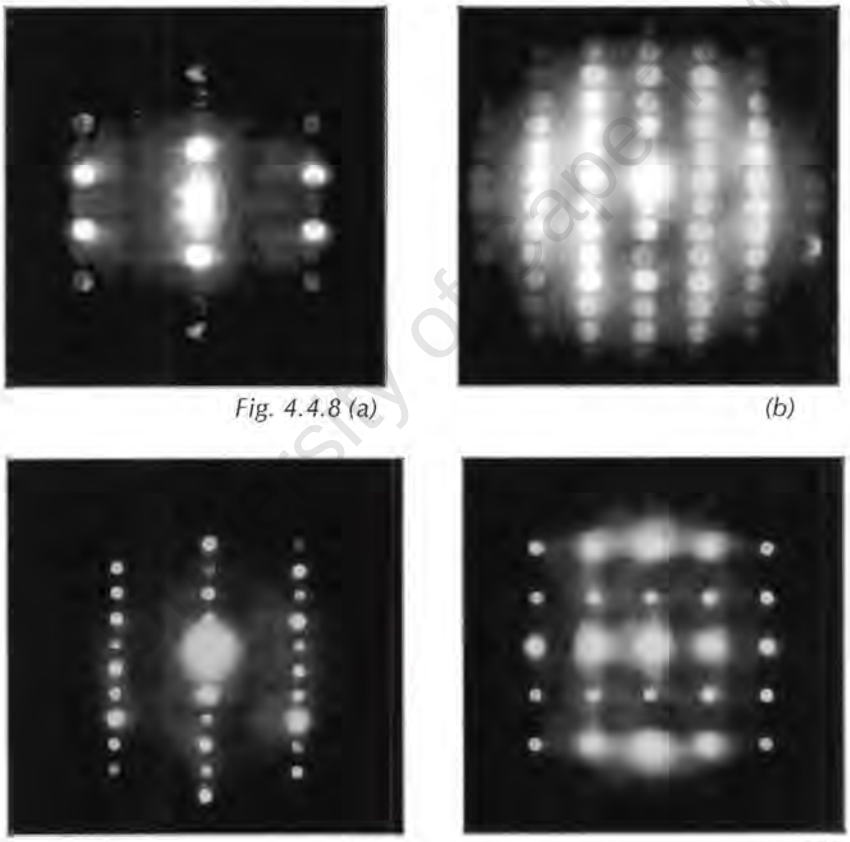

Fig. 4.4.8 (a) *(b)*

(c) *(d)*

Fig. 4.4.8 CBED patterns for the sigma phase in (a) & (b) ***alloy C (0.04wt%Nb;0.2wt%V)*** *showing the reflections for the [021] and [001] zone axes for the tetragonal system respectively and (c) & (d)* ***alloy E (0.04wt%Nb;1.18wt%V)*** *showing reflections for the [103] and [100] zone axes for the tetragonal system respectively.*

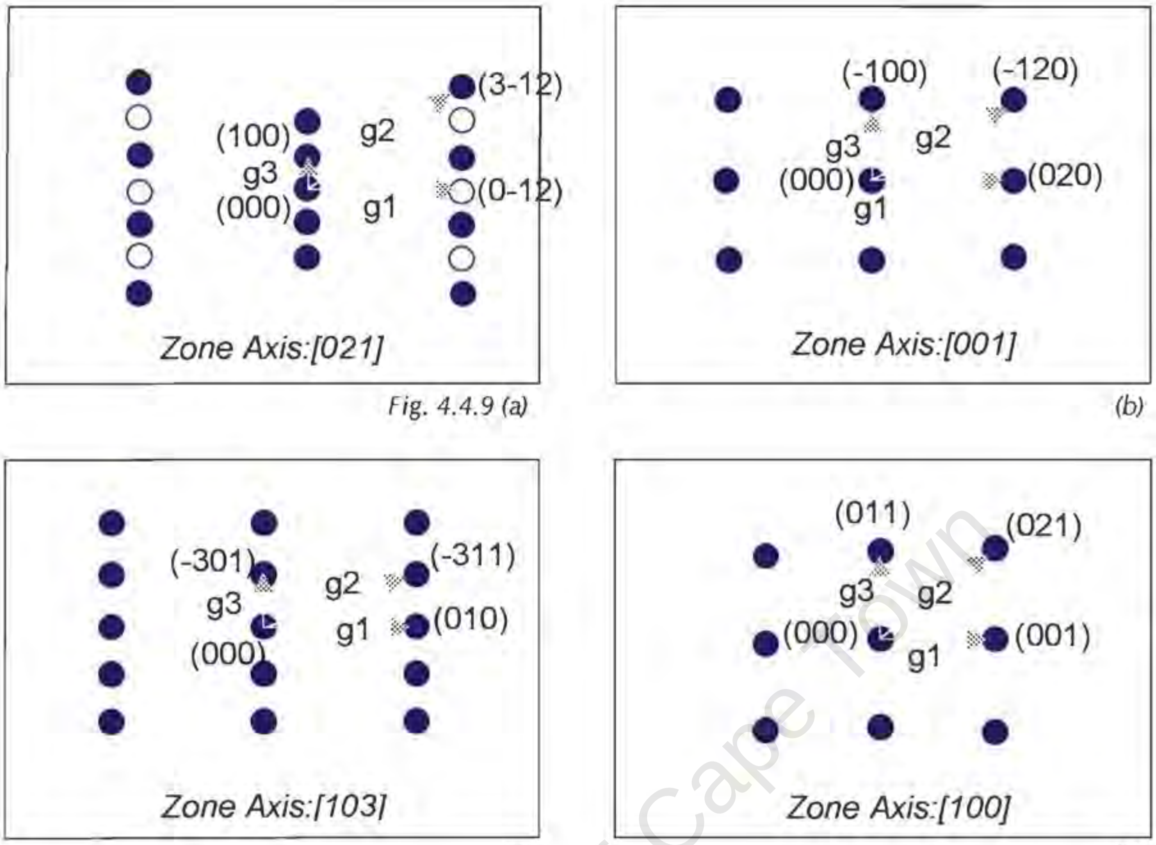

Fig. 4.4.9 (a) *(b)*

(c) *(d)*

Fig. 4.4.9 Indexing of the CBED patterns taken from sigma phase in (a) & (b) alloy C for the [021] and [001] zone axes for the tetragonal system and (c) & (d) alloy E for the [103] and [100] zone axes respectively.

Table 4.4.1 Lattice parameters calculated for sigma phase in alloys C and E, from the diffraction patterns shown above together with the published values for sigma phase[40].

	a (Å)	***c (Å)***
Sigma Phase*	**8.8**	**4.4**
Alloy C *– [021]*	8.7	4.6
Alloy C *– [001]*	8.8	
Alloy E *– [103]*	8.5	5.4
Alloy E *– [001]*	7.8	4.8

The morphology of the lamellae in the alloys after ageing at 800°C indicates that the precipitates have an M_2X stoichiometry and an HCP crystal structure. Since the isopleth diagram generated by Thermocalc for 800°C predicted that $M_{23}(CN)_6$ precipitates might form at this temperature, diffraction studies of the lamellae in alloys C and E were completed to establish whether the precipitates had a HCP crystal structure (ie M_2X type precipitates) or an FCC structure which would identify them as $M_{23}(CN)_6$.

Figures 4.4.10 (a) and (c) shows SAD diffraction patterns taken from a region including a precipitate lamella and the austenite matrix in alloy C where the [1-10] and [11-2] austenite zone axis diffraction patterns are shown respectively. Figure 4.4.10 (b) shows the CBED pattern for the [1-210] zone axis for the HCP system, taken directly from the precipitate, at the same tilt and rotation from which the [1-10] austenite zone axis was acquired. The reflections shown in this pattern correspond to the extra reflections observed in the [1-10] austenite zone axis. The [11-2] austenite zone axis diffraction pattern also shows extra reflections for the precipitate. These diffraction patterns were indexed in the same way as those generated from the precipitate lamellae in alloy E after ageing at 1100°C (figures 4.2.14 (a)-(c)). This result confirms that the lamellar precipitates that formed at 800°C in alloy C have an HCP crystal structure, with the following orientation relationship:

$$(111)\gamma//(0001)\ M_2X;[1\text{-}10]\ \gamma//[1\text{-}210]\ M_2X$$

Similarly, the diffraction patterns in figure 4.4.11, generated from the precipitate lamellae in alloy E were also indexed using the analysis shown in figures 4.2.14 (a)-(c) and show that the lamellae have an HCP structure, with the same orientation relationship as those in alloy C. The lattice parameter values were calculated from the diffraction patterns in figures 4.4.10 (a)-(c) and figures 4.4.11 (a)-(c) and are shown in table 4.4.2.

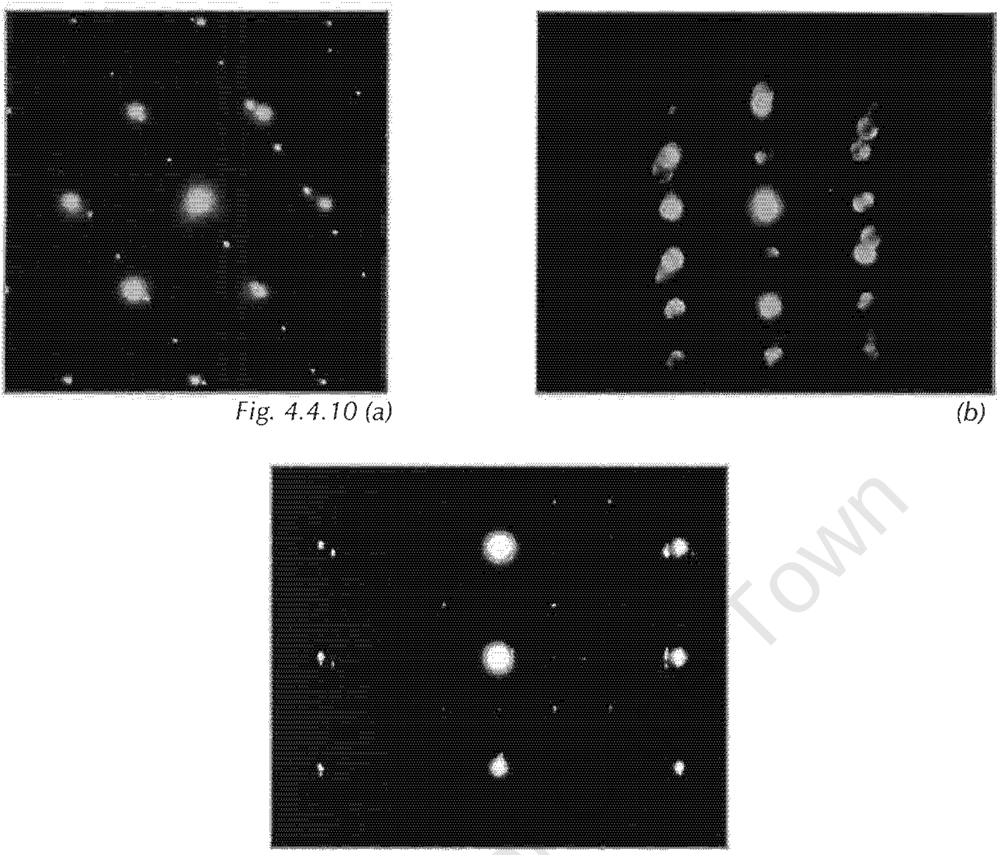

Fig. 4.4.10 (a)

(b)

(c)

Fig. 4.4.10 Diffraction patterns taken from the precipitate lamellae in ***alloy C (0.04wt%Nb;0.2wt%V)*** *after ageing for two hours at 800℃, showing (a) SAD pattern for the [1-10] austenite zone axis, with extra reflections which represent the [1-210] HCP zone axis, (b) CBED pattern taken directly from a precipitate lamella showing the reflections for the [1-210] zone axis for the HCP system, (c) SAD pattern for the [11-2] austenite zone axis showing extra reflections that correspond to the [10-10] HCP zone axis, together with superlattice reflections.*

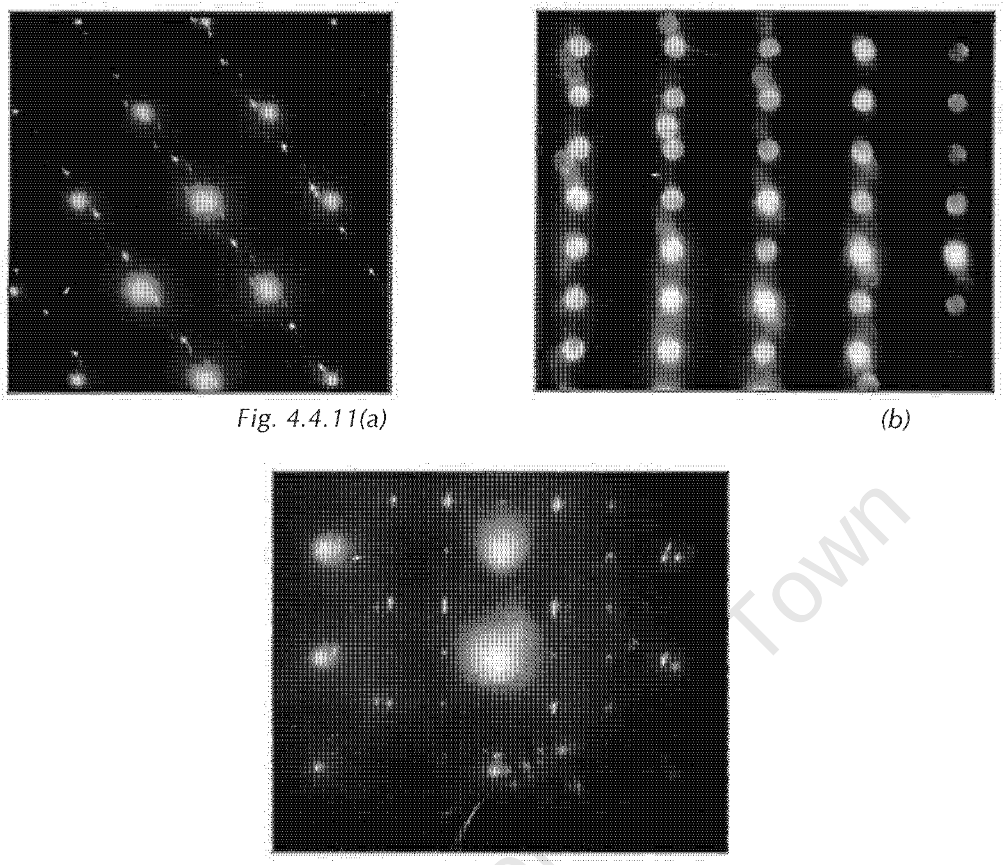

Fig. 4.4.11(a) *(b)*

(c)

*Fig. 4.4.11 CBED patterns for the precipitate lamellae in **alloy E (0.04wt%Nb;1.18wt%V)**, showing (a) the [1-10] austenite zone axis pattern, (b) the [1-210] zone axis for the HCP system and (c) SAD pattern for the [11-2] austenite zone axis showing extra reflections that correspond to the [10-10] HCP zone axis, together with superlattice reflections.*

*Table 4.4.2 Lattice parameter values calculated for the lamellar precipitates in alloy C and alloy E together with the published values *after Goldschmidt[41].*

	a (Å)	c (Å)
Chromium Nitride (Cr_2N)*	**2.75**	**4.44**
Vanadium Nitride (V_2N)*	**2.82**	**4.54**
Alloy C *(lamella) – [1-210]*	2.79	4.62
Alloy C *(lamella) – [10-10]*	2.82	4.8
Alloy E *(lamella) – [1-210]*	2.57	4.71
Alloy E *(lamella) – [10-10]*	2.82	4.66

The predictions made by Thermocalc for the eight alloys at 800°C agree with the experimental results. M_2X precipitation was observed in all eight alloys after ageing at 800°C, in the form of discontinuous cellular precipitates with a lamellar structure. Sigma phase was also observed in alloys C and E and based on the predictions it is probable that sigma phase was present in all of the alloys after ageing at 800°C. The only phase that was not observed was $M_{23}(CN)_6$. The isopleth diagram does however illustrate equilibrium conditions, which might not have been reached after ageing for 100 hours. Ferrite was only observed in alloy D but not in the other alloys as predicted by Thermocalc but this is discussed in section 3.2.7.

4.4.3 NUCLEATION AND GROWTH OF DISCONTINUOUS CELLULAR PRECIPITATES

The growth characteristics of the precipitate cells in alloy C were studied with the aid of an orientation map acquired using EBSD techniques in the same way as those presented in section 4.3.3. The orientation of the austenite in the precipitate colonies was determined with respect to the surrounding austenite matrix. The structure of the precipitate cells was much finer after ageing at 800°C compared to ageing at 1000°C; however the austenite between the precipitates could still be indexed and the orientation with respect to the surrounding grains could be determined. Figure 4.4.12 (a) shows a backscattered image showing the individual lamellae within a number of different cells with the formation of sigma phase on the cell boundaries. Figure 4.4.12 (b) shows the orientation map that was taken from the field of view shown in figure 4.4.12 (a) with like orientations in the same colour.

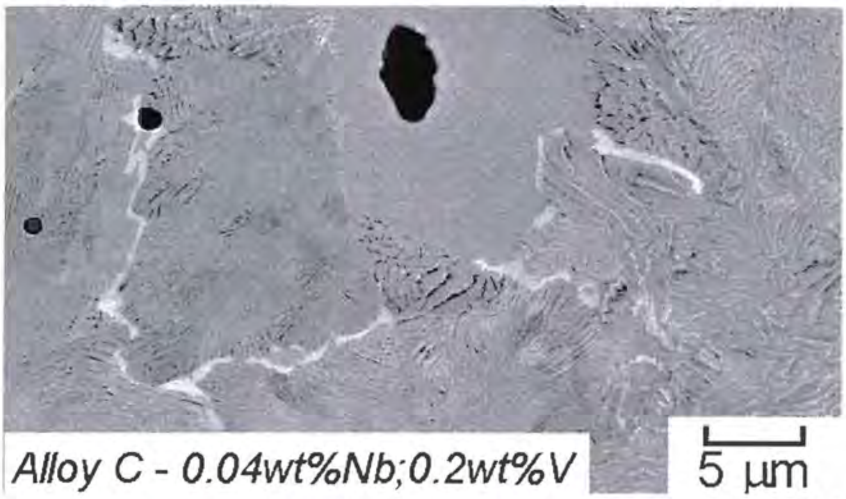

Fig. 4.4.12(a)

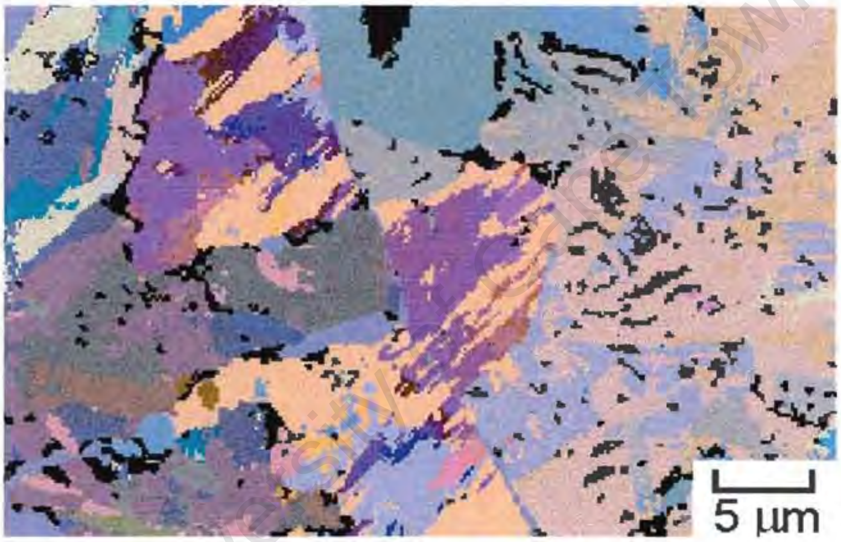

(b)

Fig.4.4.12 (a) SEM (backscattered electrons) image of alloy C after ageing for 2 hours at 1000 °C, showing the of the field of view from which the orientation map was acquired, shown in (b).

As in the case of ageing treatments at 1000°C of alloy C, the formation of twins within the precipitate cells was also observed after ageing alloy C at 800°C. Figure 4.4.13 shows a figure generated from the orientation information at the same magnification as the orientation maps, and marks the high angle grain boundaries in black and the special Σ3 twin boundaries in red. Twin formation is more prolific after ageing at 800°C than after ageing at 1000° C, which can be seen by comparing figure 4.4.13 with figure 4.3.17 (a).

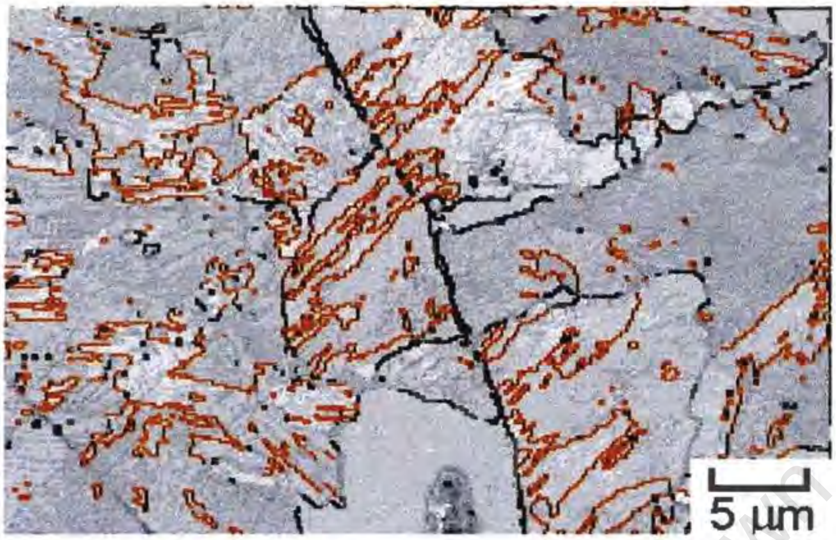

Fig. 4.4.13 Figure showing the number of special Σ3 twin boundaries to high angle grain boundaries in the field of view from which the orientation map was acquired.

Finally, the nucleation characteristics of the precipitate lamellae in alloy C were investigated by studying samples of alloy C after ageing at 800°C for 5 and 10 minutes. Evidence of the 'Pucker' mechanism proposed by Tu and Turnbull[53,54] was found and is shown in figure 4.4.14. The precipitate has formed in the boundary and appears to be pulling the boundary into what Tu and Turnbull called the 'Puckered configuration'.

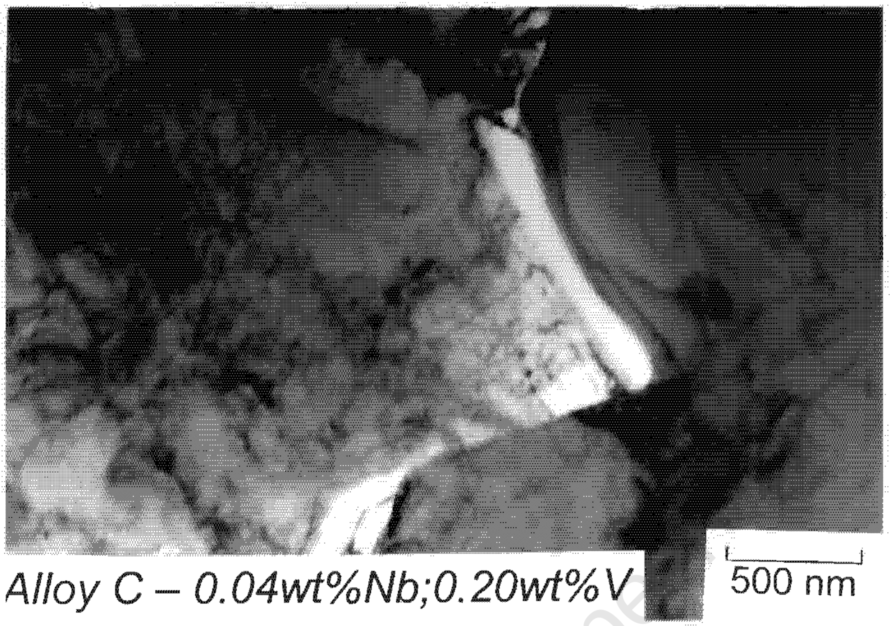

Fig.4.4.14 TEM image of alloy C after ageing for 10 minutes at 800 °C, showing nucleation of a precipitate in the grain boundary and the influence of the precipitate on the boundary.

4.4.4 MECHANICAL BEHAVIOUR

Specimens of alloys A, C, D, E and H were aged for two hours at 800°C and tensile test curves for each alloy were obtained. The tensile test curves for these alloys are shown in figure 4.4.15, together with the curve for alloy C in the solution treated condition for comparative purposes. All of the alloys showed a significant decrease in ductility as a consequence of ageing at 800°C, which can be attributed to the formation of lamellar precipitates and sigma phase. In spite of the marked increase in yield strength it was concluded that wear tests on these alloys would not be of any use. The tensile properties of each of the specimens were calculated from the tensile test data and the results are shown in table 4.4.3.

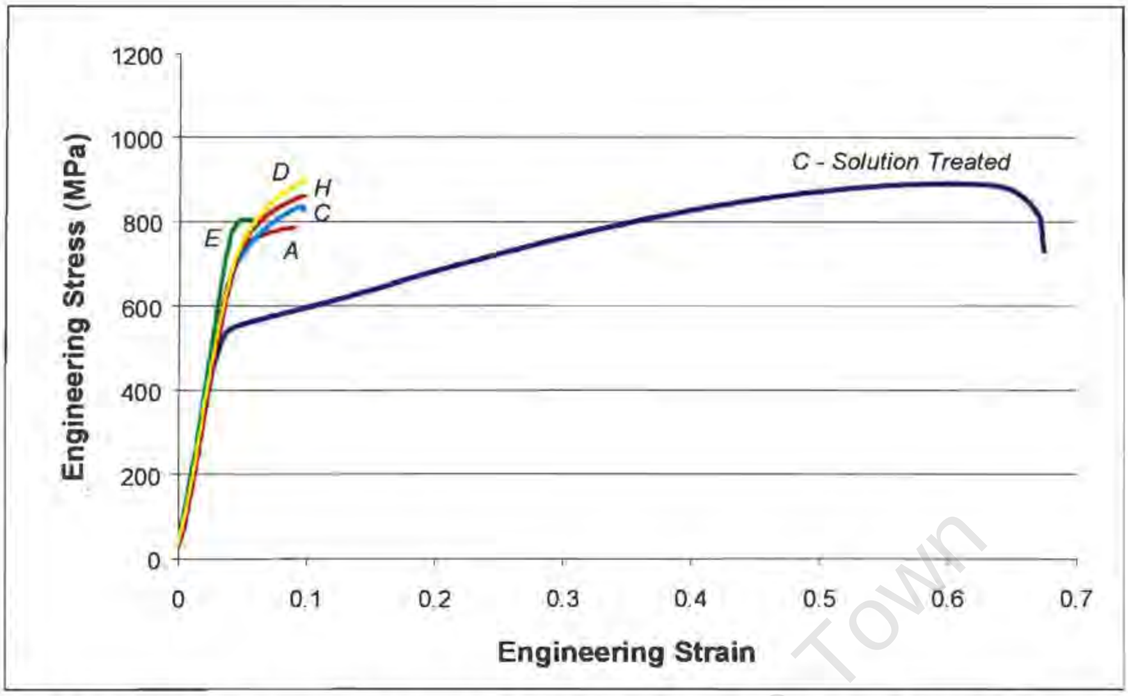

Fig. 4.4.15 Tensile test curves for alloys A, C, D, E & H after ageing at 800 °C for two hours, together with the curve for alloy C in the solution treated condition to highlight the loss of ductility as a consequence of ageing.

Table 4.4.3 *Tensile properties of alloys A, C, D, E & H after ageing for two hours at 800 °C together with the results of alloy C in the solution treated condition (C-0.0hrs) for comparative purposes.*

Alloy	***Yield Strength***	***Ultimate Tensile Strength (MPa)***	***Total Elongation to Failure (%)***	***Plastic Elongation to Failure (%)***
C Solution Treated	548	889	67	63
A	742	786	9	4
C	633	700	7	2
D	755	861	10	5
E	800	805	6	1
H	739	828	10	3

4.4.5 SUMMARY: AGEING TREATMENTS AT 800°C

Lamellar precipitation was observed in all of the alloys after ageing at 800°C. The lamellar precipitates were identified as M_2X type precipitates with a HCP crystal structure rich in chromium. Based on the results of ageing treatments at 1000°C, these precipitates are probably also rich in vanadium when they occur in alloys containing vanadium. Alloy E showed a greater volume fraction of lamellar precipitates after ageing at 800°C for two hours than the other alloys. Alloy D showed less lamellar precipitation than alloy C after ageing at 800°C. Sigma phase was observed in alloys C and E and was found to be rich in chromium and to have the expected tetragonal structure with lattice parameter values that agreed with published values. The isopleth diagram shown in figure 4.4.1 shows a good representation of M_2X precipitate formation in these alloys and can therefore be used as a summary of the microstructural evolution in these alloys. The information regarding the presence of ferrite should, however, be ignored and it should also be noted that $M_{23}(CN)_6$ precipitates could possibly form after ageing times longer than 100 hours.

Investigation of the nucleation and growth of the discontinuous precipitate cells after ageing at 800°C showed that twin formation within the cells was more prolific than after ageing treatments at 1000°C. Characteristics of the 'Pucker mechanism' during nucleation of the precipitates were also found in alloy C.

Ageing treatments at 800°C caused a significant loss in ductility of the steel as a consequence of lamellar precipitation and the formation of sigma phase. No abrasive wear tests were conducted after ageing at 800°C because of the embrittlement that resulted from such heat treatments.

4.5 SUMMARY OF PRECIPITATE FORMATION IN THE HIGH NITROGEN STEEL ALLOYS

Three different forms of precipitation were observed in the eight high nitrogen steel alloys after different heat treatments. M_2X precipitate formation was observed after ageing at 800°C, 1000°C and in some alloys 1100°C. MX precipitation formed as a solid state precipitation reaction at 1100°C and in some alloys at 1000°C. MX precipitates also formed during solidification but were larger than those that formed in the solid state. These MX precipitates had a blocky morphology and did not dissolve during any cost effective solution treatments.

The niobium and vanadium balance in the alloys influenced each of the different forms of precipitation. Alloys with niobium additions contained large blocky precipitates after solidification, while those with no niobium additions did not. MX precipitation was favoured at 1100°C by niobium and vanadium additions, but this form of precipitation was only observed in alloys with a specific niobium and vanadium balance. M_2X precipitation was observed at 1100°C in alloys in which the niobium and vanadium balance did not favour MX precipitation. Ageing at 1000°C resulted in extensive discontinuous cellular precipitation of M_2N precipitates, which was expected in this alloy owing to the high nitrogen and chromium levels. This reaction was more prolific in alloy E and less prolific in alloys A, B, F, G and H. The reaction was not observed in alloy D, ie when niobium was added without vanadium. M_2X precipitation was also observed after ageing at 800°C in all of the alloys and again was more prolific in alloy E than in the other alloys.

These three different forms of precipitation had different effects on the mechanical properties. Blocky precipitates were detrimental to the toughness of the steel, and the presence of these precipitates reduced the Charpy V-notch toughness considerably compared to alloy C, which had no blocky precipitates. The blocky precipitates also reduced the wear resistance of the high nitrogen steel alloys compared to the high nitrogen steel base alloy, (alloy C). The yield strength and elongation to failure of the alloys was not significantly influenced by the formation of the large blocky precipitates.

The formation of MX precipitates showed some potential for improving the strength of the high nitrogen steel alloys after ageing at 1100°C but reduced the ductility of the steel. M_2X precipitation had a more significant effect on the ductility of the steel, lowering it considerably especially after ageing at 800°C.

Table 4.5.1 shows a summary of the effect of ageing treatment and microstructure on precipitate formation in the high nitrogen steel alloys as well as the effect of each type of precipitate on mechanical properties.

Table 4.5.1 Summary of the effect of ageing temperature and alloy composition on precipitate formation in the high nitrogen steel alloys.

	Blocky MX Ppts	***Fine MX Ppts***	***M_2X Ppts***
Alloy Composition	Observed in alloys A, B, D, F, G & H but not C and E. Observed even at low Nb levels Favoured by Nb, V participates but does not promote the reaction. .	Observed in alloys A, D and H in the absence of M_2X ppts. Observed in alloy B together with M_2X ppts Favoured by Nb, but V participates in the reaction.	Formed more prolifically in alloy E and less prolifically in alloy D. V favoured the formation of M_2X ppts, resulting in a V and Cr rich M_2X ppt. Nb suppressed the formation of M_2X. Combined additions of Nb and V showed effects of both elements.
Heat Treatment Temperature	Form on solidification and do not dissolve during solution treatments at 1300°C.	Form as a solid state reaction on ageing at 1100°C. Also observed on ageing at 1000°C in alloy D in the absence of M_2X ppts.	Observed in all alloys at 800°C. Observed in all alloys except alloy D at 1000°C and observed in alloys B, E, F, G at 1100°C. Precipitation mode changed from discontinuous to continuous in alloys A, B, F, G and H at 1000°C and B, E, F & G at 1100°C.
Effect of ppts on Mechanical Properties	Detrimental to toughness & abrasive wear resistance. Little effect on tensile properties.	Improve strength to some extent and is dependent on ageing time at 1100°C. Reduce elongation to failure. Abrasion resistance is dependent on ageing time.	Caused loss of ductility and reduced abrasion resistance

5. DISCUSSION

The motivation for niobium and vanadium additions to the high nitrogen steel base alloy was to cause the precipitation of fine MX precipitates that would strengthen the steel for improved wear performance. Few results had been previously reported on the influence of niobium and vanadium additions on precipitation reactions in high nitrogen steels. The current investigation has shown that the addition of niobium and vanadium promotes precipitation reactions that were not expected in high nitrogen steels. These include MX precipitates that form on ageing and the formation of large blocky MX precipitates during solidification. The extent of MX precipitate formation during ageing treatments and during solidification is dependent on the niobium and vanadium balance in the alloy. Further the addition of niobium and vanadium affect the formation of precipitates that are expected in high nitrogen steels, ie chromium nitrides (Cr_2N). The presence of these precipitates all had some effect on the mechanical behaviour of the alloys. The addition of niobium and vanadium to the high nitrogen steel base alloy therefore, influenced the mechanical behaviour of the steel through the effect of these elements on the precipitation reactions observed in the system.

The evolution of each form of precipitation observed in the current system is discussed, with emphasis on the effect of niobium and vanadium additions on the precipitation reaction. In addition, the influence of these precipitation reactions on the alloys is discussed with particular reference to the wear performance of the steel. Finally, the feasibility of niobium and vanadium additions to the high nitrogen steel base alloy is discussed by considering the advantages and disadvantages for the addition of each element.

5.1 PRECIPITATE FORMATION DURING SOLIDIFICATION

5.1.1 MICROSTRUCTURAL EVOLUTION

The addition of niobium to the high nitrogen steel base composition promotes the formation of large blocky precipitates during solidification. These precipitates form eutectically with the austenite during the final stages of solidification and are rich in niobium. The formation of these precipitates is a direct consequence of the niobium additions, since these precipitates are not observed in the base alloy, but are observed when 1.17 wt% niobium was added to the base alloy (alloy D). Vanadium additions of 1.18 wt% alone to the base composition do not result in the formation of eutectic precipitates and no blocky precipitates were observed in the solution treated condition of alloy E. Although vanadium additions do not favour the formation of the blocky precipitates, they do participate in the eutectic reaction in the presence of niobium. When niobium and vanadium are both added to the base composition, regardless of the levels of each, eutectic precipitates are observed and they are rich in both niobium and vanadium.

Eutectic precipitates in binary alloys usually take on a lamellar morphology, which is termed a normal structure and occurs when both phases have low entropies of fusion[133]. It is possible however, that eutectic phases with an anomalous structure form when one of the eutectic phases has a high entropy of fusion and is capable of facetting[133]. This offers some explanation for the morphology of the eutectic precipitates observed in the high nitrogen steel alloys. It must also be considered that the current system is a multicomponent system and the behaviour of binary alloys during solidification can only be used as a guide to understand mechanisms in these more complex systems. The blocky precipitates that are observed in the current system do not possess the classic lamellar morphology of eutectic phases in binary systems, but this does not exclude the possibility that they have formed eutectically.

The Scheil-Gulliver simulations predict the solidification path of alloys under the following conditions: the solid-liquid interface is always at equilibrium, and after each step the solid that has formed is removed from the system, thus back diffusion in the solid is ignored in the calculations. One result of employing such criteria is that the segregation of alloy elements in the liquid may be overestimated. The segregation of elements such as chromium, manganese and vanadium might be overestimated by the calculations, since the diffusion of these elements into the bulk solid from the solidified surface is ignored. Niobium however, is a large element, and therefore would be expected to diffuse more slowly than the other elements. The atomic radius of iron, chromium, manganese, niobium and vanadium are given in table 5.1.1[134]. The Goldschmidt radius has also been given in the table, which gives the radius of the atom in an FCC crystal. The Goldschmidt radius therefore gives the size of the atom taking into account the co-ordination number of the atom associated with FCC packing[135]. Both values show that niobium is larger than the other elements in the system, and vanadium, chromium, manganese and iron are all a similar size. The diffusivity of niobium and vanadium was calculated in iron, and the calculations show that at 1200°C the diffusivity of niobium is three times slower than vanadium[134]. For this reason, Scheil-Gulliver simulations might not overestimate the segregation of niobium. The segregation of alloy elements during solidification promotes the formation of eutectic precipitates.

Table 5.1.1 Size of atoms of the elements present in the high nitrogen steel system.

	Atomic Radius [134] ***(Å)***	***Goldschmidt Radius*** [135] ***(Å)***
Iron	1.26	2.57
Chromium	1.27	2.57
Manganese	1.30	-
Vanadium	1.36	2.71
Niobium	1.47	2.94

The formation during solidification of blocky precipitates with an MX stoichiometry and an FCC crystal structure, has been reported in mild steels[99,100,101,112], high strength low alloy steels[104,105,108,109,110], superalloys[103], stainless steels[97,98] as well as high nitrogen steels[42]. In most of these cases these precipitates have formed eutectically, as a last phase to form during solidification together with the austenite, and it has been shown that niobium additions strongly favour the reaction, especially in the presence of nitrogen[99,105,108]. This evidence further supports the conclusion that the large blocky precipitates in the current system are a consequence of an eutectic reaction, favoured by the niobium additions to the steel and also by high nitrogen levels associated with the high nitrogen steel alloys investigated.

The large blocky precipitates in the niobium containing alloys did not dissolve during a solution treatment at 1300°C for two hours and any further treatments at 1300°C would not be cost effective in the production of the steel. Solubility product calculations for carbides and nitrides of niobium and vanadium, as well as mixed forms of these precipitates, have shown that the niobium nitrides and carbides are the most insoluble of these precipitates[109,111,112]. In the case of mixed precipitates, an increase in niobium level in the precipitate causes greater insolubility and nitrogen has the same effect[112]. Based on these reports the blocky precipitates observed in the current study are not expected to dissolve during any cost effective solution treatment. The formation of these precipitates therefore represents a considerable waste of alloy elements, since the niobium additions were intended for solid state precipitation reactions and not eutectic reactions during solidification.

A further consideration was that the precipitation of these large blocky precipitates would remove large amounts of nitrogen from solid solution and thus reduce the strengthening effect that this element has when it is in solid solution. Calculations show that if all the niobium atoms formed MX precipitates in alloy D (1.17 wt%Nb) during solidification, the amount of nitrogen that would remain in solid solution would be approximately 0.84 wt%, which is a decrease from 1.02 wt%. The influence that niobium has on solid state precipitation reactions shows that a large amount of niobium remains in solid solution after solidification. Since a significant amount of niobium remains in solid solution after solidification, the level of nitrogen that is removed as a result of eutectic precipitate formation will be less than what was calculated (0.18 wt%). When the same calculation is repeated for alloy F, and it is considered that all of the niobium and vanadium is used during eutectic precipitation, then the amount of nitrogen that would remain in solid solution is 0.58 wt%, which is a decrease from 0.98 wt%. It is not expected either that all of the niobium and vanadium is used up during precipitate formation during solidification of alloy F. Since there is evidence that there are appreciable amounts of niobium and vanadium in solid solution after solidification, it is doubtful that the decrease in nitrogen levels calculated for alloy F is as great as 0.4 wt%. In addition, the volume fraction of blocky precipitates in alloy D is similar to alloy F, which shows that approximately the same amount of nitrogen is removed from solid solution as in alloy D, which is less than 0.18 wt%.

Since the precipitates that form during solidification, as a result of niobium additions do not dissolve during any cost effective solution treatment, their influence on mechanical properties must be carefully considered. Any benefit to mechanical properties derived from precipitation reactions during ageing treatments, as a result of niobium additions, will be superimposed on the influence of the blocky precipitates.

5.1.2 MECHANICAL BEHAVIOUR

The most significant effect of the blocky MX precipitates on the mechanical behaviour of the steel is their effect on the toughness. The Charpy V-notch toughness was reduced considerably as a result of the eutectic precipitates, even when the volume fraction of the precipitates was low. Charpy V-notch test results showed that alloy C displayed a toughness of between 69-114 Joules, whereas the toughness of the other alloys was below 10 Joules. In spite of the effect of these precipitates on the toughness of the steel, their presence did not significantly limit the materials' ability to plastically deform at low strain rates. The presence of the blocky precipitates did not improve the hardness or the yield strength of the steel significantly. In view of the limited effect of the blocky precipitates on the tensile behaviour of the steel, their effect on toughness is surprising. Other authors however, have shown that niobium rich eutectics do embrittle the steel[99,100]. The formation of these precipitates is therefore not beneficial, since they reduce the toughness of the steel considerably without any improvement in strength.

The wear performance of the alloys that contain blocky eutectic precipitates further illustrates the disadvantage of these precipitates in the high nitrogen steel alloys. The blocky precipitates represent hard particles, which the abrasive particles should not be able to cut, yet the wear performance of the alloys with blocky precipitates is considerably reduced compared to alloys C and E, which contain no blocky precipitates. Alloys with blocky precipitates showed a similar capacity for plastic work to alloy C, but the abrasion resistance was considerably lower. Studies of the wear surface show that the blocky precipitates have microfractured during abrasive wear. In spite of these alloys having a good capacity to plastically deform, it is probable that the wear debris from the blocky particles participated in further material removal from the wear surface, thus increasing the wear rate of these alloys. The wear surfaces of alloys C and E in the solution treated condition show work hardened shear lips on the abraded surface, which indicates that the superior wear performance of alloys C and E is a consequence of the materials' ability to work harden.

The formation of blocky precipitates during solidification, as a result of niobium additions, was neither intended nor anticipated. Although the formation of large eutectic precipitates did not remove significant amounts of nitrogen from solid solution, and appreciable amounts of niobium and vanadium were still available for solid state precipitate reactions, the current investigation has shown that these precipitates present no advantage to the mechanical performance of high nitrogen steel alloys. Any improvement in strength, gained from the formation of precipitates during ageing, will be offset by the effect of the large blocky precipitates on the toughness and wear performance of the steel. Thus the true effect of a fine dispersion of precipitates on strength, toughness and wear performance of the high nitrogen steel alloys, as a result of niobium additions, cannot be characterised due to the formation of eutectic precipitates during solidification. Precipitate forming elements that do not result in large blocky precipitates during solidification should be added to the high nitrogen steels in order to form a fine dispersion of precipitates during ageing. Although vanadium does not result in the formation of large blocky precipitates on solidification, there are other disadvantages associated with vanadium additions to the high nitrogen steel alloy system, discussed in the sections that follow.

5.2 THE FORMATION OF FINE PRECIPITATES

5.2.1 MICROSTRUCTURAL EVOLUTION

The formation of fine precipitates in the range of alloys that were studied is most prolific at 1100°C and is largely the result of niobium additions to the base composition. Diffraction studies have shown that the fine precipitates have a NaCl crystal structure with a cube-cube orientation relationship with the matrix. Such precipitates are known to have an MX stoichiometry, where the metallic constituent of the precipitate can be a mixture of precipitate forming elements, in this case niobium and vanadium[41]. These precipitates were observed to nucleate on dislocations within the grains and on grain boundaries, resulting in a homogeneous distribution of precipitates. After short ageing times the particles are approximately 50 nm in size or smaller, but after ageing for longer times the precipitates grow to approximately 200 nm, depending on the alloy composition.

Niobium and vanadium have been added to stainless steels in the past to prevent chromium nitride precipitation (Cr_2N and $M_{23}(CN)_6$) at high temperatures by causing MX precipitates to form preferentially. The addition of niobium to the high nitrogen steel base composition has been shown to promote the formation of niobium rich MX precipitates. Further, at 1000°C where the formation of M_2X lamellae are observed in the base composition, no lamellar precipitation is observed in alloy D, which has the highest niobium level. Thus niobium additions of 1.17 wt% to the high nitrogen steel alloy system have successfully stabilised this high nitrogen steel alloy against the formation of chromium nitrides at 1000°C. The addition of niobium was not as successful at 800°C, where a small volume fraction of lamellar precipitates (compared to alloy C) were observed to form in alloy D at this temperature. Vanadium additions have the opposite effect to niobium on chromium nitride formation in the alloys. Chromium nitride precipitation was not observed to be stable at 1100°C in the base composition, but vanadium additions favoured the formation of M_2X precipitates at 1100°C. Further, at temperatures where this form of precipitation was stable in the base composition, vanadium additions enhanced the reaction. Vanadium additions therefore did not stabilise the steel against the formation of chromium nitride precipitates but rather resulted in exaggerated M_2X precipitation rich in chromium and vanadium.

Chromium nitride precipitates (Cr_2N) were expected to form in the high nitrogen steel alloys but these precipitates were not expected to be rich in vanadium. Other authors have shown some evidence that vanadium participates in chromium nitride precipitation. It has however previously been reported that vanadium additions to a stainless steel accelerated the formation of $M_{23}(CN)_6$ and promoted the formation of V_2C precipitates[93]. Chromium nitrides have an M_2X stoichiometry and it has been demonstrated that the M constituent of these precipitates can form a solid solution of elements with similar size[41]. Since V_2N and Cr_2N possess a similar lattice parameter, a mixed $(CrV)_2N$ precipitate is feasible. Further discussion on the effect of vanadium on stabilisation of the M_2X precipitate outside of the temperature range where it is observed in the base composition follows in section 5.3.1

The objective of the niobium and vanadium additions to the high nitrogen steel base composition was to promote the formation of fine MX precipitates during ageing treatments at elevated temperature. The addition of both niobium and vanadium to the current multicomponent system resulted in two precipitation reactions: MX precipitation and M_2X precipitation. These two precipitation reactions competed with one another, according to the niobium and vanadium balance in the alloy, and this competition was especially evident at 1100°C. Two extreme conditions are illustrated by the results of ageing treatments at 1100°C on alloys D and E and these results show the individual effect of niobium (alloy D) and vanadium (alloy E) on precipitate formation in the high nitrogen steel alloys. Niobium additions promote the formation of MX precipitates at 1100°C and vanadium additions promote the formation of M_2X precipitates at 1100°C. Combined additions of niobium and vanadium show the influence of either niobium or vanadium, depending on the balance of these elements, at 1100°C. Since it is the formation of MX precipitates that is required for improved mechanical behaviour, the addition of these two elements must be balanced to avoid the formation of lamellar M_2X precipitates in the temperature range where MX precipitation is expected (1100°C in the current system). The niobium and vanadium balance in alloys B, E, F and G did not achieve this objective since M_2X lamellae formed at 1100°C in all of these alloys. In contrast, the niobium and vanadium additions in alloys A, D and H were balanced so that a fine distribution of MX particles formed, without any evidence of lamellar precipitation.

The formation of M_2X precipitates in alloy E after ageing at 1100°C has been shown to reduce the wear resistance of the steel considerably. These results are shown in figures 4.2.29 and 4.2.30. In contrast, abrasive wear tests on alloys A, D and H containing fine MX precipitates that formed during ageing at 1100°C show some potential for improved wear performance (figures 4.2.28 (a)-(c) and figure 4.2.30). These results show that in order to produce a homogenous distribution of MX precipitates that have the potential to improve wear performance, the formation of M_2X precipitates at 1100°C should be avoided. It was considered useful therefore to have an index that could determine the role of niobium and vanadium on the type of precipitate (M_2X or MX) reaction that would occur on ageing at 1100°C. This index could be used in industry to predict the precipitation reaction that would occur for various combinations of niobium and vanadium not investigated in this project.

5.2.1.1 INDEX PROPOSED FOR PREDICTION OF PRECIPITATION REACTIONS AT 1100°C

An index is proposed which is calculated on the basis of the vanadium influence on M_2X formation. The equation for the index (V_{in}) is given below and is based on the microstructural characterisation of the eight high nitrogen steel alloys after ageing at 1100°C. The results show that an addition of 1.18 wt% vanadium to the base composition resulted in M_2X precipitation at 1100°C. No M_2X precipitation was observed at 1100°C in alloy C. This shows that an addition of 0.2 wt% vanadium is ineffective at forming M_2X precipitates at 1100°C. The effective concentration of vanadium, which contributes to M_2X precipitation, is therefore 0.2 wt% less than the actual concentration. For alloys with combined additions of niobium and vanadium, the influence of niobium on MX precipitation must also be included in an equation for the index. For each alloy therefore, the vanadium level less 0.2 wt% (the effective concentration for M_2X precipitation) is determined as a fraction of the total addition of precipitate forming elements. The equation given for V_{in} gives this fraction and expresses therefore the effect of vanadium on M_2X precipitation at 1100°C when both niobium and vanadium are added to the base composition. The equation is an expression of the competition between MX and M_2X precipitation at 1100°C as a function of niobium and vanadium additions. Any equation for niobium influence would have been complicated by the 0.2 wt% vanadium addition to the high nitrogen steel base composition. An index for niobium, therefore is not simply the converse of V_{in}.

$$V_{in} = \frac{wt\%V - 0.2}{(wt\%V - 0.2) + wt\%Nb}$$

The value of V_{in} for each of the alloy compositions was determined and the results are shown in table 5.2.1. These values together with the microstructural results of ageing treatments at 1100°C give an indication of which type of precipitate (MX or M_2X) to expect on ageing at 1100°C. The value of V_{in} can be determined for other combinations of niobium and vanadium and some predictions can be made regarding the formation of either MX or M_2X precipitate at 1100°C.

Table 5.2.1 V_{in} ratios calculated for each of the high nitrogen steel alloys.

Alloy	**A**	**B**	**C**	**D**	**E**	**F**	**G**	**H**
V_{in}	0.29	0.65	0.00	-0.08	0.96	0.45	0.48	0.05

The values for V_{in} for alloys D (representative of 1.17 wt% niobium) and E (representative of 1.18 wt% vanadium) give the minimum and maximum values for these calculations. The value for alloys C, D and E give the boundary conditions for the proposed index. The value for alloy C is 0.00, which corresponds to the absence of M_2X precipitation at 1100°C, and is consistent with the experimental results. In contrast, the value for alloy E is 0.96, which represents the maximum value of V_{in} for the current investigation and corresponds to the largest volume fraction of M_2X precipitation that was observed in this alloy system after ageing at 1100°C. The value of V_{in} for alloy D is –0.08, which is representative of a minimum value for the current investigation and corresponds to no M_2X precipitation at 1100°C. When these values are compared with the experimental results, they show that the index gives a reliable prediction of the precipitation reaction that will occur in each of the alloys. It is the values between V_{in} for alloy D and V_{in} for alloy E that are of most interest since these represent the competition between the effect of vanadium and niobium on M_2X precipitation and MX precipitation respectively. V_{in} for alloys H and A are below 0.3, and no lamellar precipitation was observed in these alloys at this temperature. In contrast, the values for V_{in} for alloys B, F and G are greater than 0.45 and M_2X precipitation was observed in each of these alloys. The value for V_{in} therefore must be less than 0.45 so that M_2X precipitation is avoided. There is no niobium and vanadium balance that will give a value of V_{in} between 0.3-0.45 therefore, it is not clear whether such additions will result in lamellar precipitation or not. The value of V_{in} however, has given a useful indication of whether or not M_2X precipitation will occur at 1100°C as a result of the niobium and vanadium balance in the alloy. A final consideration is that the index must be used in conjunction with the knowledge that niobium additions favour MX precipitation. When the value of V_{in} is below 0.45 no M_2X precipitation occurs, and instead MX precipitation occurs because of the niobium levels. The value for V_{in} for alloy C is also below 0.45 but because there is little niobium in this alloy no MX precipitation is observed in the absence of M_2X precipitation.

5.2.2 MECHANICAL BEHAVIOUR

5.2.2.1 *TENSILE PROPERTIES OF THE HIGH NITROGEN STEEL ALLOYS*

The tensile test results for alloys A, D and H where MX precipitation was observed have shown that the formation of these precipitates during ageing improves the strength of the steels compared to their solution treated counterparts. Thus the basic objective, to improve strength by the formation of a fine dispersion of precipitates, can be achieved in the high nitrogen steel alloys by ageing at 1100°C, provided the niobium and vanadium balance favours MX precipitation. In addition to improved strength as a result of the presence of MX precipitates, ageing at 1100°C also decreased the elongation to failure of alloys A, D and H. The tensile test results for these three alloys after ageing for 0.5 hours, 2 hours, 5 hours and 10 hours show further that there is a common trend in the tensile results as a function of ageing time. Short ageing times are associated with relatively higher yield strengths and a lower elongation to failure, whereas longer ageing times are associated with comparatively lower yield strengths and a higher elongation to failure.

The purpose of the tensile tests was to determine the optimum ageing time for alloys A, D and H that would result in the best combination of yield strength and capacity for plastic work, since both yield strength and capacity for plastic work are important for improved abrasive wear resistance[117].

5.2.2.2 *ABRASIVE WEAR PERFORMANCE*

On the basis of classic models for volume (or mass) loss during abrasive wear, the total volume loss of material should be directly proportional to the abrasive path length[116]. From these models it is expected that any abrasive wear test result that shows volume loss (or mass loss) versus abrasive path length should exhibit a linear relationship between these two parameters[116]. Further, the degree of scatter about a best-fit straight line for such data should not be large. The best-fit straight line plotted for the data should also go through the origin of the graph. Intuitively there must be a zero mass loss at a path length of zero. These criteria give some indication of the efficiency of the abrasive wear test on the characterisation of abrasive wear performance of a material. If the data used to characterise the abrasive wear performance of a material do not meet these criteria, then the measured abrasion resistance of the material cannot be considered accurate.

The abrasive wear results that have been generated for alloys A, C, D, E and H in the current investigations were plotted as cumulative mass loss versus the abrasive path length. Volume loss was not calculated since each specimen has the same density. The results of abrasive wear tests show considerable scatter about a possible best-fit line. In addition, careful study of the data shows that the best-fit line seldom goes through the origin of the mass loss versus abrasive path length axes.

The pin on belt apparatus used for the current investigation has given reasonable characterisations of the abrasive wear resistance of many engineering materials, including high nitrogen steel alloys[136,137]. The scatter in the results therefore cannot be attributed to the apparatus used for the characterisation of abrasive wear performance. A possible explanation for the experimental error observed in the abrasive wear results is the inhomogenities associated with cast materials. Cast materials are also known for extensive porosity and it is probable that the scatter in the abrasive wear test results is the result of both porosity and inhomogenities in the cast high nitrogen steel alloys.

Examination of the abrasion results of alloys A, C, D, E and H in the solution treated condition (figure 4.1.14) show that there is more scatter in the results of alloys A, D and H than alloys C and E. Further, the results from alloys C and E show that a best-fit line plotted for these results would go through the origin, which is not the case for alloys A, D and H. This suggests that the scatter observed in the abrasive wear results for alloys A, D and H might also be a result of the large blocky precipitates. It has been previously demonstrated that if there are hard particles in a softer matrix and they are of a comparable size to the scale of the abrasion damage or larger, then the material will respond to abrasive wear

heterogeneously[116]. It can be seen from figures 4.1.2 (c), 4.1.4 (a) and (d) that the abrasive wear particles are smaller than the blocky precipitates present in alloys A, D and H. Any heterogeneity associated with the blocky precipitates in alloys A, D and H will be carried though to the abrasive wear results on aged samples of these alloys because the blocky precipitates remain after the solution treatment. The abrasive wear test results therefore cannot give a comprehensive characterisation of the abrasive wear performance of the specimens tested. The results have shown however that there are some trends that are consistent for alloys A, D and H and should be discussed. These trends however, must be considered in the context of the integrity of the abrasive wear characterisation of the high nitrogen steel alloys.
The abrasive wear tests on alloys A, D and H (figures 4.2.28 (a), (b), (c) and 4.2.30) firstly show that the presence of MX precipitates in the microstructure does not improve the wear performance of the alloys compared to alloy C, which contains no MX precipitation. This is the most obvious conclusion that can be drawn from the abrasive wear tests on alloys A, D and H after various ageing treatments at 1100°C. It is difficult to gauge the effect of the fine MX precipitates on the wear performance of the high nitrogen steel alloys, since these never formed in the absence of the large blocky precipitates. As has been discussed in section 5.1.2, these blocky precipitates reduce the wear performance of the steel compared to alloy C. It cannot be determined therefore whether fine MX precipitates in the absence of large blocky precipitates would improve the wear performance compared to alloy C.

The second trend that should be noted is that in alloys A, D and H the abrasion resistance of the alloys aged for shorter times was lower than the abrasion resistance for the longer ageing times. Further, in the case of alloys D and H, specimens aged for longer times resulted in abrasion resistance similar to that of the solution treated counterpart. Thus the results of abrasive wear tests on alloys A, D and H after ageing for different times show that the wear performance is somewhat dependent on the ageing treatment that the alloy received. It has been demonstrated that improved hardness results in improved wear performance[116]. Further, it has also been demonstrated that the materials capacity for plastic work and the workhardening ability are also properties that should be optimised for improved wear resistance[117,119]. The trend in the wear results of alloys A, D and H show that when the elongation to failure is greater and the yield strength lower, the wear resistance is improved. When the strength is improved at the expense of elongation to failure at shorter ageing times the abrasion resistance is lower. Thus these results indicate that the materials' ability to plastically deform should be optimised with improved strength during precipitate formation in order for the abrasion resistance to be improved.

The third most obvious result of the abrasive wear tests is that alloy E after ageing at 1100°C shows poor wear performance. The scatter in the data about a possible best-fit line for the results of abrasion tests for alloy E is particularly large. This alloy contains lamellar colonies that are frequently heterogeneously distributed in the austenite and possibly account for the scatter in the data for the tests on alloy E. The results do show that the precipitate distribution in alloy E resulted in poor abrasion resistance compared to alloys C and E in the solution treated condition, shown in figure 4.2.29). It has been reported by Hawk *et al* that during abrasive wear of steel with M_2X colonies of lamellar precipitates, microfracture occurs in the region of the precipitate colonies[107]. Should microfracture occur in the region of the discontinuous precipitate cell colonies, the wear debris from the cell regions results in a three body abrasive wear situation, resulting in rapid material removal from the abraded surface and poorer overall wear performance. This gives an explanation for the poor wear performance of this alloy and the errors associated with abrasion wear test data from alloy E after ageing at 1100°C for two hours.

The importance of the correct niobium and vanadium additions to the high nitrogen steel base alloy for improved wear resistance is illustrated by the abrasive wear results. In spite of the scatter in the abrasive wear results it can be concluded that the formation of M_2X precipitates results in poor abrasion resistance compared to those alloys with MX precipitates. When niobium and vanadium are added to the high nitrogen base alloy the levels should be adjusted so that M_2X precipitation is avoided and MX precipitation formed instead. The value for V_{in} (discussed in section 5.2.2.1) therefore must be less than 0.45 so that MX precipitation occurs in preference to M_2X precipitation. When the value of V_{in} for the niobium and vanadium balance indicates that MX precipitates will form, the alloy should be aged for longer ageing times; greater than two hours, for better wear resistance.

5.3 THE FORMATION OF LAMELLAR PRECIPITATES

5.3.1 MICROSTRUCTURAL EVOLUTION

The formation of M_2X lamellar precipitates was most prolific in the high nitrogen steel alloys during ageing treatments at 800°C and 1000°C. The formation of the lamellar precipitates proceeded as a discontinuous cellular precipitation reaction. Cell colonies evolved on grain boundaries that contained, in most cases, lamellar precipitates. The lamellar precipitates possessed an HCP crystal structure with an M_2X stoichiometry and an orientation relationship with the austenite matrix such that the close packed planes were parallel. This type of precipitate is normally a chromium rich nitride (Cr_2N), but in the case of high nitrogen steel alloys with vanadium additions, the precipitate was rich in both chromium and vanadium.

The discontinuous precipitate cells showed features that are typical of this type of reaction in high nitrogen steels and other steel systems[31,34,76,77]. The interlamellar spacing increased as boundary migration proceeded and the boundary frequently extended ahead of the precipitate lamellae. Further, the precipitates were fragmented in the precipitate colonies in some of the alloys. The migration front was characterised by a high angle grain boundary that left a colony of precipitate cells behind it. The precipitate cell took on the orientation of the growing grain as it consumed the adjacent grain. The original position of the boundary, where nucleation of precipitates occurred, was marked by a series of dislocations. Misorientation calculations showed that these dislocations marked a low angle boundary. In addition, dislocations, stacking faults and twins were also frequently observed to form in the austenite between the precipitate lamellae.

The precipitation of M_2X, observed in high nitrogen steel alloys, is typical of high nitrogen steels where the discontinuous cellular precipitation of Cr_2N has been widely reported[31,32,124]. The reaction in the current system can be classified according to the definitions given by Williams and Butler[50] and later by Findik[138] as a type 1 precipitate reaction as follows:

$$\gamma \rightarrow \gamma' + M_2X$$

Prior to the precipitation reaction, the austenite is supersaturated with nitrogen and to a lesser degree chromium. The supersaturated austenite (γ) transforms to an M_2X precipitate and less saturated austenite (γ') containing less nitrogen and chromium. In the case of the high nitrogen steel alloys in which the M_2X precipitates are rich in vanadium, the transformed austenite (γ') will also contain less vanadium.

Williams and Butler indicated in their review that there is no single mechanism that can explain the occurrence of discontinuous cellular precipitation that can be applied to the wide range of binary, ternary and more complex alloy systems in which it has been observed[50]. Many authors have proposed theories and conditions for the occurrence of the discontinuous reaction, but many of these explanations are only relevant to those systems that were investigated by the respective authors. It is clear from the work that has been reviewed here that precipitates should nucleate on a grain boundary and that the boundary should migrate in order for the precipitation reaction to proceed as a discontinuous cellular precipitation reaction. The origin of boundary migration is possibly the most important factor in the occurrence of discontinuous cellular precipitation (DCP). The difference between a series of grain boundary allotriomorphs and a discontinuous cellular precipitate cell containing lamellar precipitates is the boundary migration associated with the DCP reaction. The driving forces for boundary migration have been discussed extensively in sections 2.2.2.1 and 2.2.2.2. Each of these driving forces will be discussed with particular reference to the discontinuous cellular precipitation of M_2X in the current system. It is not expected that any one of these driving forces contributes solely to the total driving force for boundary migration, but rather boundary migration is a consequence of more than one of these effects.

The requirements for the 'pucker mechanism[53,54] are relevant to the current system and would thus support driving forces associated with precipitate/matrix interfacial energy effects. In the current alloy system, there is a high mismatch between the HCP M_2X precipitate and the FCC matrix and it has been shown that the precipitate favours a specific orientation relationship with the austenite matrix such that the close packed planes are parallel. Tu and Turnbull's theory has been criticised by several authors and many have suggested that the interfacial energy effects associated with the formation of a grain boundary precipitate cannot account for the total driving force for the boundary migration necessary, for the development of a precipitate cell[50,58]. It has been observed in alloy C after ageing for 10 minutes at 800°C that the boundary might have been pulled into the 'puckered' configuration. This is not sufficient to prove that the interfacial energy differences represent the only driving force for boundary migration in the current system. Further, evidence that 'puckering' of the boundary leads to interface migration has been reported to be lacking in systems where 'puckering' has been observed[50]. If this mechanism operates in the high nitrogen steel alloy system it is certain that other mechanisms must contribute to the total driving force for boundary migration.

Nes and Billdal proposed that the boundary is pulled by the capillary action of the precipitates, and this effect accounts for boundary migration during the development of a precipitate cell[59]. This theory cannot be applied to the current system, since the precipitates within the cell, in some cases, have a fragmented morphology. Such fragmented precipitates that form discontinuously are not able to exert a capillary effect on the grain boundary. Further, the cell boundary often bows ahead of the precipitates, which also shows that boundary migration is not the result of a capillary action of the precipitates.

Fournelle and Clarke suggested that any polycrystalline material will seek to decrease grain boundary area at elevated temperature by grain growth and that this accounts for the initial driving force for the boundary migration necessary for discontinuous cellular precipitation[61]. This theory also cannot account for boundary migration in the current system since the reaction occurred in specimens with a large grain size. In the absence of the discontinuous reaction, the driving force for grain growth would therefore be limited. Fournelle and Clarke also said that once the precipitate has nucleated, further migration is supported by the concentration gradient of solute in the boundary[61]. Tu[57] and Meyrick[60] showed that the boundary would migrate immediately after nucleation of a precipitate in search of more solute. Meyrick stated that the search for solute was necessary to keep the boundary energy at a minimum value, whereas Tu said that the solute would feed growth of the precipitate. Either way, the formation and growth of the precipitates on a boundary could then drive boundary migration. This mechanism requires that the solute for the precipitate growth is transported along the grain boundary. Solute driven boundary migration could certainly be applied to the current system.

Sulonen proposed that the driving force for boundary migration during DCP originated from a solute enriched or solute depleted zone ahead of the boundary, which caused coherency stresses in that region[63]. It has been previously shown during precipitation of $M_{23}C_6$ precipitates in an austenitic stainless steel that it was doubtful that this mechanism could account for the boundary migration during the discontinuous cellular reaction[34]. Chromium enrichment or depletion in a region ahead of the boundary would not significantly affect the lattice parameter of the austenite and would therefore not result in any coherency strain to drive boundary migration[34]. The precipitates that form discontinuously in the current high nitrogen steel alloys are rich in chromium and vanadium, a concentration of these elements will not affect the lattice parameter of the austenite significantly. It is doubtful therefore that a solute enriched or depleted zone (in chromium or vanadium) would exert any coherency strain in that region. Thus the coherency strain model would not make a significant contribution to the driving force in the current system. Hillert and Lagneborg[34] argued that it is the concentration gradient at the boundary at the point of precipitate formation that can result in local deviation from equilibrium conditions, and can account for migration of the boundary. Boundary migration is thus solute driven. Once boundary migration is initiated then the process is self-sustaining. The model proposed by Hillert and Lagneborg can be applied to the current system and is possibly the most significant driving force for boundary migration in the current high nitrogen steel alloys.

Similar driving forces to those that have been discussed for DCP are relevant to diffusion induced boundary migration[66]. The phenomenon that connects DIGM with DCP is the diffusion of solute along a migrating boundary. It has been said that DCP is a type of DIGM process[66]. Driving forces such as coherency strain effects and solute driven boundary migration are both relevant to DIGM and DCP. Such driving forces do not require precipitates to drive boundary migration unlike the 'pucker mechanism[53,54] and the capillary effects proposed by Nes and Billdal[59]. It is proposed therefore that the nucleation and growth of precipitates on a grain boundary results in conditions that favour migration of the boundary on which the precipitates nucleated. These conditions are similar to the conditions that favour DIGM: boundary diffusion of solute and solute driven boundary migration. Should these conditions arise and the boundary be mobile, then the series of grain boundary allotriomorphs will develop into a precipitate colony by a discontinuous cellular reaction. Conversely, precipitation might result in favourable conditions but if the boundary, where nucleation occurred, is not mobile then discontinuous cellular precipitation will not occur. Possible reasons for limited boundary mobility are that the solute atoms might exert a solute drag effect on the boundary. Further, the boundary might be pinned by another form of precipitation that does not form discontinuously.

The nucleation of precipitates on the boundary creates a solute depleted region around the precipitate. The driving force for the phase change that occurs at that temperature provides a driving force for precipitate growth. As the precipitate grows it removes solute from the grain boundary. In order for the precipitates to grow further, they are fed by the boundary diffusion of solute. The boundary migrates in search of more solute as describe by Tu[57] and Meyrick[60] for DCP, and also by Louat[74] for DIGM. At this point a composition gradient can be set up in the region of the boundary, which could create coherency stress[63]. Alternatively, a chemical driving force as a result of the steep concentration gradient of solute in the boundary[34] can develop which then drives boundary migration. Either way the nucleation of the precipitates on the grain boundary, together with the boundary diffusion of solute, have provided conditions under which either of these driving forces could operate. Figures 4.3.24 (a) and (b) show the nucleation of grain boundary precipitates in alloy C at 1000°C after ageing for 10 minutes. These precipitates are expected to develop into discontinuous precipitate colonies after longer ageing times at 1000°C. The micrographs show that at the point of nucleation the boundary migrates and bows between the precipitates. This observation indicates that boundary migration is either the result of the search for solute or the result of a compositional gradient. Boundary migration observed in the micrographs might also arise from coherency strain effects as a result of solute depletion in the region of the precipitate.

Once the discontinuous precipitation reaction has initiated, and precipitate lamellae begin to grow behind the migrating boundary, it proceeds as a type of DIGM process. The boundary diffusion of solute feeds the precipitates which act as receptors for the solute. Thus like DIGM, the solute is left behind in the form of solute rich precipitates, but instead of the alloyed zone that forms during DIGM, a two phase structure is left behind the migrating boundary. The reason that the boundary migrates ahead of the precipitate cells can now be explained in terms of the two possible driving forces for boundary migration that have been proposed (coherency strain effects or solute driven boundary migration). If the boundary migrates under the coherency strain driving force then it does so to annihilate the coherency strain that builds up ahead of the boundary. If the boundary migrates to search for solute then it will do so in order to eliminate the concentration gradient in the boundary. In the case of both of these driving forces, it is possible for the boundary to bow out ahead of the precipitates.

The current results show that both niobium and vanadium additions affect the discontinuous cellular precipitation of M_2X precipitates in the high nitrogen steel alloy system in some way. When vanadium is added to the steel, in the absence of niobium (alloy E), vanadium participates in the discontinuous cellular reaction, resulting in more prolific coverage of the specimen with precipitate colonies. This is observed consistently in alloy E after ageing at 800°C, 1000°C and 1100°C. In contrast, when niobium is added to the base composition (alloy D) no evidence of the discontinuous cellular precipitation of M_2X is found at the 1100°C and 1000°C ageing treatments. Instead of the M_2X precipitates, niobium rich MX precipitates have formed. When alloy D was aged at 800°C, discontinuous cellular precipitation of M_2X precipitates was observed, as it was in all of the other alloys. The volume fraction of lamellar precipitation, however, at 800°C was less than in the base composition, indicating that niobium suppresses the discontinuous cellular precipitation of M_2X precipitates during ageing at 800°C.

The influence of niobium and vanadium on M_2X precipitation is also observed in the alloys with combined additions of these elements. During 1100°C ageing treatments the niobium and vanadium balance determines whether or not the discontinuous cellular precipitation of M_2X will occur (this has been discussed extensively in section 5.2). During ageing treatments at 1000°C, the addition of both niobium and vanadium causes the mode of M_2X precipitation to change after extended exposure at 1000°C. The M_2X precipitates in alloys A, B, F, G and H, first form discontinuously and then after some time the discontinuous cellular reaction stops and the precipitates form continuously with a plate-like morphology. This was not observed in the alloy base composition (alloy C) or in alloy E. Instead, the discontinuous cellular reaction proceeded as a discontinuous coarsening reaction following the initial extensive coverage of the specimen with discontinuous precipitate colonies. The coarsening reaction occurred in such a way that the new precipitate colonies nucleate on the boundaries of the old colonies.

The influence of niobium and vanadium on the discontinuous cellular reaction in the current system is now considered on the basis of thermodynamic and kinetic effects that these elements have on M_2X precipitation.

5.3.1.1 INFLUENCE OF NIOBIUM AND VANADIUM ON THE THERMODYNAMICS OF THE DISCONTINUOUS CELLULAR PRECIPITATION REACTION

The formation of M_2X precipitates was observed in the base composition of the high nitrogen steel alloy between temperatures of 800°C-1000°C. Vanadium additions to the base composition caused this phase to be stable at 1100°C, ie at temperatures greater than where it is stable in the base composition. It is proposed therefore, that vanadium additions to the high nitrogen steel base composition expand the phase field for the M_2X precipitate to higher temperatures, up to 1100°C.

The M_2X precipitate is expected to occur at 1000°C and 800°C and is observed in alloy C in this temperature range. Since vanadium participates in the formation of M_2X precipitates, the addition of vanadium to the base composition results in an increase in the solute level (the metallic constituent (M)) with respect to the M_2X phase between 800°C and 1000°C. An increase in solute level causes an increase in the supersaturation of solute in the matrix, which has been reported to favour the discontinuous cellular precipitation reaction by increasing the driving force for the precipitation reaction[31,62]. This is observed in alloy E, where the discontinuous cellular precipitation of the M_2X lamellae is more prolific than in the base composition alloy, namely alloy C. Furthermore, during extended ageing treatments at 1000°C the discontinuous coarsening reaction is also more prolific in alloy E than in alloy C. Thus the addition of vanadium is proposed to increase the driving force for the discontinuous cellular precipitation of M_2X precipitates in the high nitrogen steel alloy system.

The addition of niobium also influences the stability of the M_2X precipitate in the temperature range that precipitation is expected to occur in the alloy base composition. The experimental results show that no M_2X precipitation is observed after ageing for 100 hours at 1000°C when 1 wt% niobium is added, in the absence of vanadium, to the base composition. This observation was supported by the results of Thermocalc, which show that no M_2X precipitation is to be expected in alloy D at 1000°C. Niobium additions therefore suppress the formation of M_2X precipitates at 1000°C in the current system. At 800°C the driving force for M_2X precipitation is greater. This is evidenced by the finer interlamellar spacing between the M_2X lamellae within the precipitate cells in alloys A, B, C, E, F, G and H after ageing at 800°C compared to ageing at 1000°C. The volume fraction of M_2X precipitates after ageing for 100 hours at 800°C is less in alloy D than in the base composition alloy. Thus niobium additions suppress the formation of M_2X precipitates at 800°C compared to the base composition.

Combined additions of niobium and vanadium to the base composition caused the precipitation mode of M_2X to change in alloys A, B, F, G and H during ageing at 1000°C. The M_2X precipitates first formed discontinuously and later continuously. This can be explained in terms of the thermodynamic effect of niobium on the stability of M_2X precipitates. Since a high driving force for precipitation favours the discontinuous cellular reaction over the continuous reaction[62], a decreased driving force for the M_2X phase could cause the mode of precipitate formation to change from discontinuous to continuous[31,77]. It has already been proposed that niobium additions reduce the driving force for the formation of the M_2X phase. Thus when niobium is added at intermediate levels with vanadium then it is possible that the overall influence of the two elements is a reduced driving force for M_2X precipitation at 1000°C.

The difference in precipitation behaviour in alloys C and E and in alloys A, B, F, G and H further emphasises the role of niobium on the driving force for the discontinuous cellular reaction. The results of ageing treatments at 1000°C show that the discontinuous cellular reaction in alloy C does not terminate, even when the sample is covered with precipitate colonies. This shows that there is sufficient solute saturation of nitrogen in the base composition, even after extensive Cr_2N precipitation to still drive the discontinuous coarsening reaction. The formation of MX precipitates at 1000°C might also remove nitrogen from solid solution, thus reducing supersaturation in this way. Prolific formation of MX precipitates was not observed in alloys A, B, F, G and H at 1000°C and it is thus doubtful that the formation of this phase would influence the solute supersaturation significantly in the current system.

It is also possible that the formation of large blocky precipitates during solidification removed sufficient nitrogen from solid solution to decrease the driving force for M_2X precipitates to form discontinuously. Calculations similar to those discussed in section 5.1.1 for alloys D and F, were completed for alloy A and show that if all the niobium and vanadium was used up during solidification then the nitrogen level would decrease from 1.02 wt% to 0.8 wt% (a difference of 0.22 wt%). Although it is doubtful that the decrease in nitrogen level would be as large as 0.22 wt%, a decrease of 0.1 wt% from 0.5 wt% influenced the driving force for the discontinuous cellular precipitation reaction[31]. In spite of this observation, the decrease in nitrogen supersaturation is not as significant in alloy A, than a decrease of 0.1 wt% from 0.5 wt% as observed by Kikuchi *et al*[31]. The role of niobium in the high nitrogen steel alloys, on the discontinuous cellular precipitation of M_2X, is emphasised by the observation that only the alloys that contain blocky precipitates show a change in precipitation mode of M_2X precipitates. Alloys C and E do not show a change in precipitation mode and also contain no blocky precipitates during solidification. It is therefore concluded that the addition of niobium influences the driving force for M_2X precipitation which accounts for the change in precipitation mode of the M_2X precipitates in alloys A, B, F, G and H. The way in which niobium influences precipitation is possibly a combination of the effect on the formation of large blocky precipitates (and consequent removal of nitrogen from solid solution) as well the suppression of M_2X precipitation by niobium at 1000°C.

5.3.1.2 *THE INFLUENCE OF NIOBIUM AND VANADIUM ON THE KINETICS OF THE DISCONTINUOUS CELLULAR PRECIPITATION REACTION*

The results show that the addition of vanadium to the high nitrogen steel base alloy results in a larger volume fraction of discontinuous cellular precipitation of M_2X precipitates than observed in the base alloy. This is evident when comparing alloys C and E after ageing for two hours at 800°C and 1000°C. As discussed in section 5.3.1.1, vanadium additions to the high nitrogen steel base alloy results in an increase in solute saturation in the austenite matrix, which in turn favours discontinuous cellular precipitation[62]. It has been demonstrated that a high solute supersaturation will decrease the activation energy for precipitation[133], and therefore increase the nucleation rate for the discontinuous cellular precipitation reaction[55,56]. Thus the addition of vanadium also results in increased precipitation kinetics of the discontinuous precipitation of M_2X precipitates in the high nitrogen steel alloy system. This explains the observation that a larger volume fraction of lamellar precipitates is observed in alloy E compared to alloy C after the same ageing time at 800°C and 1000°C.

Niobium additions might also have a kinetic effect on the growth of precipitate colonies. A common observation in the alloys where a change in precipitation mode was observed is that the precipitates within the colony are fragmented. This might be indicative of a decrease in the boundary velocity during the discontinuous reaction. Ainsely *et al* have shown that when the boundary velocity is slow, the precipitates are particulate in nature, but when the boundary velocity is increased the precipitates have a classic unbroken lamellar structure[76]. Further, evidence was found in the current work that the velocity of boundary migration decreased as the reaction proceeded from the observation that the precipitates within the cells were swollen at the boundary. This suggests that the precipitates widened because they could not lengthen as boundary velocity decreased.

It has been shown in mild steels that the addition of niobium slowed down recrystallisation reactions because of a solute drag effect of this element on the boundaries[84]. Niobium is a large atom compared to the other elements that make up the high nitrogen steel alloy, viz chromium, iron and manganese. This was shown in section 5.1.1, table 5.1.1. It is expected that this element would segregate to the grain boundaries and exert a solute drag effect on any boundary migration that would occur in the alloys. Since boundary migration is fundamental to the occurrence of the discontinuous cellular precipitation reaction, decreased boundary mobility will slow the reaction and perhaps even stop the reaction, causing the M_2X phase to form continuously.

It is also observed in the present work that MX precipitates have nucleated on the grain boundaries, which would inhibit boundary migration. This evidence was observed in alloy D at 1000°C, but in this case it has been shown that niobium suppresses the formation of the M_2X phase at 1000°C rather than slowing the kinetics of formation. The M_2X phase was not observed in alloy D even after ageing at 1000°C for 100 hours. In alloy B however, after ageing at 1100°C, where M_2X precipitates initially formed by the discontinuous cellular reaction, and then later continuously, the MX precipitates are also present in the microstructure. In this case the addition of niobium can have a kinetic effect on the formation of M_2X precipitates. The MX precipitates do not participate in the discontinuous reaction and are therefore able to pin the boundary, slowing boundary migration and even stopping the discontinuous reaction. Further, the discontinuous reaction might have been able to proceed for some time before MX precipitates formed and imposed a pinning effect on the migrating boundary.

The indications are that both niobium and vanadium have a combined thermodynamic and kinetic effect on the discontinuous cellular precipitation of M_2X precipitates. When these elements are added together, their role on the formation of discontinuous cellular precipitation of M_2X precipitation is complex.

5.3.2 TWIN FORMATION IN THE PRECIPITATE CELLS

In a study of the nucleation and growth of discontinuous cellular precipitation of the M_2X lamellae in alloy C during ageing treatments at 1000°C and 800°C, it was shown that extensive twinning occurs within the precipitate cells. The twins were frequently noted as islands within the precipitate colonies. The twin density was greatest during the early stages of the discontinuous reaction and decreased with ageing time (with discontinuous precipitate cell growth). In an attempt to determine whether the twins originated from recrystallisation (dislocation annihilation) or from boundary migration, specimens of alloy C were cold rolled in the laboratory and then annealed for two different times (section 4.3.3). Electron backscatter diffraction (EBSD) studies of these two samples showed that the twin density was greatest following recrystallisation and decreased after further annealing and associated grain growth. The twin density is described in the current study as the number of coherent twin boundaries per unit area, as described by Form *et al*[139].

A number of theories have been proposed for the formation of annealing twins. Some explanations are based on the influence of the interfacial energy of the grain boundary during grain growth and others are more closely associated with a reduction in dislocation density during recrytallisation. Goodhew has proposed that a grain boundary will dissociate during boundary migration in order to reduce its interfacial energy, and result in the formation of an annealing twin[140]. The boundary dissociation and associated formation of twins is shown in figure 5.1.1[140]. The overall effect of the formation of the newly created grain boundary (NCGB) and the two coherent twin boundaries (CT) and the incoherent twin boundaries (IT) is a decrease in interfacial energy of the boundary, compared to the energy of the boundary before dissociation[140]. The decrease in interfacial energy of the boundary during boundary migration is the driving force for annealing twin formation.

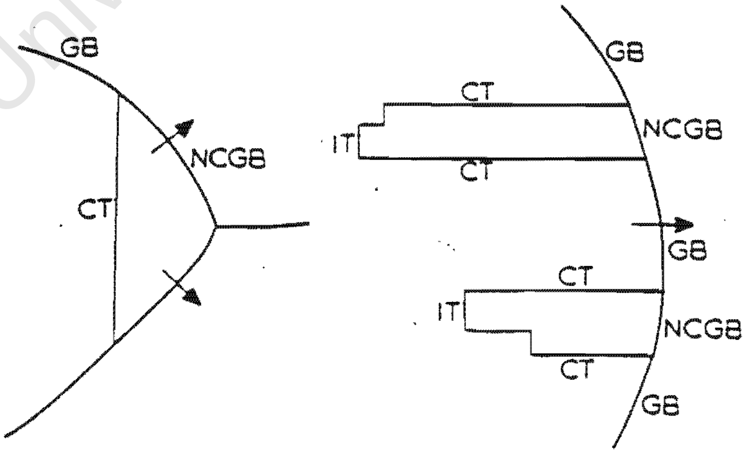

Fig 5.1.1 The formation of a twin during boundary migration as a result of dissociation of the boundary (GB) into a twin and a newly created grain boundary (NCGB) after Goodhew[140]*. The coherent and incoherent twin boundaries are indicated by CT and IT.*

A condition for the mechanism proposed by Goodhew is that twins cannot form as islands within the grains[140]. The mechanisms for twin formation proposed by Goodhew could not be applied to twin formation during discontinuous cellular precipitation since islands of twins were frequently observed within the precipitate colonies. If the driving force for annealing twin formation were a decrease in boundary energy, then following twin formation, the boundary would not dissociate back to its original configuration. In addition, if boundary migration were a prerequisite for twin formation it would be expected that twin density would increase with grain growth or at least not decrease significantly. It was shown in figures 4.3.21 (a) and (b) that twin density decreased with grain growth in the current high nitrogen steel alloy system. Further, the twin density within the precipitate colonies also decreased with increased discontinuous precipitate cell growth. These observations indicate that twin formation is not a consequence of grain boundary dissociation during boundary migration in the current high nitrogen steel system.

Form *et al* have proposed that twin formation during recrystallisation and grain growth results in an easier reaction path for the elimination of dislocations[139]. Thus twin formation is a result of dislocation annihilation during recrystallisation. This was supported by the observation that that twin density per unit area increased with the amount of cold work prior to recrystallisation[139]. The authors also observed that the twin density per unit area decreased with grain growth, which further supports the proposal that twin formation is not a consequence of altering interfacial energy during boundary migration. From this argument, no new twins form during grain growth and in fact some are even annihilated as the larger grains absorb the smaller grains.

It has already been shown that boundary dissociation cannot explain twin formation during discontinuous cellular precipitation. The results of the annealing treatments on the two cold rolled samples of alloy C indicate that twin formation is a result of dislocation annihilation in the current system. The twin boundaries that formed within the precipitate colonies during discontinuous cellular precipitation formed in spite of a fully annealed and solution treated structure prior to ageing.

The dislocations that are necessary for twin boundary formation therefore must originate from the formation of the precipitates within the colonies.

Goodhew suggested that twin boundaries nucleate as a consequence of the emission of partial dislocations at the grain boundary[140]. Goodhew also argued that if this were the case then islands of twins would be present within the grains, and since the author did not observe this mechanism of nucleation it was therefore not investigated further by Goodhew[140]. Since islands of twins in the austenite were observed within the precipitate colonies after discontinuous cellular precipitation of M_2X in the high nitrogen steel alloys, this mechanism of twin formation will be discussed further. In later work by Meyers and Murr, the authors proposed that twin boundaries could nucleate at ledges on a grain boundary[141]. Further they showed that an increase in step or ledge density on the boundary results in an increase in twin density[141]. The ledges on the boundary act as sources for dislocations and in low stacking fault energy materials these dislocations separate into partials connected by a stacking fault[141]. Twin formation is thus initiated by the emission of partial dislocations from a grain boundary[141]. Regular arrays of partial dislocations glide through the matrix resulting in a noncoherent twin boundary and during this process two parallel coherent boundaries are formed[141]. In this way the annealing twin 'pops out' of the boundary as a consequence of the formation of partial dislocations emitted from the steps and ledges on the grain boundary[141].

It has been shown that the formation of a precipitate lamella possessing an HCP crystal structure in austenite is often associated with the formation of partial dislocations at the ledges of the precipitate/austenite boundary[46]. These ledges are common to precipitates with a lamellar structure and growth of the lamellae occurs by the so-called ledge mechanism[133]. Figure 5.1.2 shows a schematic of the ledges that exist on such a precipitate.

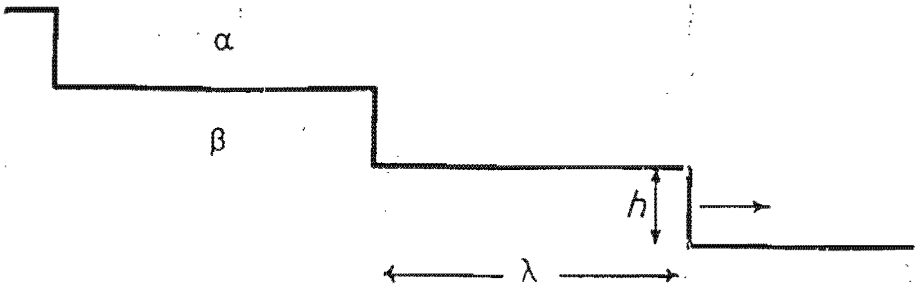

Fig 5.1.2 The ledges associated with plate-like precipitates after Porter and Easterling[133]. This diagram shows a β precipitate in an α matrix. The height of the ledge is represented by h and the length of the ledge by λ.

Furuhara *et al* reported that for an HCP precipitate in an FCC matrix, the partial dislocations form at the ledges of a precipitate in order to minimise the misfit strain energy between the precipitate and matrix[46]. This has been noted to occur in the current study from the observation of stacking faults between M_2X precipitate lamellae in the high nitrogen steel alloy system, shown in 4.3.22. Dislocations were also frequently observed between the precipitate lamellae that formed discontinuously in the high nitrogen steel alloys. The formation of partial dislocations in the current high nitrogen steel system is favoured because of the low stacking fault energy associated with the high nitrogen and manganese levels[22].

From these observations and arguments, it is first concluded that twin formation is the result of dislocation annihilation in the current system. Further it is proposed that the formation of twin boundaries within the precipitate colonies during discontinuous cellular precipitation of the M_2X lamellae originates from the development of the precipitates themselves. The precipitates have an HCP structure and grow in the FCC matrix so that the close packed planes and directions of the phase are parallel. Dislocations and partial dislocations form between the lamellae within the cells and thus provide the source of twin formation within the precipitate colonies. The edges of the plate-like lamella represent a source of ledges where partial dislocations can nucleate. As described by Meyers and Murr the ledges could act as nucleation sites for the formation of twin boundaries[141]. It follows from this argument then that twin density is proportional to the number of ledges per unit area in the steel. During the early stages of growth of the precipitate colonies, there are many ledges on the precipitate lamellae, since the lamellae are expected to grow by the ledge mechanism. After extended ageing, when the driving force for precipitate growth has decreased, there are fewer ledges on the edges of the precipitate. This explains why fewer twin boundaries are observed in the discontinuous precipitate cell colonies in alloy C after ageing at 1000°C for 10 hours (figure 4.3.22 (b)) compared to the 10 minute ageing treatment at the same temperature (figure 4.3.22 (a)). This argument is further supported by the observation that a greater twin density is observed within the precipitate colonies in alloy C after ageing at 800°C (figure 4.4.13) than after ageing at 1000°C (4.3.20 (a)) for the same period of time. The interlamellar spacing of the M_2X lamellae in alloy C after ageing at 800°C is finer than after ageing at 1000°C. This means that there will be a greater number of ledges per unit area, and therefore more nucleation sites for twin formation in the austenite between the lamellae after the 800°C ageing treatment than the 1000°C ageing treatment.

5.4 THE MECHANICAL PERFORMANCE OF HIGH NITROGEN STEEL ALLOYS WITH NIOBIUM AND VANADIUM ADDITIONS

The influence of niobium and vanadium on the microstructure and mechanical properties of the high nitrogen steel alloys is summarised in tables 5.4.1 and 5.4.2 respectively. Niobium and vanadium additions have a profound effect on the precipitation reactions in the current system. Equally the precipitation reactions in the current system play an important role in the mechanical performance of the steel.

Vanadium additions favour the formation of M_2X precipitates at 1100°C, and cause the discontinuous cellular precipitation of M_2X precipitates to be more prolific at

1000°C and 800°C. In addition vanadium additions also favour the formation of sigma phase at 800°C. It has already been discussed that these phases have a detrimental effect on the mechanical properties of the steel. The consequence therefore, of the addition of vanadium to the current system together with ageing treatments between 800°C-1100°C is a reduction in ductility and wear performance of the alloy.

The effect of vanadium additions on M_2X precipitation also has implications on the microstructural evolution during cooling through the 1100°C-800°C temperature range when casting such a steel shown in figure 4.1.11 (d). A greater volume fraction of lamellar precipitates is observed in the as cast condition in alloy E than in alloy C (figure 4.1.11 (b). Any high nitrogen steel alloy with vanadium additions must therefore be cooled rapidly through this temperature range to avoid M_2X precipitation. Alternatively, following slow cooling through 1100°C-800°C the alloy will have to be solution treated at 1300°C for approximately two hours and then water quenched to dissolve the M_2X precipitates and promote a fully austenitic structure (figure 4.1.2 (b)). The mechanical performance of a high nitrogen steel alloy (alloy E) with vanadium additions is similar to that of the base composition (alloy C). The only difference is a marked reduction in fracture toughness associated with the vanadium additions. The addition of vanadium without niobium does not favour any precipitation reaction that results in strengthening of the steel, thus there is no benefit associated with the addition of vanadium.

Niobium additions to the base composition limit the loss in ductility as a consequence of M_2X precipitation by suppressing the formation of this phase. A consequence of the effect of niobium on M_2X precipitation is that high nitrogen steel alloys with niobium additions can be cooled more slowly through the 1100°C-800°C temperature range because niobium additions suppress the discontinuous reaction. No lamellar precipitation was observed in alloy D (figure 4.1.12 (b) in the as cast condition, whereas lamellar precipitates were observed in alloy C (figure 4.1.11 (b)) in the as cast condition. Thus the addition of niobium is beneficial, in view of the effect on the discontinuous precipitation of M_2X precipitates, common to high nitrogen steels.

Niobium additions favour the formation of MX precipitates, which have some strengthening effect on the steel. These precipitates did show some potential for improved wear performance and could possibly be optimised further by different niobium and vanadium levels and ageing treatments at 1100°C.

The influence of niobium on the solidification behaviour represents a disadvantage for the addition of this element. The large blocky precipitates that formed even when niobium was added at low levels reduced the toughness of the steel considerably. High nitrogen steels have gained much popularity because of their excellent combination of high strength and good toughness thus any alloy addition which causes a reduction in the toughness of the steel is not desirable. Thus careful consideration must be given to the addition of niobium in view of its effect on the solidification behaviour of the steel.

The large blocky precipitates that form as a result of niobium additions reduce the wear performance of the high nitrogen steel alloys compared to the base alloy. Even after the formation of MX precipitates during ageing treatments at 1100°C, the wear performance of the high nitrogen steel alloys is not improved compared to the base composition (alloy C). It could not be determined whether the fine MX precipitates caused the reduction in wear resistance or if it was the large blocky precipitates inherent in alloys A, D and H that caused poorer wear performance compared to alloy C. Since niobium favours the formation of large blocky precipitates during solidification, any advantage associated with the formation of MX precipitates which is also a consequence of niobium additions, is offset by the presence of the blocky precipitates.

*Table 5.4.1 The influence of **niobium** on the microstructure and mechanical properties of the high nitrogen steel alloys alloy.*

	1300℃	***1100℃***	***1000℃***	***800℃***
Microstructure	Favours the formation of blocky precipitates that form eutectically.	Favours MX precipitation over M_2X precipitation.	Suppresses DCP of M_2X by thermodynamic and kinetic effects.	Does not suppress DCP of M_2X.
Mechanical Behaviour	Reduces toughness. Maintains yield strength & elongation to failure. Reduces wear performance.	Increases yield strength-maximum in the under aged condition together with reduced elongation to failure. Improved wear performance in over aged condition.	Decreases ductility when lamellar precipitation is not prevented.	Exaggerated reduction in ductility as a result of lamellar precipitates and sigma phase.

Table 5.4.2 *A summary of the influence of* ***vanadium*** *on the microstructure and mechanical properties of the high nitrogen steel alloys.*

	1300 °C	***1100 °C***	***1000 °C***	***800 °C***
Microstructure	Does not favour the formation of blocky precipitates that form eutectically. Participates in the eutectic reaction when niobium is added, resulting in niobium and vanadium rich blocky precipitates.	Favours M_2X precipitation over MX precipitation.	Exaggerated DCP of M_2X.	Exaggerated DCP of M_2X and sigma phase
Mechanical Behaviour	Results in the same tensile properties and wear resistance as alloy C.	Increased yield strength, with decreased elongation to failure. Low wear resistance when M_2X precipitation is favoured over MX precipitation.	Increased yield strength, with decreased elongation to failure because of M_2X precipitates.	Extreme loss in ductility as a result of lamellar precipitates and sigma phase.

6. CONCLUSIONS

- **THE INFLUENCE OF NIOBIUM ON THE HIGH NITROGEN STEEL ALLOYS**
  - Niobium additions favour the formation of large blocky precipitates, which form eutectically during solidification of the melt.
  - Niobium additions in the absence of vanadium thermodynamically suppress the formation of chromium nitride (Cr_2N) precipitates at 1000°C, but at 800°C niobium was not able to prevent this form of precipitation.
  - Niobium additions in the presence of vanadium have been proposed to have both a kinetic and thermodynamic influence on the discontinuous cellular precipitation reaction.
  - Niobium additions did result in the formation of fine niobium rich nitrides (MX precipitates) at elevated temperature. When vanadium was added with niobium the precipitate distribution was coarser and the particles were rich in both niobium and vanadium.
  - The addition of niobium to alloys with vanadium favoured the formation of fine MX precipitates in preference to the M_2X lamellae, when the niobium and vanadium balance was such that the value for V_{in} (section 5.2.1) was less than 0.45, at 1100°C.

◆ THE INFLUENCE OF VANADIUM ADDITIONS ON THE HIGH NITROGEN STEEL ALLOY

- Vanadium additions do not favour the formation of large blocky precipitates during solidification, but when added together with niobium, the vanadium participates in the eutectic reaction, resulting in large blocky precipitates rich in both niobium and vanadium.

- Vanadium additions favour the discontinuous cellular precipitation of M_2X precipitates in the high nitrogen steel alloy, by increasing the solute saturation in the austenite with respect to this precipitate. Further, vanadium additions expand the phase field for this form of precipitation to higher temperatures, ie 1100°C, compared to the base composition, where it is observed up to 1000°C.

- Vanadium additions favour the formation of MX precipitates, but only when niobium is also added to the steel and the niobium and vanadium balance is optimised to avoid the formation of M_2X precipitates. If the elements are not balanced correctly any advantage of MX precipitation is offset by M_2X precipitation.

- Vanadium additions favour the formation of sigma phase at 800°C in the high nitrogen steel alloys.

◆ DISCONTINUOUS CELLULAR PRECIPITATION IN THE HIGH NITROGEN STEEL ALLOYS

- The boundary diffusion of solute and the ability of the boundary to migrate is of fundamental importance to the formation of discontinuous cellular precipitates in the high nitrogen steel alloys.

- The boundary migration necessary for the reaction originates from conditions that are set up by the nucleation of the chromium rich (and in the case of vanadium alloyed samples, chromium and vanadium rich) M_2X precipitates. Immediately after nucleation, the boundary migrates in search of solute to feed growth of the precipitates. At this point the possible driving forces that exist for boundary migration are the search for solute, the steep concentration gradient ahead of the boundary and possibly a coherency strain effect.

- Evidence found for the 'pucker mechanism' suggests that this mechanism might operate during the initial stages of cell development. Based on criticisms and observations by other authors, it is not proposed that this mechanism accounts for the total driving force for discontinuous precipitation in the high nitrogen steel alloy.

- Once the reaction has initiated, it proceeds as a type of diffusion induced boundary migration process. The boundary therefore, migrates to feed solute to the growing precipitates and a type of co-operative effect between precipitate growth and boundary migration is established.

◆ THE INFLUENCE OF PRECIPITATION REACTIONS ON THE MECHANICAL BEHAVIOUR OF THE HIGH NITROGEN STEEL ALLOYS

- The formation of blocky precipitates during solidification does not have a significant effect on the tensile properties of the steel, but reduces the toughness considerably.

- The presence of blocky precipitates in the steel reduces the wear performance of the steel compared to the base composition alloy.

- The influence of MX precipitation on the tensile properties shows some sensitivity to the ageing time at 1100°C.

- Equally, the wear performance of the alloy with fine MX precipitates shows some sensitivity to the ageing time at 1100°C. The general trend is that the wear performance of alloys with MX precipitates was better after longer ageing times than shorter ageing times.

- The high nitrogen steel base composition showed superior wear resistance to alloys that contained any form of precipitation, including those with a favourable distribution of MX precipitates for wear resistance.

- The formation of M_2X precipitates at 1000°C results in increased yield strength, and reduction in ductility. The loss in ductility is a consequence of M_2X precipitation and is exaggerated after ageing at 800°C as a consequence of the formation of sigma phase.

- The formation of M_2X precipitates reduced the abrasive wear performance of the steel considerably compared to the CROMANITE™ base composition.

REFERENCES:

[1] Heinmann, W., Oppenheim, R., Weβling, W., in 'Steel, A Handbook for Materials Research and Engineering, Volume II: Applications, Eds: Veriein Deutscher Eisenhuttenleute, Springer, Düsseldorf, 1992

[2] Bavay, J.C., in 'Stainless Steel' Eds: Lacombe, P., Baroux, B., Beranger, G., Les Edditions de Physique Les Illis, France, 1993

[3] Marshall, P., in 'Austenitic Stainless Steels', Elsevier Applied Science, London, 1984

[4] Irvine, K.J., Llewellyn, D.T., Pickering, F.B., JISI, 1961

[5] Rawers, J., Gurjicic, M., Mat. Sci. Eng., **A207**, p 1996

[6] Gavriljuk, V.G., ISIJ Int., **36**, p738, 1996

[7] Uggowitzer, P.J., Madowski, R., Speidel, M.O., Proc. Innovative Stainless Steels, Florence, Italy, p2.359, 1993

[8] Gunia, R.B., Woodrow, G.R., J. Mat., **5**, p413 1970

[9] Reed, R.P., JOM, March, p16, 1989

[10] Menzel, J., Kirschner, W., Stein, G., ISIJ Int., **36**, p893, 1996

[11] Uggowitzer, P.J., Bähre, W.-F., Wohlfromm, H., Speidel, M.O., Mat. Sci. Forum, **318-320**, p663, 1999

[12] Columbus Stainless, Private Communication

[13] Simmons, J., Metall. Mater. Trans., **26A**, p2085, 1996

[14] Rechsteiner, A., Speidel, M.O., Proc. Inoovative Stainless Steel, Florence, Italy, October, p2.107, 1993

[15] Rawers, J. , Petty, A.V., Jnr., J. Mat. Sci., **28**, p3489, 1993

[16] Berns, H., Z. Metalkde., **86**, p156, 1995

[17] Lula, R.A., Proc, International Conference on High Nitrogen Steels, ohio

[18] Rama Rao, P. Kutumbarao, V.V., Int. Mat. Rev., **34**, p69-86, 1989

[19] Uggowitzer, P.J. & Harze nmoser, M., Proc International Conf HNS

[20] Werner, E., Mat. Sci. Eng., **A101**, p93, 1988

[21] Norström, L.-Å., Metal Science, June, p208, 1977

[22] Stoltz, R. E., Vandersande, J.B., Metall. Trans. **11A**, p1033, 1980

[23] Schram, R.E., Reed, R. P., Metall. Trans., **6A**, 1975

[24] Müller, P., Solenthaler, C., Uggowitzer, P., Speidel, M.O., Mat. Sci. Eng., **A146**, p164, 1993

[25] Degallaix, S., Foct, J., Hendry, A., Mat. Sci. & Tech., **2**, p946, 1986

[26] Ohkubo, N., Miyakusu, K., Uematsu, Y.& Kimura, H., ISIJ Int., **34**, p764, 1994

[27] Paulus, N., Uggowitzer, P.J., Müller, Speidel, M.O., Proc. Innovative Stainless Steel, Florence, Italy, October, p3.315, 1993

[28] Müller, P., Solenthaler, C., Speidel, M.O., Acta Metall. Mater. **42**, p1727, 1994

[29] Tomota, Y., Xia, Y., Inoue, K., Acta. Mater., **46**, p 1577 1998

---

[30] Müller, P., Solenthaler, C., Uggowitzer, P.J. Speidel, M.O., Acta Metall. Mater., **42**, p22117, 1994

[31] Kikuchi, M., Kajihara, M., Choi, S., Mat. Sci. Eng., **A146**, p131, 1991

[32] Vanderschaeve, F., Taillard, R., Foct, J., J. Mat. Sci., **30**, p6035, 1995

[33] Shankar, P., Sundaraman, D., Ranganathan, S., Scripta. Metall. Mater., **31**, p589, 1994

[34] Hillert, M., Lagneborg, R., J. Mat. Sci., **6**, p208, 1971

[35] Mukherjee, J.K., Nijhawan, B.R., JISI, Jan., p62, 1967

[36] Ustinovshikov, Y., Ruts, A., Bannykh, O., Blinov, V., J. Mat. Sci., **29**, p5449, 1994

[37] Ustinovshikov, Y., Ruts, A., Bannykh, O., Blinov, V., Acta Mater., **44**, 3, p1119, 1996

[38] Rayaprolu, D.B., Hendry, A., Mat. Sci. Tech., **5**, p328, 1989

[39] Jargelius-Pettersson, R.F.A., Scripta. Metall. Mater., **30**, p1233, 1994

[40] 'Convergent Beam Electron Diffraction of Alloy Phases' The Bristol Group, John Steeds, compiled by John Mansfield, Adams Hilger Limited, p27, 1984

[41] Goldschmidt, H.J., in 'Interstitial Metal Alloys', Butterworths, London, 1967

[42] Simmons, J.W., Atteridge, D.G., Rawers, J., J. Mat. Sci., **27**, p6105, 1992

[43] Sundararaman, D., Shankar, P., Raghunathan, V.S., Metall. Mat. Trans., **27A**, p1175, 1996

[44] Williams, D.B. & Barry Carter, B., Transmission Electron Microscopy, Plenum Press, New York, 1996

[45] Presser, R., Silcock, J.M., Metal Science, **17**, p241, 1983

[46] Furuhara, T., Maki, T., Scripta. Mater., **34**, p929, 1996

[47] Howie, J.M., Dahmen, U., Gronski, R., Phil. Mag., **A 56**, p31, 1987

[48] Khalid, F.A., Edmonds, D.V., Acta Metall., **41**, p3421, 1993

[49] Jargelluis-Pettersson, R.F.A., Scr. Metall., Mater., **28**, p1399, 1993

[50] Williams, D.B. & Butler, E.P., Int. Met. Rev., **3**, p153,1981

[51] Doherty, R.D., Physical Metallurgy II, eds:Cahn, R.W. & Haasen, P., North-Holland Physics Publishing, Amsterdam, 1983

[52] Fournelle, R. A., Acta Metall. **27**, p1135, 1979

[53] Tu, K.N., Turnbull, D., Acta Metall., **15**, p369, 1967

[54] Tu, K.N., Turnbull, D., Acta Metall., **15**, p1317, 1967

[55] Turnbull, D., Treaftis, H.N., Acta Metall., **3**, p43, 1955

[56] Turnbull, D., Acta Metall., **3**, p55, 1955

[57] Tu, K.N., Metall. Trans., **3**, p2769, 1972

[58] Aaronson, H.I., Aaron, H.B., Metall. Trans., **3**, p2743,1972

[59] Nes, E., Billdal, H., Acta Metall., **25**, p1039, 1977

[60] Meyrick, G., Scripta. Metall., **10**, p649, 1976

[61] Fournelle, R.A., Clarke, J.B., Metall. Trans., **3**, p2757, 1972

[62] Hornbogen, E., Metall. Trans. **3**, p2717, 1972

[63] Sulonen, M.S., Acta Metall., **8**, p669, 1960

---

[64] Sulonen, M.S., Acta Metall, **12**, p749, 1964

[65] Hillert, M., Metall. Trans., **3**, Nov, p2729, 1972

[66] King, A.H., Int. Mater. Rev., **32**, p173,1987

[67] Yoon, D.Y., Int. Mater. Rev., **40**, p149, 1995

[68] Balluffi, R.W., Cahn, J.W., Acta Metall., **29**, p493, 1981

[69] Li, C.M., Chaturvedi, M.C., Tandon, K.N., Mater. Characterisation, **30**, p89, 1993

[70] Hillert, M., Scripta Metall., **17**, p237, 1983,

[71] Rabkin, E., I., Scripta Metall. Mater., **30**, p1443, 1994

[72] Ma, C.Y., Rabkin, E., Gust, W., Hsu, S.E., Acta Metall. Mater., **43**, p3113, 1995

[73] Louat, N., Phil. Mag. A, Letters, **51**,pL73, 1985

[74] Kasen, M.B., Phil. Mag. A, Letters, **54**, pL31, 1986

[75] Faulkner, R.G., Mat. Sci. Tech., **9**, p118, 1993

[76] Ainsely, M.H., Cocks, G.J., Miller, D.R., Metal Science, p20, 1979

[77] Ainsely, M.H., Cocks, G.J., Miller, D.R., Scripta Metall., **14**, p539, 1980

[78] Hagel, W.C., Beattie, H.J., Trans. AIME, **215**, p967, 1959

[79] Cahn, R.W., Haasen, P., Physical Metallurgy I, North Holland Physics Publishing, Amsterdam, 1983

[80] Lücke, K, Detert, K., Acta Metall., **5**, p628, 1975

[81] Gupta, D., Metall. Trans., **8A**, p1431, 1977

[82] Zi-Kui Liu, Metall. Mat. Trans. **28A**, p1625, 1997

[83] Suehiro, M., Zi-Kui Liu, Ågren, J., Metall. Mat. Trans. **29A**., p1029, 1998

[84] Suehiro, M., JISI, p547, 1998

[85] Baumann, S.F. & Williams, D.B., Proc. 37th Annual Meeting of the Electron Microscopy Society of America, **646**, p194, 1979

[86] Pickering, F.B.,in 'Physical Metallurgy and Design of Steels', eds:Kelly, A., Elsevier, New York, 1978

[87] Karlsson, L., Henjered, A., Andrén, H. -O., Nordén, H., Mat. Sci. Tech., **1**, p337, 1985

[88] Boothby, R.M., Mat. Sci. Tech., **2**, p78, 1986

[89] Cottrell, A.H., Mat. Sci. Tech., **11**, p329, 1995

[90] Andrén, H.-O., Henjered, A., Nordén, H., J. Mat. Sci., **15**, p2365, 1980

[91] Dunlop, G.L., Turner, P.J., Metal Science, **9**, p370, 1975

[92] Jack, D.H., Jack, K.H., JISI, p790, 1972

[93] Shinoda, T., Ishii, T., Tanaka, R., Mimino, T., Kinoshita, K., Minegishi, I., Metall. Trans., **4**, p1213, 1973

[94] Dunlop, G.L., Honeycombe, R.W.K., Metal Science, p367, 1978

[95] Miyhara, K., Bae, D. Shimoide, Y., J. Nucl. Mat., **212-215**, p766, 1994

[96] Källqvist, J., Andrén, H.-O., Mat. Sci. Eng. **A270**, p27, 1999

---

[97] Wen-Tai, H., Honeycombe, R.W.K., Mat. Sci. Tech., **1** May, p385, 1985

[98] Wen-Tai, H., Honeycombe, R.W.K., Mat. Sci. Tech., **1**, May, p390, 1985

[99] Heikkinen, V.K., Packwood, R.H., Scand. J. Metall., **6**, p170, 1977

[100] Hannerez, N.E., Lindborg, U., Lehtinen, B. JISI, p68, 1968

[101] Vodopivec, F., Gabrovšek, M., Ralic, B., Metal Science, **9**, p324, 1975

[102] Itman, A., Cardoso, K.R., Kestenbach, H. –J., Mat. Sci. Tech., **13**, p49, 1997

[103] Dupont, J.N., Robino, C.V.,Marder, A.R., Acta Mater., **46**, p4781, 1998

[104] Albarran, J.L., Camplillo, B., Estevez, F., Martinez, L., Scripta Metall., **23**, p1099, 1989

[105] Campillo, B., Albarran, Estevez, F., R., Lopez, D., Martinez, L. Scripta Metall., **23**, p1368, 1989

[106] Jiang, W.H., Pan, W.D., Ren, Y.L., Han, X.L., J. Mat. Sci. Letters, **17**, p1527, 1998

[107] Hawk, J.A., Simmons, J.W., Rawers, J.C., J. Mat. Eng. Performance., **3**, p259, 1994

[108] Campillo, B., Flores, O., Albarran, J.L., Juarez-Islas, J., Perez, R., Martinez, L., Lopez, D. J. Mat. Sci., **27**, p1365, 1992

[109] Xiaodong, L., Solberg, J.K., Gjengedal, R., Kluken, A., Mat. Sci. Eng., **A188**, p247, 1994

[110] Rios, P.R., Mat. Sci. Tech., **4**, p324, 1988

[111] Xiaodong, L., Solberg, J.K., Gjengdal, R., Kluken, A., Scripta Metall. Mater., **31**, p1607, 1994

[112] Nordberg, H., Aronsson, B., JISI, p1263, 1968

[113] Speer, J.G., Michael, J.R., Hansen, S.S., Metall. Trans., **18A**, p211, 1987

[114] Stoltz, E., Steel, in 'A Handbook for Materials Science and Research', Vol 1:Fundamentals, eds: Verein Deutdcher Eisenschuttenleute, Springer, Düsseldorf, 1992

[115] Rabinowicz, E., in 'Friction and Wear of Material', John Wiley & Sons Inc., USA, 1995

[116] Hutchings, I.M., Tribology, in 'Friction and Wear of Engineering Materials', Edward Arnold, London, 1992

[117] Ball, A., Wear, **91**, p201, 1983

[118] Ball, A., J. S. Afr. Inst. Min. Metall., **86**, p1, 1986

[119] Mills, D.J., Knutsen, R.D., Wear, **215**, p83, 1998

[120] Lenel, U.R., Knotts, B.R., Metall. Trans., **18A**, p847, 1987

[121] Basak, A., Roy, D.K., Dutta, G.L., Wear, **18**, p241, 1995

[122] Nicholson, R.B., 'The Effect of Second Phase Particles on the Mechanical Properties of Steel', Iron and Steel Institute, London,p1, 1971

[123] Rawers, J.C., Dunning, J.S., Asai, G., Reed, R.P., Metall. Trans., **23A**, p2061, 1992

[124] Simmons, J.W., Metall. Mat., Trans., **26A**, p2085, 1995

[125] Chandra Holm, H., Uggowitzer, P.J., Speidel, M.O., Scripta Metall., **21**, p513, 1987

[126] Simmons, J.W., Atteridge, D.G., Rawers, J.C., Corrosion, **50**, p491, 1994

[127] Chouby, R., Gibbons, T.B., Prasad, K., Metals Tech., p524, 1977

[128] Hamerton, R.G., Jaeger, D.M., Jones, A.R., Proc. Innovative Stainless Steel, Florence, Italy, October, p2.421, 1993

[129] Humphreys, J., Manchester Materials Science Centre and UMIST

[130] Thomson, M. N., Electron Optics Reporter, **30**, 1EM, p1, 1983

[131] Cotton*, J.A., Knutsen., R.D. & Sundman, B., Mat. Sci. Forum, **318-320**, p89, 1999

*(*Cotton, J.A. now married, Basson, J.A., author of the current thesis)*

[132] Edington, J.W., in 'Practical Electron Microscopy in Materials Science', Philips' Gloeilampenfabrieken, Eindhoven, 1976

[133] Porter, D.A., Easterling, K. E., in 'Phase Transformations in Metals and Alloys', Van Nostrand Reinhold (UK), Co. Ltd., Berkshire, England, 1981

[134] Smithels, C.J., in 'Metals Reference Book', Vol I & II, Butterworths, London, 1962

[135] Darken, S.L., Gurry, R.W., in 'Physical Chemistry of Metals', Mc Graw-Hill, New York, 1953

[136] Harris, J.B., M.Sc Thesis, University of Cape Town, 1983

[137] Mills, D.J., M.Sc. Thesis, University of Cape Town, 1996

[138] Findik, F., J. Mater. Sci. Letters, **17**, p79, 1998

[139] Form, W., Grindraux., G., Mlyncar, V., Metal Science, p16, 1980

[140] Goodhew, P.J., Metal Science, p108, 1979

[141] Meyers, M.A., Murr, L.E., Acta Metall., **26**, p951, 1978

'For every house is built by someone, but God is the builder of everything.'

-HEBREWS CH 3VS 4 (NIV)